Universität Bremen

Unraveling Atmosphere and Sea Ice in the Arctic

Advancements in a Multi-Parameter Retrieval using Satellite Microwave Radiometer Data

Dissertation by

Janna Elisabeth Rückert

in fulfilment of the requirements
for the degree of

Doctor of Natural Sciences (Dr. rer. nat.)

submitted to

Faculty for
Physics and Electrical Engineering
University of Bremen

Submission: 19 January 2024
Colloquium: 12 April 2024

1st Reviewer: Dr. Gunnar Spreen
Institute of Environmental Physics
University of Bremen

2nd Reviewer: Prof. Dr. Susanne Crewell
Institute for Geophysics and Meteorology
University of Cologne

This dissertation was written in the working group 'Remote Sensing of Polar Regions' of the Institute of Environmental Physics, University of Bremen.

Abstract

The Arctic undergoes accelerated warming compared to Global Warming, known as Arctic amplification. To understand this phenomenon, studying key variables at various scales is crucial. Every day, satellite radiometers measure Arctic-wide emissions of microwave radiation in terms of brightness temperatures. These observations carry information about both the surface, e. g., sea ice coverage, and the atmosphere, e. g., water vapor content. We use the distinct sensitivities of observations at different frequencies to atmospheric and surface parameters, aiming to disentangle the satellite signal and improve a multi-parameter retrieval. The retrieval involves inverting a forward model with an optimal estimation method to attribute satellite measurements (6.9 to 89 GHz) to a specific geophysical state. For that, sea ice and snow emissions need to be well represented in the forward model. We study surface emissions by considering the theoretical concept of emissivity followed by an analysis of brightness temperature measurements and derived emissivities that we obtained during a summer ship campaign. Results show a clear distinction between sea ice and open ocean for frequencies between 22 and 31 GHz, vertical polarization. Sea ice emissivities at 243 GHz, horizontal polarization, vary widely and can be both higher and lower than open ocean emissivities.

In a MOSAiC expedition case study, we examine the impact of changing surface emissions on sea ice concentration (SIC) satellite retrievals. Warm air intrusions modify surface properties, affecting microwave emission and scattering characteristics. Our findings indicate that SIC algorithms underestimate true SIC when there is a thin ice crust atop the snow caused by the warm air.

The core of this thesis is the improvement of the multi-parameter retrieval by a better representation of the sea ice and snow emissions in the forward model for non-melting conditions. Both forward model and retrieval are evaluated against ground truth, including datasets from the MOSAiC expedition. The forward model succeeds in simulating realistic temporal evolution and distributions of brightness temperatures. The retrieval output agrees well with reference data with regard to SIC. While the retrieval of cloud liquid water path and snow depth are promising, some disagreements are identified and we compile a comprehensive collection of potential further improvements and extensions of the method. Focusing on atmospheric total water vapor (TWV), our analysis demonstrates a good agreement with numerous reference datasets, including campaign and coastal station data. We find a substantial improvement over the previous version of the method. After applying the retrieval to satellite data from the last two decades we find dry conditions in winter over sea ice. Mean values are below $4\,\mathrm{kg\,m^{-2}}$ and variabilities range from $0.5\,\mathrm{kg\,m^{-2}}$ to $2.5\,\mathrm{kg\,m^{-2}}$ and are higher in the regions closer to the ice edge. In some areas over sea ice we observe a robust moistening trend in winter but whether the Arctic atmosphere has become wetter or drier strongly depends on the region, month and considered time span.

Zusammenfassung

Im Vergleich zur globalen Erwärmung erwärmt sich die Arktis stärker und schneller, ein Phänomen, das als arktische Verstärkung bekannt ist. Um dieses zu verstehen, ist die Beoboachtung von geophysikalischen Größen, wie der Meereisbedeckung oder des atmosphärischen Wasserdampfgehalts, von entscheidender Bedeutung. Jeden Tag messen Satellitenradiometer arktisweit Emissionen von Mikrowellenstrahlung in Form von Helligkeitstemperaturen. Mikrowellenstrahlung wird, abhängig von der Frequenz, unterschiedlich stark von den verschiedenen atmosphärischen und Oberflächenparameter beeinflusst. Wir nutzen diesen Umstand, um das Satellitensignal zu entschlüsseln und eine satellitenbasierte gleichzeitige Bestimmung mehrere Parameter, ein sogenanntes Multi-Parameter Retrieval, zu verbessern. Die Methode beinhaltet die Umkehrung eines Vorwärtsmodells mit einem bayesschen Verfahren, um Satellitenmessungen (6.9 bis 89 GHz) einem bestimmten geophysikalischen Zustand zuzuordnen. Dazu müssen die Emissionen vom (schneebedeckten) Meereis im Vorwärtsmodell gut dargestellt werden.

Wir beleuchten zunächst das theoretische Konzept der Emissivität, und analysieren dann Helligkeitstemperaturen und daraus abgeleitete Emissivitäten, die wir während einer Schiffskampagne in der arktischen Eisrandzone im Sommer 2022 gemessen haben. Wir finden einen klare Unterschied zwischen Meereis und offenem Ozean für Messungen zwischen 22 und 31 GHz bei vertikaler Polarisation. Die Emissivität von Meereis bei 243 GHz, horizontaler Polarisation, variiert stark und kann sowohl höher als auch niedriger sein als die Emissivität des offenen Ozeans.

In einer Fallstudie von der MOSAiC-Expedition untersuchen wir die Auswirkungen veränderter Oberflächenemissionen auf die Satellitenmessungen der Meereiskonzentration. Warmlufteinbrüche verändern die Oberfläche und wirken sich auf die Mikrowellenemission und die Streuungseigenschaften aus. Wir können zeigen, dass einige Meereiskonzentrationsalgorithmen die tatsächliche Meereiskonzentration unterschätzen, wenn sich auf dem Schnee eine dünne Eiskruste, verursacht durch die warme Luft, befindet.

Das Kernstück dieser Arbeit ist die Verbesserung des Multi-Parameter Retrievals durch eine bessere Darstellung der Meereis- und Schneeemissionen im Vorwärtsmodell. Sowohl das Vorwärtsmodell als auch das Retrieval werden anhand von Daten der MOSAiC-Expedition evaluiert. Mit dem Vorwärtsmodell gelingt es, eine realistische zeitliche Entwicklung und Verteilung der Helligkeitstemperaturen zu simulieren. Der Großteil der Abweichungen zwischen den Ergebnissen des Vorwärtsmodells und den Satellitenmessungen kann durch die Wahl der Modellparameter erklärt werden.

Die abgeleiteten Meereinskonzentrationen aus dem Multi-Parameter Retrieval stimmen gut mit den Referenzdaten überein. In Bezug auf Wolkenflüssigwasser und Schneehöhe sind die Ergebnisse vielversprechend, aber wir stellen auch einige Unstimmigkeiten fest und legen umfassende mögliche Verbesserungen und Erweiterungen der Methode dar.

Unsere Analyse konzentriert sich auf den atmosphärischen integrierten Wasserdampfgehalt und zeigt eine gute Übereinstimmung mit zahlreichen Referenzdatensätzen, einschließlich Kampagnendaten und küstennahen Landstationsdaten. Wir stellen eine wesentliche Verbesserung gegenüber der vorherigen Version der Methode fest. Die Satellitendaten bestätigen, dass im Winter über dem Meereis trockene Bedingungen herrschen: Mittelwerte des integrierten Wasserdampfgehalts liegen unter $4\,\mathrm{kg\,m^{-2}}$ und die Variabilitäten reichen von $0.5\,\mathrm{kg\,m^{-2}}$ bis $2.5\,\mathrm{kg\,m^{-2}}$. Nach Anwendung der Methode auf Satellitendaten der letzten zwei Jahrzehnte finden wir einen robusten Anstieg des integrierten Wasserdampfgehalts in einigen Regionen über Meereis. Ob die Atmosphäre trockener oder feuchter geworden ist, hängt stark von der betrachteten Region, dem Monat und der untersuchten Zeitspanne ab.

Acronyms

AA Arctic amplification

ACSYS Arctic Climate System Study

(AC)^3 Arctic Amplification: Climate Relevant Atmospheric and Surface Processes and Feedback Mechanisms

AIDJEX Arctic Ice Dynamics Joint Experiment

AIRS Atmospheric Infrared Sounder

AMSR-E Advanced Microwave Scanning Radiometer - Earth Observing System

AMSR2 Advanced Microwave Scanning Radiometer 2

AMSU Advanced Microwave Sounding Unit

ARM Atmospheric Radiation Measurement

ASI ARTIST Sea Ice

ATWAICE ATlantic WAter pathways to the ICE in the Nansen Basin and Fram Strait

CDR Climate Data Record

CEAREX Coordinated Eastern Arctic Experiment

CIMR Copernicus Imaging Microwave Radiometry

CO Central Observatory

EASE Equal-Area Scalable Earth

ECMWF European Centre for Medium-range Weather Forecasts

ERA5 ECMWF Reanalysis v5

FOV field of view

FYI first-year ice

GNSS Global Navigation Satellite System

HALO High Altitude and long Range Aircraft

HATPRO Humidity and Temperature Profiler

IFOV instantaneous field of view

IGRA Integrated Global Radiosonde Archive

IMU intertial motion unit

IR infrared

LOFZY LOFoten ZYklonen

LWP liquid water path

mae mean absolute error

MIZ marginal ice zone

MIZEX Marginal Ice Zone Experiment

MEMLS Microwave Emission Model for Layered Snowpacks

MODIS Moderate Resolution Imaging Spectroradiometer

MOSAiC Multidisciplinary drifting Observatory for the Study of Arctic Climate

MWR Microwave Radiometer

MYIF multiyear ice fraction

MYI multiyear ice

N-ICE Norwegian young sea ice cruise

NOAA National Oceanic and Atmospheric Administration

n.s. not specified

NSIDC National Snow and Ice Data Center

PAMTRA Passive and Active Microwave TRAnsfer

PDF probability density function

PD polarization difference

RRDP Round Robin Data Package

SAR synthetic-aperture radar

SIC sea ice concentration

SIMBA Snow and Ice Mass Balance Apparatus

SMP SnowMicroPen

SMRT Snow Microwave Radiative Transfer

SND snow depth

SSL surface scattering layer

SSM/I Special Sensor Microwave Imager

SMMR Scanning Multichannel Microwave Radiometer

SST sea surface temperature

SYI second-year ice

T2m 2 m air temperature

TB brightness temperature

TLS terrestrial laser scanner

TWV total water vapor

VIS visual

WSP wind speed

Contents

1 Introduction **1**

1.1 The Stage: The Changing Arctic 1

1.2 The Protagonists: Sea Ice, Snow, Clouds & Water Vapor 4

1.3 Human Audience: Monitoring the Arctic 9

1.3.1 By Many Paths and by Many Means: Expeditions 10

1.3.2 The Loge in Outer Space: The Satellite Era 10

2 Theoretical Background **13**

2.1 Microwave Remote Sensing 13

2.1.1 Black-body Radiation 13

2.1.2 Radiometry 14

2.1.3 Radiative Transfer 18

2.1.4 The Atmosphere: Water Vapor and Cloud Liquid Water 26

2.1.5 The Surface: Open Ocean, Sea Ice, and Snow 28

2.2 Inverse Methods: Optimal Estimation 32

2.3 Evaluating Satellite Retrievals: The Curse of Remote Sensing 36

3 Sea Ice Emissivity: Concept and Measurements **39**

3.1 The Concept of Sea Ice Emissivity 39

3.1.1 Measurements of Sea Ice Emissivity: Literature Review 40

3.2 Results from Expedition PS131 of R/V Polarstern 50

3.2.1 Calculation of Surface Emissivities 50

3.2.2 Campaign and Measurement Setup 51

3.2.3 Results and Discussion 55

3.2.4 Conclusions and Outlook 66

4 Influence of Surface Properties on Satellite Retrievals of Sea Ice Concentration **71**

4.1 A Case Study from the MOSAiC Expedition 71

4.1.1 Introduction 71

4.1.2 Data 74

4.1.3 Results . . . 78
4.1.4 Discussion . . . 89
4.1.5 Conclusion . . . 91

5 Multi-parameter Retrieval 93
5.1 Introduction . . . 93
5.2 Data . . . 95
5.2.1 Satellite Brightness Temperatures . . . 95
5.2.2 Reanalysis Data . . . 96
5.2.3 ASCAT/AMSR2: Multiyear Ice Fraction . . . 96
5.2.4 Merged Warren-AMSR2 Climatology: Snow Depth . . . 96
5.2.5 Round Robin Data Package . . . 96
5.2.6 Utqiaġvik ARM Site: Liquid Water Path . . . 96
5.2.7 MOSAiC Datasets . . . 96
5.3 Methodology: Forward Model . . . 98
5.4 Forward Model Evaluation . . . 105
5.4.1 Brightness Temperature Observations . . . 105
5.4.2 Uncertainty Analysis: Effective Measurement Uncertainty $\mathbf{S}_e$ . . . 109
5.5 Retrieval: A Priori Information . . . 112
5.6 Retrieval Evaluation . . . 115
5.6.1 MOSAiC Expedition . . . 115
5.6.2 Sea Ice Concentration: Round Robin Data Package . . . 116
5.6.3 Snow Depth: Operation Ice Bridge . . . 116
5.6.4 Liquid Water Path: Utqiaġvik Land Station . . . 116
5.6.5 Arctic-wide Retrieval Evaluation . . . 121
5.7 Summary and Conclusion . . . 130

6 Focus Water Vapor 133
6.1 Water Vapor Retrieval: Evaluation and Comparison . . . 133
6.1.1 Retrieval Evaluation with Campaign Data . . . 134
6.1.2 Retrieval Evaluation with Radiosoundings from Land Stations . . . 142
6.1.3 Comparison to Reanalysis ERA5 Data . . . 147
6.1.4 Summary . . . 148
6.2 Trends and Variability of Arctic Water Vapor . . . 152
6.2.1 Introduction . . . 152
6.2.2 Spatiotemporal Variability . . . 154
6.2.3 Regional Time Series . . . 156
6.2.4 Changes in Arctic Total Water Vapor . . . 159
6.2.5 Outlook: Water Vapor Feedback . . . 165

7 Conclusions and Outlook **167**
7.1 Summary and Conclusions . . . 168
7.2 Outlook: Further Method Development . . . 172

Appendices **177**

A Angle of Transmission **179**

B MOSAiC Expedition Case Study **181**
B.1 Site Perspective: Ground-based Radiometry . . . 181
B.1.1 Brightness Temperatures from Ground-based Radiometers . . . 181
B.1.2 Model Experiment On-ice Site: Simulation of a Glaze Ice Layer . . . 184
B.1.3 Supplemental Text S1 - Ground-based Radiometer Observations . . . 184
B.1.4 Supplemental Text S2 - Glaze Layer Observations . . . 186
B.1.5 Supplemental Text S3 - MEMLS_ice Initialization . . . 187
B.1.6 Supplemental Text S4 - SnowMicroPen (SMP)-based Modelling . . . 189

C Multi-parameter Retrieval **191**
C.1 Brightness Temperature Comparison: RRDP . . . 191
C.2 Sea Ice Extent . . . 192
C.3 Uncertainties . . . 193
C.4 Shortfall of the Retrieval . . . 194
C.5 Monthly Maps . . . 195
C.5.1 Multiyear Ice Fraction . . . 195
C.5.2 Surface and Interface Temperature . . . 196

D Water Vapor Retrieval Evaluation **197**
D.1 Evaluation with Observational Data from ATWAICE . . . 197
D.2 Land Stations: Radiosondes . . . 198
D.3 Comparison against Reanalysis . . . 201

E Water Vapor: Time series and Changes **203**
E.1 Sensor Differences . . . 203
E.2 Regional Time Series . . . 204
E.3 Trend Uncertainties . . . 206

Chapter 1

Introduction

1.1 The Stage: The Changing Arctic

Looking at the northern sky we can observe the Great Bear, and nearby, the star Polaris, showing us the direction of the North Pole. The Greek word ἀρκτικός, near the bear, is therefore the eponym of the fascinating northernmost region of our planet: the Arctic. Different geographic definitions exist, but most commonly, the Arctic is defined as the area north of the Arctic Circle at about 66.5°N. In the Arctic one encounters complete darkness during winter and the midnight sun in summer. Most of the Arctic area is ocean, up to several kilometers deep. Its frozen blanket, the Arctic sea ice, controls fluxes of heat, moisture and momentum between ocean and atmosphere, even though with thicknesses of the order of meters it is thin compared to the ocean.

The Arctic is the stage for this thesis, and the stage design is changing: As the Arctic is warming rapidly, and at a much higher pace than areas at lower latitudes (Serreze and Barry, 2011; Wendisch et al., 2023), the sea ice component of the cryosphere is strongly affected. During the last decades, the September Arctic sea ice extent declined by about 12.7% per decade (Meier et al., 2022), which corresponds to a loss of 79 400 km^2 per year[1] (Meier and Stroeve, 2022). Sea ice extent is calculated from gridded data of the area fraction of sea ice to open ocean (sea ice concentration) and is defined as the total area of grid cells covered by ice of at least 15% concentration. During the last 30 years, Arctic near-surface air temperature have increased between 0.87 °C to 1.63 °C, depending on season and compared to the preceding 30 years. Globally, the increase was of the order of 0.58 °C to 0.62 °C (Wendisch et al., 2023). The larger change of temperature at the high latitudes compared to the global average change is called Arctic amplification (AA) (Serreze and Francis, 2006; Serreze and Barry, 2011). A new Arctic climate is emerging (Landrum and Holland, 2020).

[1] For comparison, the Czech Republic has an area of 78 871 km^2.

The changes in the Arctic have a myriad of consequences both locally and outside of the Arctic (Semmler et al., 2012; Intergovernmental Panel on Climate Change, 2023, e.g.,). These include, among other, threats to traditional human livelihoods (Post et al., 2019), e. g., more coastal erosion (Fritz et al., 2017), effects on the Arctic ecosystem, e. g., wider and earlier phytoplankton blooms (Hill et al., 2018), and effects on mid-latitude extreme weather events (Post et al., 2019). While there is growing evidence for mid-latitude linkages (Screen, 2021), currently models still struggle to represent atmospheric circulation and meridional transport modifications (Wendisch et al., 2023) and a clear understanding of how Arctic amplification is influencing weather at lower latitudes is still missing (Cohen et al., 2020).

Local and remote processes and feedback mechanisms cause the amplified changes in the Arctic climate system which are ultimately fueled by human-induced global warming. The intertwined chains of effects that are involved in Arctic amplification are depicted in Figure 1.1. Positive feedback mechanisms enhance and negative mechanisms dampen AA. The reader may notice that this scheme is lacking land-related processes. In fact, the melting of the Greenland ice sheet (Shepherd et al., 2020) or thawing of permafrost (van Huissteden, 2020) are other key processes. It is intelligible that the "Arctic climate puzzle" (Wendisch et al., 2023) has even more pieces to connect. Clearly, the changing Arctic system cannot be understood from one discipline or viewpoint alone.

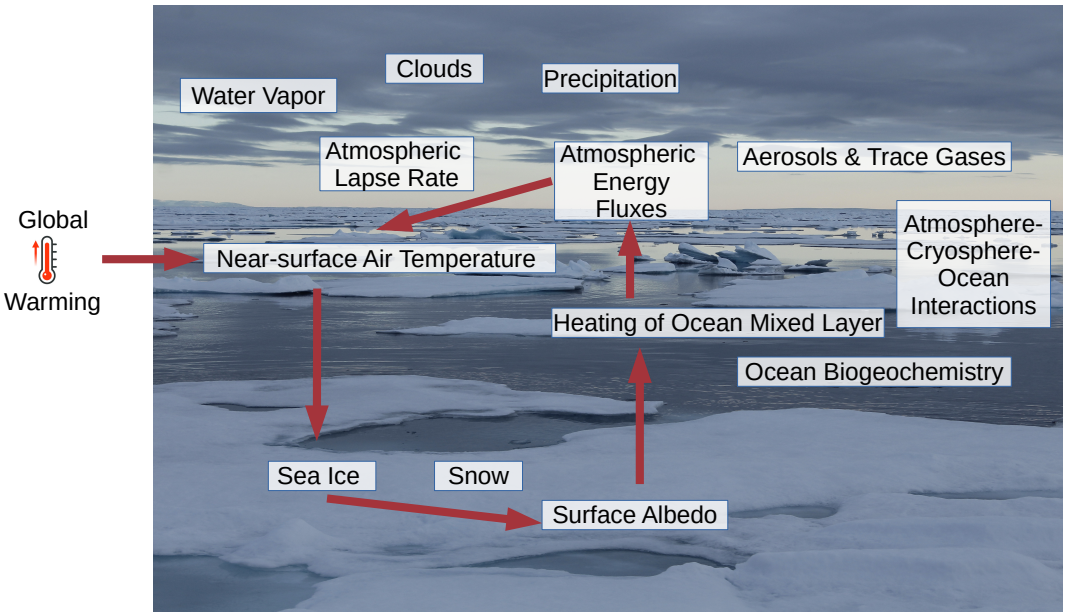

Figure 1.1: Scheme of processes and parameters involved in Arctic amplification. Inspired by Wendisch et al. (2023). Red arrows illustrate the positive ice-albedo feedback.

Observations are the key to improve our understanding of the different mechanisms and processes contributing to Arctic amplification. For example, monitoring the temporal and spatial variability of water vapor in the Arctic is needed to assess its role in Arctic

amplification (the so called water vapor and lapse rate feedbacks) but is hampered by the sparseness of in situ measurements and the challenges using satellite microwave observations for atmospheric sounding over sea ice (Kang et al., 2023; Crewell et al., 2021). Here, the major challenge is the high and highly variable emission of microwave radiation of the snow-covered sea ice. Every day, numerous satellite observations are not assimilated in reanalysis products or used in atmospheric soundings because of that issue. There lies a huge potential of improving our observational toolset of the Arctic. This thesis explores the possibilities of microwave radiometry in the Arctic by tackling the issue of snow and sea ice emissions in several ways:

- providing an overview of concept and measurements of surface emissivities and reporting on a ship-borne measurement method and its results (Chapter 3),
- underlining the importance of surface emissions for satellite retrievals of sea ice concentration in a case study of an event during the Multidisciplinary drifting Observatory for the Study of Arctic Climate (MOSAiC) expedition involving warm and moist air intrusions (Chapter 4),
- improving the characterization of surface emissions using a physical model which is used in a combined satellite retrieval of atmospheric, including water vapor and cloud liquid water, and surface parameters, including sea ice concentration, multiyear ice fraction and snow depth (Chapter 5),
- evaluating the retrieval output using campaign data and reference datasets, both satellite and reanalysis products (Chapter 5), with a particular focus on evaluating the water vapor retrieval (Chapter 6),
- applying the multi-parameter retrieval on satellite observations from the last 20 years to derive spatiotemporal evolution, variabilities and trend patterns of the retrieved water vapor including an outlook on AA and water vapor feedback (Chapter 6),
- providing overall conclusions and suggestions for further method development and research (Chapter 7).

Having established the Arctic as scenery of this thesis we can now continue by introducing the protagonists.

1.2 The Protagonists: Sea Ice, Snow, Clouds & Water Vapor

The protagonists of this thesis are all related to H_2O in its various forms: sea ice, snow, clouds and water vapor. We will briefly explain each of the four, including typical Arctic conditions with respect to them, their role in different feedback mechanisms, and observed changes. This thesis focuses on these quantities, especially on water vapor. Of course, this choice of protagonists will not encompass all feedback mechanisms at play in Arctic amplification here, e. g., we do neither dwell on the role of the ocean, nor do we outline their roles from a natural and human ecological perspective.

Sea Ice

Sea ice is frozen seawater. While this sounds simple at first, the world of sea ice is complex and fascinating when we take a closer look. Most notably, seawater contains salt ions. Ice in its ordinary hexagonal crystal form, I_h, has a lower density than its liquid form, one of the many anomalies of water (Gallo et al., 2016), and the lattice form restricts incorporation of ions. The sea salt ions are rejected from the ice during ice growth and accumulate at the interface or are retained in liquid inclusions: entrapped brine. These inclusions scatter light, making sea ice appear bright (Petrich and Eicken, 2017). The amount of brine trapped in the ice depends on the ice growth and seawater salinity. The brine is not stationary but moves vertically for example because of flushing (percolation of fresh water through the ice), expulsion or gravity drainage (Lubin and Massom, 2005). When the ice ages it therefore looses brine and gets more air pockets. Ice that did not completely melt in summer becomes multiyear ice (MYI).

From this microscopic perspective, which will be of importance later in Chapter 2, we now take a step back and look at the life of brine. The idealized growth starts with the formation of frazil ice, randomly oriented crystals, at around $-1.86\,^{\circ}\mathrm{C}$. Depending on the weather conditions the frazil ice is turned to a smooth ice sheet called nilas (calm conditions) or it forms pancake ice, tiny floes that are caused by turbulent conditions (ocean swell and waves). Due to the insulating effect of ice, the growth rate slows. Congelation growth takes over: long, columnar crystals start forming onto the underside of the ice (Lubin and Massom, 2005). Besides these thermodynamic growth processes which depend on the thickness itself, ice can thicken via dynamic processes (deformation).

Sea ice undergoes a seasonal cycle and reaches its maximum in terms of extent and area in late February or March. In 2023, the maximum extent comprised $14.79 \times 10^6\,\mathrm{km}^2$ based on the ARTIST Sea Ice (ASI) satellite product (Spreen et al., 2008). In September, the sea ice extent reaches its minimum, which was $4.33 \times 10^6\,\mathrm{km}^2$ in 2023 based on ASI, corresponding to around 30% coverage of the total area of the Arctic Ocean. Sea ice plays

a major role in Arctic feedback processes. The surface albedo feedback is a well know mechanisms already described by Arrhenius (1896): Melting of sea ice as a consequence of increasing air temperatures results in a decrease of the Arctic Ocean's albedo. This in turn increases the absorption of solar radiation and thus heats up the ocean mixed layer. The enhanced atmospheric energy fluxes then increase near-surface air temperatures and we are back at the start of this feedback loop. This direct surface albedo feedback is an important cause of AA in spring (Screen and Simmonds, 2010; Wendisch et al., 2023). In addition to this direct effect, the solar energy absorbed in the Arctic Ocean in spring and summer is released later, delaying refreezing and possibly causing thinner ice in fall. Thinner ice grows faster than thicker (Maykut, 1986) (negative feedback), but facilitates more sensible heat transfer from ocean to the atmosphere during fall and winter contributing to AA (Goosse et al., 2018).

From satellite observations, we know that the Arctic sea-ice area has decreased in every month of the year from 1979 to today (Fox-Kemper et al., 2021) and that it has become thinner and younger in the past two decades, i. e., the amount of MYI decreased (Kwok et al., 2009), especially the oldest and thickest ice (Maslanik et al., 2007). Studies suggest that the Arctic will become seasonally ice-free in the coming decades (Meier and Stroeve, 2022; Kim et al., 2023)). The climate response to sea ice is nonlinear, regionally-dependent and remains uncertain (Levine et al., 2021) as other (atmospheric) feedback mechanism may amplify the effect of sea ice loss.

Snow

Snow falls as solid precipitation to the ground and transform towards a monomineralic *metamorphic rock*. In this thesis we focus on snow on the ground, that is, the sea ice. On the ground snow undergoes metamorphism. The homologous temperature of the snow, given by the ratio of the snow temperature to the snow's melt temperature, is very high, and combined with the high vapor pressure of water the ice particles in the snow undergoes constant sublimation and deposition (recrystallization). This metamorphism is influenced by temperature gradients in the snow and can lead to distinct layers with different snow types that can be classified according to Fierz et al. (2009). At the melting point, liquid water is present in the snow pore space as well, thus water can coexist in all three phases in snow on the ground. On Arctic sea ice, snow undergoes metamorphism under strong temperature gradients and depth hoar often makes up the base layer of the snowpack. Depth hoar consists of large-grained, cup-shaped ice crystals that form due to the upward water vapor flux caused by the temperature gradient (Colbeck, 1983). Icy layers and ice lenses can be found in Arctic snow as well, formed, e. g., by rain-on-snow, freezing mist or thaws (Sturm and Massom, 2017). The reader will encounter ice layers in Chapter 4. Finally, even saline basal snow layers have been found, especially in the Antarctic, that can for example form when the snowpack comprises highly-saline frost flowers, which are

ice crystals formed on new ice (Sturm and Massom, 2017). The different microstructures of snow due to metamorphism translate into different physical properties of the snow. Their influence on microwave remote sensing will be discussed later in Chapters 2 and 4. One important quantity is the total height of the snowpack, the snow depth. Snow depth varies seasonally and spatially. Maximum values over Arctic multiyear ice are reached in May (34 cm) based on Soviet North Polar Drifting stations[2] (Barry and Gan, 2021) with highest values North of Greenland and the eastern Canadian Archipelago (Warren et al., 1999). During August, the ice is largely snow free and the ice surface consists of a snow-like layer called surface scattering layer (SSL) (Smith et al., 2022). Despite its fundamental role, large-scale measurements of snow depth are lacking but the development of satellite retrievals is an active field of research (Lubin and Massom, 2005) and this thesis adds to it. Here we want to highlight two aspects of snow for the Arctic climate: the snow albedo and its role as thermal insulator. The insulation of snow depends primarily on its density and compared to ice snow has an exceedingly low thermal conductivity (Sturm et al., 1997) (roughly one order of magnitude lower). Thus, snow acts as a natural barrier of heat exchange between the cold Arctic winter atmosphere and the warmer ocean and therefore effects sea ice growth rates. A few centimeters of snow on half a meter sea ice can already reduce the conductive heat flux by 50% (Petrich and Eicken, 2017). Snow also contributes to the surface albedo feedback which acts the same way as the ice-albedo feedback, however, snow albedo values are higher than those of bare ice (Perovich, 2017; Perovich et al., 1998).

Based on satellite observations, a reduction of snow depth up to 3 cm/decade in March has been observed over the time period of 2003–2020 (Wendisch et al., 2023; Rostosky et al., 2018,0).The future of snow on Arctic sea ice is still uncertain (Sturm and Massom, 2017). Difficulties in modeling snow make it hard to predict the interactions of ice and snow, and the predictions of future precipitation (changes) are uncertain: will there be more snowfall or will it be rain? How will the precipitation patterns align with freeze-up dates of the ice?

Clouds

Droplets, ice crystals, snow flakes and other forms of condensed water form clouds. Clouds and related thermodynamical processes are complex and this applies to their impact on the Arctic climate system as well. In fact, clouds are one of its least understood components (Devasthale et al., 2020). From Climate Data Records (CDRs) based on satellite observations we know that the Arctic is cloudy: average annual cloud fractions range from 60 to 70% depending on the CDR with even higher values in the summer months[3]. It is not only the occurrence of clouds that determines its role in the climate system but

[2]These measurement campaigns will be mentioned again in Section 1.3.1.

[3]In Norse mythology the land in the North is called Nivlheim: The home of mist (Nansen, 1897). When moist air is transported from the open ocean to the colder ice, temperatures drop and condensation takes place, so fog in the marginal ice zone is very common.

also the microphysical properties. Similar to snow, water can exist in the liquid and solid phase in clouds, often even simultaneously in so-called mixed-phase clouds. Interestingly, supercooled liquid water is present within Arctic clouds over the entire year (Devasthale et al., 2020).

One quantity to describe the liquid water content in clouds, which impacts the radiation properties, is cloud liquid water path (LWP), the amount of liquid water present in the atmospheric column. At the Arctic observation site Ny-Ålesund, LWP shows a seasonal cycle with values from 10 to more than $100\,\mathrm{g\,m^{-2}}$ in summer, while in winter and early spring, typical monthly median values are below $10\,\mathrm{g\,m^{-2}}$ (Ebell et al., 2020).

In general, Arctic clouds have a strong cooling effect in summer and a warming effect in winter (Kay et al., 2016). However, significant uncertainties exist, e. g., in terms of their response to sea ice loss, but also because of large uncertainties of the observations of cloud properties. Therefore Devasthale et al. (2020) states that the "exact role of clouds in the Arctic climate system and future cloud feedbacks in a warming world remain an enigma".

Water Vapor

Water vapor is a very important gaseous absorber in the Earth's atmosphere (Shine et al., 2012). Under clear sky, i. e., when no clouds are present, water vapor contributes to 60% of the radiative forcing, which is the difference of the longwave flux at the top of the atmosphere with and without greenhouse absorbers (Kiehl and Trenberth, 1997). It is also a key element of the hydrological cycle, with a residence time of one week in the Arctic atmosphere (Vihma et al., 2016), providing resources for clouds and storms. The total amount of water in the atmosphere, mainly governed by air temperature, is around 0.25 % of the atmospheric mass (Stevens and Bony, 2013). If all atmospheric water were precipitated, the globally averaged depth would be only 2.5 cm (Colman and Soden, 2021) which sounds astonishingly small when one thinks about the significant radiative impact of water vapor. Unlike for example oxygen, water vapor has a heterogeneous vertical distribution. In the Arctic, inversions are common in both temperature as well as (specific and relative) humidity (Vihma et al., 2016). Inversions are atmospheric layers where the values increase instead of decrease with height. The vertical profiles effect, for example, cloud formation but have also direct effects on the radiative transfer in the atmosphere (Vihma et al., 2016).

In this thesis we will not investigate moisture profiles but study the total water vapor or integrated water vapor, also called precipitable water, which is the mass of water vapor contained in a vertical atmospheric column of unit cross section. In the Arctic this quantity has a pronounced seasonal cycle due to its close relation to the air temperature, with mean monthly values of about $13\,\mathrm{kg\,m^{-2}}$ to $14\,\mathrm{kg\,m^{-2}}$ in July and $2\,\mathrm{kg\,m^{-2}}$ to $3\,\mathrm{kg\,m^{-2}}$ in January according to reanalysis data (Rinke et al., 2019).

With increasing temperatures, the capacity of the troposphere to hold water vapor

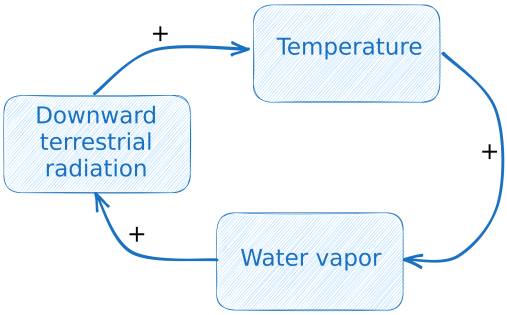

Figure 1.2: Water vapor feedback scheme. After Ghatak and Miller (2013).

increases exponentially according to the Clausius-Clapeyron equation, resulting in an increase of downward longwave radiation and subsequent air temperature increase: the positive water vapor feedback. This is schematically depicted in Figure 1.2. Already in 1967 Manabe and Wetherald (1967) suggested that this feedback doubles the response of temperature to external forcing such as changes in atmospheric CO_2. In addition to local evaporation, enhanced due to sea ice retreat (Boisvert et al., 2015), the Arctic's atmospheric moisture is a result from transport from lower latitudes. Most of the poleward moisture transport occurs as pulses of anomalously warm and moist air intruding into the Arctic (Pithan et al., 2018). Such moist warm air intrusions increase the downward longwave radiation flux and the surface temperature and thus contribute to Arctic warming in winter (Woods et al., 2013; Hao et al., 2019). In addition, there is the release of latent heat at condensation; and after condensation there is an increase in cloudiness which has, at least in winter, a warming effect in the Arctic. This threefold consequence is called water vapor triple effect (Taylor et al., 2022). Evidence for an increase in meridional heat and moisture transport (Graham et al., 2017; Valkonen et al., 2021; Rinke et al., 2017; Hao et al., 2019; Henderson et al., 2021; Woods and Caballero, 2016; Zhang et al., 2023) underlines the importance of the water vapor feedback.

Overall, Arctic moistening is observed in reanalyses from 1979–2016 but the different reanalysis products disagree on the magnitude. The trends also vary depending on season and region including regions with negative trends (Rinke et al., 2019). Based on satellite data from an infrared sounder from 2003–2013 Boisvert and Stroeve (2015) conclude as well that most of the Arctic is getting warmer and wetter during the majority of the months. Locally, moistening in winter over the time period of 1993 to 2014 is observed in radiosonde data from Ny-Ålesund (Maturilli and Kayser, 2016). Also, positive trends dominate at Arctic sites when analyzing water vapor data from Global Navigation Satellite System (GNSS) from 1998 to 2017 (Negusini et al., 2021). In a modeling study Ridley et al. (2023) predict an increase of water vapor in the Arctic, where the rate of increase is enhanced due to sea ice loss and shows a pronounced seasonality.

The Ensemble

Now that we have introduced the protagonists, we want to stress the importance of their interplay. In the last paragraph we already outlined some interactions: the interplay of sea ice loss and water vapor increase due to more evaporation and of moisture transport and cloud formation. The effects may also be delayed. For example, more water vapor in autumn could lead to warmer air and surface temperatures due to increased cloud fraction which remain warmer later in the season and affect earlier melt onset of the sea ice in spring (Boisvert and Stroeve, 2015). In addition to changes in total water vapor, the loss of sea ice and the corresponding changes in surface turbulent heat fluxes affect the vertical moisture and temperature profiles. These are intertwined with the Arctic lapse rate feedback, which describes the weaker atmospheric cooling because of bottom heavy warming in the Arctic compared to vertically uniform warming. Changes in liquid water content of clouds and related precipitation patterns may affect snow depth. Models predict a transition from a snow- to rain-dominated Arctic in the summer and autumn (McCrystall et al., 2021) and negative (positive) trends in days with solid (liquid) precipitation are already observed in the Atlantic sector of the Arctic (Łupikasza and Cielecka-Nowak, 2020). Changes in atmospheric or oceanic circulation influence our protagonists as well. The different processes are acting on different spatial and temporal scales, further complicating their analysis. In order to investigate the mechanisms behind AA it is elemental to monitor our protagonists and their interplay.

1.3 Human Audience: Monitoring the Arctic

Long before Pytheas narrated about “Ultima Thule”, the area in the extreme North, in the 4th century BC, the Arctic region has been populated and explored by the indigenous peoples (Lainema and Nurminem, 2009). Siberia, for example, has been inhabited for more than 40,000 years (Sikora et al., 2019). In the early medieval period, the Vikings started exploring the frozen seas. Descriptions of the “wonderful nature” (Nansen, 1897) of sea ice can be found in *The King’s mirror* of about 1240 (Lainema and Nurminem, 2009). Sledges, kayaks and ships were the means of new discoveries, but remote sensing leveraged explorations in the last decades. Remote sensing, i. e., the ability to observe from a distance without direct contact with physical objects provides a way to monitor the Arctic in which humans do not disturb the fragile Arctic ecosystem. This includes airborne measurement campaigns and space-borne observations. For climate sciences, remote sensing is especially important, as satellite observations cover time spans long enough for climatological assessments. For example, information about the Arctic sea ice in the last report of the Intergovernmental Panel on Climate Change (2023) mostly stems from remote sensing.

1.3.1 By Many Paths and by Many Means: Expeditions

"By many paths and by many means mankind has endeavored to penetrate this kingdom of death" (Nansen, 1897). One particular expedition was the voyage of exploration of the ship *Fram* 1893–96, led by Fritjof Nansen who the quote above is attributed to. A similar approach was adopted by the Soviet-Russian operation of North Polar drifting stations, measurement stations set up on and drifting with the sea ice. It was run, with breaks, from 1937 to 2015. In recent years suitable ice floes were difficult to find and the operation of ice camps came to an end (Barry and Gan, 2021). 126 years after the *Fram* expedition, the MOSAiC expedition (Nicolaus et al., 2022; Shupe et al., 2022; Rabe et al., 2022) followed up on Nansen's idea. It provided the unique opportunity of measurements in the central Arctic in winter: the icebreaker and research vessel *Polarstern* (Knust, 2017) drifted passively with the pack ice anchored to a second-year ice floe for a full year from October 2019 to September 2020, with one relocation during the summer. Observations from the MOSAiC campaign will play a central role in Chapter 5.

Despite these tremendous efforts, the central Arctic is harsh and difficult to access and many lives were lost in the attempts. In situ observations remain sparse both temporally and spatially. Satellites are therefore a great tool for scientific explorations of the Arctic especially in winter.

1.3.2 The Loge in Outer Space: The Satellite Era

At the end of the 19th century, Nansen wrote that "darkness still broods over vast tracts around the Pole" (Nansen, 1897). This has certainly changed with the beginning of observations of the Arctic from space that keep providing whole new possibilities for exploring the polar regions. Satellite remote sensing encompasses a variety of sensing methods: passive and active, including infrared or visual imaging as well as microwave remote sensing. Inferred products include sea ice concentration (Ludwig et al., 2020), ice thickness (Huntemann et al., 2014), sea ice drag (Mchedlishvili et al., 2023), snow depth (Rostosky et al., 2018), ice classification (Kortum et al., 2022), melt pond fraction (Niehaus et al., 2023), lead detection (Murashkin et al., 2018), but also atmospheric variables such as water vapor (Triana-Gómez et al., 2019), methan and carbon monoxide (Schneising et al., 2019).

According to the Union of Concerned Scientists (2023), as of January 1, 2023 there are 1167 Earth observation satellites in orbit, most of them in a sun-synchronous, low-Earth orbit. These are orbits with a period of 128 minutes or less and a high inclination angle to the equator (polar orbits), enabling the same illumination of the surface as sun-synchronous orbits observe any given point at the same local mean solar time. The polar orbits enable daily Arctic-wide coverage.

Passive Microwave Remote Sensing in Polar Regions

With the advent of satellites, passive microwave radiometers have been measuring energy emitted in the microwave regime from the Earth's surface and atmosphere. One of the early satellites, Cosmos 234, was launched in 1968 and showed the possibility of sea ice monitoring. Basharinov et al. (1971) reported from its observations which indicated that brightness temperatures of sea ice depend on a variety of ice properties (Gloersen et al., 1973). Multichannel satellite observations extend back to Nimbus 5 launched 1972 which allows climatological assessments of key quantities such as sea ice area.

The atmospheric influence on the satellite measurements in the microwave region is rather small, an advantage in the cloudy Arctic. The measurements are independent of sunlight, enabling observations during polar night. Also, microwave remote sensing enables frequent and spatially complete coverage of the Arctic despite relatively poor spatial resolution of the order of tens of kilometers. The view from space has unraveled many mysteries of the Arctic but has also raised new questions and opened up novel observation possibilities.

Curtains up for microwave remote sensing!

Chapter 2

Theoretical Background

In this chapter we provide the theoretical background of microwave remote sensing from basic principles to the inversion scheme used in the retrieval method in Chapter 5. We also briefly discuss the means and pitfalls of evaluating parameters derived from satellite data using *ground truth*.

2.1 Microwave Remote Sensing

We outline the basic principles of microwave remote sensing following closely Ulaby and Long (2014) if not indicated elsewise. All quantities in formulas are given in SI units if not mentioned differently. We use the convention to call the electromagnetic spectrum from 0.3 GHz to 300 GHz the microwave region.

We will see that most of the formulated relations we use in microwave remote sensing follow from basic principle like the notion of a black body and conservation of energy. We first outline the measuring principle in radiometry and introduce the measured quantity called brightness temperature. For explaining radiative transfer and, ultimately, observations of satellite radiometers, we then also discuss the propagation of waves in media and at boundaries of different media. Equipped with these basics, we then turn our attention to the four protagonists introduced in Chapter 1 and contemplate how they determine the satellite signal.

2.1.1 Black-body Radiation

In 1860 Kirchoff introduced the notion of a "schwarzer Körper", a black body, which is an ideal absorber of radiation, i. e., no radiation is reflected or transmitted by this body, at all wavelengths and all angles of incidence (Kirchhoff, 1860). From this definition alone we can deduce further properties such as: the black body is also an ideal emitter at any wavelength, its radiation is isotropic, and the total emitted energy of radiation is a monotonously increasing function of thermodynamic temperature only (Sharkov,

2003). Laws describing the approximate spectral distribution of the black-body radiation like the Wien radiation law, the Rayleigh-Jeans law and the Stefan-Boltzmann law, as well as Wien's displacement law were formulated proceeding from classical thermodynamic arguments (Howell et al., 2021). However, these laws were not sufficient, e. g., the Wien radiation law fails to describe the energy distribution at long wavelengths while the Rayleigh-Jeans law fails for short wavelengths ('ultraviolet catastrophe'; Ehrenfest (1911)). Only with the advent of quantum theory it was possible to derive a quantitative expression valid also for high temperatures and long wavelengths.

Planck's Law By assuming that emitted radiation occurs in discrete energy quanta, Planck derived the formula named after him in 1900 which describes the spectral intensity distribution I_f of a black body:

$$I_\mathrm{f} = \frac{2hf^3}{c^2}\left(\frac{1}{\exp(hf/k_\mathrm{B}T) - 1}\right), \tag{2.1}$$

where h is Planck's constant[1], f is frequency, c is the velocity of light[2], k_B is Boltzmann's constant[3] and T is the body's temperature. Here, I_f is the intensity per frequency interval emitted by the black body of unit surface area through one unit (steradian, sr) of solid angle. For low frequencies, Planck's law can be approximated by the Rayleigh-Jeans law which had been derived around the same time based on classical assumptions:

$$I_\mathrm{f} \approx \frac{2k_\mathrm{B}T}{\lambda^2}, \tag{2.2}$$

where λ is the wavelength[4] of the radiation. Figure 2.1 shows the excellent agreement between the two laws in the microwave region, i. e., from 0.3 GHz to 300 GHz. At 300 K and 300 GHz the Rayleigh-Jeans law deviates from Planck's expression by about 3%.

2.1.2 Radiometry

We now outline how a remote-sensing antenna intercepts radiation and measures incoherent radiant electromagnetic energy. First of all, a typical antenna detects radiation along a single polarization direction[5] according to its radiation pattern $F(\theta, \phi)$. $F(\theta, \phi)$ characterizes the normalized, relative distribution of power received or transmitted by the antenna in the far-field[6]. As most antennas are reciprocal, $F(\theta, \phi)$ is the same for both

[1] h=6.626 070 15 $\times$ 10^{-34} J Hz^{-1}

[2] c=299 792 458 m s^{-1}

[3] k_B=1.380 649 $\times$ 10^{-23} J K^{-1}

[4] Note that $f = \frac{c}{\lambda}$ and $\mathrm{d}f = \frac{-c}{\lambda^2}\,\mathrm{d}\lambda$

[5] The notion of polarization will be introduced in more depth in Section 2.1.3.

[6] When the wavefront of a wave radiated by a transmitting point can be considered planar across the antenna aperture because the distance between transmitter and receiver is sufficiently large, the receiving antenna is in the far-field region. This is the case for most satellite applications.

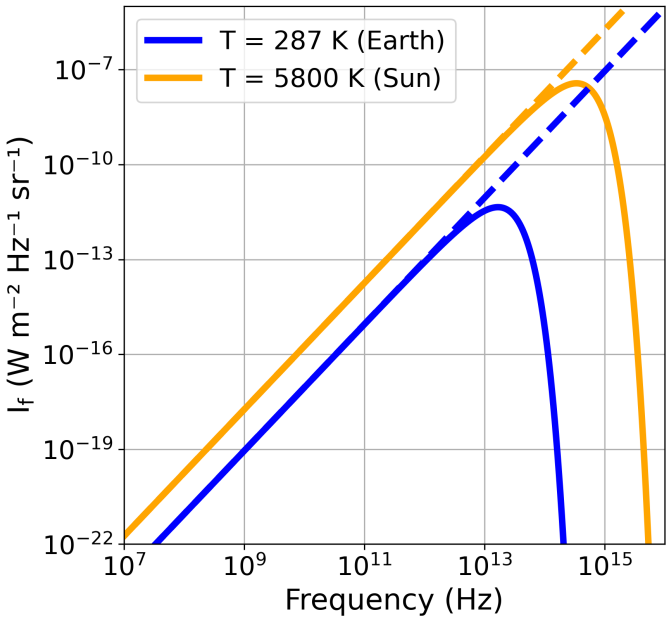

Figure 2.1: Planck's radiation law (solid lines) of black bodies with different temperatures in comparison to the Rayleigh-Jeans approximation (dashed lines). Shown are the intensities of a body at T = 258 K (blue lines, black-body model of the Earth) and at T = 5800 K (orange lines, black-body model of the Sun).

transmission and reception. The total amount of power P over the frequency range f_1 to f_2 that is received by the antenna is given by

$$P = \frac{1}{2} A_\mathrm{r} \int_{f_1}^{f_2} \iint_{4\pi} I_\mathrm{f} F(\theta, \phi) \, \mathrm{d}\Omega \, \mathrm{d}f, \tag{2.3}$$

where A_r is the effective aperture of the antenna given by the fraction of the power density of an incident wave to the intercepted power. The integration is over the complete solid angle Ω to account for all directions. A_r is related to the antenna pattern via the pattern solid angle Ω_p as

$$\begin{aligned} \iint_{4\pi} F(\theta, \phi) \, \mathrm{d}\Omega &= \Omega_\mathrm{p} \\ \Omega_\mathrm{p} &= \frac{\lambda^2}{A_\mathrm{r}}. \end{aligned} \tag{2.4}$$

In the low-frequency approximation (Equation 2.2) we simplify Equation 2.3 to

$$P \approx k_\mathrm{B} T B \frac{A_\mathrm{r}}{\lambda^2} \iint_{4\pi} F(\theta, \phi) \, \mathrm{d}\Omega = P_\mathrm{bb}, \tag{2.5}$$

where we assumed the detection to be limited to a narrow bandwidth $B = f_2 - f_1 << f$ over which I_f is constant. The integral in Equation 2.5 is related to the effective aperture

(Equation 2.4), and a direct linear relationship between temperature and power can be derived as

$$P_{\mathrm{bb}} = k_{\mathrm{B}} T B. \tag{2.6}$$

This is a significant relation and we will elaborate on it a bit further. Nyquist (1928) studied the electronic noise in conductors stemming from the thermal agitation of the charge carriers, independent of applied voltage. From thermodynamics and statistical mechanics Nyquist deduced that this Gaussian thermal noise is proportional to the resistance and temperature of the conductor. His theorem was later generalized in terms of a quantum-mechanical derivation of the fluctuation-dissipation theorem (Callen and Welton, 1951). It is now possible to derive Equation 2.6 from Nyquist's formula. Here, we think of the antenna as a resistor with a certain impedance inside a black-body enclosure where the enclosure has temperature T, see Figure 2.2 When we match the impedance of

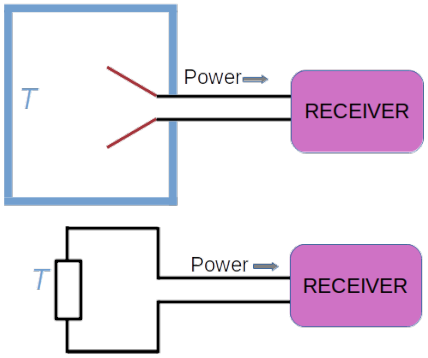

Figure 2.2: Thought experiment: Power received from within a black-body enclosure with temperature T by an antenna (top) is equivalent to the noise power delivered by a resistor with physical temperature T (bottom).

the resistor to our antenna measurement system in a way that maximizes power transfer (from source to receiver), the thermal noise signal reformulated in terms of power gives Equation 2.6, which, in differential form where P_{f} is a spectral density, reads

$$P_{\mathrm{f}}\,\mathrm{d}f = k_{\mathrm{B}} T_{\mathrm{A}}\,\mathrm{d}f. \tag{2.7}$$

This allows to identify the antenna temperature T_{A} (which is not the physical temperature of the antenna) as the thermodynamic temperature of a matched noise resistance.

Brightness Temperatures So far we have considered idealized black bodies. While there are objects in nature that can be described well as a black body, for example our sun or the cosmic background, most natural materials emit less than a black body does. We may now define the black-body equivalent radiometric temperature and call it brightness

temperature T_B so that Equation 2.2 takes the form

$$I_\mathrm{f}(\theta,\phi,f) = \frac{k_\mathrm{B}}{\lambda^2} T_\mathrm{B}(\theta,\phi,f) \tag{2.8}$$

where we introduced the direction dependence of I_f and multiplied by the factor $1/2$ to obtain the singular-polarized brightness intensity. Again, we consider the antenna to be a resistor inside an enclosure, only this time it is not a black body but the enclosure is emitting according to a brightness temperature distribution $T_\mathrm{B}(\theta,\phi,f)$. Thus, along the lines of Equation 2.3, the spectral density received is given by

$$P_\mathrm{f}\,\mathrm{d}f = \frac{1}{2} A_\mathrm{r}\,\mathrm{d}f \iint_{4\pi} I_\mathrm{f}(\theta,\phi,f) F(\theta,\phi)\,\mathrm{d}\Omega \tag{2.9}$$

$$= \frac{1}{2} A_\mathrm{r}\,\mathrm{d}f \iint_{4\pi} \frac{k_\mathrm{B}}{\lambda^2} T_\mathrm{B}(\theta,\phi,f) F(\theta,\phi)\,\mathrm{d}\Omega. \tag{2.10}$$

By employing Equation 2.7 and 2.4 we derive a relationship between brightness temperature and antenna temperature from Equation 2.10. This relationship is expressed as

$$T_\mathrm{A}(f) = \frac{\iint_{4\pi} T_\mathrm{B}(\theta,\phi,f) F(\theta,\phi)\,\mathrm{d}\Omega}{\iint_{4\pi} F(\theta,\phi)\,\mathrm{d}\Omega}. \tag{2.11}$$

Within the power passband B, assuming no change of T_A within, we then obtain the total power to be

$$P = k_\mathrm{B} T_\mathrm{A} B. \tag{2.12}$$

T_A includes indiscernible contributions from different directions. The main part of received power of an antenna with a specified directional pattern is localized within a narrow mainlobe zone (giving the antenna directivity) but there are also contributions from the so-called sidelobes which are usually undesired. The beam efficiency as the ratio of the pattern solid angle and the mainlobe solid angle may be used to describe the significance of these unwanted sidelobe contributions. In the previous discussion we considered ideal antenna systems, i. e., without ohmic losses. In reality, a radiometer receiver measures voltage proportional to the antenna temperature including ohmic losses and thermal noise of antenna, receiver and transmission line.

Radiometric, Spectral and Spatial Resolution Due to the stochastic nature of noise the signal must be averaged. The detected voltage is integrated over the integration time τ_int and the estimate of antenna temperature carries an uncertainty ΔT, called radiometric resolution, as it is the detection limit. One can show that ΔT of a total-power radiometer is given by

$$\Delta T = T_\mathrm{SYS} \left[\frac{1}{\sqrt{B\tau_\mathrm{int}}} + \left(\frac{\Delta G}{G} \right)^2 \right]^{1/2}, \tag{2.13}$$

where T_{SYS} is the sum of antenna temperature and combined receiver and transmission line input noise temperature and B is the bandwidth. The minimum bandwidth determines the spectral resolution. The second term accounts for fluctuations of the system gain G, i. e., it takes ohmic losses in the antenna itself into account: $\overline{G}$ is the average system power gain and ΔG is the root mean square of its fluctuations.

Now that we have discussed the radiometric and spectral resolution we lastly note the spatial resolution of an antenna, usually given as instantaneous field of view (IFOV). The beamwidths of the main lobe of an antenna with pattern $F(\theta, \phi)$ are defined as the angular width in a given plane where the magnitude of $F(\theta, \phi)$ is, expressed in decibels, $-3\,\mathrm{dB}$. The area on the ground that is covered by the beam, constrained by the beamwidths, is the IFOV. For today's space-borne radiometers this is rather coarse – on the order of 5 to 50 km.

2.1.3 Radiative Transfer

After having established the basics for sensing radiated energy, we shall now consider the actual satellite measurement system. Figure 2.3 shows a simple scheme where the

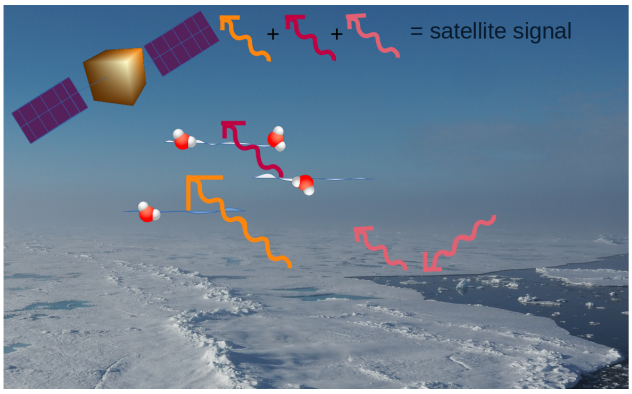

Figure 2.3: Idealized scheme of a satellite measurement: the instrument on the satellite measures the atmospheric brightness temperatures emitted upwards by clouds and water vapor (red arrow), the downwelling brightness temperatures that are scattered upwards at the surface (pink arrow) and the emissions from the surface (orange arrow). At the low microwave frequencies, the latter are the dominant contribution to the overall signal measured at the satellite.

contributions to the satellite are divided into a part emitted by the atmosphere (the upwelling atmospheric brightness temperatures), the downwelling atmospheric brightness temperatures that are scattered upward towards the satellite, and the emissions by the terrain. When the electromagnetic radiation arrives at the space-borne radiometer it has interacted with the matter of the terrain and the atmosphere by emission and extinction (absorption and scattering). We shall now consider these energy transformations within a volume element. The loss in intensity by scattering and absorption can be described by the extinction coefficient κ_{e} over a distance $\mathrm{d}\mathbf{R}$ that can be expressed as increment of

opacity $\mathrm{d}\tau$ by

$$\mathrm{d}\tau = \kappa_\mathrm{e}\,\mathrm{d}\mathbf{R}. \tag{2.14}$$

The extinction coefficient is the sum of the linear processes of scattering (scattering coefficient κ_s) and absorption (absorption coefficient κ_a). Along some distance intensity can be gained by thermal emission and by scattering of radiation in the propagation direction ($\hat{\mathbf{R}}$). Assuming local thermal equilibrium within the integration time and the volume element, Kirchhoff's law states that emission is equal to absorption. The radiative transfer equation is given by an energy balance equation for some volume element at $\mathbf{R}$ on the propagation path. In terms of brightness temperature it can be written as

$$\frac{\mathrm{d}T_\mathrm{B}}{\mathrm{d}\tau} + T_\mathrm{B} = (1-a)T + aT_\mathrm{VS}, \tag{2.15}$$

where $a = \frac{\kappa_\mathrm{s}}{\kappa_\mathrm{e}}$, T is the local physical temperature of the volume element, and T_VS is called volume scattered radiometric temperature. The latter is a function of location and propagation direction and is given by integration of the scattering phase function $\Phi(\hat{\mathbf{R}}, \hat{\mathbf{R}}')$ which dictates the redirection fractions from $\hat{\mathbf{R}}'$ to $\hat{\mathbf{R}}$ during the scattering process:

$$T_\mathrm{VS} = \frac{1}{\kappa_\mathrm{s}} \iint_{4\pi} \Phi(\hat{\mathbf{R}}, \hat{\mathbf{R}}') T_\mathrm{B}(\hat{\mathbf{R}}, \hat{\mathbf{R}}')\,\mathrm{d}\Omega. \tag{2.16}$$

In case of a nonscattering, nonrefractive atmosphere, valid for gaseous absorption in the microwave spectrum below 10 GHz, we can solve the radiative transfer equation and obtain at position s with $\tau(0,s) = \sec(\theta)\int_0^s \kappa_\mathrm{e}\,\mathrm{d}z$ (Waters, 1976; Chandrasekhar, 1950):

$$T_\mathrm{B}(s) = T_\mathrm{B}(0)\exp(-\tau(0,s)) + \int_0^s T(s')\exp(-\tau(s',s))\kappa_\mathrm{a}(s')ds', \tag{2.17}$$

where the first term represents attenuation as the radiation, $T_\mathrm{B}(0)$, emitted and scattered from the surface, passes from 0 to s and the second accounts for the emission along the path s (upwelling atmospheric brightness temperature, $T_\mathrm{B,up}$). When we express the path s in terms of height z and zenith angle θ we can define $T_\mathrm{B,up}$ as

$$T_\mathrm{B,up} = \sec(\theta)\int_0^\infty T(z')\exp(-\tau(z',\infty))\kappa_\mathrm{a}(z')\,\mathrm{d}z', \tag{2.18}$$

and along the same lines the downwelling atmospheric brightness temperature, $T_\mathrm{B,down}$, reads

$$T_\mathrm{B,down} = \sec(\theta)\int_0^\infty T(z')\exp(-\tau(0,z'))\kappa_\mathrm{a}(z')\,\mathrm{d}z'. \tag{2.19}$$

The upper limit of the integral in Equations 2.18 and 2.19 is in principle the height of our satellite radiometer, here chosen to be ∞ as $\kappa_\mathrm{a}(\infty) = 0$ for free space.

Plane-wave Propagation in Media So far we have derived the radiative transfer theory from principal energy considerations. We now introduce wave equations to describe the propagation of radiation in media and at boundaries of different media. Electromagnetic waves are described by time-varying electric and magnetic fields that can be depicted by vectors. For sinusoidal time variations with angular frequency ω, the electric field can be split in a spatial component $\mathbf{E}(x, y, z)$ and a time-dependent one described as $\mathbf{E}(x, y, z, t) = \mathrm{Re}(\mathbf{E}(x, y, z) \exp(i\omega t))$. From Maxwell's equations the homogeneous wave equations for both electric field and magnetic field can be derived and take on the form:

$$\nabla^2 \mathbf{E} + k^2 \mathbf{E} = 0.^7 \tag{2.20}$$

The wavenumber k is given by

$$k = \omega \sqrt{\mu \epsilon \epsilon_0}, \tag{2.21}$$

where μ is the magnetic permeability, ϵ is the relative permittivity and ϵ_0 is the permittivity of free space, where the latter two describe the polarizability of the medium. We note that ϵ and k are complex numbers and introduce the refractive index n given by $n = \sqrt{\epsilon}$. The imaginary part of ϵ is also called dielectric loss. A solution for the wave equation is given by plane waves, i. e., electric and magnetic field are constant through any plane that is perpendicular to the direction of propagation. In case of an electric field in x-direction traveling along the z-direction, the solution to Equation 2.20 is

$$\mathbf{E}(z) = E_{x0} \exp(-\alpha z) \exp(-i\beta z) \hat{\mathbf{x}}, \tag{2.22}$$

where E_{x0} is the amplitude; and attenuation coefficient α and phase constant β (the complex-valued wavenumber) are related to the permittivity via

$$\alpha = -\omega \sqrt{\mu \epsilon_0}\, \mathrm{Im}(\sqrt{\epsilon}) \tag{2.23}$$

$$\beta = \omega \sqrt{\mu \epsilon_0}\, \mathrm{Re}(\sqrt{\epsilon}). \tag{2.24}$$

The distance that a wave can penetrate into a lossy medium can be described by the skin depth $\delta_\mathrm{s} = 1/\alpha$, where the electric field magnitude has fallen to $1/e$ of its initial value. In terms of power, the counterpart quantity is the penetration depth. In a scatter-free medium the power density is of exponential form with a power absorption coefficient given by 2α. The penetration depth given by $\delta_\mathrm{p} = \delta_\mathrm{s}/2$ indicates the maximum depth of the medium that contributes to the brightness temperature (Hallikainen and Winebrenner, 1992).

[7] The same equation is valid for the magnetic field by replacing $\mathbf{E}$ with $\mathbf{H}$.

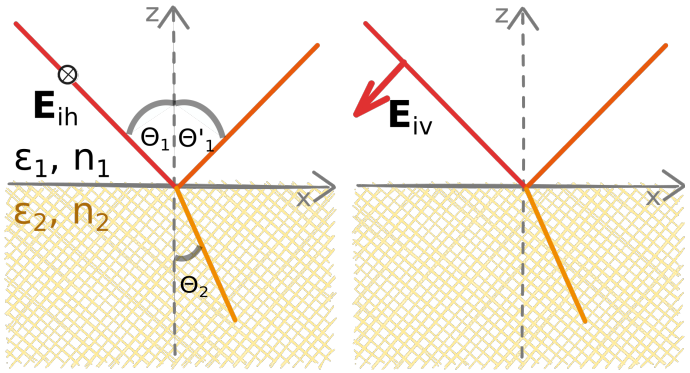

Figure 2.4: Reflection and refraction at a boundary of medium 1 (characterized by ϵ_1 and n_1) and medium 2 (characterized by ϵ_2 and n_2). On the left, the incident light (red line), propagating in negative z-direction, is horizontally polarized shown by the electric field vector $\mathbf{E}_{\mathrm{ih}}$ and vertically polarized on the right ($\mathbf{E}_{\mathrm{iv}}$). The yellow lines within the medium 2 with an angle of θ_2 to the surface normal denote the refracted wave and the orange lines with an angle of $\theta_1' = \theta_1$ to the surface normal are the reflected waves.

Dielectric Permittivity We have seen that permittivity plays a fundamental role in radiative transfer. In a real material such as sea ice or snow (heterogeneous mixtures) the permittivity is inhomogeneous and can be approximated by an effective permittivity which is often described by 'mixing' the intrinsic dielectric permittivity of a host material, for example ice, with the one from the inclusions, for example brine. This will be discussed in more detail later (Section 2.1.5).

Polarization The locus of the tip of the electric field vector is described by the polarization. In case of transmission and reflection at oblique incidence (for example for satellite observations of the Earth's surface) two orthogonal polarization configurations are used to describe the wave: horizontal polarization (denoted by subscript h) and vertical (denoted by subscript v) polarization. The two polarizations are shown in Figure 2.4.

Reflection and Transmission With the previous introduction of permittivity and polarization we may now describe what happens when a planar wave encounters a boundary. The planar boundary separates two dielectric media, that we call medium 1 and medium 2, with different dielectric properties, ϵ_1 and ϵ_2[8]. The incident wave coming from medium 1 is partly reflected to medium 1 and partly refracted (or transmitted) in medium 2. The angles of incidence, θ_1, reflection, θ_1', and refraction, θ_2, shown in Figure 2.4, are related by Snell's laws: $\theta_1 = \theta_1'$ and $\sin(\theta_2)/\sin(\theta_1) = n_1/n_2$. The attentive reader might have noticed that the expression for the angle is complex (if the imaginary part of the permittivity is nonvanishing) and does not have the significance of a refraction angle in the traditional sense. Considering instead the angle formed by the planes of waves with constant phase

[8]In principle the discontinuity at a boundary applies also to magnetic permeability. As we deal with nonmagnetic materials, we consider μ to be equal to μ_0, the permeability of vacuum.

offers a physical interpretation of a refraction angle. For the expressions of that angle see Stratton (1941). For small values of the dielectric loss term, we can approximate the angle of transmission with Snell's law using the real part of the refractive index, see Appendix A.

Across a boundary, that is a discontinuity in terms of dielectric properties, the electric and magnetic field vectors may also change but one can derive boundary conditions, for example, that the tangential component of the electric field vector is continuous (Born and Wolf, 2019). This boundary conditions allow to determine the reflection coefficients for both vertical (ρ_v) and horizontal (ρ_h) polarization, given by the fraction of the amplitudes of the reflected and the incident electric fields. They are described by the Fresnel equations as

$$\rho_\mathrm{v} = \frac{\sqrt{\epsilon_2/\epsilon_1 - \sin^2(\theta_1)} - \epsilon_2/\epsilon_1 \cos(\theta_1)}{\sqrt{\epsilon_2/\epsilon_1 - \sin^2(\theta_1)} + \epsilon_2/\epsilon_1 \cos(\theta_1)}, \tag{2.25}$$

$$\rho_\mathrm{h} = \frac{\cos(\theta_1) - \sqrt{\epsilon_2/\epsilon_1 - \sin^2(\theta_1)}}{\cos(\theta_1) + \sqrt{\epsilon_2/\epsilon_1 - \sin^2(\theta_1)}}, \tag{2.26}$$

for an incident plane wave propagating in negative z-direction as depicted in Figure 2.4; and the transmission coefficients (fraction of the amplitudes of the transmitted and the incident electric fields) then read: $t_\mathrm{h} = 1 + \rho_\mathrm{h}$ and $t_\mathrm{v} = (1 + \rho_\mathrm{h})(\cos(\theta_1)/\cos(\theta_2))$.

The absolute values of the Fresnel coefficients are proportional to the reflected electric field amplitudes. We can now come back to our energy considerations from the previous Section 2.1.2. The ratio of reflected to incident power, the reflectivity, for each polarization is simply given by the square of the absolute value of the corresponding Fresnel coefficient. Because of conservation of power, the sum of reflectivity and transmissivity (ratio of transmitted to incident power) equals one. The absolute squares of the reflection coefficients of an ice-air and a water-air boundary are shown in Figure 2.5. We can see that in both cases there is an incidence angle when ρ_v equals zero, meaning that the vertically polarized component is transmitted completely (no reflection). This angle is called *Brewster angle*. In an absorbing material, i. e., with nonzero imaginary part of the permittivity, ρ_v does not go to zero and the *Brewster angle* corresponds to the angle where ρ_v has a minimum.

Scattering We restrict ourselves to the case of a static scattering, where the electromagnetic field is incident on a medium with constant dielectric properties. We rewrite Equation 2.20 describing the space-dependent part of the electric field that is incident on a medium with refractive index $n(\mathbf{r}, \omega)$ as (Born and Wolf, 2019)

$$\nabla^2 \mathbf{E}(\mathbf{r}, \omega) + \frac{\omega^2}{c^2} n^2(\mathbf{r}, \omega) \mathbf{E}(\mathbf{r}, \omega) = 0. \tag{2.27}$$

In most cases approximate techniques are needed to solve this equation which describes the scattered field. For dense media like snow, where the scatterers do not scatter inde-

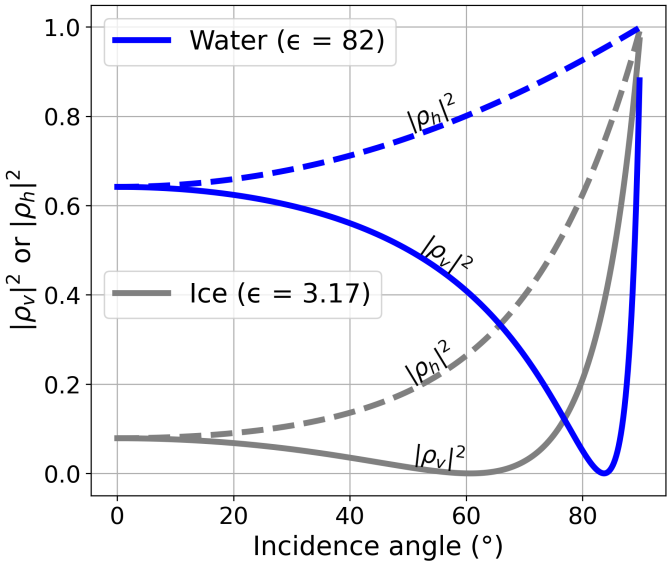

Figure 2.5: Absolute squared values of the Fresnel reflection coefficients for vertical polarization, $|\rho_\mathrm{v}|^2$, and for horizontal polarization, $|\rho_\mathrm{h}|^2$, of an air-water boundary (blue) and an air-ice boundary (grey). Note that the imaginary part of the permittivity is neglected here.

pendently (they can 'shield' each other) the dense media radiative transfer framework can be used. Tsang et al. (2016) first solve Maxwell's equations numerically over samples of a few wavelengths. The hereby derived relevant quantities like phase matrix and extinction coefficients are then used in equations describing the intensity. The authors also utilized the discrete dipole approximation to solve Maxwell's equations numerically over a whole snowpack which enables even fully coherent modeling, i. e., taking into account changing phase relations of the scattered waves. For special cases, exact solutions of Equation 2.27 can be found. Let us now consider such a case of spherical scatterers, like rain drops.

Mie and Rayleigh Scattering: Spherical Particles The ratio of scattered power to incident power, the scattering cross section, can be calculated for spherical scatterers using the solution of Maxwell equations by Mie (1908) which depends on the radius of the scattering particle, r, the dielectric permittivities of scatterer and background and on the wavelength. For particles that are much smaller than the wavelength, the solution can be simplified using Rayleigh approximations.

Figure 2.6 shows the scattering regimes as function of radiation frequency f and particle radius r. Here we used the size parameter $x = 2\pi r f/v$ where v is the wave's phase velocity (speed of light in air) as rough boundaries to distinguish the regimes as done in Petty (2006). We can see that in the microwave region for a non-precipitating atmosphere, scattering can either be neglected or described by Rayleigh scattering.

In the Rayleigh regime with a background medium air the expression for the scattering cross section Q_s of a spherical particle with radius r and dielectric permittivity ϵ is given

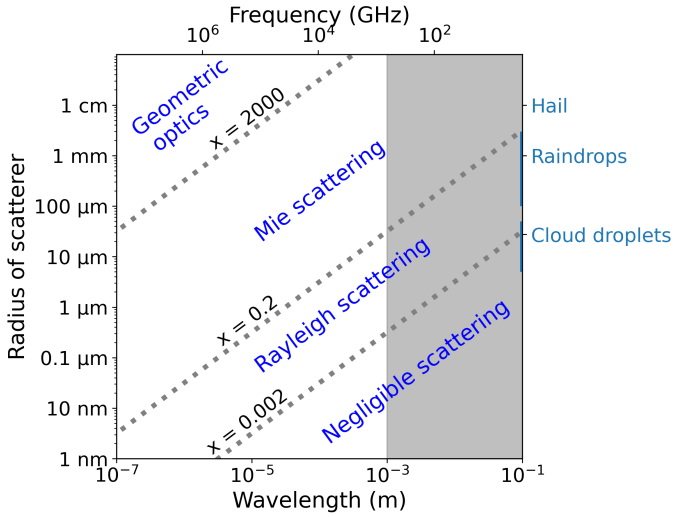

Figure 2.6: Scattering regimes as function of radiation frequency and particle radius r. The size parameter $x = 2\pi r/\lambda$ (λ being the wavelength) separates the broad scatterings regimes. Note that also lower values for the boundary between Mie scattering and geometric optics are used in literature (Gimmestad and Roberts, 2023). Typical values for atmospheric particles are shown on the right axis. The shaded area indicates the microwave region. Adapted from Petty (2006).

by

$$Q_\mathrm{s} = \frac{2\lambda^2}{3\pi}(2\pi r/\lambda)^6\left(\left|\frac{\epsilon-1}{\epsilon+2}\right|\right)^2. \tag{2.28}$$

The analog to Q_s in terms of absorbed power is the absorption cross section Q_a, which can be approximated in this regime as

$$Q_\mathrm{a} = -\frac{\lambda^2}{\pi}(2\pi r/\lambda)^3\mathrm{Im}\left(\frac{\epsilon-1}{\epsilon+2}\right). \tag{2.29}$$

Note that for Rayleigh scattering the strength of scattering is proportional to λ^{-4} while the absorption cross section is a function of λ^{-1}. Mie and Rayleigh scattering as described above apply to single scatterers. In a cloud, for example, we assume randomly distributed particles with sizes following a drop-size distribution and the scattering is described in terms of a scattering cross section per unit volume.

Born Approximation Rigorous derivation of scattering from the Maxwell equations results in the integral equation of potential scattering[9] (Eq 2.27, Born and Wolf, 2019). The approximate solution obtained using perturbation methods is called Born approximation, which is accurate if the incident field is large compared to the scattered field. An improved Born approximation can be used in a granular media such as snow (Mätzler, 1998) to derive absorption and scattering coefficients and cross sections as well as phase functions.

[9]It is a pretty coincidence that this differential equation is mathematically equivalent to the time-independent, non-relativistic Schrödinger equation.

Statistical information about the microstructure of such media can be described by the autocorrelation function $C(\mathbf{r})$. For a medium with two phases, the phase indicator function is 1 for points $\mathbf{r}$ within the volume consisting of phase one and zero otherwise. The autocovariance of this phase indicator function yields the correlation function $C(\mathbf{r})$ (Proksch et al., 2015). By fitting $C(\mathbf{r})$ to an exponential form so that $C(\mathbf{r}) \propto \exp(-|\mathbf{r}|/I_{\text{exp}})$ we can obtain the exponential correlation length I_{exp} that is often used in parametrizations of scattering of snow.

Surface Scattering In case of a specular surface (without roughness) the scattered energy can be calculated using the reflectivity derived from the Fresnel equations 2.25. Assuming a downwelling brightness temperature $T_{\text{B,down}}$ the upward reflected, p-polarized (either horizontal or vertical) fraction $T^p_{\text{B},\Omega}(\theta, f)$ is given by $T_{\text{B},\Omega}(\theta, f) = |\rho_{\text{p}}|^2 T_{\text{B,down}}$. A Lambertian surface scatters uniformly in all directions (perfect roughness). The angular response of a real surface which consists of multiple scales of roughness can be characterized by a combination of specular and Lambertian surface scattering.

To compute non-specular scattering one needs to integrate the product of $T_{\text{B,down}}$ and the bistatic-scattering coefficient[10] over the upper hemisphere. Alternatively, diffuse scattering can be represented by downwelling radiation at an effective angle (Mätzler, 2005). Mätzler (2005) shows that at zenith angles around 55° the differences between specular reflection and scattering by a Lambertian surface are insignificant. Yet another way to describe rough surfaces is to modify the surface reflectivities using roughness parameters obtained from the height distribution of the surface (Choudhury et al., 1979). Further methods to treat surface scattering include the small perturbation model (Tsang and Kong, 2009), the advanced integral equation method (Chen et al., 2003) or even numerical solutions of Maxwell's equations in three dimensions (Zhou et al., 2004). In this thesis, we will assume zenith angles around around 55° and treat the surface as specular scatterer.

Satellite-observed Brightness Temperatures Coming back to our measurement scheme in Figure 2.3 we can come up with an equation for the brightness temperatures ($T_{\text{B,sat}}$) measured via the antenna temperature by the satellite radiometer. We first define the total transmittance of the atmosphere as

$$\Upsilon^p(\theta, f) = \exp\left(-\sec(\theta) \int_0^\infty \kappa_{\text{e}}^p(f)\, \mathrm{d}z \right) \tag{2.30}$$

and then obtain

$$T^p_{\text{B,sat}}(\theta, f) = T_{\text{B,up}}(\theta, f) + \Upsilon^p(\theta, f)(T^p_{\text{B},\Omega}(\theta, f) + T^p_{\text{B,surf}}(\theta, f)), \tag{2.31}$$

[10]The term bistatic-scattering coefficient refers to the ratio of re-radiated power and incident power density (both polarized) per surface area.

where superscript p denotes the polarization (either h or v), $T^p_{\mathrm{B},\Omega}(\theta, f)$ is the upward scattered fraction of $T_{\mathrm{B,down}}$ and $T^p_{\mathrm{B,surf}}$ is the surface-emitted brightness temperature.

The treatment of the question of microwave remote sensing has been very general so far. We will now look into the Earth's atmosphere and surfaces, in particular, in the Arctic, and discuss how these parameters influence the microwave signal. To do so we will mainly focus on the four protagonists introduced in the last chapter.

2.1.4 The Atmosphere: Water Vapor and Cloud Liquid Water

In the microwave regime, the atmosphere of the Earth ranges from near-total opacity to total transparency. The surface signal is transmitted up to 480 GHz at the poles because of the dry atmosphere (Wang et al., 2017). At low frequencies (<15 GHz) the atmosphere can be considered transparent even in the presence of clouds. However, the microwave spectrum also contains absorption lines due to atmospheric gases. Emission and absorption take place when molecules transition from one discrete energy level to another. These energy levels depend on the electronic, vibrational and rotational energy. Figure 2.7 shows these absorption lines due to the gases water vapor (at 22.235 GHz and 183.31 GHz) and oxygen (50 GHz to 70 GHz and 118.75 GHz). Because of line broadening, most notably pressure broadening due to molecular collisions, these lines have a finite width. The line shape can be formally described (Ben-Reuven, 1965; Van Vleck and Weisskopf, 1945) and is a function of both temperature and pressure. Other constituents of the atmosphere such as nitrogen dioxide absorb in the microwave frequency range, too, but are negligible compared to water vapor and oxygen. The absorption coefficient by gases is given as the sum of the absorption coefficients of the individual transitions for the different atmospheric gases. This is valid as long as spectral lines do not significantly overlap, i. e., the radiation from different transitions is incoherent (Waters, 1976). In addition to absorption by gases, there is also interaction of the electromagnetic radiation with hydrometeors as present in clouds, fog or rain. The scattering and absorption efficiency depends on the dielectric spectrum and we can therefore order it depending on the type of hydrometeor: water particles exhibit strong scattering and absorption, while ice particles are weak absorbers. In the microwave spectrum below 100 GHz the description of atmospheric attenuation in case of no precipitation can be reduced to the most important components: the absorption of water vapor α_{V}, oxygen α_{O} and liquid water in clouds α_{L}. The total absorption coefficient is thus given as $\kappa_{\mathrm{a}} = \alpha_{\mathrm{V}} + \alpha_{\mathrm{O}} + \alpha_{\mathrm{L}}$. The vertically integrated oxygen absorption is nearly constant over the globe (Wentz and Meissner, 2000). We will therefore focus on water vapor and cloud liquid water and describe their interactions with the electromagnetic radiation in the atmosphere in the following. We will consider a non-precipitating atmosphere only, therefore we do not need Mie theory to describe scattering by rain drops. Because oriented, non-spherical hydrometeors are not considered in the following the transmittance $\Upsilon(\theta, f)$ does not depend on the polarization.

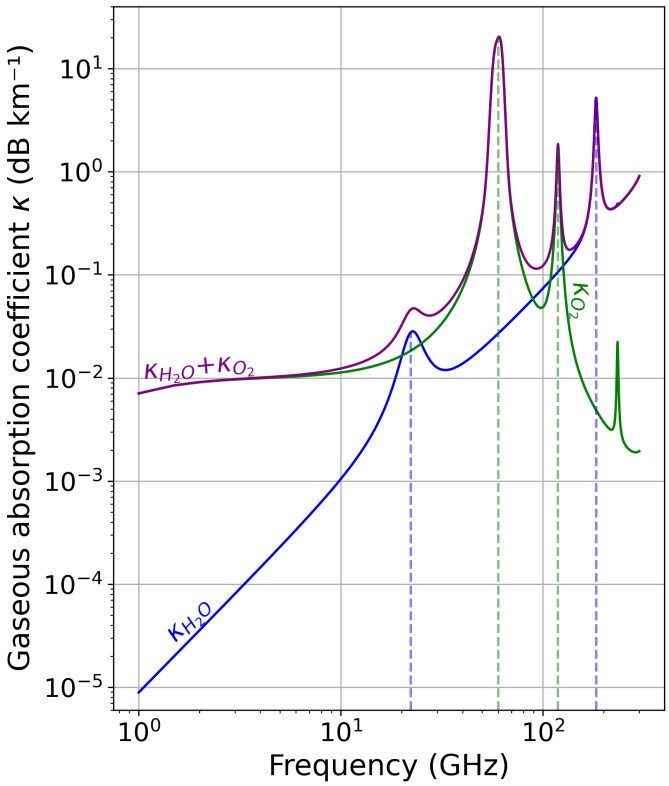

Figure 2.7: Absorption coefficients κ_a of water vapor (blue line), oxygen (green line) and their sum at sea level under conditions resembling the dry and cold Arctic atmosphere (pressure is 1013 hPa, temperature is −18 °C and water vapor density is 1 g m^{-3}). The coefficients are computed based on Rosenkranz (2017). The vertical dashed blue lines indicate the water vapor rotation lines at 22.235 GHz and 183.31 GHz while the vertical green lines indicate the oxygen absorption bands around 60 GHz and at 118.75 GHz.

Water vapor Water is a polar molecule and due to its low symmetry it has three independent moments of inertia. In the microwave regime, the interaction of the electromagnetic field of the incident wave with the electric dipole of the polar water vapor molecule results in two significant rotation lines at 22.235 GHz (the hyperfine components of this line due to spin interactions are described in Bluyssen et al., 1967) and 183.31 GHz. In the near- and mid-infrared the rotational modes combine with the vibrational ones and result in closely packed absorption lines, the vibration-rotation band. Within the rotational and vibrational-rotational bands, and between, in the windows, we find the residual absorption, the so called water vapor continuum. The underlying causes of the continuum are still under debate (Shine et al., 2012). While it is of less importance within the strongly absorbing rotational bands, it is the dominant source of absorption in the windows.

In the atmospheric column of unit cross section, the mass of water vapor is given by

the integrated or total water vapor (TWV) which is formally defined as

$$\mathrm{TWV} = \int_0^\infty \rho_\mathrm{v}(z)\,\mathrm{d}z, \tag{2.32}$$

where the water vapor density ρ_v is integrated over the altitude z.

The absorption coefficient α_V is a function of water vapor density. Based on radiosonde measurements and expressions from Liebe (1985), Wentz and Meissner (2000) parameterize α_V as a second-order polynomial function of TWV with frequency-dependent coefficients.

Cloud liquid water path Similar to the integrated water vapor we define cloud liquid water path LWP as the amount of liquid water present in the atmospheric column of unit area. For a cloud of height H we get

$$\mathrm{LWP} = \int_0^H m_\mathrm{L}(z)\,\mathrm{d}z, \tag{2.33}$$

where m_L is the cloud liquid water content. In clouds, drops are small and the attenuation is independent of the drop-size distribution and proportional to the total water content per unit volume (Goldstein, 1951). This is because the scattering coefficient is proportional to the radius of the drop r to the power of six (Rayleigh scattering, see Equation 2.28), while the absorption cross section is a function of r^3 so that attenuation in clouds is caused almost entirely by absorption for sufficiently small drops. Wentz and Meissner (2000) parameterize the vertically integrated absorption coefficient α_L as a linear function of liquid water path (LWP) and mean cloud temperature using frequency-dependent coefficients.

2.1.5 The Surface: Open Ocean, Sea Ice, and Snow

The surface in Figure 2.3 acts both as emitter and as a scatterer of downwelling atmospheric radiation. Different material properties such as temperature and density determine the dielectric properties. These then dictate absorption, emission and scattering within the media and at boundaries.

Open Ocean Microwave emission from open water depends mainly on surface temperature and surface roughness related to wave and foam formation. The permittivity of the sea water is a function of temperature T and salinity S (Debye, 1929) and the dielectric loss term is higher than for fresh water due to the free charge carriers (dissolved salts). Several parameterizations of the sea water's permittivity exist (Stogryn, 1971; Klein and Swift, 1977). Here, we use the formulation by Meissner and Wentz (2004) with a double Debye relaxation frequency law

$$\epsilon(T,S) = \frac{\epsilon_s(T,S) - \epsilon_1(T,S)}{1 + i\nu/\nu_1(T,S)} + \frac{\epsilon_1(T,S) - \epsilon_\infty(T,S)}{1 + i\nu/\nu_2(T,S)} + \epsilon_\infty(T,S) - i\frac{\sigma(T,S)}{2\pi\epsilon_0\nu}, \tag{2.34}$$

where ν is the radiation frequency (in GHz), ν_1 and ν_2 (the relaxation frequencies), as well as ϵ_1 and ϵ_∞ are fit parameters (expressions given in Meissner and Wentz, 2004 and Meissner and Wentz, 2012); and σ is the conductivity of sea water.

In case of calm waters the ocean surface is specular and its reflectivity can be described by the Fresnel equations (Equation 2.25). The emission is highly polarized. Wind roughens the ocean surface and has a threefold effect on the surface emissions (Wentz and Meissner, 2000). Depending on the wavelength, ocean waves can change the zenith angle locally (if their wavelength is large compared to the radiated one) or lead to diffraction in case of wavelengths which are small compared to the radiated microwaves. In addition, the sea foam as a mixture of air and water changes the dielectric properties. In this thesis, the parameterization of Wentz and Meissner (2000) is used, which is based on a geometrical optics model, accounts for diffraction effects and includes a factor to account for the foam effect on the reflectivity.

Sea Ice In contrast to the ocean, where the major contribution to the radiation is emitted in the upper micrometers, in the radiometry of sea ice, each layer of the water-ice-snow system contributes to the radiation. Penetration depths can be on the order of centimeters to meters (Mathews, 2007). Therefore, vertical profiles of temperature and permittivity influence the observed microwave signal. To calculate the emitted radiation, the propagation of a wave in a dense media needs to be considered. This includes reflections at (possibly rough) interfaces and multiple scatterings. In dense media the assumption about independent scattering is not valid and the scatterers are correlated (Tsang and Kong, 2008). Multiple reflection can either be treated coherently, by adding electric fields, or incoherently, arising from inconsistent phase relations of the scattered waves. Incoherent reflections can be described by adding power components directly.

One approach to model radiative transfer in sea ice is the use of stacked planar layers as done by the MEMLS_ice model (Mätzler and Wegmuller, 1987; Tonboe et al., 2006) or the Snow Microwave Radiative Transfer (SMRT) model (Picard et al., 2018) where each layer has its own dielectric and physical properties. Then the radiative transfer across the layers is solved using numerical techniques like six-flux theory (Emslie and Aronson, 1973) or the discrete ordinate and eigenvalue method (Picard et al., 2013).

The relative permittivity of sea ice is an effective one (mentioned already in Section 2.1.3) that can be derived by mixing the permittivity of air, ice and brine with ice as the background medium which contains inclusions of brine and air. The real part of the permittivity of freshwater ice can be considered constant with a value of 3.17 (Hallikainen and Winebrenner, 1992). The imaginary part was parameterized by Hufford (1991): it increases with temperature and frequency and is of the order of $<10^{-2}$. In brine, salinities can exceed 200 ppt (Hallikainen and Winebrenner, 1992) and the parameterization derived for seawater (Equation 2.34) has to be modified (typical salinities for ocean water

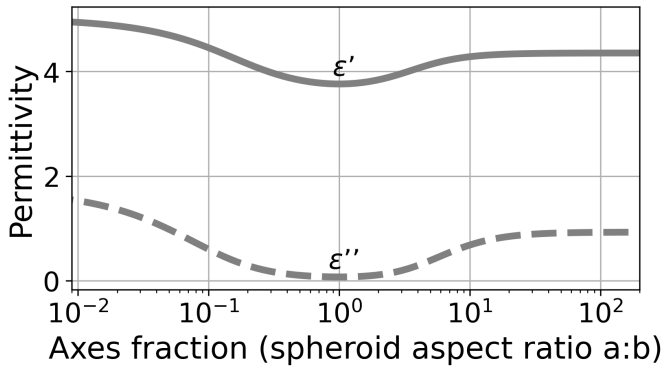

Figure 2.8: Effective permittivity of sea ice calculated for different brine inclusion shapes following Polder and van Santeen (1946). Aspect ratios (ratio of the two axis) smaller one indicate oblate spheroids and higher values prolate spheroids. An aspect ratio of unity, spherical inclusions, yield the lowest effective values. The permittivity of brine is $6.83 + 42\mathrm{i}$ calculated from a brine volume fraction of 0.06 and a temperature of $-4\,^{\circ}\mathrm{C}$. The background permittivity of ice is set to 3.17.

are on the order of 35 ppt). The permittivity of brine is expressed as an empirical function of temperature and brine volume content (Stogryn and Desargant, 1985). Both real and imaginary part are of the order of 10 to 100 and increase with temperature. Brine pockets are typically narrow and long. The dielectric mixture is not linear but depends on the inclusions shape according to Polder and van Santeen (1946). In that model the effective permittivity is calculated assuming ellipsoidal inclusions characterized by depolarization factors. For spheroid inclusions the permittivity shows a minimum in case of spherical inclusions and increases toward prolate and oblate shapes, see Figure 2.8. Polder and van Santeen (1946) assumes the ellipsoids are randomly orientated. In real sea ice we might encounter spatial anisotropy, for example because of aligned congelation growth and vertically oriented brine channels (Tucker et al., 1992). Other models exist to compute effective permittivities, e. g., by Garnett and Larmor (1904), the coherent potential approximation (Kerner, 1956) or even exact formalism like the strong-contrast expansion (Torquato and Kim, 2021), which enable to model spatial anisotropies.

In sea ice, volume scattering effects of the brine pockets and the air bubbles are important. Due to the high brine content and the strong contrast between the permittivity of brine and ice, brine pockets can be considered the dominant scatterers in first-year ice. In multiyear ice with low salinity scattering takes mainly place due to the air inclusions. The microstructure may be described by an autocorrelation function in terms of an exponential correlation length. From air bubble diameters measured by Shokr and Sinha (1994), Rostosky et al. (2020) estimate an exponential correlation length of 0.28 mm for multiyear ice. Rostosky et al. (2020) assume the value 0.15 mm for first-year ice[11]. In this thesis the MEMLS_ice model which applies the improved Born parameterization (Mätzler, 1998,

[11]This is confirmed by Rasmus Tonboe, who derived similar values from thin ice slices, personal communication, May 2022.

more details on model parameter choices in Section 2.1.3) is used to simulate microwave emissions from layers of sea ice and snow.

Because of the dielectric contrast of air and ice, the polarization difference, given by difference between vertically and horizontally polarized brightness temperature, is usually non-zero, especially when observing close to the Brewster angle. Also, brightness temperatures of sea ice are higher than of open ocean in the range of 1 GHz to 100 GHz: the open ocean is radiometrically colder than ice.

Snow Snow is a dense stratified medium as well and needs to be treated similarly to sea ice, including multiple scattering, effective permittivities, and reflections at interfaces. Dry snow is a mixture of air and ice with the air as background medium. The permittivity of dry snow is a function of density, verified by experimental results (Tiuri et al., 1984, e.g.), and its real part can vary from about 1.2 to 2.8 while the imaginary part is on the order of 10^{-4} to 10^{-2} (Tsang et al., 2000). At intermediate densities (larger $450\,\mathrm{kg\,m^{-3}}$) the assumption about the background medium no longer holds and existing theories become inaccurate (Picard et al., 2022). Also, structural anisotropy, that is a preferential orientation of the nonspherical ice particles in snow, further influences the effective permittivities (Leinss et al., 2016).

Wet snow is a mixture of air, ice and water. Because of the high dielectric loss term of liquid water compared to the one of dry snow, the spectral behavior of the wet snow mixture is dominated by the dispersion behavior of water (Hallikainen et al., 1986). Again, different dielectric mixing models can be considered when dealing with wet snow, some are presented in Hallikainen et al. (1986). Brine-wetted snow will be treated along the same lines in this thesis.

Because snow is a dense medium the particles do not scatter independently. One approach to describe absorption and scattering in snow is the improved Born approximation (Mätzler, 1998) which is used in this thesis. Here, the microstructure is characterized by the exponential correlation length, that varies depending on the snow type (Mätzler, 2002). For terrestrial Arctic snow, exponential correlation lengths have been determined from computer tomography to be of the order of 0.055 mm to 0.390 mm (Proksch et al., 2015). At very low frequencies (particle size << wavelength) scattering can be neglected (Tsang et al., 2000).

We have now discussed the microscopic models of different constituents of the ocean, the snow-covered sea ice, and atmosphere that determine the satellite signal. In combination these models form a forward model F that simulates satellite brightness temperatures from a set of geophysical parameters. Thus, by inverting such a forward model we can draw conclusions about the geophysical state of atmosphere and surface at the time of the satellite observation. The inversion method will be discussed in the next Section.

2.2 Inverse Methods: Optimal Estimation

For retrieving physical state parameters expressed as $\mathbf{x}$ from satellite-measured brightness temperatures $\mathbf{T}$B, we invert the forward model F

$$\mathbf{T}_\mathrm{B} = F(\mathbf{x}) \tag{2.35}$$

using an optimal estimation method. The description of the inversion scheme in this section is adopted from Rückert et al. (2023a).

Inverting the forward model leads to retrieved parameters that are physically consistent in model space, e. g., ice type fractions add up to the total sea ice concentration. Here, we use an optimal estimation method for the inversion that additionally retrieves an estimate of the uncertainty for each parameter.

The inversion method is a Bayesian approach based on Rodgers (2000) using the conditional probabilities

$$P(\mathbf{x}|\mathbf{y}) = \frac{P(\mathbf{y}|\mathbf{x})P(\mathbf{x})}{P(\mathbf{y})}, \tag{2.36}$$

where $P(\mathbf{x}|\mathbf{y})$ is the probability of a state $\mathbf{x}$ (state vector, here: vector of geophysical quantities including sea ice concentration and total water vapor) given measurements $\mathbf{y}$ (measurement vector, here: brightness temperatures of different frequencies and polarizations), $P(\mathbf{y}|\mathbf{x})$ is the conditional probability density of $\mathbf{y}$ given $\mathbf{x}$, and $P(\mathbf{y})$ and $P(\mathbf{x})$ are the prior probability densities of the measurement and state, respectively.

The general idea is to find the set of parameters that, when mapped to brightness temperatures through the forward model, will give the best match when compared to the measured brightness temperatures, under some constraints imposed by a priori knowledge about probable states. The metric that defines the 'best match' is given by a cost function and the optimal estimation method finds the state that maximizes $P(\mathbf{x}|\mathbf{y})$ by minimizing the cost function χ^2

$$\chi^2(\mathbf{y}, \mathbf{x}, \mathbf{S}_e, \mathbf{S}_a, \mathbf{x}_a) = (\mathbf{y} - F(\mathbf{x}))^\intercal \, \mathbf{S}_e^{-1}(\mathbf{y} - F(\mathbf{x})) + (\mathbf{x}_a - \mathbf{x})^\intercal \mathbf{S}_a^{-1}(\mathbf{x}_a - \mathbf{x}), \tag{2.37}$$

where $\mathbf{S}_e$ is the measurement uncertainty covariance matrix of the input brightness temperatures. A priori information are included by $\mathbf{x}_a$ as the a priori state, i. e., the most likely state prior to the measurements, e. g., the mean of a climatology. The differences of the state to the a priori state is weighted by $\mathbf{S}_a$ as the covariance matrix of the a priori values. F is the forward model introduced in Equation 2.35. All other quantities will be discussed in more detail in Chapter 5. The maximum a posteriori solution is given by $\hat{\mathbf{x}}$ as (Rodgers, 2000)

$$\hat{\mathbf{x}} = \hat{\mathbf{S}}(\mathbf{S}_a^{-1}\mathbf{x}_a + \mathbf{K}^\intercal \mathbf{S}_e^{-1}\mathbf{y}) \tag{2.38}$$

with the associated uncertainty

$$\hat{\mathbf{S}} = (\mathbf{K}^\intercal \mathbf{S}_e^{-1} \mathbf{K} + \mathbf{S}_a^{-1})^{-1}, \tag{2.39}$$

where $\mathbf{K}$ is the Jacobian at $\hat{\mathbf{x}}$ of the forward model F. For Equation 2.38 to be fully valid, we have assumed that the forward model is only moderately non-linear and that the parameter distributions are Gaussian. The degree of nonlinearity, c^2, can be determined by (Rodgers, 2000)

$$c^2 = \delta\mathbf{y}^\intercal \mathbf{S}_e^{-1} \delta\mathbf{y}, \tag{2.40}$$

where $\delta\mathbf{y}$ is given by $\delta\mathbf{y} = F(\hat{\mathbf{x}}) - F(\mathbf{x}) - \mathbf{K}(\hat{\mathbf{x}} - \mathbf{x})$ and $\mathbf{x}$ is given by values one standard deviation away from $\hat{\mathbf{x}}$ using $\hat{\mathbf{S}}$ to determine the standard deviation. $c^2 < 1$ indicates cases where the problem is nearly linear. The assumption of Gaussian parameter distributions is valid for most of the parameters but, e. g., liquid water path and sea ice concentration may differ in their distributions from a Gaussian. In cases of non-Gaussian probability density functions (PDFs) (prior and posterior) it is not clear whether the maximum a posteriori solution is appropriate (or whether, e. g., the expected value solution is better suited)[12].

Iterative Procedure

For the non-linear forward model the maximum a posteriori solution is found iteratively, depicted in Figure 2.9. In order to find the minimum of the cost function Equation 2.37 we implemented automatic differentiation (Revels et al., 2016), which allows efficient computing of Jacobians. For minimizing we use the Levenberg-Marquard algorithm where the step of the iteration from $\mathbf{x}_i$ to $\mathbf{x}_{i+1}$ is controlled by the parameter γ_i that is either reduced or increased with each step[13] depending on the difference of the cost functions (Rodgers, 2000):

$$\mathbf{x}_{i+1} = \mathbf{x}_i + [(1+\gamma_i)\mathbf{S}_a^{-1} + \mathbf{K_i}^\intercal \mathbf{S}_e^{-1} \mathbf{K}_i]^{-1} \{\mathbf{K}_i^\intercal \mathbf{S}_e^{-1} [\mathbf{y} - F(\mathbf{x_i})] - \mathbf{S}_a^{-1} [\mathbf{x}_i - \mathbf{x}_a]\}. \tag{2.41}$$

We further constrain our parameter space to physically meaningful values (e. g., only positive values of TWV or sea ice concentration (SIC)). If, during the iteration, such nonphysical state vectors are obtained, we re-start using a different start guess (e. g., small but positive values of TWV or SIC). To define a convergence criterion we follow Rodgers (2000) and test whether $d^2 = (\mathbf{x}_i - \mathbf{x}_{i+1})^\intercal \hat{\mathbf{S}}^{-1} (\mathbf{x}_i - \mathbf{x}_{i+1})$ is less than the number of retrieval parameters.

[12] A possible workaround is to transform the quantities with non-Gaussian distributions to ones that do follow a Gaussian PDF.

[13] The start value is $\gamma_0 = 10^{-5}$, and it is either reduced by a factor of 10 or increased by a factor of 100.

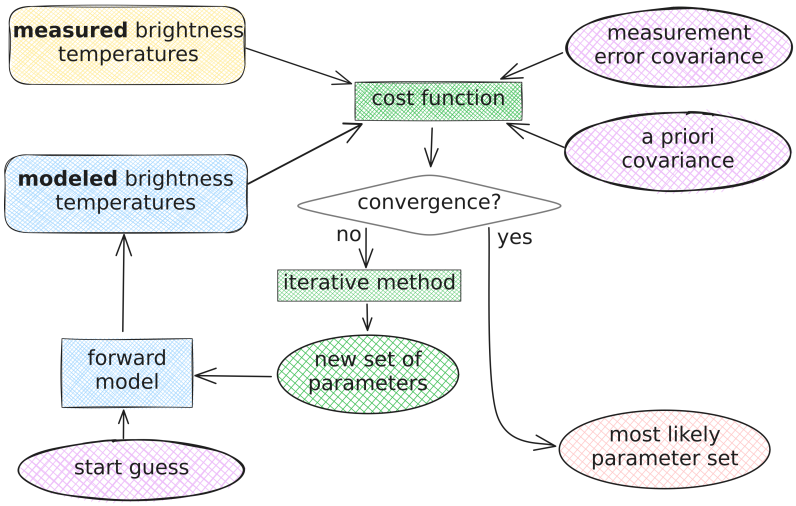

Figure 2.9: Scheme of optimal estimation method.

Computational Architecture

Model and inversion are implemented using the programming language Julia (Bezanson et al., 2017) allowing for fast computations needed in satellite retrievals. The modules of the retrieval are depicted in Figure 2.10. The different parts of the retrieval are connected with well-defined in- and outputs. This way, it is possible to change the frequency channels used in the method and to even retrieve additional quantities, if appropriate satellite observations are provided. One example is retrieving ice thickness by adding observations at 1.4 GHz as done in Scarlat et al. (2020).

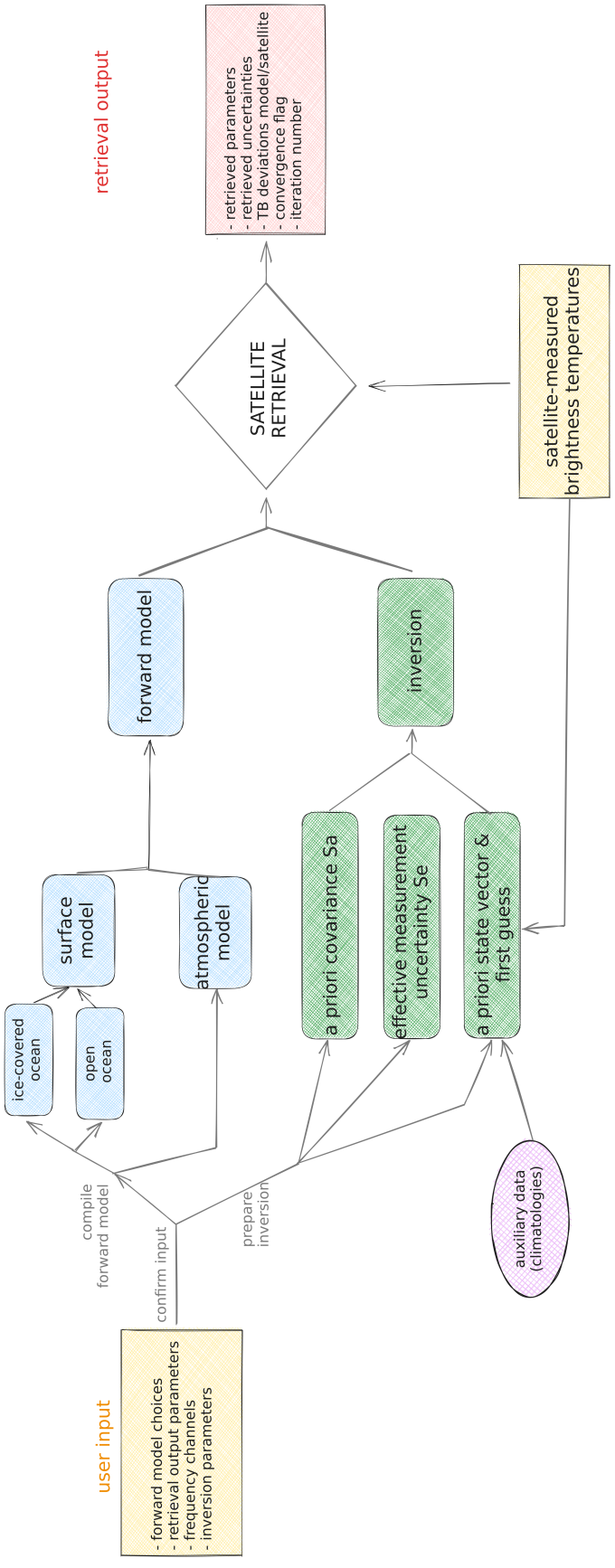

Figure 2.10: Modular structure of the satellite retrieval. Input is indicated by yellow color (configurations and measured brightness temperatures), components related to the forward model are blue, and components of the inversion are green.

2.3 Evaluating Satellite Retrievals: The Curse of Remote Sensing

The "curse of remote sensing" is a term from Ulaby and Long (2014). In order to evaluate a satellite retrieval we want to compare it to the *ground truth*. However, obtaining an in-situ measurement on a satellite footprint scale is a challenge by itself and the precision of the *ground truth* already limits the possibilities of validating a retrieval algorithm. Spatial diversity and temporal variability add to this "curse of remote sensing". In addition we have a representativeness uncertainty: The integrated retrieval presented here uses all frequency channels simultaneously. This requires that all channels measure the same area on ground. As input to the retrieval we therefore use effective observations in terms of resampled brightness temperatures where the higher-resolution data is spatially averaged to match the coarser resolution of the lower-resolution frequency channels. For the Advanced Microwave Scanning Radiometer - Earth Observing System (AMSR-E) (2002-2011) this is the Level 2A product (Ashcroft and Wentz, 2019) and in case of the Advanced Microwave Scanning Radiometer 2 (AMSR2) we use the Level 1R product (Maeda et al., 2016) (more details on the products follow in Section 5.2.1). In both cases the higher-resolution data is spatially resampled based on the Backus-Gilbert method.

In addition there are uncertainties when the retrieval output from geolocated satellite swath data is resampled to a uniform projected grid, for example to get daily gridded values. Several subtleties need to be considered here:

- non-uniform sampling due to the polar orbit, i. e, more satellite overpasses close to the pole and a gap at the so-called pole hole,
- different overpass times of the several overpasses per day,
- the swath geometry and the target grid geometry,
- the satellite footprint size,
- the resampling procedure.

In general the decision for the resampling depends on the aim or research question. For a visualization of Arctic wide data for a quick look or qualitative assessment as done in Section 5.6.5 this decision will be of little importance. For, e. g., ice-edge detection, however, the resampling choices might affect the outcome. The same holds for quantitative comparisons against reference datasets, here, we also need to consider possible differences in land masking.

In this thesis we use the Gaussian resampling method that is characterized by a number of neighbors that are considered within a search radius. The data points are then weighted by a Gaussian with a provided σ using the pyresample software package (Hoese et al.,

2023). As an example, Figure 2.11a) shows the available number of satellite observations per grid cell for the EASE grid (Brodzik et al., 2012) at 25 km resolution on January 10, 2020. The sampling density is a lot higher close to the pole hole. The weighted standard deviation of the retrieval output for TWV shown in Figure 2.11b), calculated by Gaussian resampling with a σ of 5 km, a radius of 12.5 km and 12 neighbors, is a measure for the sampling uncertainty ($\sigma_{smoothing}$). The median sampling uncertainty for this day is 0.14 kg m^{-2} and it is largest in areas with little data points and at the ice edge (seen for example in Fram strait). We will later see that $\sigma_{smoothing}$ is on average small compared to the retrieval uncertainty (which can be on the order of 4 kg m^{-2} over sea ice), see Section 5.6.5.

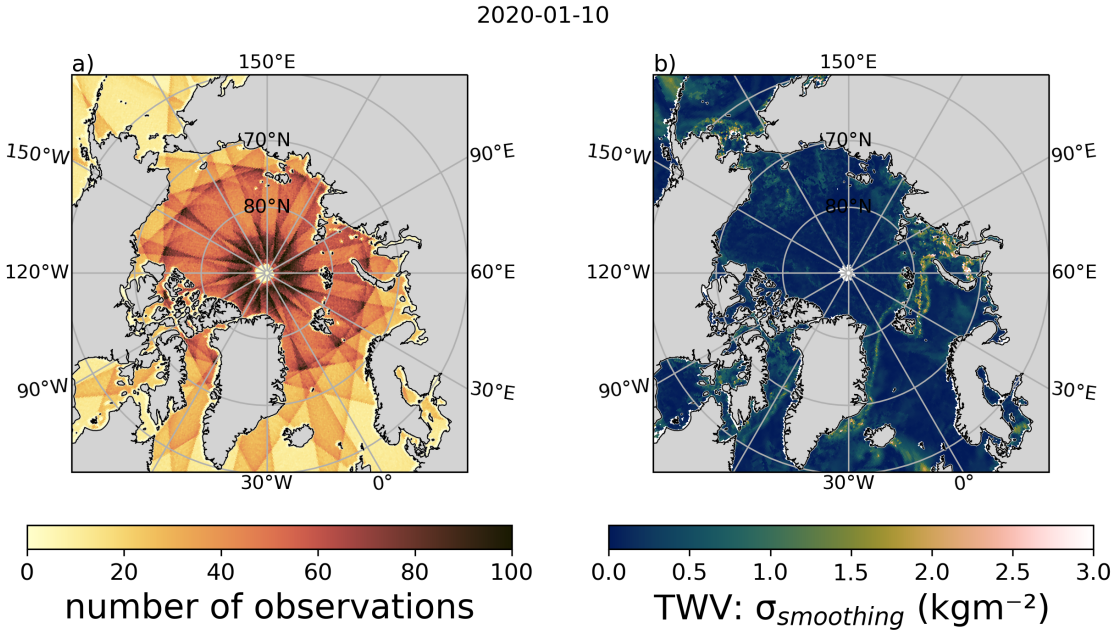

Figure 2.11: The number of satellite observations by the sensor AMSR-2 per grid cell of 25 × 25 km^2 in one day (here exemplary January 10, 2020) is shown in the left panel. The right panel shows the smoothing uncertainty of the variable total water vapor (TWV) resulting from resampling satellite swath data to gridded (25 × 25 km^2) daily values.

Chapter 3

Sea Ice Emissivity: Concept and Measurements

In this chapter we give a short theoretical introduction into the concept of emissivity and provide an overview of studies reporting values from measurement campaigns. We want to stress the importance of underlying assumptions that might effect intercomparisons of emissivity measurements. We believe a thorough understanding is necessary in order to successfully use these observational data in (developing) satellite retrievals as many satellite retrievals are based on empirically derived relationships between the geophysical parameter and the microwave emissions at different frequencies or polarizations or combinations of them. The second part of this chapter is a case study from a measurement campaign in summer 2022 where surface emissivities were estimated from ship-borne radiometer measurements which has been submitted for publication (Rückert et al., 2023d).

3.1 The Concept of Sea Ice Emissivity

The microwave signatures of sea ice have been measured and accounted for in studies in the past decades (e.g. Wilheit et al., 1971; Gloersen et al., 1973; Mätzler et al., 1984; Hollinger et al., 1984; Grenfell and Lohanick, 1985; Comiso, 1986). One main quantity that is commonly reported is the directional spectral emissivity, formally defined as $e = I_{\text{real}}/I_{\text{blackbody}}$, where I_{real} is the spectral intensity of the thermal emission by a real surface at a certain observation angle (depending on observation angle and wavelength but also on the body's temperature and composition) and $I_{\text{blackbody}}$ is the spectral intensity of a black-body at the same temperature, wavelength and observation angle. In the Rayleigh-Jeans approximation (see Equation 2.2), this is equivalent to defining an emissivity for a given frequency and polarization as

$$e(\theta, \phi) = \frac{T_{\text{B}}(\theta, \phi)}{T}, \tag{3.1}$$

where θ and ϕ are the zenith and azimuth angles, respectively, to account for the directionality. T is the physical temperature of the body. This definition considers a semi-infinite homogeneous and isothermal medium (Ulaby and Long, 2014). There is another way to define emissivity using arguments from radiative transfer. Consider the case of a nonscattering medium m with a physical temperature profile $T(z)$ at the specular boundary to another medium, here let us assume it to be the atmosphere. Along the lines of Equation 2.18 we can define the 'upwelling' brightness temperature within m, $T_{\mathrm{B,m}}(\theta_{\mathrm{m}})$, that will be incident upon the boundary at $z = 0$ from below at some incidence angle θ_m:

$$T_{\mathrm{B,m}}(\theta_{\mathrm{m}}) = \sec(\theta_{\mathrm{m}}) \int_{-\infty}^{0} \kappa_a(z') T(z') \exp\left(- \int_{z'}^{0} \kappa_a \sec(\theta_{\mathrm{m}})\, \mathrm{d}z'' \right) \mathrm{d}z'. \tag{3.2}$$

Note that the right-hand side is not specific for one polarization, as the emission within the medium is randomly polarized. At the boundary however, Fresnel equations (Equation 2.25) dictate the fraction per polarization p that is transmitted ($T^p_{\mathrm{B,t}}$) under zenith angle θ which is given by

$$T^p_{\mathrm{B,t}}(\theta) = (1 - |\rho_p|^2) T_{\mathrm{B,m}}(\theta_m). \tag{3.3}$$

Under the assumption of a uniform temperature profile $T(z) = T$ and a semi-infinite medium, that is,

$$\exp\left(- \int_{-\infty}^{0} \kappa_a(z'') \sec(\theta_m)\, \mathrm{d}z'' \right) = 0, \tag{3.4}$$

Equation 3.2 simplifies to $T_{\mathrm{B,m}}(\theta_m) = T$ and we can identify the term $(1 - |\rho_p|^2)$ in Equation 3.3 as emissivity e. Note that here, we have assumed a specular boundary of a semi-infinite isothermal medium and no scattering within the medium. We shall later see the implications of these assumptions.

3.1.1 Measurements of Sea Ice Emissivity: Literature Review

Microwave emissions have been measured from various platforms, including on-ice stations, ships, aircraft and satellites. Studies on sea ice emissivity often report emissivity values calculated from the measured brightness temperatures and auxiliary measurements. The exact calculations differ due to several reasons. First of all, the downwelling atmospheric radiation that is reflected by the surface contributes to the measured radiation. Some studies assume specular reflection as surface scattering while others consider the surface to be diffuse. Mätzler (2005) pointed out that the difference between specular and Lambertian surface scattering is minimal near 55°, but that the emissivity is overestimated when one uses that assumption near nadir[1]. Depending on the measurement platform, the measured radiation has a component related to upwelling atmospheric radiation in addition and is affected by the transmittance of the atmospheric path between surface

[1]The statement is independent on frequency but derived assuming a zenith opacity below 0.5.

and radiometer. Second, Equation 3.1 is only an approximation and contains the physical temperature. As described in Section 2.1, in the radiometry of sea ice and snow, each layer of the snow-ice-water system emits radiation and contributes to the observed brightness temperatures by a certain temperature- and frequency-dependent amount. Especially in winter, strong temperature gradients in snow and ice exist because of the cold atmosphere and the comparably warm ocean. Thus the unique physical temperature in Equation 3.1 is not well defined and all measurement campaigns that will be discussed in the following use assumptions to derive an effective temperature (or effective emissivity). In addition to these implications following from the assumption of an isothermal medium in the definition of emissivity, subtleties arise from assuming the medium to be semi-infinite. In reality, the ice is not necessarily opaque enough to 'shield' all ocean emissions, especially for low frequencies. Therefore emissivity should not be understood as material property in sea ice remote sensing but as an ancillary, effective quantity.

Table 3.1 contains data from measurement campaigns, including the assumptions used to calculate the effective emissivity. This compilation is not complete but provides the grounds to discuss the impact of different (implicit) assumptions used to derive a surface emissivity. Here, we focus on the three assumptions mentioned above: atmospheric contribution and reflections (surface scattering) and the effective temperature. Table 3.1 only lists studies that actually calculate emissivity. We also exclude studies from the Baltic Sea (like Hewison and English, 1999) to constrain the analysis to the Arctic. Also note that Table 3.1 includes only those data presented in the corresponding publications that refer to the emissivity calculations, not all the available measurements from the associated campaigns.

When comparing the reports on emissivity presented in Table 3.1 we find different assumptions with respect to the atmospheric contributions and the assumed scattering. For example, Livingstone et al. (1987b) do not account for atmospheric contributions at 19 GHz, Wilheit et al. (1971) assume Lambertian surface scattering, while the derivation of emissivity by Haggerty and Curry (2001) implies specular reflection; and all three studies derive emissivity from aircraft measurements at similar angles. The significance of these differences need a careful assessment. First, atmospheric contributions are less significant for low frequencies than for high frequencies (recall Section 2.1.4). When observing at low frequencies, different assumptions about the negligibility of the atmospheric contributions cause less deviations in e, which may be insignificant, compared to observations at high frequencies. Second, the difference between Lambertian surface and specular reflections is smallest at certain observation angles (Mätzler, 2005). When observing at these angles different assumptions about the specularity of the surface scattering cause less deviations in e, which may be insignificant, than at other angles.

Some of the differences in the assumptions are simply a consequence of the measurement setup: It is clear, for example, that the upwelling atmospheric radiation may be

neglected for surface-based measurements but that this likely does not hold for satellite measurements, at least not for all frequencies. We note that there are also different assumptions with regard to the effective temperature: the temperature T of the target is approximated in different ways, and sometimes effective temperatures or the snow-ice interface temperature are taken into account rather than surface temperatures. The impact of this assumption of course depends on the snow and ice conditions, and as many campaigns are conducted in summer, the temperature gradients and, hence, the deviations in e caused by this assumption are likely small. Still, Haggerty and Curry (2001) discuss the uncertainties in deriving e and conclude that, potentially, the largest uncertainty stems from the isothermal assumption. The magnitude of this uncertainty on e depends on the temperature gradients and on the assumed emitting layer temperature, which in turn depends on frequency.

We can easily come up with a simplified yet plausible situation in which an emissivity was calculated using the snow-ice interface temperature which we call e_{si} and that e_{si} shall be of the order of 0.9. If someone would now consider this quantity to calculate brightness temperatures using *surface* temperatures which might differ by 10 K from the snow-ice interface temperature (which, in case of a winter snowpack, is a realistic assumption), the brightness temperatures resulting from the two different temperatures would differ by 9 K.

For certain frequencies (see for example brightness temperature (TB) measurements at 243 GHz in the next section) and under certain circumstances, this difference can be as high as the difference in TB between ice and open ocean. The situation is less drastic for many sea ice concentration (SIC) algorithms that are often based on ratios of TB (more on that in Chapter 4) and the situation outlined above would result in little change in the retrieved SIC. For example, we estimate the change of SIC by the so-called NASA-TEAM algorithm, which will be introduced later in Section 4.1.2, to be of the order of 1%.

We want to conclude by stressing the importance of carefully examining these assumptions when using literature values of emissivity. The high natural variability of (multiyear) ice emissivities (Eppler et al., 1992) complicates interpretations of measurement data even further. Single values of emissivity fall short of the reality and there is the need for reporting distributions instead. This is of particular importance for developing new and improving existing satellite retrieval algorithms over sea ice. For satellite retrievals the challenges of highly variable emissivities can be partly mitigated, for example by using dynamic tie points (Lavergne et al., 2019). Another approach is to use a physical model to simulate surface emissions instead of (semi-)empirical emissivity values. This is aimed for in Chapter 5.

Table 3.1: Measurements of Arctic sea ice sorted by measurement type (i. e., satellite or airborne or ground/ship-based), with emissivity e, physical temperature T_s, measured T_B from surface observation, and the atmospheric parameters of upwelling radiation $T_{B,up}$, downwelling radiation $T_{B,down}$ and atmospheric transmissivity Υ; ice types are given as first-year ice (FYI), second-year ice (SYI), multiyear ice (MYI) or additional ice types; the table lists also measured frequencies (f), polarizations (pol.) which are either none (nadir observations), horizontal (H-pol), vertical (V-pol) or both (dual), and observation angles (off-nadir); the entry not specified (n.s.) means that no information could be found in the corresponding reference

Reference	campaign	time / area	ice types	f (GHz) / pol.	angles (°)	Definition	Assumptions
Comiso (1983)	satellite (SMMR)	1 day per month Nov. 1978 – Sep. 1979, pan-Arctic	all	6.6, 10.7, 18.0, 21.0, 37.0 (dual)	50.2	$e = \frac{T_B}{T_{s,eff}}$	temperature: (effective) ice-snow interface temperature $T_{s,eff}$ from a linear fit using infrared sounder data (satellite) as input; atmosphere: no extra account; surface scattering: no extra account
Comiso (1986)	satellite (SMMR)	monthly means Feb., Mar., Apr. 1979, pan-Arctic	all	10.7, 18.0, 37.0 (dual)	50.2	see above (Comiso, 1983)	see above (Comiso, 1983)
Mathew et al. (2008)	satellite (AMSU)	full year 2005, 2 test regions (Kara Sea, north of Greenland)	FYI, MYI	15 channels between 23–89, 5 between 89–183 (channel-dependent polarization)	−57–57 [2]	$e = \frac{(T_B - T_{up} - \Upsilon T_{B,down})}{(\Upsilon T_{eff} - \Upsilon T_{B,down})}$	temperature: effective temperature of emission layer (snow or ice) from linear regression assuming frequency-dependent penetration depths; atmosphere: atmospheric variables from radiative transfer model using reanalysis as input, no scattering; surface scattering: specular
Mathew et al. (2009)	satellite (AMSR-E)	monthly means full year (2005), 2 test regions (Kara Sea, north of Greenland)	FYI, MYI	6.9, 10.6, 18.7, 23.8, 36.5, 89.0 (dual)	55	see above (Mathew et al., 2008)	see above (Mathew et al., 2008)

[2] These are the local zenith angles, note that they differ from the instrument's scanning angle because of Earth's curvature.

Table 3.1: Measurements of Arctic sea ice sorted by measurement type (i. e., satellite or airborne or ground/ship-based), with emissivity e, physical temperature T_s, measured T_B from surface observation, and the atmospheric parameters of upwelling radiation $T_\mathrm{B,up}$, downwelling radiation $T_\mathrm{B,down}$ and atmospheric transmissivity Υ; ice types are given as first-year ice (FYI), second-year ice (SYI), multiyear ice (MYI) or additional ice types; the table lists also measured frequencies (f), polarizations (pol.) which are either none (nadir observations), horizontal (H-pol), vertical (V-pol) or both (dual), and observation angles (off-nadir); the entry not specified (n.s.) means that no information could be found in the corresponding reference

Reference	campaign	time / area	ice types	f (GHz) / pol.	angles (°)	Definition	Assumptions
Wilheit et al. (1971)	airborne	May 1967 & June 1970, Sea north of Point Barrow, Alaska	old & new FYI	10.69, 19.35, 22.235, 37.0, 53.65, 54.9, 58.8, (single pol., dual for 10.69 & 37.0)	0, 45, 50	$e = \frac{(T_\mathrm{B} - T_\mathrm{B,down})}{(T_\mathrm{s} - T_\mathrm{B,down})}$	temperature: surface temperature from infrared radiometer; atmosphere: $T_\mathrm{B,down}$ from atmospheric radiative transfer model, assuming Lambertian reflection; surface scattering: Lambertian
Gloersen et al. (1973)	airborne [3]	Mar. 1971, Beaufort Sea	FYI, MYI	1.42, 2.69, 4.99, 10.69, 37, 94 (dual)	0, 45, scanning	n.s.	temperature: n.s. ; atmosphere: n.s., surface scattering: n.s.
Troy et al. (1981)	airborne	Apr. 1977, Greenland Sea	new, young, FYI, MYI,	14, 19, 31, 90 (all dual except 31 only V-pol)	0 (55 for small sample size)	$e = \frac{(T_\mathrm{B} - T_\mathrm{up} - \Upsilon T_\mathrm{B,down})}{(\Upsilon(T_\mathrm{s} - T_\mathrm{B,down}))}$	temperature: surface temperature T_s from infrared radiometer[4] ; atmosphere: modeled from measured atmospheric humidity and temperature; surface scattering: n.s.
Livingstone et al. (1987b)	airborne	Mar. 1979 to July 1982, Beaufort Sea, Baffin Bay, Labrador Sea	nilas, FYI, SYI, MYI	19.4 (H-pol)	45	$e = \frac{T_\mathrm{B}}{T_\mathrm{s}}$ (implicit)	temperature: surface temperature from infrared measurements; atmosphere: neglected, surface scattering: n.s.

[3] Connection to ground-based AIDJEX campaign.

[4] The authors do point out that T_s should be the weighted temperature over depth from which microwave radiation is emitted and argue that taking the surface temperature instead is a reasonable assumption due to low temperature changes across the emitting layers.

Table 3.1: Measurements of Arctic sea ice sorted by measurement type (i. e., satellite or airborne or ground/ship-based), with emissivity e, physical temperature T_s, measured T_B from surface observation, and the atmospheric parameters of upwelling radiation $T_{B,up}$, downwelling radiation $T_{B,down}$ and atmospheric transmissivity Υ; ice types are given as first-year ice (FYI), second-year ice (SYI), multiyear ice (MYI) or additional ice types; the table lists also measured frequencies (f), polarizations (pol.) which are either none (nadir observations), horizontal (H-pol), vertical (V-pol) or both (dual), and observation angles (off-nadir); the entry not specified (n.s.) means that no information could be found in the corresponding reference

Reference	campaign	time / area	ice types	f (GHz) / pol.	angles (°)	Definition	Assumptions
Gray et al. (1982)	airborne	Mar. 1979, Apr. 1979, June 1980, Beaufort Sea, Canadian Arctic	grey-white, FYI, SYI, MYI, ice island	19.4 (H-pol)	45	e calculated "using an estimation of sky temperature and surface temperature"	temperature: n.s.; atmosphere: n.s., surface scattering: n.s.
Hollinger et al. (1984)	airborne	Oct. 1981, Beaufort Sea & Mould Bay	new, young, SYI, MYI, shore-fast	19.3, 22.2, 31.4, 90, 135	0	$e = \frac{(T_B - T_{up} - \Upsilon T_{B,down})}{(\Upsilon(T_s - T_{B,down}))}$	temperature: average based on surface observations; atmosphere: modeled from meteorological data, surface scattering: n.s.
Haggerty and Curry (2001)	airborne (FIRE SHEBA)	May/July 1998, Beaufort Sea	primarily MYI	37 and 90 (dual), 89, 150, 220	0–60 (e for 0 and 50)	$e = \frac{(T_B - T_{up} - \Upsilon T_{B,down})}{(\Upsilon(T_s - T_{B,down}))}$	temperature: surface temperature from infrared data (assuming isothermal temperature profile in agreement with measurements during that time of the year); atmosphere: modeled from measured temperature and humidity profiles, no scattering; surface scattering: n.s. (equation implies specular)

Table 3.1: Measurements of Arctic sea ice sorted by measurement type (i. e., satellite or airborne or ground/ship-based), with emissivity e, physical temperature T_s, measured T_B from surface observation, and the atmospheric parameters of upwelling radiation $T_{B,up}$, downwelling radiation $T_{B,down}$ and atmospheric transmissivity Υ; ice types are given as first-year ice (FYI), second-year ice (SYI), multiyear ice (MYI) or additional ice types; the table lists also measured frequencies (f), polarizations (pol.) which are either none (nadir observations), horizontal (H-pol), vertical (V-pol) or both (dual), and observation angles (off-nadir); the entry not specified (n.s.) means that no information could be found in the corresponding reference

Reference	campaign	time / area	ice types	f (GHz) / pol.	angles (°)	Definition	Assumptions
Hewison et al. (2002)	airborne (POLEX-SEPOR)	Mar. 2001, Barents/ Greenland Sea (Svalbard area)	nilas, FYI, MYI, glacial ice, marginal ice zone (MIZ)	24, 50, 89, 157, 183±1, 183±3, 183±7	-40–40 (e only nadir)	$e = \frac{(T_{B,eff} - T_{B,down,eff})}{(T_{s,eff} - T_{B,down,eff})}$	temperature: effective temperature accounting for penetration depths retrieved from TB measurements at 183 GHz; atmosphere: downwelling $T_{B,down,eff}$ modeled and measured, corrections on T_B and $T_{B,down,eff}$ to account for atmospheric absorption below aircraft; surface scattering: specular[5]
Harlow (2011)	airborne (POLEX/ CLPX-II)	Mar. 2002, north of Svalbard; Feb. 2008, Chukchi & Beaufort Sea	thin, FYI (pack and fast), acMYI	89, 157, 183±1, 183±3, 183±7 (mixed)	0 – 50 (e for nadir)	$e = \frac{(T_B - T_{up} - \Upsilon T_{B,down})}{(\Upsilon(T_{s,eff.} - T_{B,down}))}$	temperature: effective temperature at 183 GHz derived using the three passbands with two methods, see Harlow (2009); atmosphere: non-scattering, observed and extrapolated to the surface using dropsonde data; surface scattering: specular and Lambertian (but better results for Lambertian)
Risse et al. (2024)	airborne (ACLOUD/ AFLUX)	May–June 2017, Mar.–April 2019; Fram Strait	nilas, young, FYI, MYI, MIZ	89 (H-pol), 183, 243, 340	0, (25 at 89 GHz)	$e = \frac{(T_B - T_{up} - \Upsilon T_{B,down})}{(\Upsilon(T_s - T_{B,down}))}$	temperature: surface temperature from infrared data (assuming isothermal sea ice but accounting for temperature gradients in uncertainty estimate); atmosphere: non-scattering, radiative transfer simulations; surface scattering: Lambertian

[5]The authors do note that the assumption of specular reflection does not hold for most snow and ice surfaces but want to be consistent with the treatment of the sea surface.

Table 3.1: Measurements of Arctic sea ice sorted by measurement type (i. e., satellite or airborne or ground/ship-based), with emissivity e, physical temperature T_s, measured T_B from surface observation, and the atmospheric parameters of upwelling radiation $T_\mathrm{B,up}$, downwelling radiation $T_\mathrm{B,down}$ and atmospheric transmissivity Υ; ice types are given as first-year ice (FYI), second-year ice (SYI), multiyear ice (MYI) or additional ice types; the table lists also measured frequencies (f), polarizations (pol.) which are either none (nadir observations), horizontal (H-pol), vertical (V-pol) or both (dual), and observation angles (off-nadir); the entry not specified (n.s.) means that no information could be found in the corresponding reference

Reference	campaign	time / area	ice types	f (GHz) / pol.	angles (°)	Definition	Assumptions
NORSEX (1983)	ship-based (NORSEX)	Sept./Oct. 1979, marginal ice zone north of Svalbard	FYI, MYI	4.9, 10.4, 21, 36, 94 (dual)	50	$e = \frac{(T_\mathrm{B} - T_\mathrm{B,down,eff})}{(T_\mathrm{s} - T_\mathrm{B,down,eff})}$	temperature: ice temperature T_s of $-1\,^\circ$C instead of taking snow surface temperature; atmosphere: $T_\mathrm{B,down,eff}$ measured at angles depending on surface scattering type; surface scattering: diffuse/specular depending on ice type ($T_\mathrm{B,down,eff}$)
Mätzler et al. (1984)	ship-based (NORSEX)	Fram Strait 1979	MYI	4.9, 10.5, 21, 35, 94 (dual)	50	$e = \frac{(T_\mathrm{B} - T_\mathrm{B,down,eff})}{(T_\mathrm{s} - T_\mathrm{B,down,eff})}$	temperature: physical target temperature; atmosphere: effective $T_\mathrm{B,down}$ (at elevation 30°); surface scattering: diffuse (by taking effective $T_\mathrm{B,down}$)
Livingstone et al. (1987a)	airborne and surface-based (RADARSAT/ FIREX)	June 1982, Canadian archipelago (Crozier Channel)	fast ice, FYI, MYI	surface: 10 (dual), 18.7 (H-pol); aircraft: 19.4 (H-pol)	45	$e = \frac{(T_\mathrm{B} - T_\mathrm{B,down})}{(T_\mathrm{s} - T_\mathrm{B,down})}$ discussed in detail in Livingstone et al. (1983)	temperature: surface temperature from ground measurements; atmosphere: $\Upsilon = 1$, $T_\mathrm{B,up}$ neglected, and $T_\mathrm{B,down}$ assumed to be 18 K; surface scattering: specular (Livingstone et al., 1983)
Rückert et al. (2023d)	ship-based (ATWAICE)	July/ Aug. 2022; Fram Strait	nilas, SYI, fast ice	7 channels between 22–31 (V-pol), 243 (H-pol)	53	$e = \frac{(T_\mathrm{B} - T_\mathrm{B,down})}{(T_\mathrm{s} - T_\mathrm{B,down})}$	temperature: surface temperature from infrared data (assuming isothermal temperature profile in agreement with measurements during that time of the year); atmosphere: downwelling TB accounted for ($T_\mathrm{B,down}$), estimated by regression from zenith measurements; surface scattering: specular

Table 3.1: Measurements of Arctic sea ice sorted by measurement type (i. e., satellite or airborne or ground/ship-based), with emissivity e, physical temperature T_s, measured T_B from surface observation, and the atmospheric parameters of upwelling radiation $T_{B,up}$, downwelling radiation $T_{B,down}$ and atmospheric transmissivity Υ; ice types are given as first-year ice (FYI), second-year ice (SYI), multiyear ice (MYI) or additional ice types; the table lists also measured frequencies (f), polarizations (pol.) which are either none (nadir observations), horizontal (H-pol), vertical (V-pol) or both (dual), and observation angles (off-nadir); the entry not specified (n.s.) means that no information could be found in the corresponding reference

Reference	campaign	time / area	ice types	f (GHz) / pol.	angles (°)	Definition	Assumptions
Onstott et al. (1987)	ship/sled (MIZEX)	June/July 1983 & 1984, Fram Strait (MIZ)	MYI, FYI	4.9, 6, 10, 18, 19.4, 21, 35, 37, 90, 94 (dual)	50	n.s.[6]	temperature: n.s.; atmosphere: n.s.; surface scattering: n.s.
Grenfell and Lohanick (1985)	surface-based[7]	late spring & early summer 1982; Canadian archipelago, southeastern Beaufort Sea	FYI, MYI	10, 18.7, and 37 (dual)	0–60	$e = \frac{T_B}{T_s}$ (implicit)	temperature: uniform ice temperature (273 K, confirmed by measurements) ; atmosphere: not accounted for, surface scattering: n.s.
Tucker III et al. (1991)	ship/sled (MIZEX)	Mar./ Apr. 1987; Fram Strait	nilas, pancake, FYI, MYI, flooded MYI	10, 18, 37, 90 (alternating polarizations)	50	$e = \frac{(T_B - T_{B,down})}{(T_s - T_{B,down})}$	temperature: snow-ice interface temperature ; atmosphere: downwelling TB accounted for ($T_{B,down}$) ; surface scattering: specular (implicit)
Grenfell (1986)	surface-based (MIZEX)	Feb. 1983, Bering Sea; June/July 1983, Greenland Sea	new ice to MYI	10, 18, 37, 90 (dual)	0-60	n.s.	temperature:; atmosphere: n.s., surface scattering: n.s.

[6]However, there are references to Grenfell and Lohanick (1985) and Mätzler et al. (1984), and a comparison to emissivities from NORSEX (1983).
[7]Connected to aircraft campaign RADARSAT/FIREX.

Table 3.1: Measurements of Arctic sea ice sorted by measurement type (i. e., satellite or airborne or ground/ship-based), with emissivity e, physical temperature T_s, measured T_B from surface observation, and the atmospheric parameters of upwelling radiation $T_{B,up}$, downwelling radiation $T_{B,down}$ and atmospheric transmissivity Υ; ice types are given as first-year ice (FYI), second-year ice (SYI), multiyear ice (MYI) or additional ice types; the table lists also measured frequencies (f), polarizations (pol.) which are either none (nadir observations), horizontal (H-pol), vertical (V-pol) or both (dual), and observation angles (off-nadir); the entry not specified (n.s.) means that no information could be found in the corresponding reference

Reference	campaign	time / area	ice types	f (GHz) / pol.	angles (°)	Definition	Assumptions
Grenfell (1992)	surface-based[8]	Sept. 1988; Mar.–July 1983/84, 1987; eastern Arctic Basin, Beaufort Sea, Canadian archipelago, Greenland Sea	MYI	6.7, 10, 18.7, 37, 90 (dual)	50	$e = \frac{(T_B - T_{B,down})}{(Ts - T_{B,down})}$	temperature: snow-ice interface temperature; atmosphere: $T_{B,down}$ measured; surface scattering: n.s. (implying specular)
Grenfell and Comiso (1986)	laboratory	winter (1983/84 & 1984/85)	young ice	10, 18, 37, 90 (dual)	40-60	$e = \frac{(T_B - T_{B,down})}{(T_s - T_{B,down})}$	temperature: measured surface temperature; atmosphere: $T_{B,down}$ measured (upward-facing TB measurements); surface scattering: n.s. (implying specular)
Lohanick (1993)	laboratory	Dec.-Jan.	FYI	10, 85 (dual)	45	$e = \frac{T_B}{T_s}$	temperature: 268 K (ice surface temperature) for 10 GHz, snow surface temperature for 85 GHz; atmosphere: neglected; surface scattering: n.s. (implying specular)
Shokr et al. (2009)	laboratory	early winter (2001/02 & 2005/06)	thin ice	19, 37, 85 (dual)	53	$e = \frac{T_B}{T_s}$	temperature: average physical temperature of radiating layer; atmosphere: neglected as no continuous record of $T_{B,down}$ was obtained; surface scattering: n.s. (implying specular)

[8]Compilation of experiments with campaign data from CEAREX, MIZEX, and RADARSAT/FIREX.

3.2 Results from Expedition PS131 of R/V Polarstern

The following section is based on the submitted manuscript titled "Measuring microwave sea ice and ocean brightness temperature and emissivity between 22 and 243 GHz by ship-based radiometers with rotatable mirrors" (Rückert et al., 2023d). Janna Rückert contributed to conceptualization, data curation and methodology of this study, wrote the first draft of the paper; and did the data analysis and interpretation with the contribution of all authors. Passive and Active Microwave TRAnsfer (PAMTRA) simulations and the retrieval of atmospheric total water vapor (TWV) were performed by Andreas Walbröl, the sky camera data was analyzed by Nils Risse.

Introduction

In the following we present an instrumentation setup allowing for atmospheric and surface measurements. Two mirrors fixed to the stand of two Microwave Radiometers (MWRs) operated on the research vessel *Polarstern* in summer 2022, enabled alternating surface and atmosphere observations. The measurements were performed in the marginal sea ice zone during the cruise ATlantic WAter pathways to the ICE in the Nansen Basin and Fram Strait (ATWAICE) (Kanzow, 2023). The mirror construction allowed us to observe the surface hourly at different zenith angles. Measurements during ATWAICE provided the possibility to measure emissivities in varying ocean and ice conditions in a wide frequency range from 22 to 243 GHz, including measurements of horizontal variability during transects. This is particularly important for satellite retrievals as satellite footprints are of the order of kilometers.

In this manuscript, we first describe the calculation of surface emissivities and the principal instrumentation setup. We then show results from the surface brightness temperature (TB) measurements. We finally estimate surface emissivities using additional surface observations by thermal infrared imagery and estimations of downwelling atmospheric radiation.

3.2.1 Calculation of Surface Emissivities

When observing a surface target with a radiometer close to the surface, the brightness temperature T_B is related to the physical target temperature T and an emission coefficient e (hereafter called emissivity) via

$$T_\mathrm{B} = eT + (1 - e)T_\mathrm{B,down}, \tag{3.5}$$

where $T_\mathrm{B,down}$ is the downwelling radiation emitted by the atmosphere. In principle, e is a function of frequency and is determined by the dielectric properties of the surface material and the interface properties, e. g., roughness, between the surface and the atmosphere.

Because the microwave radiation can be emitted from within the snow-ice-water system, vertical gradients of the temperature and the microstructure influence T_B. In our case, we assume an isothermal target. This is a reasonable assumption during summer which is supported by the low temperature gradients measured during the ice stations (see next section). Therefore, we use the surface temperature T_s as T here. Thus, e is given by

$$e = \frac{(T_\mathrm{B} - T_\mathrm{B,down})}{(T_\mathrm{s} - T_\mathrm{B,down})}, \tag{3.6}$$

where the additional quantities $T_\mathrm{B,down}$ and the surface temperature T_s are required and must be estimated by auxiliary observations. For Equation 3.6 to be valid, the interaction of the radiation with the atmosphere between the radiometer and the target (i. e., the surface) must be negligible.

3.2.2 Campaign and Measurement Setup

Expedition PS131 ATWAICE

The expedition PS131 of *Polarstern* named ATWAICE (Kanzow, 2023) took place from 28 June to 17 August 2022, both starting and ending in Bremerhaven (Figure 3.1). The multidisciplinary study of the marginal ice zone began on 11 July 2022. The measurement program included several transects from the ice-free ocean across the marginal ice zone into the pack ice. In the pack ice, three ice floe stations with atmosphere, ice, and ocean measurements were established and revisited one week after their first visits. From 23 to 26 July, *Polarstern* passed through compact ice to the Aurora vent field around 82°58′N with higher ice thicknesses. Afterward, the three ice station floes were each revisited for the third and final time. On 3 August, *Polarstern* headed toward East Greenland and entered fast ice (less than 1 m ice thickness). On 7 August, *Polarstern* moved south and reached Scoresby Sund, Greenland, near 70°N on 9 August. We ended our MWR measurements on 12 August.

Various sea ice and atmospheric conditions were sampled during the cruise (Figure 3.2). The sea ice concentration varies mostly from 60 to 100% as derived from visual observations within one nautical mile from *Polarstern* following the Ice Watch observation protocol (Hutchings et al., 2020) between 11 July and 9 August available at https://icewatch.met.no/. These values might not be representative for the sea ice concentration near the ship viewed by the radiometers. Open melt ponds were observed all the time, with the highest area fractions above 50% on the fast ice. The median air temperatures measured on board *Polarstern* at about 29 m above sea level from 11 July to 21 August is 0.4 °C with a minimum of −1.7 °C (4 August) and maximum of 10.7 °C (July 18) when moist and warm air reached the Fram Strait.

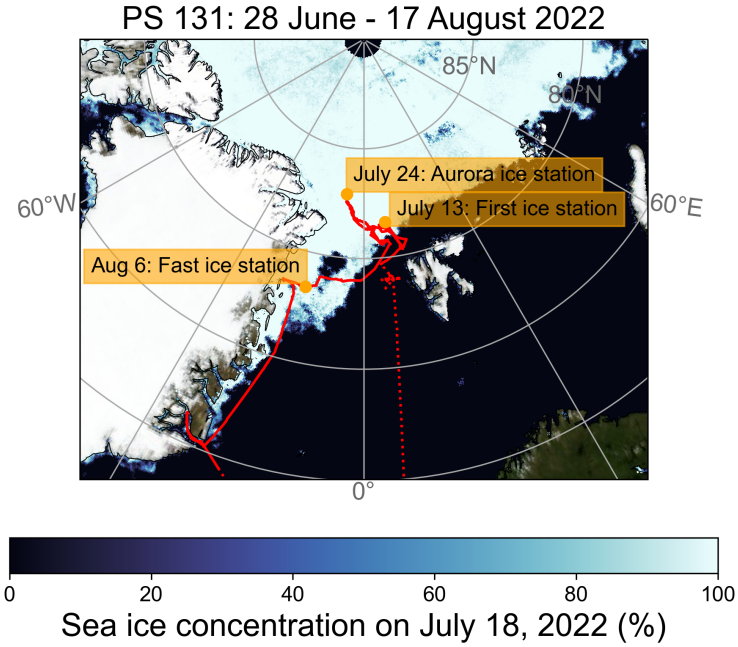

Figure 3.1: Polarstern track (red line) during ATWAICE. Shown in the background is the sea ice concentration product on July 18, 2022, operationally available at www.seaice.uni-bremen.de (ASI algorithm; Spreen et al., 2008).

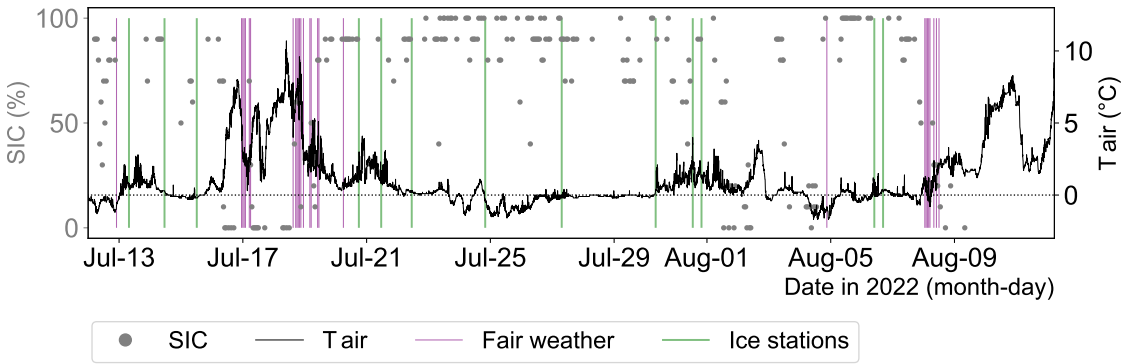

Figure 3.2: Time series of sea ice concentration (SIC), air temperature (T air, secondary axis), fair weather intervals, and occurrence of ice stations from 12 July to 12 August 2022. The sea ice concentration is estimated in steps of 10% until 9 August 2022.

Instrumentation

The measurements described here were conducted as part of the WAter vapor, cloud Liquid water, and Surface Emissivity over the Arctic marginal ice zone in summer (WALSEMA) project embedded within the Transregional Collaborative Research Centre TRR-172 'ArctiC Amplification: Climate Relevant Atmospheric and SurfaCe Processes, and Feedback Mechanisms (AC)^3' (Wendisch et al., 2023).

Microwave Radiometers The two microwave radiometers Humidity And Temperature PROfiler (HATPRO; Rose et al., 2005) and Microwave Radar/radiometer for Arctic Clouds - Passive (MiRAC-P; Mech et al., 2019) were installed on *Polarstern's* top deck ('Peildeck') on starboard (see Figure 3.3). HATPRO measures TBs at seven channels between 22 and 31 GHz under vertical polarization with the 22.24 GHz channel being close to the water absorption line, and at seven channels in the 58 GHz oxygen absorption complex under horizontal polarization. MiRAC-P utilizes six channels along the 183 GHz water vapor line with a vertical polarization and two window channels at 243 and 340 GHz with a horizontal polarization. Unfortunately, the receiver at 340 GHz failed at the beginning of the cruise. Both MWRs measure with 1 s integration time. The instruments' specifications are listed in Table 3.2. An absolute calibration with liquid nitrogen was performed twice during the cruise (7 and 30 July 2022). The radiometers pointed zenith for 45 minutes per hour to derive temperature and humidity profiles, TWV, and liquid water path (LWP), and toward the mirrors for about 15 minutes per hour.

Mirrors Fixed to the stands of the MWRs, aluminum plates with a size of 0.55 m^2 were installed as rotatable mirrors (see Figure 3.4). This mirror setup was developed for this cruise and deployed for the first time. It redirects upwelling radiation from 53° zenith angle, i. e., the typical angle of operational satellite microwave imagers, to the MWR receivers. Ship motions resulted in a few degree deviations from this target zenith angle. We routinely manually dried the mirror surface in foggy conditions due to the lack of preventive measures like heating. However, the presence of liquid droplets creates potential uncertainty. The mirror was rotated manually five times during the cruise to scan various zenith angles. However, these scans are inconclusive due to heterogeneous ice surfaces, such as melt ponds and leads, and not presented here.

Auxiliary Measurements A visual (VIS) camera (GoPro HERO 10) and an infrared (IR) camera (InfraTec VarioCAM HD, 7.5 to 14 µm) observing the surface as well as a sky camera (VIS and IR) were complementing the microwave measurements and provide context for the interpretation of the data. The surface-facing cameras were installed next to the radiometers on the deck (see Figure 3.3) and took images every 5 s. An intertial motion unit (IMU) measuring roll and pitch angles was installed on top of the IR camera.

Table 3.2: The HATPRO and MiRAC-P frequency, polarization (Pol.), beamwidth, and footprint geometry. The footprint geometry is calculated for 53° zenith angle, 22 m instrument height, and without ship motion.

Instrument	Frequency (GHz)	Pol.	Beamwidth (°)	Footprint (m^2)
HATPRO	22.24, 23.04, 23.84, 25.44, 26.24, 27.84, 31.4	V	3.7–3.3	4.0×2.4–3.6×2.2
HATPRO	51.26, 52.28, 53.86, 54.94, 56.66, 57.3, 58.0	H	2.5–2.2	2.7×1.6–2.4×1.4
MiRAC-P	183.31±0.6, ±1.5, ±2.5, ±3.5, ±5.0, ±7.5	V	1.3	1.4×0.8
MiRAC-P	243	H	1.25	1.4×0.8
MiRAC-P	340[a]	H	1.1	1.1×0.7

[a]The 340 GHz receiver was malfunctioning.

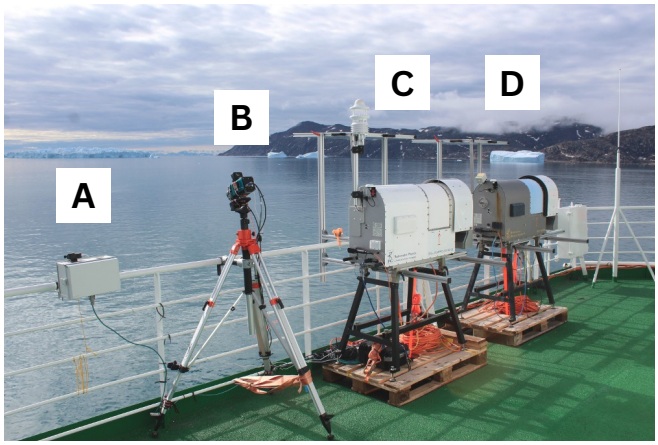

Figure 3.3: (A) Sky camera, (B) infrared surface camera with visual surface camera on top, (C) MiRAC-P, and (D) HATPRO on board Polarstern.

The resulting angles measured with the IMU were used to project the IR data to the ground. Missing IMU data due to instrument or recording issues were filled using linear interpolations.

Additionally, on-ice measurements of the ice and surface conditions conducted during twelve ice stations are available. Here, ice cores were taken to measure vertical profiles of density, temperature, and salinity in the sea ice (Rückert et al., 2023e) and (Rückert et al., 2023c). The surface scattering layer was described using traditional snow pit methods. The microwave radiometer footprint was sampled on 24 July, 31 July, and 6 August. Results of most of the measurements are given in the cruise report (Kanzow, 2023). In summary, the spatial variability of some of the surface and ice parameters, e. g., the diameters of the crystals making up the uppermost layer or the ice thickness in some cases, was high and could change significantly within a few meters.

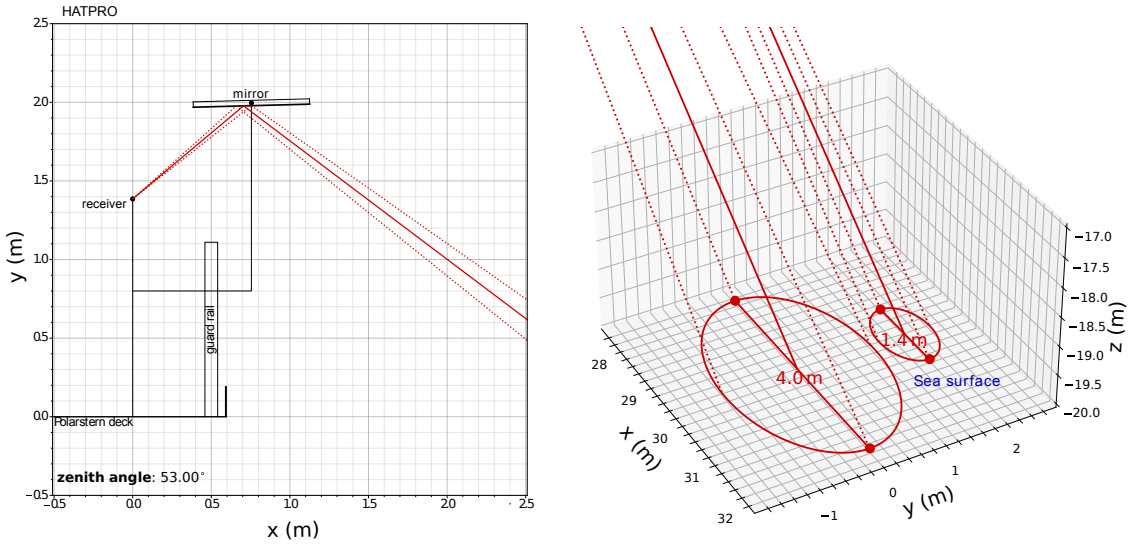

Figure 3.4: Mirror setup. Left: The receiver of the radiometer is positioned at x=0 m with an elevation angle of 40°. Because of the mirror alignment, this results in a zenith angle of 53°. The red lines are the path of rays of the microwave radiation with the center and the outer rays obtained from the beam width. Right: projected footprints of HATPRO (left ellipse) and MiRAC-P (right ellipse) on the surface.

3.2.3 Results and Discussion

Surface Observations: Brightness Temperatures

Before looking at the overall statistics of the measured surface TBs during the ship cruise, we first focus on two case studies, which help to introduce and interpret the MWR observations. In addition, we show observations from July 19, 2022, focusing on TBs at 243 GHz. The two cases of MWR surface observations under different atmospheric and sea ice conditions on July 18 and August 8, 2022, are shown in Figures 3.5 and 3.6, respectively. Small gaps in the time series correspond to internal instrument calibrations. In addition, IR and VIS imagery at three times are also shown and calculated MWR footprints are marked by ellipses in the IR imagery. These ellipses might be slightly misplaced because of uncertainties in the timestamp and slightly changing zenith angles due to ship motion. However, we still expect them to be within the black rectangle shown in the IR imagery. In the following, we refer to the observations in the different channels using the observed frequencies, which always implies a specific channel-dependent polarization (listed in Table 3.2).

Case 1: July 18, 2022 On July 18, 2022 (Figure 3.5), *Polarstern* was moving slowly with a mean speed of 0.25 m s^{-1} and we can see small ice floes drifting in and out of the footprint. The distance from the start (at 80°49.48′N, 9°9.96′E) to the endpoint of the measurements is about 0.2 km. The sea ice temperatures are around 0 °C and

ocean temperatures are slightly colder. On this day, a warm air intrusion occurred in the measurement area and air temperatures were well above freezing with an average of 7.0 °C during the surface observation. The atmospheric HATPRO measurements right before and after the surface observation yield TWV values of 16.4 and 16.1 kg m^{-2}, respectively.

Figure 3.5a and b show the HATPRO TBs at 22 to 31 GHz and at frequencies in the 58 GHz oxygen absorption complex, respectively. TBs at 22 to 31 GHz show lower values (about 160 K) over open ocean than over sea ice (about 250 K). In addition to the surface-driven variability of the TBs resulting in TB changes of up to 90 K, small periodic oscillations of the order of a few Kelvin are visible at these frequencies.

At 51.26 and 52.28 GHz, TBs over open ocean are about 220 and 240 K, respectively, and about 265 K over sea ice. Qualitatively, their behavior is similar to the 22 to 31 GHz range. At frequencies between 54.94 to 58 GHz, an opposite behavior can be seen with slightly higher (about 3 K) TBs over the ocean than over the sea ice, with TBs ranging between 273 to 278 K. No changes with changing surface conditions are observed at 53.86 GHz, showing almost constant TBs of about 273 K (with a standard deviation below 1 K).

Figure 3.5c and d show the TBs measured by the MiRAC-P radiometer at frequencies in the 183 GHz water vapor line and at 243 GHz, respectively. Due to instrument settings, the measurement period ended about 2 minutes earlier than the HATPRO measurements. TBs in the 183 GHz water vapor line change little (about 1 K) during the observation period and are around 277 K. At the 243 GHz window channel, TBs show lower values (about 264 K) over open ocean than over sea ice (about 269 K).

We can conclude that we find a clear surface signal from ice and ocean in the TBs of the frequencies for which the atmosphere is rather transparent, i. e., where $T_{\mathrm{B,down}}$ in Equation 3.5 is low (in this case 22 to 31 GHz, 51.26 and 52.28 GHz). Lower TBs occur over the highly reflective ocean compared to the highly emissive ice for the vertically-polarized TBs between 22 to 31 GHz and horizontally-polarized TBs at 51.26 and 52.28 GHz. The small-scale oscillations correspond to changing zenith angles due to periodic ship motions. However, at frequencies in the oxygen absorption complex where the atmosphere is rather opaque (54.94 to 58 GHz), an opposite behavior can be seen with higher TBs over the ocean and lower TBs over the sea ice. For these frequencies, the reflected atmospheric signal $T_{\mathrm{B,down}}$ originates only from the lowest few kilometers of the atmosphere. Due to the warm air intrusion, the lower atmosphere was very warm on this day. Therefore, a distinct reflected atmospheric signal can be found for the TBs over the ocean, which is more reflective than the sea ice.

We observe no apparent changes in TB with changing surface conditions at frequencies in the 183 GHz water vapor line (vertical polarization). Here, the surface and atmospheric contributions cannot easily be disentangled. The atmospheric water vapor content is relatively high. Thus, atmospheric downwelling TB is of the same order as the surface

temperatures. Therefore, the measured TBs are insensitive to changes in emissivity of different surface types (see Equation 3.5).

At the 243 GHz window channel, the surface signal is again visible: here, the contribution by $T_{\mathrm{B,down}}$ is lower than at frequencies along the 183 GHz water vapor line and thus differences in ice and ocean emissivities can be detected. We find higher TBs (by about 5 K) over ice than over open ocean. Still, atmospheric emissions are an order of magnitude larger than at 22 to 31 GHz and thus significantly decreases the sensitivity to surface emissivity changes. We attribute the dip seen around 17:20 UTC in the TBs at 243 GHz to a fraction of open ocean within the footprint. Because HATPRO has a larger footprint, the signal of open ocean within the footprint is less pronounced here. Since the footprints do not overlap, the decrease in TBs is not observed simultaneously.

Case 2: August 8, 2022 During the second case on August 8, 2022, *Polarstern* traveled through an area with small ice floes (around 76°14.11′ N and 15°37.36′ W; Figure 3.6), covering a distance of about 3.3 km with a mean speed of 3.4 $\mathrm{m\,s^{-1}}$. Ice and ocean surfaces had similar temperatures (below 0 °C). On that day, the general ice conditions are different from the first case as we can also observe the formation of new ice, e. g., around 5:43 UTC, which is slightly visible in the VIS and IR images. Air temperatures were close to but below 0 °C. Atmospheric HATPRO measurements right before and after yield TWV values of 10.7 to 10.9 $\mathrm{kg\,m^{-2}}$.

The TBs at the frequencies between 22 and 31 GHz (Figure 3.6a) and at 51.26 to 52.28 GHz (Figure 3.6b) change more rapidly than in the first case. Due to the faster speed of the vessel on that day, surface conditions also changed more rapidly. Here, the TBs show a qualitatively similar behavior compared to the case on July 18 with high TBs over sea ice (for example 240 to 260 K for frequencies between 22 and 31 GHz, and 240 and 250 K for 51.26 and 52.28 GHz around 5:37:20 UTC) and lower TBs over open ocean (around 155 K for frequencies between 22 and 31 GHz, and 220 and 235 K for 51.26 and 52.28 GHz). Around 5:42 UTC over new ice, TB values higher than over open ocean are detected. At frequencies between 53.86 to 58 GHz, no distinct changes with changing surface conditions are observed with slightly lower TBs at 53.86 GHz of 270 K and TBs ranging between 271 to 275 K for the other frequencies that vary little during the time period (standard deviations below 1 K).

The TBs at the four lower frequencies of the 183 GHz water vapor line (Figure 3.6c) are around 271 K and also vary little during the observation period (standard deviations below 0.5 K). However, the TBs at 190.81 GHz (and to some extent also at 188.31 GHz) do vary with changing surface types. Here, we observe the opposite of what has been seen in the 22 and 31 GHz channels: lower TB values over ice at 190.81 GHz (for example 261 K at 5:37:20 UTC, indicated by B in Figure 3.6) compared to the TBs over ocean (around 267 K). At the 243 GHz window channel, the same behavior can be found as well: TBs

over ice (246 K at 5:37:20 UTC) are about 10 K lower than over ocean (around 256 K). Interestingly, the young ice (indicated by C in Figure 3.6) shows another signature, where the TBs at 243 GHz are up to 263 K and thus higher than the ones observed over ocean. Such higher TBs can also be observed at earlier times during the observation period, when the VIS imagery also suggests that new ice could have been present.

Again, we conclude that distinct surface signals can be observed in the TBs of the frequencies between 22 to 31 GHz and 51.26 to 52.28 GHz. Here, also different TB signatures of ice and ocean surfaces are seen at 190.81 GHz (and to a certain extent at 188.31 GHz) because of the lower atmospheric moisture content on 9 August compared to July 18. The influence of the surface is also clearly visible at 243 GHz. TBs at 243 GHz are lower over ice than over ocean, except for the young ice, where they are higher, suggesting differences in emissivity between different ice types.

Additional Case: July 19, 2022 In the two cases, we observe higher *and* lower horizontally polarized TBs over ice than over ocean at 243 GHz. But we also encountered cases when the TBs were the same: In Figure 3.7 ice and ocean are not distinguishable at all at 243 GHz. Figure 3.7 shows the TB measurements around 80°57.38′N, 8°41.01′E on July 19, 2022, 01:13 to 01:22 UTC when the vessel was traveling with a mean speed of $0.2\,\mathrm{m\,s^{-1}}$. Atmospheric HATPRO measurements right before and after yield TWV values of 17.5 to $17.7\,\mathrm{kg\,m^{-2}}$. The averaged air temperature during the observation period is 2.9 °C. The bright spots in IR imagery are seabirds. Here, ocean and ice have similar physical temperatures (Figure 3.7f). We assume that for this case, the emissivities of ice and ocean are alike at 243 GHz, which could explain why there is no signal in TB at 243 GHz of the floe around 01:19 UTC, which is visible in the TBs of the 22 and 31 GHz channels (Figure 3.7a).

The different behavior of TBs at 243 GHz in the three cases is attributed to the interplay of $T_{\mathrm{B,down}}$ (which is, for example, lower on August 8 compared to July 18), and different ice temperatures and emissivities. For example, we do not expect surface melt on August 8 in contrast to July 18, and the presence of liquid water strongly affects the dielectric permittivity and, in turn, the emissivity of the ice surface.

Brightness Temperature Statistics Before analyzing the surface emissivities in more detail, we examine the statistics of all measured surface TBs during the campaign. The distribution of the surface TBs of all measurements during the cruise is shown for the 22 to 31 GHz channels in Figure 3.8 and for the 243 GHz channel in Figure 3.9 as density plots.

The surface signal is most evident for the vertically polarized TBs between 22 to 31 GHz. The prominent peaks around 160 K correspond to open water, while the peaks around 260 K correspond to observations of the ice. At the frequencies along the 183 GHz

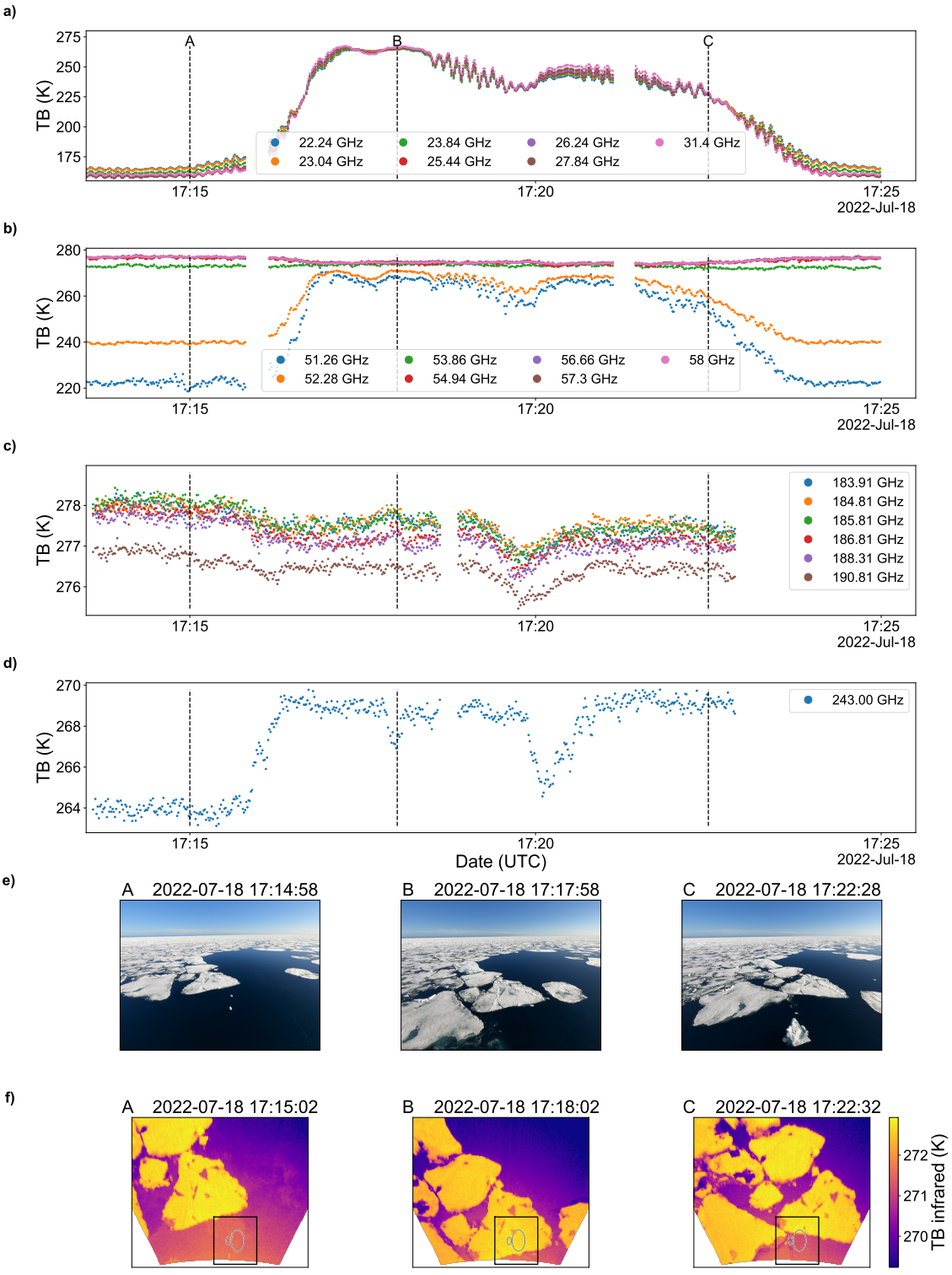

Figure 3.5: HATPRO and MiRAC-P TBs on July 18, 2022 from 17:13 to 17:25 UTC for a) 22.24 to 31.4 GHz (vertical polarization), b) 51.26 to 58 GHz (horizontal polarization), c) 183.31 GHz (vertical polarization) and d) 243 GHz (horizontal polarization) measured at 53° zenith angle. The dashed vertical lines indicate the times of the e) visual and f) infrared camera images A, B, and C. The calculated footprints of the radiometers are indicated by the green ellipses in the IR imagery within the black rectangle.

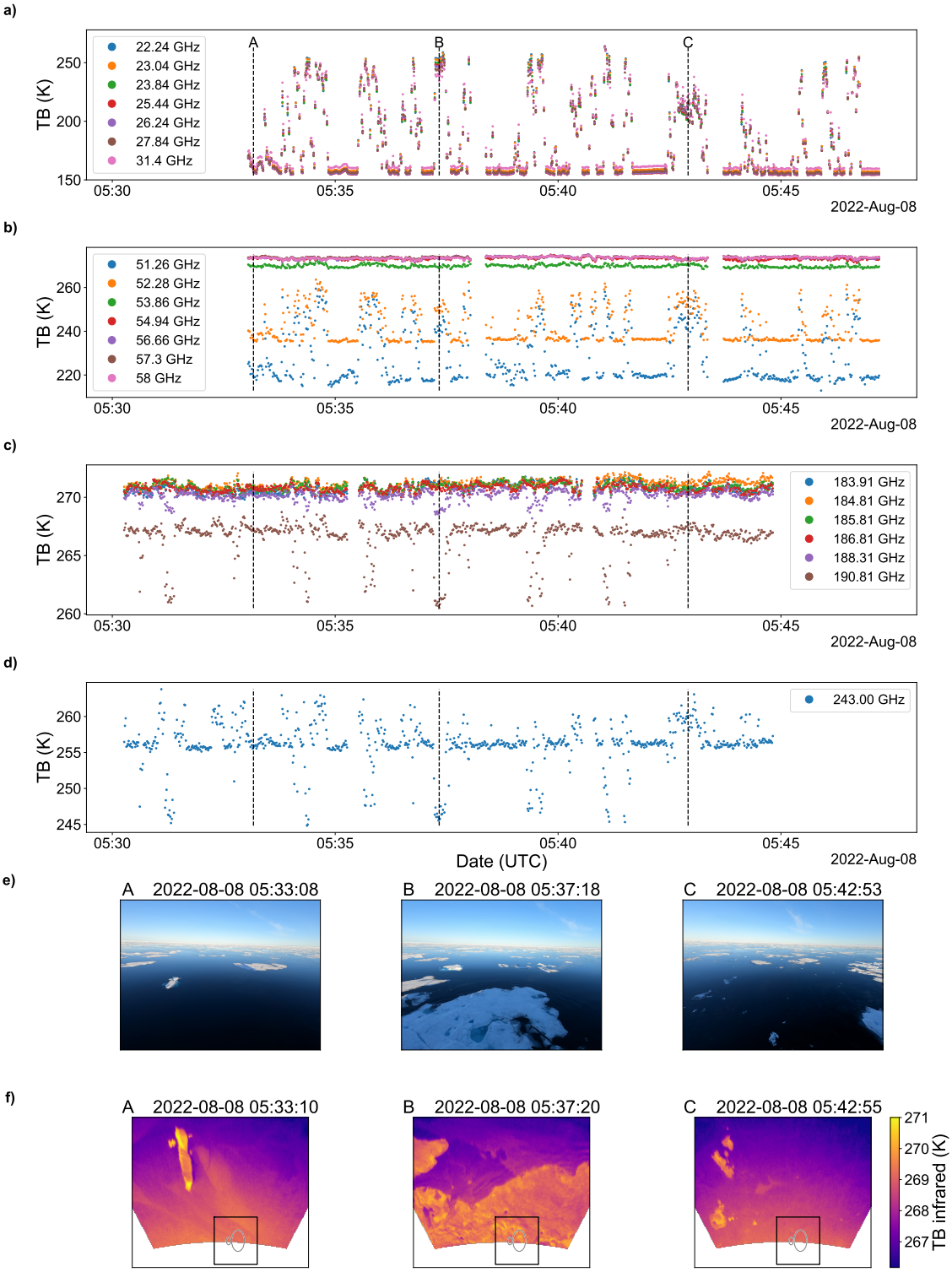

Figure 3.6: Same as Figure 3.5 but for August 8, 2022, 5:30 to 5:47 UTC.

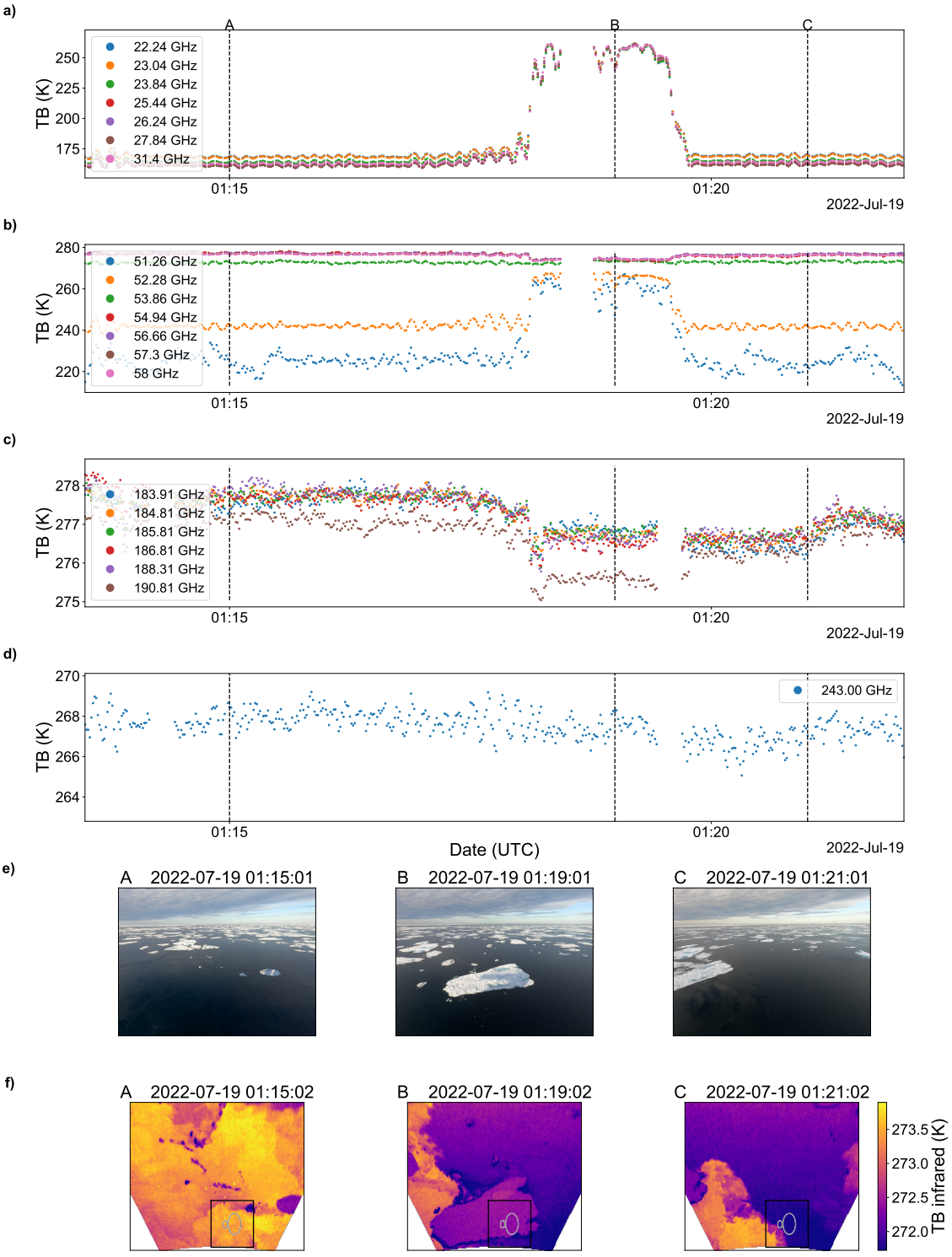

Figure 3.7: Same as Figure 3.5 but for July 19, 2022, 01:13 to 01:22 UTC.

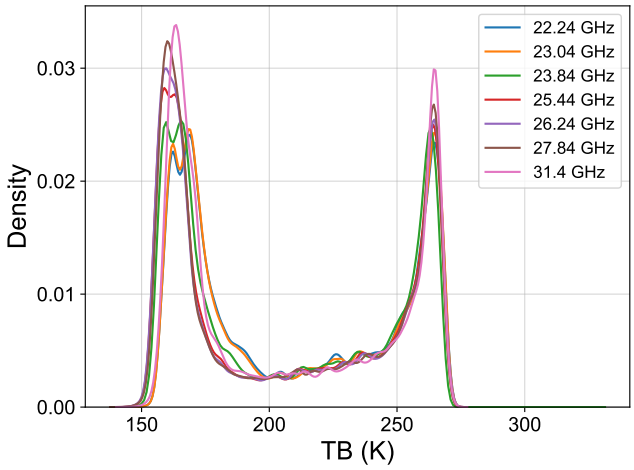

Figure 3.8: All surface TB observations during ATWAICE at frequencies between 22 to 31 GHz at a 53° zenith angle (vertical polarization). The total number of measurements is 492,021 (equivalent to about 137 hours). The data is shown as probability density using kernel density estimation with a Gaussian kernel.

water vapor line and in the 58 GHz oxygen absorption complex, the downwelling TB of the atmosphere is higher and the distinction between ice and open ocean is less clear (not shown). At 243 GHz (Figure 3.9, horizontal polarization), we do not see the bimodal structure as for the 22 to 31 GHz channels. At this frequency and polarization, the influence of the atmospheric moisture is higher, and ice and ocean appear to have less distinct emission signatures.

In summary, these examples show that the general idea of our measurement setup is working: the mirrors allow observations of the surface as we can identify different surface types in the measurements. We can attribute differences in the TBs at different frequencies to varying sensitivities to atmospheric parameters like water vapor. In addition, surface emissivities depending on the surface type influence the TBs and thus we continue by estimating surface emissivities.

Surface Emissivity e

Due to the short atmospheric pathway (about 37 m), we neglect atmospheric radiation and atmospheric absorption between the surface and the radiometer in our study as also done in Tucker III et al. (1991) or NORSEX (1983) and use Equation 3.6 to derive surface emissivities. This assumption is neither fully valid for the 183 GHz water vapor line and the 58 GHz oxygen absorption complex nor in the case of low-level fog for all frequencies. Therefore, to reduce the uncertainty in calculating e, we consider clear-sky cases only in the following and constrain our estimates to the channels between 22 to 31 GHz and 243 GHz. The selection criteria are (i) observation periods in sea ice areas and (ii) clear-sky. We distinguish clear-sky conditions by analyzing the red-blue-ratio (e.g., Long et al.,

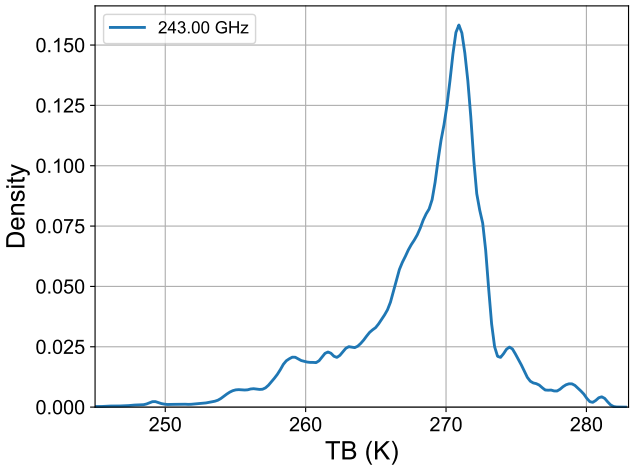

Figure 3.9: Same as Figure 3.8 but for 243 GHz, horizontal polarization. The total number of measurements is 617,746.

2006) captured by the sky camera and categorize pixels with a red-blue-ratio exceeding 0.7 as cloudy. In addition, we exclude conditions when atmospheric downwelling TBs are unsteady by rejecting observations if the standard deviations of the zenith observations in the 15 minutes before the surface observation are above the assumed uncertainties in $T_{\mathrm{B,down}}$ (see next paragraph). The hereby selected times are indicated in Figure 3.2. The mean air temperature during the selected periods was 2.9 °C (with minimum and maximum values of -1.0 and 9.2 °C, respectively).

Estimation of $T_{\mathrm{B,down}}$ Due to the mirror position, it was not possible to directly measure the downwelling TBs under a zenith angle of 53° (see Figure 3.4). When we assume specular reflections, these TBs would equal $T_{\mathrm{B,down}}$ in Equation 3.5. Therefore, we estimate them using an empirical relation for the measured TBs of the radiometers viewing in zenith direction measured directly before and after the surface observations. To derive an empirical relation, we use the radiosondes launched at least twice a day (12:00 and 00:00 UTC) as model input to the Passive and Active Microwave TRAnsfer tool (PAMTRA; Mech et al., 2020) to calculate the downwelling TBs at zenith angles of 0° ($T_{\mathrm{B,down,0°}}$) and 53° ($T_{\mathrm{B,down}}$). The scatter plots and fitted linear least-squares relations are shown in Figure 3.10. $T_{\mathrm{B,down}}(t)$ at time t is then given as $T_{\mathrm{B,down}}(t) = a_1 \cdot T_{\mathrm{B,down,0°}}(t) + a_2$, with the coefficients a_1 and a_2 given by the regression (annotated in Figure 3.10). $T_{\mathrm{B,down,0°}}(t)$ is derived from linearly interpolating measured $T_{\mathrm{B,down,0°}}$ before and after the surface observations.

Based on the scatter plots and the measurement uncertainty of the radiometers as well as on the standard deviations of the atmospheric observations within 15 min before the surface observations (on the order of 0.15 K around 22.24 GHz and 0.6 K for 243 GHz), the overall uncertainty of $T_{\mathrm{B,down}}$ is estimated to be 1 K for the frequencies around 22.24 GHz

and 3 K for 243 GHz.

Estimation of T_s Using the opening angles of the IR camera and the MWRs, we estimate a footprint position and size within the IR measurements. Note that the elliptical footprints differ depending on the frequency. We have to account for uncertainties originating from a drift in the timestamps recorded by the IR camera and uncertainties of the measured zenith angle affecting the projection of the IR imagery. The timestamp was manually corrected by comparing the IR imagery to the VIS images that provide a GPS-derived timestamp. Still, to consider these uncertainties, we use a rectangular box here (larger than the calculated elliptical footprints, shown as a black outline in Figure. 3.5 and 3.6) and estimate the uncertainty of the surface temperature using the variability of T_s within that rectangle. Because the cruise was conducted in the melting season, the IR temperatures of ocean, ice, and melt pond are similar. The standard deviation within our defined rectangle is usually below 1 K.

The thermal IR measured TBs averaged within the rectangular footprint are then converted to physical surface temperatures using an IR emissivity of 0.996 (Thielke, 2023). The uncertainty of the IR emissivity adds to the overall uncertainty of T_s, which we estimate to be 1.5 K. Every 5 s, a thermal IR image is taken, and for the following calculation we select the coinciding TB measurements.

Estimation of Emissivities and their Uncertainties The uncertainty of the derived emissivities Δe can be estimated using a Gaussian propagation of uncertainty. The resulting expression is given by

$$\Delta e = \frac{1}{T_s - T_{B,down}} \sqrt{(\Delta T_B)^2 + \frac{(T_{B,down} - T_B)^2}{(T_s - T_{B,down})^2}(\Delta T_s)^2 + \frac{(T_b - T_s)^2}{(T_s - T_{B,down})^2}(\Delta T_{B,down})^2} \tag{3.7}$$

Equation 3.7 contains the individual uncertainties of T_s, ΔT_s, estimated to be 1.5 K, of $T_{B,down}$, $\Delta T_{B,down}$, which are 1 and 3 K between 22 to 31 GHz and 243 GHz, respectively, and the uncertainty of the radiometer TB measurements, ΔT_B, estimated to be 0.5 K. Also, Δe is proportional to $(T_s - T_{B,down})^{-1}$. That means Δe is high when the downwelling $T_{B,down}$ is close to the surface temperature T_s. This is of importance at 243 GHz, where $T_{B,down}$ and T_s are of the same order of magnitude. Therefore, we exclude calculated values of e with uncertainties higher than 0.025 in the following. For the remaining data, the resulting calculated average uncertainties are 0.005 between 22 to 31 GHz and 0.022 for 243 GHz. The difference between specular and Lambertian reflections is minimal near our observation angle (Mätzler, 2005), so our assumption about specular reflections in deriving $T_{B,down}$ hardly contributes to our uncertainty estimates. To support the interpretation of the derived surface emissivities, we extracted the RGB values from the VIS camera

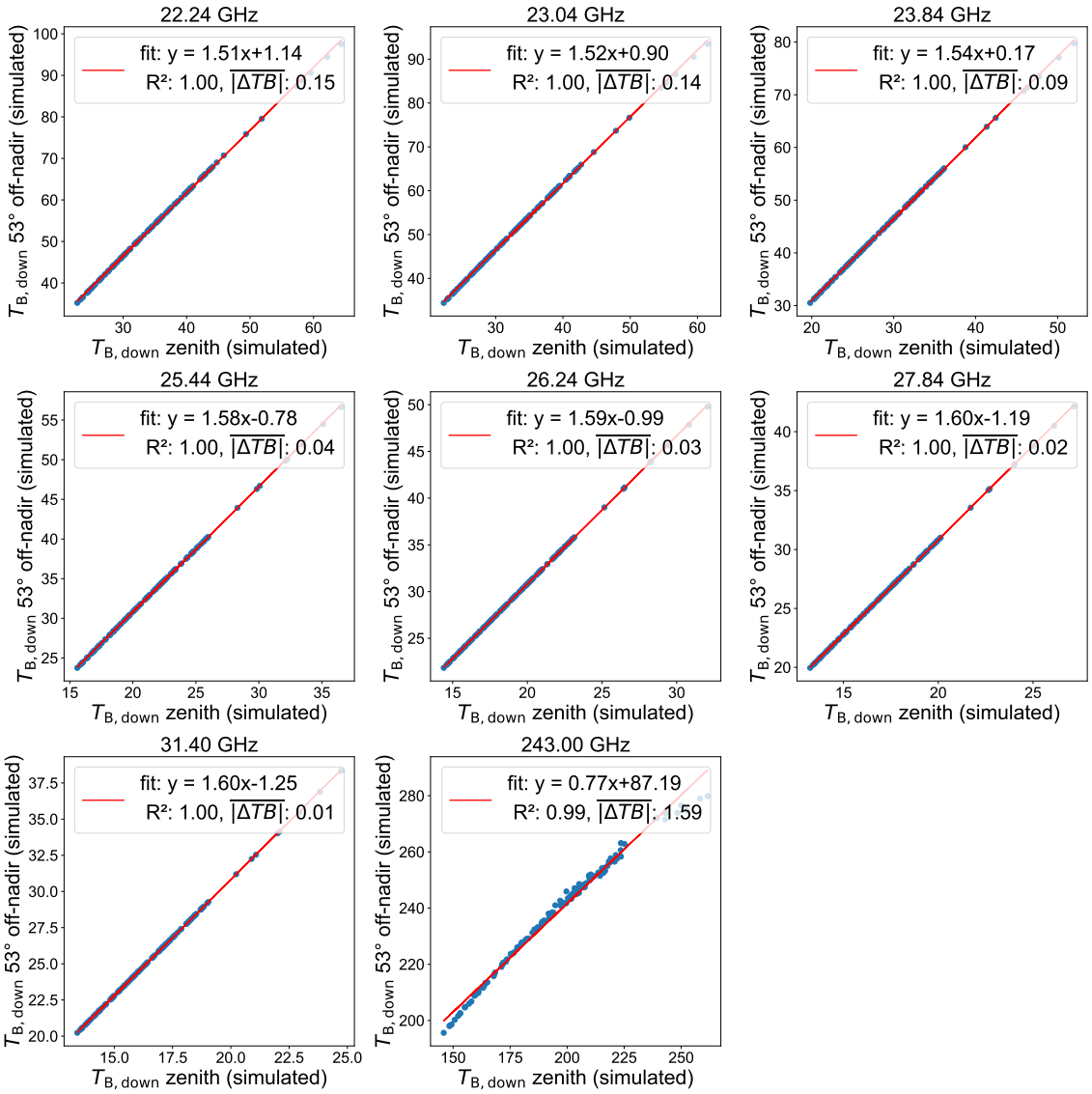

Figure 3.10: Scatterplots of simulated TBs of different frequencies under a zenith angle of 53° and of 0°. Input to the simulations with PAMTRA are the radiosonde data from the ATWAICE campaign. The number of simulations is 124. Annotated in the plots are the coefficients from a linear least-squares regression and the mean absolute difference between the data and predicted values.

observation closest in time and within an area containing the radiometer footprints. A statistical analysis of emissivity and RGB values provides reasonable results, despite high co-location uncertainties.

Figure 3.11a shows a scatter plot and histograms with kernel density estimates of the ratio of red (R) to blue (B) from the VIS camera and the emissivities at 22.24 GHz. The left, low emissivity peak of e corresponds to open ocean (low R to B values) and the peak at the higher emissivities to ice surfaces (high R to B value). The calculated emissivities for the other frequencies between 22 and 31 GHz are shown in Figure 3.12. The maximum of the ocean emissivity shifts with increasing frequencies (from 0.51 to 0.55), while the maximum emissivity of ice lies between 0.95 and 0.96. We often observe values between the two peaks that we attribute to different surface types being present within the footprint.

Figure 3.11b shows the derived emissivities at 243 GHz. For this frequency, the distinction between different surface types is less pronounced. Here, we attribute the second peak around 0.78 to the ocean and the higher values above 0.8 to ice and mixed surface types. These higher values correspond for example to the sea ice observed on July 18 (Figure 3.5) and to the young ice observed on August 8 (Figure 3.6). Note that for the young, dark-looking ice we do not expect high R to B values. In addition, we can observe a small and broad peak around 0.67. These are emissivities of ice as well, observed e. g., on August 8 (corresponding to the low TBs in Figure 3.6d).

The widths of the modal peaks for the different surface types can be attributed to a variety of causes. In addition to the natural variability of emissivity for different ice types and the induced uncertainties, we might observe mixed surface types (ice and open water) in the footprint, as discussed before. Furthermore, varying zenith angles (e. g., by ship movement) contribute to a high variability of e over open ocean and, likely to a lesser degree, also over ice. Table 3.3 summarizes the estimated emissivities by listing the maximum values of the surface modes and their widths. The values are found by fitting bi- and trimodal distributions, given as sum of normal distributions, to the data, i. e., the values are means and standard deviations of the fitted Gaussian distributions.

3.2.4 Conclusions and Outlook

The presented mirror construction is a low-cost addition for ship-based, upward-viewing MWRs that complements the atmospheric measurements by allowing for surface observations in the microwave spectrum along a ship track. In particular, for the TBs of the frequencies between 22 and 31 GHz, different surface types are clearly distinguishable. Such measurements are very beneficial since they can be used to describe the spatial variability of TBs and, thus, the spatial variability of surface emissivity at these frequencies for a larger area, i. e., a satellite footprint. In contrast to on-ice MWR surface measurements, the along-track observations can resolve the spatial variability of the surface conditions, including small-scale features like leads and melt ponds. Especially in summer and in

Table 3.3: Calculated emissivities e at 53° zenith angle for different surface types and their variability σ_e, given by the width of Gaussian functions fitted to the multimodal distribution of the data

Frequency (GHz)	Polarization	ocean e	ice e
22.24	V	0.508 ± 0.012	0.952 ± 0.016
23.04	V	0.512 ± 0.012	0.953 ± 0.016
23.84	V	0.514 ± 0.011	0.947 ± 0.017
25.44	V	0.521 ± 0.010	0.956 ± 0.013
26.24	V	0.526 ± 0.010	0.958 ± 0.011
27.84	V	0.533 ± 0.010	0.958 ± 0.010
31.4	V	0.550 ± 0.010	0.959 ± 0.011
243.0	H	0.783 ± 0.010	0.668 ± 0.032 (ice 1)
			0.825 ± 0.036 (ice 2)

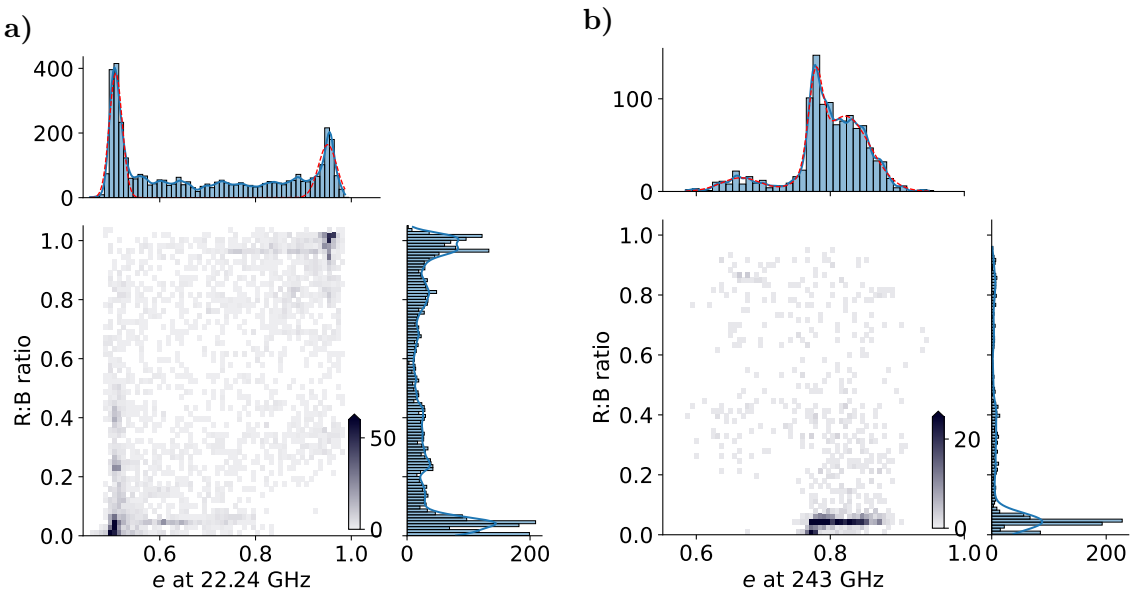

Figure 3.11: Bivariate and marginal histograms with kernel density estimates (blue line) of the red (R) to blue (B) ratio of the RGB values from the visual camera and the calculated microwave emissivities e in a) for 22.43 GHz (vertical polarization) and in b) for 243 GHz (horizontal polarization). The shown cases have been manually selected for clear-sky situations and uncertainties in e smaller than 0.025, resulting in 3,730 (a) and 1,100 (b) measurements. The R to B ratio has been calculated for the MWR footprint area. The dashed red lines are Gaussian functions fitted to the data.

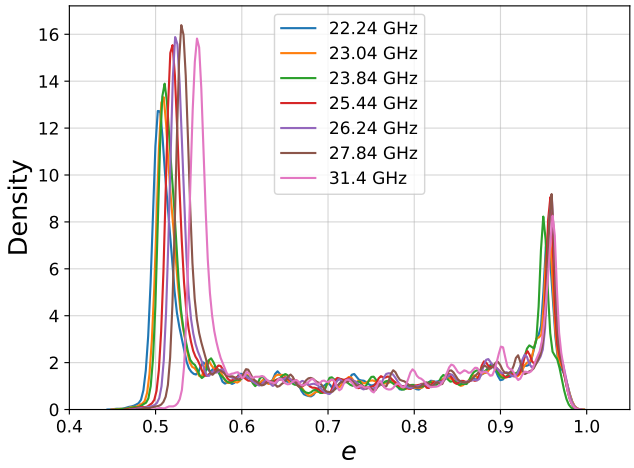

Figure 3.12: Kernel density estimate of the distribution of emissivities (e) calculated for the frequencies between 22 and 31 GHz for manually selected times with clear sky (N=3730).

the marginal ice zone, these small-scale features, which the satellite footprints cannot resolve, pose a great challenge for microwave satellite retrievals, in particular regarding the description of the surface emissivity. Therefore, our measurements help to improve the understanding of surface emissivity variability on a satellite footprint scale. Our data might help to further characterize surface contributions to the satellite signals also at 243 GHz where little in-situ data is currently available. This is also of interest for upcoming satellite missions like the Metop-SG Ice Cloud Imager which will use high frequencies, i. e., 183 GHz and above, for improved atmospheric sounding. In addition, our TB data and the complementing in-situ ice observations can be used in further modeling studies. Understanding the wide range of calculated emissivities at 243 GHz over ice requires additional measurements and more detailed analysis. Here, observations at both polarizations would be helpful, in particular for measurements close to the Brewster angle where difference between the polarizations are potentially large. Analyzing the zenith-angle dependence of the emitted radiation was not feasible because it was impossible to separate the angle dependence from the changing surfaces in the field of view. In the future, this is an option for ocean surfaces or cases with less spatial surface heterogeneity.

Calculating emissivities is challenged by a variety of uncertainties. Besides surface temperature uncertainties, the highest ones stem from the atmosphere. Under foggy conditions, the atmosphere between the radiometer and the ground cannot be neglected. Also, the reflected atmospheric radiation needs to be considered, which could not be directly measured. To circumvent this limitation, we estimated the $T_{\mathrm{B,down}}$ at a zenith angle of 53° using a regression method based on the zenith atmospheric observations of the MWRs. This estimate of $T_{\mathrm{B,down}}$ is thus also related to some uncertainties.

Despite these constraints, the measurement setup allowed us to measure microwave emissions of ice and ocean surfaces and their variability on a spatial scale that resembles a

satellite footprint. For the frequency range between 22 to 31 GHz, vertical polarization, we find that open water emissivities are between 0.508 and 0.550 (increasing with frequency). The widths of the modal peaks in the emissivity distributions serve as a measure of the variability and are between 0.010 and 0.012. Over sea ice, emissivity values range from 0.947 to 0.959 and the variabilities from 0.010 to 0.017. In this frequency range the uncertainty of e is estimated to be 0.005 and thus lower than the variability derived from the distribution. At 243 GHz, horizontal polarization, the modal peaks in the emissivity distribution are not as strictly separated as at the low frequencies. We attribute the modal peak around around 0.783 with a variability of 0.010 to open water. The other two broader modes correspond to sea ice, with one at a lower emissivity around 0.668 and one at a higher emissivity around 0.825. The variabilities of the modes are 0.032 and 0.036.

In the future, the measurement design will be improved to quickly switch between surface and atmospheric scans under varying zenith angles. This data and observations from upcoming measurement campaigns will thus greatly help improve and develop satellite retrieval algorithms, particularly for microwave frequencies higher than 183 GHz that will become operational on future satellite missions.

Chapter 4

Influence of Surface Properties on Satellite Retrievals of Sea Ice Concentration

Now that we have established some of the challenges of characterizing the surface emissions of Arctic sea ice and snow, we present an example of how the surface conditions influence satellite retrievals of sea ice concentration. The case study, published as "Sea ice concentration satellite retrievals influenced by surface changes due to warm air intrusions: A case study from the MOSAiC expedition" (Rückert et al., 2023b), illustrates the interplay of atmospheric events and subsequent surface changes and the sensitivity of retrieval algorithms to such effects. Philip Rostosky and Janna Rückert contributed equally to this study. Janna Rückert contributed to concept and design, as well as analysis and interpretation of the data with a focus on the satellite data. Philip Rostosky's contributions about on-site modeling and the ground-based radiometer measurements are added to this thesis for completeness in the Appendix B. The main contributor of the following sections is Janna Rückert, except for the paragraphs "Snow Accumulation and Metamorphism" and "Floe Perspective: Microwave Emission Modeling" in Section 4.1.3 where Philip Rostosky is the main contributor.

4.1 A Case Study from the MOSAiC Expedition

4.1.1 Introduction

Sea ice concentration retrievals Retrievals of sea ice concentration (SIC) using passive microwave sensors take advantage of the different emissions of ice and ocean measured as brightness temperatures by the satellite. Microwave emission from open water depends mainly on surface temperature and surface roughness related to wave and foam forma-

tion. The microwave emission of the snow-ice system, on the other hand, depends on snow and sea ice properties such as density, temperature, salinity, stratification and microstructure. Retrieval algorithms are either (i) based on polarization difference, (ii) combine different frequencies at the same polarization, or (iii) use both different polarizations and frequencies. Overviews and intercomparisons of different retrieval algorithms are given, for example, in Andersen et al. (2006), Andersen et al. (2007), Ivanova et al. (2015) and Kern et al. (2022). In this case study, involving two moist and warm air intrusions in April 2020, we have investigate the performance of common SIC retrievals of type (i) and (iii).

Warm air intrusions and surface glazing Moist warm air intrusions transporting water vapor poleward play an important role in the Arctic climate system. They increase the downward longwave radiation flux and the skin temperature and thus contribute to Arctic warming in winter (Woods et al., 2013; Hao et al., 2019). There is evidence for an increase in the frequency of extreme warming events, atmospheric rivers and cyclones in the central Arctic in winter related to an increase in meridional heat and moisture transport (Woods and Caballero, 2016; Graham et al., 2017; Rinke et al., 2017; Hao et al., 2019; Henderson et al., 2021; Valkonen et al., 2021; Zhang et al., 2023). We refer to these events as *warm air intrusions* in the following, acknowledging that for specific events they can be different, e. g., in terms of moisture. Warm air intrusions and associated wind and temperature changes can alter the SIC by ice advection, breaking the ice and opening leads, or, to a lesser degree, by melting the ice (mainly in connection with upwelling of warmer, e. g., Atlantic, water along the ice margins but also by direct melting of the ice surface). However, warm air intrusions can also significantly influence the atmosphere and the surface in ways that alter satellite-measured microwave brightness temperature (TB) (Liu and Curry, 2003). These alterations can cause spurious changes in SIC products based on TB (Tonboe et al., 2003), i. e., they can cause wrong ice concentration retrievals in some cases. One possible effect on the snow surface is surface glazing. By glazing we mean the formation of a thin ice layer or crust on top of the snow due to melt or precipitation (Stroeve et al., 2022) or other mechanisms, e. g., winds, as observed in Antarctica (Scambos et al., 2012). Onstott et al. (1987) found that a crust reduces emissivity at 37 GHz and 94 GHz significantly because of scattering within this layer. Smith (1996) and Comiso et al. (1997) conjectured that ice layers in the snow can be a reason for an underestimation of ice concentration, referring to Mätzler et al. (1984). Mätzler et al. (1984) showed that ice layers introduce interfaces with different refractive indices, affecting especially the horizontally polarized TB close to the Brewster angle as described by the Fresnel equations, and therefore alter the polarization difference. Rees et al. (2010) also observed this effect due to ice lenses on snow on land in the Arctic.

Multidisciplinary drifting Observatory for the Study of Arctic Climate Changes in occurrences of surface glazing events thus have the potential to introduce biases in (regional) SIC trends if they are not accounted for. Opportunities to study and quantify the impact of surface glazing in the central Arctic are rare, but the Multidisciplinary drifting Observatory for the Study of Arctic Climate (MOSAiC) expedition (Nicolaus et al., 2022; Shupe et al., 2022; Rabe et al., 2022) provided such a unique setting. To study and increase the understanding of the various processes that lead to the strong recent changes in the Arctic climate, MOSAiC was conducted for a full year from October 2019 to September 2020. The research icebreaker R/V *Polarstern* (Knust, 2017) was moored to a sea ice floe and drifted with it. During the campaign ship-based, ground-based, and airborne measurements of the ocean, sea ice, atmosphere, biogeochemistry and ecosystem in the vicinity of the ship were collected.

The area within about 2 km of *Polarstern* — named the Central Observatory (CO) — was studied intensively. At the start of the expedition the CO was on second-year ice with low ice salinities in the upper layers. Due to new ice formation during winter, a mixture of dominating second- and first-year ice prevailed on the scale of satellite footprint.

Warm air intrusions in April 2020 After a long period of cold winter conditions, two warm and moist air intrusions in April 2020 dramatically warmed the CO (Shupe et al., 2022). During these warm air intrusions, air temperatures increased by up to 30 K at the MOSAiC site, getting close to and even above 0 °C. The atmospheric events included record-breaking total water vapor (Rinke et al., 2021) and high cloud liquid water path, increased wind speeds and precipitation, as well as changes in the aerosol regime (Dada et al., 2022) and triggered surface snow metamorphism, i. e., transformation processes altering the snow microstructure. Of particular interest here is the large-scale surface glazing, observed at the MOSAiC CO, which can affect the microwave emissions as described above. Before, during, and after the warm air intrusions the actual SIC in the vicinity of MOSAiC was high (>95%). Single leads opened during the events but nothing major in comparison to the periods before and after as confirmed by optical (Moderate Resolution Imaging Spectroradiometer (MODIS)) and radar (Sentinel-1) satellite data, by observations from the expedition participants, and by helicopter-borne thermal infrared imagery (Thielke et al., 2022). The latter gives a value for lead fraction, i. e., fraction of open water and thin (<30 cm) young ice, which was on the order of 1.5% over the CO on April 23, about three days after the intrusions. Still the warm air intrusion events affected satellite products of SIC based on microwave radiometry. In conjunction with the warming events, and lasting for several days after them, most satellite products showed a (wrong) decrease in SIC and inter-product variability increased.

In this study, we examined differences between several satellite ice concentration products during the April 2020 warm air intrusions. To explain the differences, we investigated

the effect of these events on microwave TB. We present the suite of such observations at *Polarstern* by satellite at the frequencies 6.9 GHz,19 GHz and 89 GHz. The observations of the ground-based radiometers on the ice floe measuring at the same frequencies taken at the Remote Sensing Site during MOSAiC are presented in the Appendix B. We used in-situ snow and ice observations and microwave emission modeling to explore the impacts of glazing and snow metamorphism on TB and, consequently, on SIC retrievals. The results are structured by the different scales of the observations, from a satellite view (Section 4.1.3) via a floe-wide perspective (Section 4.1.3) to a specific on-ice site (Appendix B).

4.1.2 Data

Sea ice concentration: satellite products

In this section we compare SIC around *Polarstern* based on different algorithms developed for satellite passive microwave remote sensing using different frequencies and polarization combinations. The datasets used are described in more detail in the following subsections. Table 4.1 provides an overview including the frequency channels that are used to compute SIC and the grid spacing. All products are available daily. The co-location procedure is the same for all products. In order to account for drift we use *Polarstern's* position resampled to hourly values and then choose the closest grid point in the satellite product for each hour. We then averaged over the whole day. Note that the ARTIST Sea Ice (ASI) SIC product has a higher spatial resolution compared to the others. It can thus be considered more representative of the local ice conditions.

ASI SIC algorithm

The ASI algorithm exploits the high spatial resolution of near 90 GHz channels and was initially developed for Special Sensor Microwave Imager (SSM/I) sensors (Svendsen et al., 1987; Kaleschke et al., 2001). It was later adapted for the Advanced Microwave Scanning Radiometer - Earth Observing System (AMSR-E) and Advanced Microwave Scanning Radiometer 2 (AMSR2) sensors (Spreen et al., 2008; Melsheimer, 2019). The polarization difference (PD), described as

$$\mathrm{PD} = \mathrm{TB\,V} - \mathrm{TB\,H}, \tag{4.1}$$

where V denotes vertical polarization and H horizontal polarization, at 89 GHz (called PD(89) in the following) is larger over open ocean than over sea ice. This difference is used by the algorithm to distinguish between these two surface types. The SIC is retrieved by a third-order polynomial of PD where the coefficients are determined by the tie points, i. e., typical values of PD over water and consolidated ice (100% ice concentration). To correct for weather influences over open ocean, weather filters are applied. Here, we used the dataset operationally available on a 6.25 km grid at https://seaice.uni-bremen.de and

https://meereisportal.de.

NASA Team algorithm

The NASA Team algorithm (Cavalieri et al., 1984,9) uses vertically and horizontally polarized TB channels to calculate the polarization ratio, PR = PD/(TB V + TB H), of 19.35 GHz, called PR(19) in the following, and the spectral gradient ratio, GR = (TB 37V − TB 19V)/(TB 37V + TB 19V), between TB 19.35V and TB 37V, which is called GR(37/19) in the following. These two ratios are then compared in a scatter plot where they form clusters. These clusters can be identified as being correspondent to three surface types (first-year ice, multiyear ice and ice-free ocean), and for each type three constant tie points are determined (for each frequency channel). Values between the tie points are then interpreted as mixtures of surface types. Weather filters are applied additionally to correct for weather influence over open ocean. We used the NASA Team SIC operational product provided as part of the National Oceanic and Atmospheric Administration (NOAA)/National Snow and Ice Data Center (NSIDC) Climate Data Record of Passive Microwave Sea Ice Concentration, Version 4 (Meier et al., 2021).

NSIDC climate data record

The NSIDC provides SIC estimates as a Climate Data Record (CDR) starting in 1978 (Meier et al., 2021). Here, SIC is computed both by NASA Team (see above) and the Bootstrap algorithm (Comiso, 1986; Comiso et al., 2017). The Bootstrap algorithm is based on relationships of TB combinations of 19V and 37V, and 37V and 37H. Clusters of pure surface types are determined in TB scatter plots of these combinations. Tie points are derived daily based on these clusters. Additionally, weather filters are applied. Then, the higher concentration value from the two algorithms is chosen for each grid cell. We used the NSIDC CDR operational product provided by the NOAA/NSIDC Climate Data Record of Passive Microwave Sea Ice Concentration, Version 4 (Meier et al., 2021).

OSI SAF climate data record

OSI SAF global sea ice concentration interim climate data record (OSI SAF iCDR), release 2, provides daily SIC, starting in 2016 and using data from the SSMIS sensors from NOAA CLASS (EUMETSAT Ocean and Sea Ice Satellite Application Facility, 2017). This SIC dataset, OSI-430-b, is based on a dynamic algorithm (Lavergne et al., 2019), generalizing the Bristol algorithm (Smith, 1996). TB at 19V, 37V and 37H span a 3-D space. Within this space, clusters or shapes close to lines for closed-ice and water are existent. The algorithm then projects the TB data on an optimized plane. This projection is found using daily updated training datasets, one for fully ice-covered and one for open water areas. The unit vector of this plane is found by principal component analysis (direction

Table 4.1: Summary of sea ice concentration products used

Algorithm/product	Frequencies	Grid spacing	Sensor
ASI	89V, 89H	6.25 km	AMSR2
NSIDC NASA Team	19.35V, 19.35H, 37V	25 km	SSMIS
NSIDC CDR	19.35V, 19.35H, 37V, 37H	25 km	SSMIS
OSI SAF iCDR	19.35V, 37V, 37H	25 km	SSMIS

of highest variance in brightness temperature) and is then rotated to maximize accuracy. The final SIC is then calculated by a weighted linear combination of SIC computed from an algorithm dynamically tuned to perform better over open water and one dynamically tuned to perform better over high-concentration ice conditions, both applied in the respectively optimized planes in TB space. The TB are corrected using the European Centre for Medium-range Weather Forecasts (ECMWF) ERA-Interim reanalysis data to account for atmospheric influences due to water vapor, wind speed and near-surface air temperature, with a weather filter (open-water filter) applied after the correction.

Tie points and truncation

All presented satellite products rely on tie points that are average representations of certain ice conditions, e. g., 100% SIC. Naturally, this procedure leads to retrievals varying around 100%, including cases with SIC above 100%. The effects of truncating the data at 100% SIC, as done in all presented products (only the OSI SAF iCDR provides additionally non-truncated 'raw' data to the users), are discussed in more detail in Kern et al. (2019). They concluded that the NSIDC CDR (note that they used version 3 while we analyzed version 4) systematically overestimates SIC (the non-truncated distribution has a modal value larger than 100%). This overestimation will be of relevance later when we discuss the sensitivity of the presented products to the warm air intrusions.

Space-borne microwave radiometry: brightness temperatures

We investigate TB measured by the scanning radiometer AMSR2 on the GCOM-W1 spacecraft from the Japan Aerospace Exploration Agency, launched May 18, 2012. AMSR2 orbits the Earth at an altitude of 700 km in a near-polar, sun-synchronous sub-recurrent orbit with a swath width of 1450 km. The dual-polarized sensor has instantaneous fields of view ranging from 62 km × 35 km at 6.9 GHz to 5 km × 3 km at 89 GHz. We used the swath data, both ascending and descending, of the Level 1R product matched to the resolution of 6.9 GHz (Maeda et al., 2016), corresponding to an instantaneous field of view (FOV) of 62 km×35 km. This product matches antenna patterns so that the TB for all frequencies have the same field of view, facilitating comparisons between different frequencies. For every overflight of *Polarstern* we chose the measurement closest to the vessel's hourly position. There are between five and seven overflights per day. We show

daily averaged values of TB at 6.9 GHz, 18.7 GHz, 36.5 GHz and 89 GHz in Section 4.1.3.

Snow data

Detailed snow measurements were performed during MOSAiC. In this study, we analyzed 132 SnowMicroPen (SMP) profiles (Macfarlane et al., 2021) taken between April 08 and April 27 to support our interpretation of the observed satellite signals. From the raw SnowMicroPen (SMP) observations (penetration resistance) snow density and specific surface area (SSA) were estimated using empirical models (Proksch et al., 2015; King et al., 2020). From density and SSA, the exponential correlation length was calculated (see Appendix Text S3), a parameter describing the microstructure of the snow which is used in common snow microwave emission models (Tonboe et al., 2006).

Supporting data

Met Tower temperature For atmospheric temperature, we used the 2 m air temperature recorded from the 10 m meteorological mast (Met Tower) installed on the CO ice floe (Cox et al., 2021).

Precipitation To illustrate the timing of precipitation, we used data from the Vaisala Present Weather Detector 22 (PWD22) precipitation gauge, an optical device that was installed on the deck of *Polarstern* and operated by the US Department of Energy Atmospheric Radiation Measurement program (Shi, 2019). Here, we used 1-minute mean precipitation rates. This product was also used as reference product in an intercomparison of different snow precipitation sensors by Wagner et al. (2022).

Total water vapor from radiosondes The Level 2 dataset of balloon-borne radiosondes from the MOSAiC expedition (Maturilli et al., 2021) was used to calculate total water vapor (TWV) from the measured temperature, pressure and relative humidity profiles from the *Polarstern* helicopter deck (at about 10 m height) to about 30 km altitude using the formula for vapor pressure over liquid water below 0 °C by Hyland and Wexler (1983) as in Walbröl et al. (2022). During the warm air intrusions, the radiosondes were launched more often, up to seven times a day, while during the other periods they were launched four times a day.

Liquid water path from HATPRO radiometer We used liquid water path (LWP) retrieved from the ground-based Humidity and Temperature Profiler (HATPRO) microwave radiometer operated in zenith mode onboard *Polarstern* as input parameter to model the atmosphere. The retrieved LWP is based on the retrieval algorithm as described in Nomokonova et al. (2019) using the vertically polarized TB measurements between

22.24 GHz and 31.4 GHz. The radiometer has a temporal resolution of 1 second. More information on this dataset can be found in Walbröl et al. (2022).

Reanalysis ERA5 From ECMWF fifth generation reanalysis ERA5 (Hersbach et al., 2020) we used longwave and shortwave radiation from the grid cell closest to *Polarstern* for the SNOWPACK model simulations (Section 4.1.3).

Terrestrial laser scanner TLS Supporting information about the snow surface topography was derived from terrestrial laser scanner (TLS) data taken on April 17 and April 22 (Clemens-Sewall et al., 2022b). The TLS uses a scanning, 1550 nm laser, to generate a three-dimensional point cloud of the snow and ice surface at centimeter-scale resolution. See Deems et al. (2013) for a review of TLS applications to snow depth measurements. Wind-blown snow particles were filtered out of TLS data using the FlakeOut method (Clemens-Sewall et al., 2022a). From the measured topography and its changes, we deduced the changing snow thicknesses and effective incidence angles (i. e., the incident angle of the tilted surface with respect to the radiometer) within the footprints of the ground-based radiometers. The TLS data also include the backscatter reflectance of the surface at 1550 nm. Glaze ice areas are identifiable in this dataset, because surface glazing reduces the backscatter reflectance (glazing increases forward scattering and absorption).

4.1.3 Results

In the following we describe the temporal development of the retrieved SIC and satellite-measured microwave TB, first on a large scale and then locally around *Polarstern*. For the local analysis, we further describe the floe by using the SMP measurements as model input to analyze the evolution of TB. In a second step we change the perspective to an even smaller scale and study the data obtained by the ground-based radiometers. We then discuss the integration of the observations from the different scales. Finally, these steps allow us to develop an interpretation of the satellite signal and the resulting differences in SIC estimates.

Figure 4.1 shows the temporal evolution of TWV from ERA5 over 4 days. The first intrusion, reaching the ship around April 16, originated in northwestern Russia and passed the Barents Sea, while the second one around April 19 was approaching from the North Atlantic, illustrating the large area exposed to the warm air intrusions.

Satellite perspective

The two warm air intrusions were large scale events (Figure 4.1) and thus also visible at large scale in the satellite data. The large scale becomes evident when examining spatial maps of SIC (Figure 4.2). In this figure we show the mean SIC based on different satellite

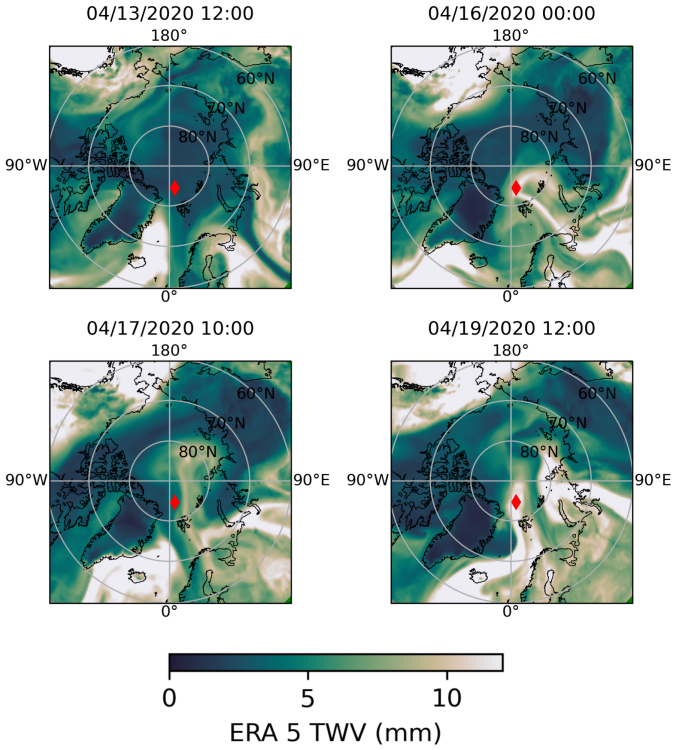

Figure 4.1: Total columnar water vapor during two warm air intrusion events. Shown are hourly values for total water vapor (TWV) from the reanalysis ERA5. The left panels show TWV one day prior to the events (upper panel) and in-between the two events (lower panel). The right panels show TWV at the time of the first (upper panel) and second (lower panel) warm air intrusion. Dates are month/day/year. The red diamond indicates the position of Polarstern at the day.

retrieval products for four consecutive days both prior and after the two events and the difference between the two time periods. Note that the SIC from ASI (first row) has a much higher spatial resolution (6.25 km grid spacing compared to 25 km for all other products, see Table 4.1). In all products except for the NSIDC CDR, decreases of SIC are visible in the Central Arctic to different extents (black ovals in Figure 4.2) as well as in the marginal ice zone. The strongest effect is observed for the ASI product, followed by NASA Team. Deviations between different products increased after the events for all products.

The MOSAiC measurements of total water vapor, liquid water path and 2 m air temperature at *Polarstern* allowed us to examine the effect of these warm intrusions locally. For both warm air intrusions, the rising temperatures (up to0 °C) coincided with increased amounts of TWV (up to 13.4 mm) and LWP (up to around 0.47 mm) as shown in Figure 4.3. In our field observations, no dramatic decrease in ice concentration was observed and SIC was high (>95%), as described earlier in Section 4.1.1. These findings are also confirmed by SIC derived from satellite thermal infrared data (MODIS instrument, only available for clear sky; not shown). A significant drop in SIC cannot be seen in optical

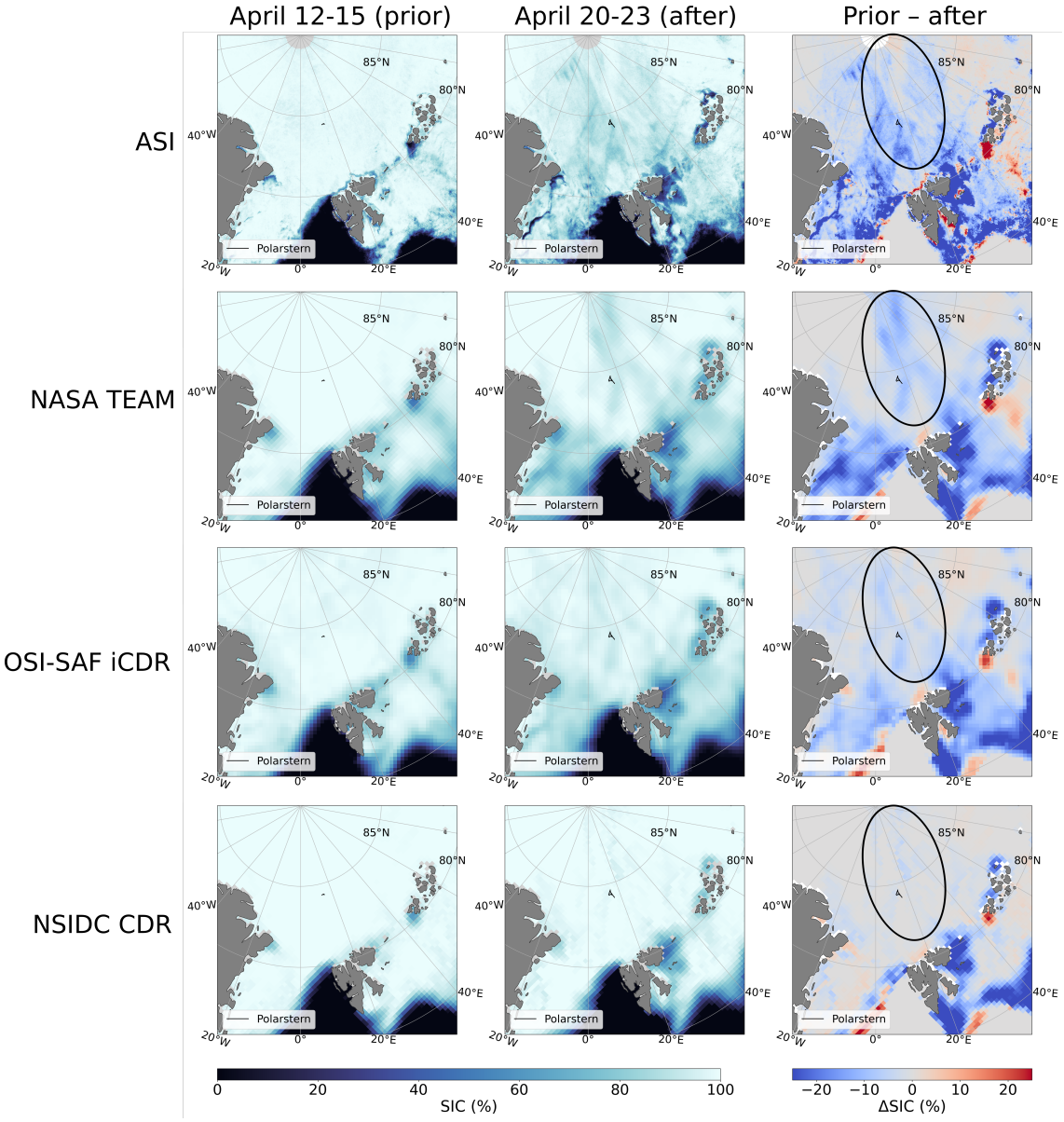

Figure 4.2: Sea ice concentration from different satellite retrievals before and after two warm intrusion events. Shown are 4-day averages of sea ice concentration (SIC) prior (first column) and after (second column) the intrusions. The third column shows the difference between the second and first column. Blue colors denote a reduction in SIC after the events. The black oval in the third column marks a region where the different satellite products deviate from each other after the events. Polarstern's drift track is shown by a black line.

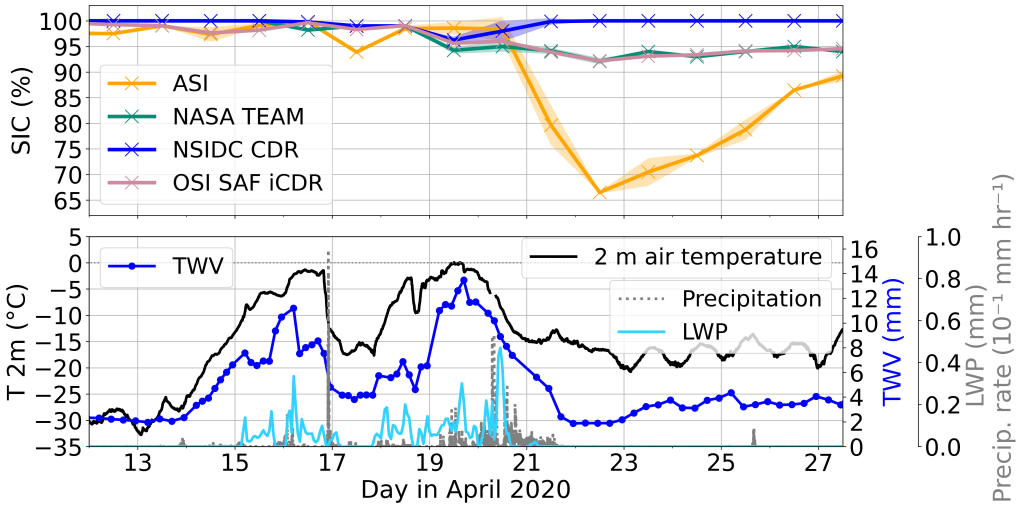

Figure 4.3: Sea ice concentration and meteorological conditions during the April 2020 warm air intrusion events. Upper: sea ice concentration (SIC) from four different operational satellite products co-located with Polarstern. Shown are daily averages at 12:00 UTC on the respective day with the shaded area indicating the standard deviation which is larger zero if the drift of Polarstern covered several grid cells. Lower: air temperature at 2 m (black) from the Met Tower, total water vapor (TWV, dark blue) from radiosondes, liquid water path (LWP, light blue) from the HATPRO microwave radiometer (resampled to hourly values), and 1-minute precipitation rates (grey) from the precipitation gauge (PWD22) installed on deck.

(MODIS) and radar (Sentinel-1) satellite data (not shown) either, where lead formations can be observed during the events but nothing major in comparison to the periods before and after. During the clear-sky day on April 17, temperatures dropped and clear-sky conditions with a high longwave radiation loss prevailed (Rinke et al., 2021). Images from the Panomax webcam onboard the ship (https://www.mosaic-panorama.org/) reveal a lead opening close to the ship on that day.

In considering the SIC estimates from different products collocated to MOSAiC, we observe for the high-resolution ASI algorithm based on 89 GHz a drop in SIC between the two warm air intrusions corresponding to the clear sky day on April 17 and a strong decline after the second event (Figure 4.3). The SIC from NASA Team and OSI SAF iCDR shows less variability during the intrusions but decreases in both cases to 92% on April 22 and does not recover thereafter. The NSIDC CDR, on the other hand, shows 100% SIC after the intrusions. This algorithm includes both NASA Team and the Bootstrap algorithm (Section 4.1.2) with the latter compensating for the decrease observed in SIC from NASA Team as discussed later. Before the events, all algorithms showed high SIC around 100%. Similar to the large scale view (Figure 4.2), the spread between different products increased after the events. Using the NSIDC CDR data as reference, we observe SIC differences of around 8% for OSI SAF iCDR and for NASA Team. Compared to the higher-resolution ASI product the differences are as high as 34% which cannot be explained by the smaller footprint.

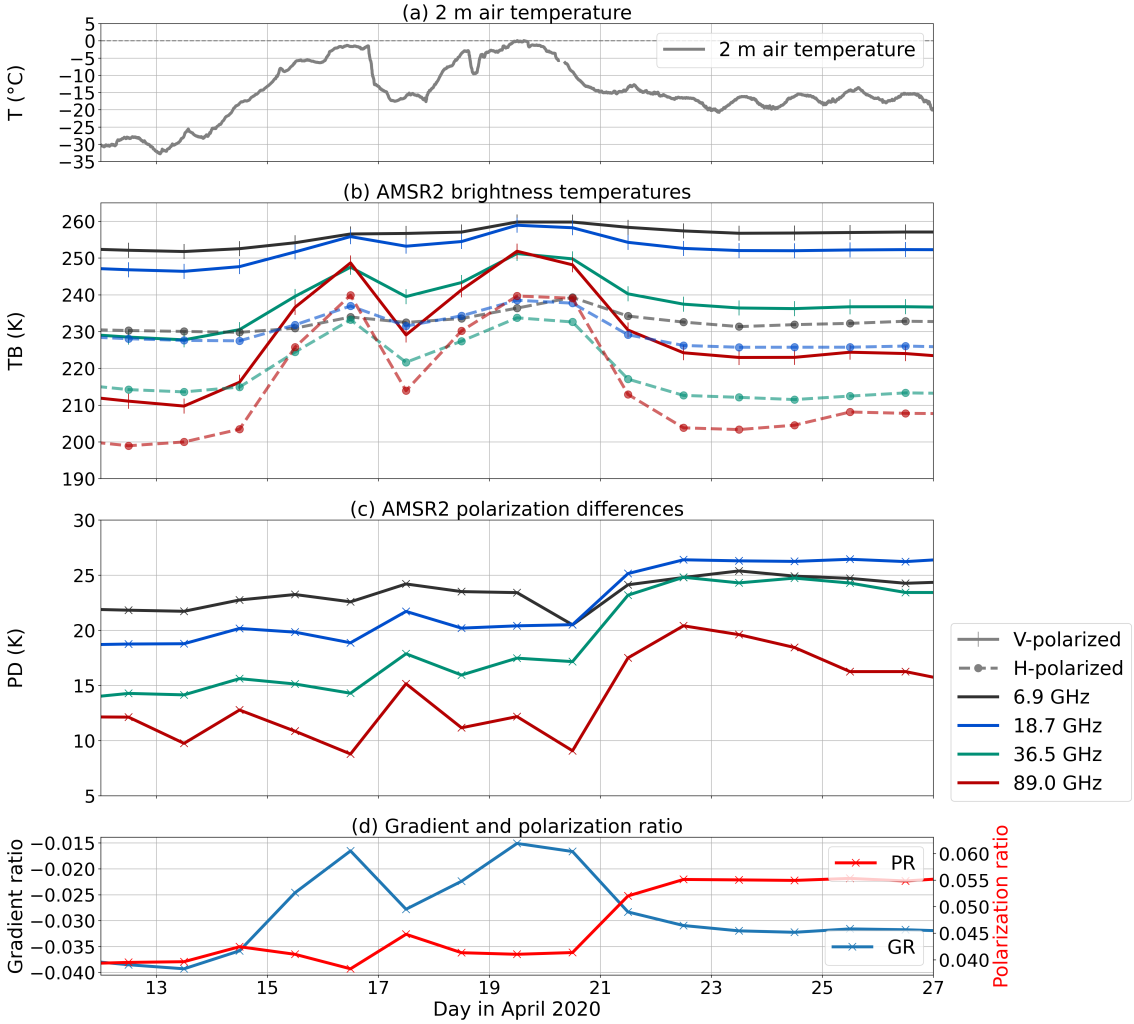

Figure 4.4: Effect of warm air intrusion on satellite-measured brightness temperatures. Shown are a) the air temperature at 2 m; b) the co-located satellite measurement of brightness temperatures (TB) and c) polarization differences (PD) around Polarstern (daily averages); and (d) the gradient ratio of 36.5 GHz and 18.7 GHz and polarization ratio of 18.7 GHz as defined in Section 4.1.2.

Although Tjernström et al. (2015) observed that warm air advections can cause rapid ice melt, and that dynamic effects can decrease SIC up to 3% in the high SIC domain (Schreiber and Serreze, 2020; Aue et al., 2022), here the low SIC values at MOSAiC retrieved by some algorithms are underestimating the actual sea ice concentration. To understand this underestimation, we analyzed daily satellite AMSR2 TB data (Figure 4.4 (b)). The signature of the warming events is clearly visible in the TB time series at these frequencies. The higher frequencies (i. e., 36.5 GHz and 89 GHz) follow the 2 m air temperature evolution (Figure 4.4 (a)) more closely. All frequencies show an increased PD after the events as can be seen in the Figure 4.4 (c). Again, the higher frequencies show a larger increase. The PD increase on April 22 compared to the mean of April 10-13 ranges from a few Kelvin (approximately 3 K) for 6.9 GHz up to around 9 K and 11 K for 89 GHz and 36.5 GHz, respectively. A smaller increase in PD at 89 GHz of a few Kelvin (approximately 4 K) is already visible around April 17 between the two warm air intrusions. During the second warm air intrusion, PD for 89 GHz initially decreases, again coinciding with rising TWV and LWP values. After this second event the rise in PD can be observed at all frequencies but most strongly at the higher frequencies. Figure 4.4 (d) illustrates that both the gradient ratio and the polarization ratio show higher values after the intrusions (after April 20). The gradient ratio shows even higher values during the intrusions.

Especially ASI and NASA Team make use of polarization differences and polarization ratios, respectively. For such SIC estimates the changes in these quantities result in (too) low retrieved SIC values as shown in Figures 4.2 and 4.3. The decrease of SIC in the high-resolution ASI product on April 17 is possibly real, related to the lead opening described above. Directly relating the effect of these TB changes to SIC from OSI SAF iCDR is not as straightforward due to the complex retrieval method. We note, however, that this algorithm is based on the three-dimensional diagram in TB space of 19V, 37V and 37H, so that strong changes in these frequencies relative to each other, as observed, will affect the retrieval. The OSI SAF iCDR product provides two uncertainty estimates: algorithm uncertainty and 'representativeness' uncertainty, i. e., uncertainty due to resampling and mismatch of footprints at different channels (Lavergne et al., 2019). Here, the sum of these two uncertainties (given as one standard deviation) increases from below 2% before the events to up to 5.6% on April 21 (not shown) for the co-located data shown in Figure 4.3, i. e., the uncertainty estimates identify a potential problem in the retrieved SIC. In this case, the higher uncertainty is caused by a higher representativeness uncertainty.

For the NSIDC CDR the higher value of the SIC estimates from the Bootstrap algorithm and NASA Team is chosen. The SIC estimate from NASA Team exhibits a decrease as described above, thus the Bootstrap algorithm is responsible for the low sensitivity of the NSIDC CDR SIC estimate to the warm air intrusions. For high ice concentration values as in this case, the Bootstrap algorithm is based on 37V and 37H. However, as described in Section 4.1.2 and discussed by Kern et al. (2019), the fact we do not observe

a decrease here, although the relationship of 37V and 37H is changed, might be due to an overestimation and consequent truncation at 100% of the values derived by the Bootstrap algorithm.

Direct atmospheric influence

In the few days after the warm air intrusions, the 2 m air temperature and TWV were on average higher than before, while LWP was as low as during the first 2 weeks of April (Figure 4.3). Previous studies (Oelke, 1997; Andersen et al., 2007) demonstrated that atmospheric events can also increase retrieved SIC, although we observed a decrease in our case. Emissions from water vapor or liquid water path contributing to the satellite signal are in general not polarized (Ulaby and Long, 2014) and would thus not increase PD. Scattered radiation, e. g., by ice particles in clouds, may have a polarized component. However, Troitsky et al. (2003) observed values of PD and duration of periods with polarization differences that are too small to explain the development of PD that we observed here. Also, compared to the surface emissions, the contribution of the atmosphere is small at the low frequencies 6.9 and 19 GHz and thus is not not the most likely candidate for the PD increase. Factors other than direct atmospheric effects must explain the increase in PD. We thus focus on explanations related to changed surface emission.

Snow accumulation and metamorphism

Wagner et al. (2022) described a significant snowfall event from April 16 to April 21 accompanying the warm air intrusions. Snowfall events could have had an increasing effect on PD due to atmospheric scattering, but we observed the increase *after* the snowfall. A detailed analysis suggests that much of the fresh snowfall during this event may have been lost into leads (Clemens-Sewall et al., 2023). According to snow buoy measurements (Nicolaus et al., 2021), the average snow depth on a regional scale around the MOSAiC floe was around 20 cm until April 20 and 24 cm afterwards (not shown here). If snow accumulates on level ice, we would expect the fresher snow (less dense with refractive index between that of air and ice) to decrease the PD as described by the Fresnel equations and also reported in Hwang et al. (2007) and Tonboe (2010). For the large-scale area, this snowfall cannot explain the microwave signal. The surface conditions at the Remote Sensing Site on the MOSAiC floe were not representative of the larger area, mainly because the instruments themselves posed obstacles that caused artificial snow accumulation. Thus, for the ground-based radiometers the snowfall is relevant to the interpretation (Section B.1).

For understanding and modeling the observed microwave emission, temperature profiles of the snow are important. Here we have used temperature profiles from simulations with the SNOWPACK model (Bartelt and Lehning, 2002; Lehning et al., 2002b,0; Wever et al., 2019). The model was initialized with a snow pit from April 08 and driven with

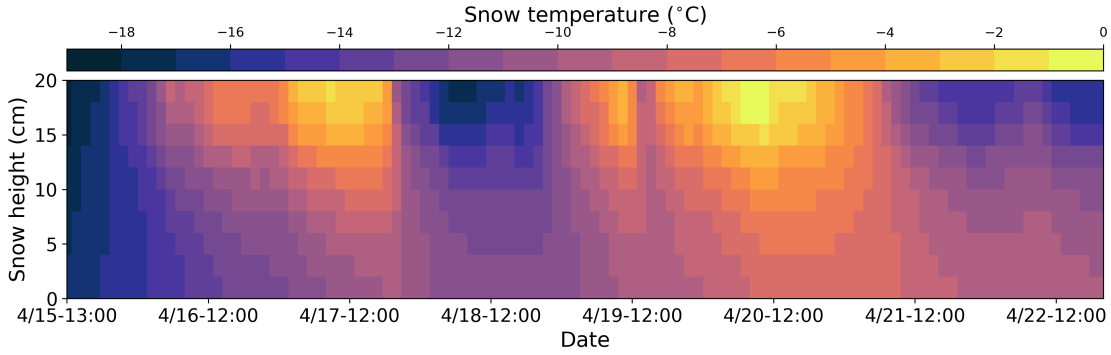

Figure 4.5: Snow temperature profile from a SNOWPACK simulation initialized with 20 cm of snow. Dates are month/day-hour in 2020.

MET tower 2 m air temperature and 10 m wind speed. Longwave and shortwave radiation was obtained from ERA-5 reanalysis data (Hersbach et al., 2020). In these simulations, snowfall was omitted. At the time the simulations were performed, radiation measurements from MOSAiC were not available. However, we generally found a good agreement between our simulated snow temperature profiles and temperature measurements from snowpits (average difference <2 K) and concluded that the performance of the model is sufficient for the purpose of this study. For simulating the brightness temperature of the snow/ice system of the MOSAiC floe, density and correlation length from the SMP profiles were used (Appendix Text S3 and Text S4) together with the temperature profiles from the SNOWPACK simulations. To match the varying snow height of the SMP profiles, simulations with a snowpack of 10 cm to 30 cm in 5 cm steps were performed.

Figure 4.5 shows the simulated snow temperature for a 20 cm deep snowpack. Overall, the snow temperature increased by more than 10 K. After the events, the snow temperature remains higher at the lower part of the snowpack for several days. These data serve as input for the microwave emission modeling presented in Section 4.1.3.

The changes of the snow microstructure caused by the warm air intrusions are evident when one examines the SMP profiles shown in Figure 4.6. A shift towards lower density and SSA and higher correlation length after the warm air intrusions is visible in the data, suggesting that the warm air intrusions led to snow metamorphism. The strong and even inverted temperature gradient affects the migration of water vapor (deposition and sublimation) in the snow, and we would expect larger snow structures (i. e., depth hoar) resulting in lower SSA, which is indeed visible in the data. The changes in density are mainly in the upper layers (5 cm) of the snow, which indicates that at least a thin layer of fresh snow accumulated on top of the snow.

The change in increased correlation length affects the scattering strength of the snow: in general higher correlation lengths lead to stronger scattering. On the other hand, higher snow temperatures (Figure 4.5) increase emissions. To understand how these sur-

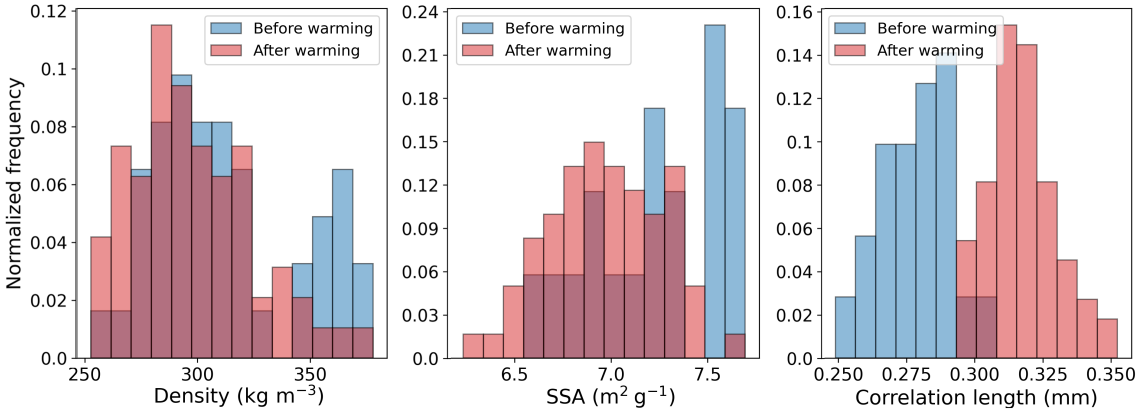

Figure 4.6: Histogram of average density, specific surface area (SSA) and correlation length of 132 SnowMicroPen profiles. The data are color-coded for the period of April 08–15 (blue) before the warm air intrusions and the period of April 21–27 (red) after the intrusions, and are normalized to 1.

face changes affect TB in more detail we therefore modeled the microwave emissions as indicated in the following section.

Floe perspective: microwave emission modeling

We further adopted the floe-wide perspective by using a statistical approach in modeling the TB. If we assume that the SMP measurements are representative of the CO (at a length scale of approximately 2 km) in terms of statistical distributions of the measured quantities, we should be able to simulate the effect of the warm air intrusions on the microwave signature. The following simulations were performed with the sea ice version of the Microwave Emission Model for Layered Snowpacks (MEMLS) (Wiesmann and Mätzler, 1999; Tonboe et al., 2006). Details about the model setup and initialization are given in the Appendix (Text S3 and Text S4). The simulations were not tweaked to match the satellite observations because we do not consider an atmosphere in our simulations. For the simulations, we assumed a second-year ice floe (Table B.2), while on satellite scale, the ice was a mixture of second-year ice and first-year ice. In addition, the snow height might be different on the MOSAiC floe, compared to the surrounding larger area. Consequently, the absolute values presented in the following can differ from what the satellites observe. The focus of the analysis is mainly on a qualitative level.

Brightness temperatures from modeling In Figure 4.7 we show the modeled polarization ratio of 18.7 GHz (PR(19)), the gradient ratio of 36.5 GHz and 18.7 GHz at vertical polarization (GR(37/19)) and the polarization difference at 89 GHz (PD(89)) before and after the warming events. The model output for the individual frequencies is shown in Figure B.6. In general, the model output shows a clear increase of TB for all frequencies (at both polarizations) except for 36.5 GHz, where the situation is reversed (Appendix

Text S4). Qualitatively, an increase is also seen in the satellite data (Figure 4.4) for all frequencies but the horizontally polarized TB at 18.7 GHz and 36.5 GHz.

When examining the ratios that are used in many SIC algorithms, the polarization ratio at 18.7 GHz remains mostly unchanged in the simulations (upper panels in Figure 4.7). GR(37/19) increases noticeably compared to the values prior to the warming events, and PD at 89 GHz shows only a slight increase. From a satellite perspective we observe an increase in all three quantities (Figure 4.8), which differs from what we observe in the model. Understanding the pronounced rise in satellite-measured PD, which causes the strong drop in SIC from the ASI algorithm, is key for potentially improving such PD-based SIC algorithms. As discussed earlier, the change in PD(89) cannot be explained by variability in downwelling radiation due to cloud cover and thus must be due to changes in the snow surface which, however, are not captured by the quantities derived from SMP profiles (density, SSA and correlation length). In the following, we propose an explanation for the observed changes in brightness temperature including a thin glaze ice layer in our simulations.

Model experiment floe: simulation of a glaze ice layer Visual observations during the expedition and also the TLS reflectance data (Appendix Text S2, Figures B.3 and B.4) suggest the development of a glaze ice layer, which formed in some spots of the ice floe during the first warming event, and almost everywhere during the second one. Glaze ice layers at the top of the snowpack can have a strong impact on the microwave emission of the snow (Smith, 1996; Mätzler et al., 1984; Grenfell and Putkonen, 2008; Rees et al., 2010). Studies on the effect of such ice layers at the surface of the snowpack have shown that, close to the Brewster angle (AMSR2 has an incident angle of 55°), they usually have a minor impact on vertically polarized TB, but strongly influence horizontally polarized TB (Rees et al., 2010) due to the high dielectric contrast between the snow and the ice layer. Thus, algorithms utilizing polarization differences or ratios (e. g., ASI and NASA-Team) will be influenced by the presence of such layers. How strong a certain frequency is impacted depends generally on the thickness of the ice layer (Montpetit et al., 2013). When we include such an ice layer in the SMP-based modeling, the modeled data (bottom panels in Figure 4.7) show relative changes (increase in PR(19) and PD(89)) that are qualitatively comparable to the ones observed from satellite (Figure 4.8). GR(37/19) is hardly affected because it is based on vertically polarized TB, while PD at 37 GHz also shows a strong increase (not shown). As described in the Appendix, Text S3 and Text S4, several assumptions and simplifications had to be considered in the model setup. Therefore, we do not expect to match the satellite observations and do not analyze quantitative changes in detail. We believe that the strength of our modeling results lies in the qualitative understanding they provide of what has caused the observed changes in the satellite observations.

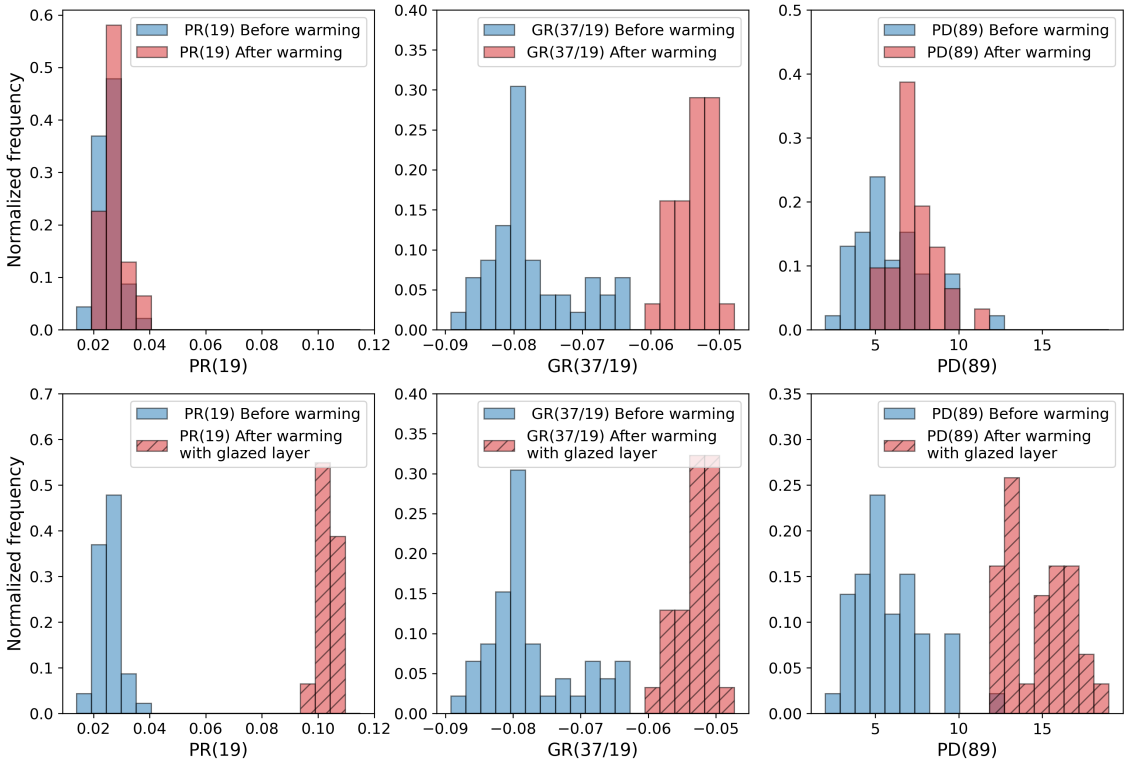

Figure 4.7: Histogram of simulated polarization ratio, gradient ratio and polarization difference for 84 SnowMicroPen profiles. The data for polarization ratio, PR(19), gradient ratio, GR(37/19), and polarization difference, PD(89), are color-coded for the period of April 08–15 (blue) before the warm air intrusions and the period of April 21–27 (red) after the intrusions, and are normalized to 1. In the bottom panels, a thin ice layer (2 mm) was added on top of the snow (red, hatched) to simulate the effect of surface glazing after the second warming wave.

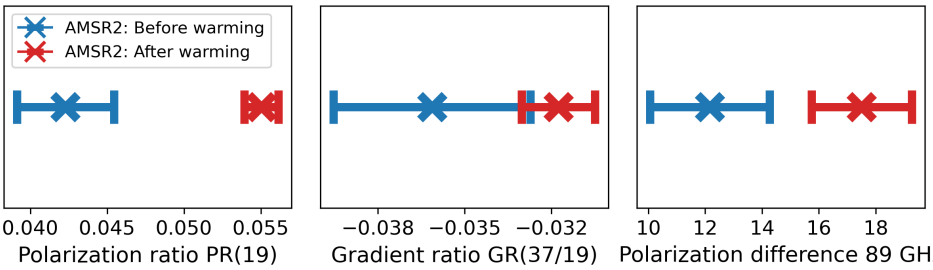

Figure 4.8: Statistics for polarization ratio, gradient ratio and polarization difference derived from satellite observations. The mean (x) and standard deviation (error bars) for polarization ratio, PR(19), gradient ratio, GR(37/19) and polarization difference, PD(89), are color-coded for the period of April 08–15 (blue) before the warm air intrusions and the period of April 21–27 (red) after the intrusions, matching the modeled periods in Figure 4.7. Values are derived from AMSR2 brightness temperature data co-located to Polarstern (Figure 4.4).

Site perspective: ground-based radiometers

The site perspective is discussed in the Appendix B.

4.1.4 Discussion

The effects of the warm air intrusions on SIC retrievals are manifold, but we believe that we have identified dominant mechanisms for the case study presented here. First, the changed temperature gradients in the snow and snow metamorphism (increase in correlation length) influence SIC estimates that rely on the gradient ratio GR(37/19). While the polarization ratio is considered largely independent of physical temperature (Cavalieri et al., 1984; Comiso et al., 1997; Tonboe et al., 2006), such independence is not necessarily the case for the gradient ratio due to different penetration depths (and temperature-dependent permittivities) at 18.7 GHz and 36.5 GHz. Comiso et al. (1997) argued that the effect should be small unless the snow cover emits a sizable fraction of the measured TB. We assume the latter to be the case for 36.5 GHz. Thus we attribute the increase in GR(37/19) to the changed snow temperature (gradient) which is not fully compensated by snow metamorphism, i. e., grain coarsening, which decreases GR(37/19). GR(37/19) can also be influenced by changes in snow height (due to increased scattering at 36.5 GHz), but observations from buoys deployed around the MOSAiC floe show that the (average) snow depth only changed by less than 5 cm during the investigated period (not shown).

Second, we attribute the strong increase of satellite-measured PD after the warm air events to a glaze ice layer on top of the snow surface that was present on a large scale. Such glazing was observed in the field, and model results suggest that it can explain the observed satellite microwave TB. The alteration of TB because of the glazing causes a decrease in SIC in some SIC products that we investigated in this study, significantly for the algorithms that mainly rely on PD(89), as ASI does, or on PR(19) as NASA Team does. We hypothesize that the increase in PD at 36.5 GHzalso caused the decrease in SIC by the OSI SAF algorithm that uses the TB space spanned by both polarizations at 36.5 GHz. The dual algorithm approach of the NSIDC CDR largely mitigates the glazing impact in this case, as the Bootstrap algorithm gives a high value for SIC. This algorithm is also based on both polarizations at 36.5 GHzbut no decrease in SIC is observed after the warming events. A possible explanation here is an overestimation and subsequent truncation of SIC to 100%. While this effect is an advantage for the case presented here, this approach might also overestimate SIC in other situations. For example, the Northeast Water polynya that opened at the Greenland coast after the events (middle column, first three rows in Figure 4.2), is hardly visible in the NSIDC CDR product.

We note a stronger response of the microwave emissions to the warming events at higher frequencies that have smaller penetration depths into the snow than at lower frequencies.

A thin ice crust also has a greater effect at these frequencies while the wavelengths of the lower frequencies are large compared to the thickness of the crust. SIC retrievals using vertical polarization or ones that are based on lower frequencies like 6.9 GHz are less affected.

Hypothesizing that such glazing events should increase in a warming Arctic, as not only warm air intrusions but also rain on snow events can cause them (Stroeve et al., 2022), we find that algorithms based on low frequencies/vertical polarization could be a more robust choice for the future. In the study by Rees et al. (2010) about an ice crust on snow on land 6.9 GHz also showed the least response to the ice crust. As a difference to our case, PD at 19 GHz was affected most in their study, which is likely due to a different thickness of the ice crust and different snow conditions.

Modeling snow and ice microwave emission remains a challenge especially at satellite-footprint scale, even if a large amount of observational data is available. The challenge is partly due to the local heterogeneity which makes matching radiometer observations and ground-based observations difficult. For example, we did not only observe differences in the snow cover between the ground-based radiometer footprints at the same site but also within one footprint (Figure B.5). We overcame this problem by using the vast amount of snow profiles from the SMP measurements in combination with modeling, providing a statistical description of expected surface TB (Figure 4.7). If, however, the radiometers measure snow conditions that are not representative of the surroundings (due to snow accumulation), then comparisons to these TB measurements are impeded. The statistical description might be more comparable to a satellite observation in the case of negligible atmospheric effects. We cannot be certain, however, that the SMP data are representative of a satellite footprint on the order of tens of kilometers. Also, certain parameters, such as surface roughness that are important for emission modeling of satellite observations, were not directly available. Coherence effects, that depend on frequency and layer thickness, are another source of uncertainty. Nevertheless, the temporal evolution of the ground-based radiometer measurements can be reproduced by a microwave emission model if the glaze ice layer is included. Similarly, including a glaze layer allowed us to qualitatively model relative changes as observed from space using the SMP measurements as input. This study is one of the few existing cases where a spurious change in satellite SIC can be fully explained by the observed surface changes from ground-based measurements (snow and ice physics and radiometers). We are confident that adopting the three perspectives from the different scales (satellite, floe, site) allowed for a plausible interpretation of the observations.

4.1.5 Conclusion

Arctic amplification, i. e., the more rapid and stronger increase of temperatures in the Arctic compared to low latitudes (Serreze and Barry, 2011; Screen and Simmonds, 2010; Comiso and Hall, 2014; Wendisch et al., 2017,0), can lead to an increased occurrence of warm air intrusions above the ice cover (Graham et al., 2017). As shown in this study, they can affect TB measured by satellite microwave radiometers and cause uncertainties and errors in the derived SIC products. In our case, the warm air intrusions led to a large-scale spurious strong decrease in SIC and an increase in the deviations between different SIC products in the central Arctic. These deviations lasted for several days. Only one product was minimally affected. It, however, has the tendency to always produce high SIC values, which was the correct solution in this case.

Here we have offered an interpretation of the satellite signals based on observations from the MOSAiC expedition and by microwave emission modeling, taking into account atmospheric effects as well as surface snow metamorphism. As an explanation for the changed microwave emissions during and after the warming events, we propose the formation of a large-scale glaze ice layer, which persists even days after the warm air intrusion.

Many recent SIC studies (Lu et al., 2022) focus on how the atmosphere influences TB and thus SIC retrievals. In our case, the surface changes are highly relevant and should be included in future evaluations of SIC retrieval algorithms. Ivanova et al. (2015) conjectured that near 90 GHz algorithms might be less sensitive to changes within the snow compared to the lower frequencies because of the small penetration depth. However, as shown in this study, certain surface effects like glazing can have a strong influence on these algorithms. Identifying similar events, their scale in time and space and their frequencies of occurrence can provide additional insights to quantify whether this effect is significant on longer temporal and spatial scales and for climate data records. Inter-comparison studies of SIC algorithms could also benefit from an evaluation of the performance of the algorithm during events like warm air intrusions or rain-on-snow events, which can lead to the formation of a glaze ice layer. In the future, due to a projected increase in warm air intrusions, the relevance of their effects on sea ice climate records from satellites and the distinction between actual influence of climate warming on sea ice, as described for example by Merkouriadi et al. (2020), and retrieval uncertainties will become more important. The effects of warm air intrusions need to be considered in the estimation of product uncertainties, possibly by using dynamic uncertainty estimates, i. e., uncertainties that are neither constant nor dependent only on SIC. An example is the OSI SAF iCDR product which provides estimates that show an increased uncertainty after the events, even though the higher uncertainty is caused, in this case, by a higher representativeness uncertainty. As a follow-up from this study, Rostosky and Spreen (2023) assessed the relevance of warm air intrusions for climate data records and found that several algorithms underestimate SIC during and after warm air intrusions.

Multi-frequency methods exploiting the synergy of the robustness of 6.9 GHz and the high spatial resolution of 89 GHz are a promising approach for future retrievals. Upcoming satellite missions like the Copernicus Imaging Microwave Radiometer (Donlon, 2020) will provide measurements at 6.9 GHz at a much higher spatial resolution (around 15 km) than current satellite sensors, which makes it well suited for SIC retrievals at higher spatial resolution (5 km at 37 GHz) and higher accuracy (using 6.9 GHz) than what is available today. One multi-frequency method for a multi-parameter retrieval including SIC is introduced in the next Chapter.

Chapter 5

Multi-parameter Retrieval

This chapter is based on Rückert et al. (2023a). Janna Rückert contributed by conceptualizing this work, developing the methodology, curating the data and writing the first draft of the paper. In addition the chapter contains unpublished extended comparisons against *ground truth* and reference data, namely the Sections 5.6.4 and most of 5.6.5.

5.1 Introduction

We build upon works of Melsheimer et al. (2008); Scarlat et al. (2017); Scarlat (2018); Scarlat et al. (2020) to further develop an integrated retrieval of atmospheric and surface variables in the Arctic. Scarlat et al. (2017,0) took results from Mathew et al. (2008) to derive an effective emissivity and emitting layer temperature of the sea ice for the surface component of a forward model. We refer to this emissivity as empirical emissivity in the following. This model is inverted by an optimal estimation method to simultaneously retrieve several geophysical parameters, namely total water vapor (TWV), liquid water path (LWP), sea ice concentration (SIC), multiyear ice fraction (MYIF), surface temperature, and wind speed (WSP) (over open ocean), from brightness temperatures measured at six frequencies ranging from 6.9 GHz to 89 GHz. When studying the derived atmospheric quantities from this method, we note a bias for TWV when compared to radiosonde measurements during field campaigns over sea ice, which is strongly reduced over open ocean (Crewell et al., 2021). This can also be seen in Figure 5.1 where satellite-retrieved values of TWV are compared to radiometer observations onboard the research vessel *Polarstern* during the Multidisciplinary drifting Observatory for the Study of Arctic Climate (MOSAiC) expedition 2019–2020. Also, this approach shows unrealistic high values of liquid water path over first-year ice, and thus a false gradient when the ice type changes from predominately first-year to multiyear, illustrated in Figure 5.2.

We attribute these issues in retrieved TWV to the assumed fixed surface emissivities (that are distinguished by ice type), especially at the high-frequency channels, which carry

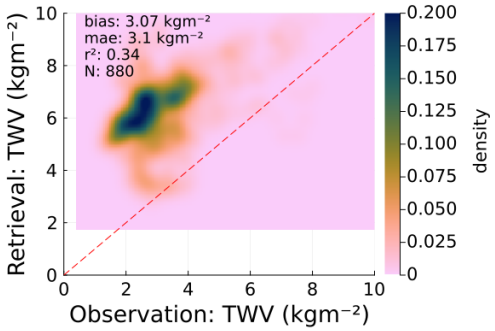

Figure 5.1: Scatter plot of retrieved total water vapor using the model with empirical emissivities vs. MOSAiC measurements described in Section 5.2. Included in the plot are bias, mean absolute error (mae) and the coefficient of determination given by the squared Pearson correlation coefficient r^2.

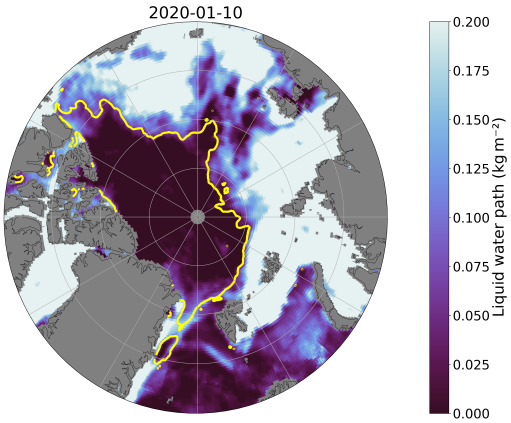

Figure 5.2: Map of retrieved liquid water path (daily gridded data) using the model with empirical emissivities for January 10, 2020. The 0.5 contour line of retrieved multiyear ice fraction is shown in addition.

most of the information about the atmospheric state. At these frequencies in particular, both scattering and emission in the snow play a role, but also the vertical temperature profiles in both snow and ice which depend on the depth of the insulating snow. These aspects lead to a high variability in surface emissions that is not well represented by a mere distinction in surface emissions based on sea ice type. In order to better represent these highly-variable surface emissions in the forward model, we exchange the empirical parameterization with the Microwave Emission Model for Layered Snowpacks (MEMLS) extended to sea ice, called MEMLS_ice model (Wiesmann and Mätzler, 1999; Mätzler and Wiesmann, 1999; Tonboe et al., 2006; Tonboe, 2010) and include snow depth and snow-ice interface temperature as new retrieval parameters. The MEMLS_ice emission model uses a stack of planar homogeneous layers characterized by the physical snow and sea ice quantities relevant for scattering and absorption, like the layer thickness, correlation length, a measure of scatter size and distribution, density, salinity, and temperature.

First, an idealized layer input to MEMLS_ice is established based on literature and campaign data for the layer parameters. The sensitivity to the model layer choices is analyzed and used as uncertainty estimate in the inversion method. To showcase the impact of the physical ice emission model we make use of the extensive datasets collected during the year-long MOSAiC expedition. Here, we study the brightness temperatures simulated by the new forward model using *ground truth* input from MOSAiC and compare them to satellite observations. Then, the model is inverted and the retrieval output is analyzed. Finally, we apply the retrieval on Arctic-wide available satellite data to generate daily maps of all retrieved quantities.

Table 5.1: Satellite sensors used in the analysis

Name	platform	available time span	product level	spatial resolution
AMSR-E	AQUA	May 2, 2002 - December 4, 2011	2A	75 km×43 km
AMSR2	GCOM-W1	May 17, 2012 - today	1R	62 km×35 km

5.2 Data

5.2.1 Satellite Brightness Temperatures

We use brightness temperatures measured by the radiometers Advanced Microwave Scanning Radiometer - Earth Observing System (AMSR-E), onboard of the spacecraft AQUA and functioning from May 2, 2002 until December 4, 2011 and Advanced Microwave Scanning Radiometer 2 (AMSR2), the microwave scanning radiometer on the GCOM-W1 spacecraft from the Japan Aerospace Exploration Agency, launched May 18, 2012, see Table 5.1. Both sensors are conically-scanning multifrequency total-power microwave radiometer and they both detect horizontally and vertically-polarized brightness temperatures at 6.925, 10.65, 18.7, 23.8, 36.5, and 89.0 GHz at a constant angle of 55°. AMSR2 additionally measures at 7.3 GHz for radio-frequency interference detection.

AMSR-E has an instantaneous field of view (IFOV) ranging from 75 km×43 km at 6.9 GHz to 6 km×4 km at 89 GHz and a swath width of 1445 km. Its near-polar, sun-synchronous sub-recurrent circular orbit is at an altitude of about 705 km.

AMSR2 has an IFOV ranging from 62 km×35 km at 6.9 GHz to 5 km×3 km at 89 GHz and a swath width of 1450 km. Its near-polar, sun-synchronous sub-recurrent circular orbit is at an altitude of about 700 km.

In case of AMSR-E, we use the Level 2A product with geolocated brightness temperatures at different frequencies that are resampled to a common resolution. In case of AMSR2, we use the swath data, both ascending and descending, of the Level 1R product matched to the resolution of 6.9 GHz (Maeda et al., 2016), corresponding to an IFOV of 62 km×35 km. This product is resampled using the antenna gain patterns for each channel so that the brightness temperatures for all frequencies have the same field of view. We use the land mask contained in the product to mask out land observations. In this analysis, we also use data of overpasses over the icebreaker *Polarstern* (Knust, 2017) during MOSAiC. For every overpass, the satellite measurement closest to the vessel's hourly position is taken and used in Section 5.4.1. There are up to seven overpasses of *Polarstern* per day. Additionally, we use daily gridded Level 1B AMSR2 data projected onto a polar stereographic grid with a nominal resolution of 25 km to derive a climatology in Section 5.5.

5.2.2 Reanalysis Data

From the European Centre for Medium-Range Weather Forecasts (ECMWF) fifth generation reanalysis ERA5 (Hersbach et al., 2020) we obtain climatological mean values further described in Section 5.5.

5.2.3 ASCAT/AMSR2: Multiyear Ice Fraction

For a climatology of multiyear ice fraction, i. e., the fraction of sea ice that survived one melting season, we use the operationally available product from https://seaice.uni-bremen.de/ based on ASCAT scatterometer and microwave AMSR2 radiometer data (Ye et al., 2016b,0).

5.2.4 Merged Warren-AMSR2 Climatology: Snow Depth

For a climatology of snow depth, we use a merged product described in Hendricks and Paul (2022) of monthly snow depth data based on merging the Warren snow climatology (Warren et al., 1999) and daily snow depth over first-year sea ice from AMSR2 data (Rostosky et al., 2018).

5.2.5 Round Robin Data Package

The Round Robin Data Package (RRDP; Pedersen et al. (2021)) is a collection of co-located sea ice measurements from buoys, flight campaigns, melt pond satellite retrievals, 100% and 0% sea ice concentration reference areas, and satellite measurements of microwave brightness temperatures and backscatter produced and maintained by ESA's Climate Change Initiative project. We use the RRDP Version 3.

5.2.6 Utqiaġvik ARM Site: Liquid Water Path

A long-term LWP ground-based dataset is available from the U.S. Department of Energy's Atmospheric Radiation Measurement (ARM) program. The ARM site near Utqiaġvik, Alaska, is located at 8 m altitude at the coast, 71.323°N and −156.609°E. From the ground-based TB measurements of two-channel microwave radiometers, LWP is retrieved using a complementary combination of two retrieval techniques described in Turner et al. (2007). Data is available from 2002, covering the entire AMSR time series, at a temporal resolution of about one second (Zhang, 2023).

5.2.7 MOSAiC Datasets

The datasets used in this Chapter as *ground truth* are described in the following. Note that they have different spatial extents, but we assume that the data is representative of

the satellite footprint. Therefore, we also use estimations of uncertainties of the *ground truth* datasets in Section 5.4.1.

In Chapter 4 a case study from the MOSAiC expedition has been presented already. Here, we again make use of the extensive measurements during that campaign. Figure 5.3 shows the drift track of MOSAiC from September 2019 – September 2020, which covered different Arctic regions.

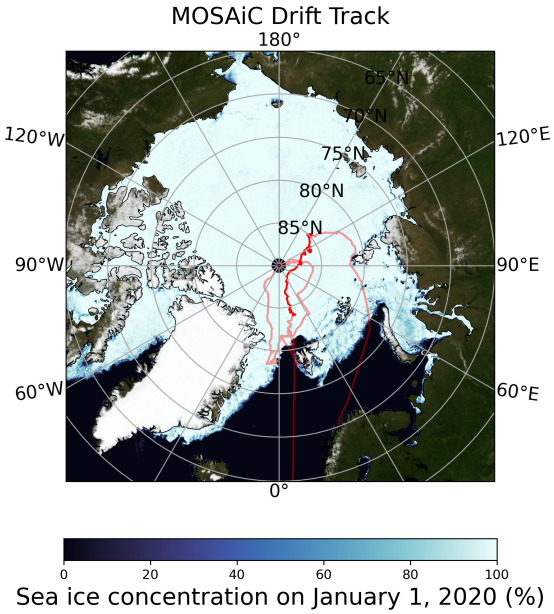

Figure 5.3: MOSAiC expedition track from September 2019 – September 2020. The darker red line shows the time period October – April. The maps shows the daily sea ice concentration (SIC) from the operationally available ARTIST Sea Ice (ASI) SIC product (described in Section 4.1.3).

A compilation of the datasets where the different measured geophysical parameters are co-located to satellite overpasses has been made publicly available under Rückert (2023). The different variables available within that compilation are described in the following and in Section 5.4.1.

HATPRO Radiometer: Total Water Vapor and Liquid Water Path We use TWV and LWP retrieved from the ground-based low frequency Humidity and Temperature Profiler (HATPRO) microwave radiometer operated onboard the research vessel *Polarstern* during MOSAiC. More information on this data can be found in Walbröl et al. (2022). Here, we are using only data that was not flagged as bad data in the quality check.

SIMBA Buoys: Snow depth and snow-ice interface temperature For snow depth and snow-ice interface temperature measurements during the MOSAiC campaign, we use data from 19 Snow and Ice Mass Balance Apparatus (SIMBA) buoys, which are thermistor string type ice mass balance buoys that were deployed in proximity to *Polarstern*

(distributed network and the Central Observatory (CO)) (Lei et al., 2021). Note that not all buoys were operational at the same time but that we have data from at least ten buoys at different locations within the CO at the same time during our period of interest.

TerraSAR-X ScanSAR Images: Sea Ice Concentration and Multiyear Ice Fraction We use 49 classified scenes for November 2019 – March 2020 from Guo et al. (2023) based on X-band TerraSAR-X scanning synthetic aperture radar images in a 70 km ×70 km square around the CO. We resampled the data to daily values by linear interpolation and fill missing values with the mean of the whole time series. The SIC is estimated using the fraction of classified lead ice (representing openings, i. e., an upper bound for the open water fraction), while the multiyear ice fraction is estimated to be the sum of the fractions of the deformed and heavily deformed ice classes.

Polarstern: Wind Speed and Sea Surface Temperature Measurements of wind speed and sea surface temperature are provided by the vessel's synoptical reports (Schmithüsen et al., 2021a,0,0).

Infrared Thermometer: Surface Temperature For the snow-air interface temperature, we use skin temperature calculated based on infrared thermometer data measured at the Met City location within the CO and from three additional stations in the distributed network (with average distances to the vessel between 10 and 23 km) (Herrmannsdörfer et al., 2023; Cox et al., 2023a,0,0,0).

5.3 Methodology: Forward Model

Let us recall from Chapter 2.1 what the upwelling, p-polarized (either horizontal or vertical) brightness temperatures, $T^p_{\mathrm{B,sat}}$, which a satellite observes at an incidence angle θ for a given frequency f, are composed of:

$$T^p_{\mathrm{B,sat}}(\theta, f) = T_{\mathrm{B,up}}(\theta, f) + \Upsilon(\theta, f)(T^p_{\mathrm{B},\Omega}(\theta, f) + T^p_{\mathrm{B,surf}}(\theta, f)), \tag{5.1}$$

where $T_{\mathrm{B,up}}$ is the upwelling emission of the atmosphere, Υ is the total transmittance (see Equation 2.30), $T^p_{\mathrm{B},\Omega}$ is the downwelling, p-polarized radiation scattered upward by the surface and $T^p_{\mathrm{B,surf}}$ is the radiation emitted by the surface. These expressions allow us to separate the terms into an atmospheric part ($T_{\mathrm{B,up}}$ and Υ), a surface contribution $T^p_{\mathrm{B,surf}}(\theta, f)$ and a term containing both as $T^p_{\mathrm{B},\Omega}$ contains atmospheric downwelling radiation as well as the surface reflectivity.

We consider the surface contribution as a linear combination of sea ice and open ocean

(OW) weighted by SIC as also done in Scarlat et al. (2017,0):

$$T^p_{\mathrm{B},\Omega}(\theta, f) + T^p_{\mathrm{B,surf}}(\theta, f) = \mathrm{SIC} \cdot T_{\mathrm{B,ice}} + (1 - \mathrm{SIC}) \cdot T_{\mathrm{B,OW}}, \tag{5.2}$$

with $T_{\mathrm{B,ice}}$ being the brightness temperatures of the sea ice surface and $T_{\mathrm{B,OW}}$ being the brightness temperatures of the ocean surface. Both terms include the reflected downwelling radiation of the atmosphere by the respective surfaces. Along the same lines we may now also split the forward model in terms describing the atmosphere, the ice surface and the ocean surface. We model the atmosphere and ocean following Wentz and Meissner (2000) with recent improvements (Meissner and Wentz, 2004,0). The surface temperature is given by the weighted mixture of sea surface temperature and snow-air interface temperature. We now focus on modeling $T_{\mathrm{B,ice}}$ in the following Section.

Surface Model

Our aim is to construct a surface model setup that (i) covers the most important quantities influencing the brightness temperatures in order to simulate plausible brightness temperatures, polarization differences and their variabilities and (ii) reflects a realistic snowpack including its temperature gradients by using model parameters from literature. Our chosen setup is characterized by four input variables: the snow-air interface temperature T_{sa}, the snow-ice interface temperature T_{si}, the ice type (either first-year ice (FYI) or multiyear ice (MYI)) and the snow depth (SND). We use the MEMLS_ice model to simulate brightness temperatures at the top of multiple stacked planar layers of ice and snow. MEMLS_ice calculates the radiative transfer in a multi-layer media, including internal reflections (Fresnel equations) and scattering. Absorption and scattering coefficients are hereby derived from six-flux theory, taking all space directions into account. The model is described in Wiesmann and Mätzler (1999); Mätzler and Wiesmann (1999) and was extended to include sea ice by Tonboe et al. (2006); Tonboe (2010).

The model input consists of downwelling brightness temperatures that are obtained from the atmospheric model (see above), and parameters for each layer, namely thickness, density, correlation length, liquid water content, salinity and temperature. The incidence angle is set to the satellite incidence angle of 55°. Snow and ice are highly variable both temporally, e. g., due to snow metamorphism or ice growth, and spatially, for example because of different ice types or horizontal inhomogeneity of the snow surface. In our retrieval method we do not have enough degrees of freedom in our satellite measurements to retrieve all snow and ice parameters that are needed as input for the MEMLS_ice model so that it can produce a realistic output. Therefore we constrain some of them. Using relations between these parameters (i.e. their co-variances) to reduce their effective number is hindered by the high variability of the atmosphere that partly determines the ice and snow structure during initial formation (Fuhrhop et al., 1998). It is therefore clear

that our layer setup represents a simplified, idealized ice and snowpack.

We model snow and ice using four and five layers, respectively, in order to capture temperature and salinity profiles as well as layering observed in snow on Arctic sea ice (King et al., 2020; Merkouriadi et al., 2017). This is especially important as the radiation from the surface is the result of emission, scattering and reflection within the snow and ice pack, so that each layer contributes to the observed brightness temperatures (Hallikainen and Winebrenner, 1992). For different frequencies the relative contributions vary and can be related to 'penetration depths': low frequencies have higher penetration depths than high frequencies influencing brightness temperature (TB) differences among them.

All fixed model parameters are shown in Table 5.2 and are chosen from literature or observations as discussed below. To estimate the influence of these model parameters on the model output (the top-of-atmosphere brightness temperatures) and to quantify the uncertainty that we are introducing by not being able to account for the model parameters' natural variability, we perform model simulations which are described in Section 5.4.2. There we determine the TB sensitivity to the model parameters, which can be later used in the optimal estimation scheme.

Temperatures The snow-air interface temperature and the snow-ice interface temperature are free parameters and are retrieved in the final satellite product. They are treated as independent parameters, i. e., we are not assuming thermal equilibrium within the snow and ice. This allows us to model changing satellite brightness temperatures due to fast temperature changes in the upper snow layers, which is of particular importance for the higher frequency channel TBs. The temperature profile in the snow is assumed to be linear. The same is true for the ice temperature profile, where we assume a temperature of 271.35 K for the ocean, the freezing point of seawater with a salinity around 35 ppt.

Snow Parameters While snow depth is a free parameter, the other parameters related to the microphysical structure of snow, namely exponential correlation length and density, are chosen in a way to resemble a layer of wind slab snow on top, a faceted layer in the middle and a layer of depth hoar snow at the snow-ice interface, as it was observed on Arctic sea ice (King et al., 2020; Merkouriadi et al., 2017). Note that in reality the distributions and relative thicknesses might vary depending on the ice type and so does the density. For example, higher bulk density of snow over second-year ice compared to FYI has been observed (Merkouriadi et al., 2017). For simplicity and to avoid over-emphasizing the ice type parameter, such a distinction is not made and the snowpack model parameters are independent of the ice type.

For snow densities, we take average values from field measurements in April (King et al., 2020). We note the high variability in both the density distributions and fractions to the overall snow depth (e. g., King et al. (2020) find that the depth hoar layer for

MYI makes up 50% of the snowpack but only 20% over FYI). We simplify by setting the fractions of the three layer to one third, and we take average values of FYI and MYI. In our model, wind slab and faceted snow has the highest density ($327\,\mathrm{kg\,m^{-3}}$ and $314\,\mathrm{kg\,m^{-3}}$) and depth hoar the lowest ($250\,\mathrm{kg\,m^{-3}}$), yielding a bulk density of $297\,\mathrm{kg\,m^{-3}}$ in the range of literature values (Warren et al., 1999). The snow permittivity of each layer in the model, as a function of snow density, is calculated as a dielectric mixture of air and ice described in Wiesmann and Mätzler (1999) following Mätzler (1998).

Over first-year ice, brine-wetted snow has been observed (Barber et al., 1995; Crocker, 1992; Geldsetzer et al., 2009) and its effect on satellite altimetry was discussed in Nandan et al. (2017). The highest salinities are found in the bottom 4 cm to 8 cm of the snow cover and range from 1 to over 20 ppt (Barber et al., 1995; Geldsetzer et al., 2009). As our implementation of the MEMLS_ice model does not include saline snow permittivity models, we implemented a dielectric mixture model (Maxwell Garnett (Garnett and Larmor, 1906,9)) assuming ellipsoid brine inclusions in the snow. We set the axes fraction of the inclusions to 0.072, corresponding to oblate spheroids (Denoth, 1980; Barber et al., 1995). We only adapted the dielectric function, but not the scattering coefficients. However, we also note that our model differs from the one derived in Geldsetzer et al. (2009). They derive a semi-empirical model based on measurements at 50 MHz. For the same input, their model provides higher values for the real and imaginary part of the permittivity ϵ and a resonant behavior of the imaginary part around 9 GHz, which our implementation does not show. However, our approach is comparable to the recent implementation of saline snow in the Snow Microwave Radiative Transfer (SMRT) model (option 'saline_snow_permittivity_scharien' in the snow module, Picard et al. (2018)).

In summary, our implementation of the dielectrics of brine-wetted snow is an interim solution, as more research on dielectric properties of brine-wetted snow is needed to achieve reliable parameterizations.

We might think of this layer in our model setup as an intermediate layer between ice and snow to avoid high gradients in the refractive index, as nature is likely more continuous than our model. Note that this conception is also limited as such an intermediate layer has wavelength-dependent effects and might be coherent for large wavelengths. We choose an upper limit of 6 cm for the saline snow layer over first-year ice with a salinity of 11.4 ppt. Over multiyear ice, we assume no brine in the snow.

The scattering in the snow strongly depends on the microstructure of the snow and MEMLS_ice uses the exponential correlation length as corresponding parameter. Within MEMLS_ice, different scattering mechanisms are parameterized. We model the scatterers of the upper two layers as spheres and for the bottom layer, which we want to resemble depth hoar, we choose shell scattering, described in Wiesmann and Mätzler (1999).

The correlation lengths are estimated based on SnowMicroPen MOSAiC measurements from October-April (Macfarlane et al., 2021). Snow surface and snow bottom at the ice

interface were automatically detected in the SnowMicroPen measurements and then the snowpack was simply divided in three layers of equal thickness. Mean correlation lengths for each layer were computed using the parameterization given in Proksch et al. (2015) and were then averaged over the whole time series. The values fit to the ones given by Mätzler (2002) for Alpine snow for the faceted and depth hoar snow type.

Ice Parameters Solid ice, liquid brine, and air bubbles make up the sea ice. As that composition changes over time, for example due to desalination as result of expulsion of brine, first-year and multiyear ice differ in their microwave emission signature. Thus, ice type is the free parameter determining the microphysical parameters that are assumed for the model ice layers. We are using two ice classes: first-year ice and multiyear ice.

Sea ice thickness defined as the distance from ice surface to ice bottom, is strongly variable and ranges from a few centimeters (new ice/nilas) over 1 meter to 3 meter for level first- and multiyear ice, to tens of meters for ridged ice. Here, we assume a 1 m ice layer for first-year ice and 2.5 m for multiyear ice. Ridges can be up to tens of meters and individual adjacent floes can strongly vary in their mean thicknesses (Hallikainen and Winebrenner, 1992) but we argue that on a satellite footprint it is eligible to assume some mean thickness. The main influence of ice thickness on the modeled TB is given by the thickness-dependent temperature gradients. Due to the inclusion of the snow-ice interface temperature T_{si} as free parameter, this influence is partly reduced. The natural seasonal dependence of sea ice thickness is currently not implemented and the used thicknesses can be understood as some plausible mean winter value for first-year ice and multiyear ice comparable to Kwok et al. (2020).

For the first-year ice density, we follow the literature value of around $916\,\mathrm{kg\,m^{-3}}$ (Alexandrov et al., 2010). Multiyear ice that survived one melting season usually contains more air inclusions and has a lower density above sea level. The first 25 cm of the ice in our setup can be considered freeboard with lower densities (here the upper ice layer density is constant at $895\,\mathrm{kg\,m^{-3}}$), while the other layers are below sea level with values comparable to first-year ice (Jutila et al., 2022).

Saline ice mainly impacts the dielectric loss term. Nakawo and Sinha (1981) observed a quasi-stable value within a few weeks after ice formation with top layer ice salinities of around 11.4 ppt, and we distribute the salinity in the ice with a C-shaped salinity profile model for first-year ice (Weeks and Lee, 1962). Salinity in multiyear sea ice is much lower than in first-year ice especially near the surface because of the summer melt processes (Cox and Weeks, 1974). We choose a linear model to distribute salinity in multiyear ice with 1 ppt in the top layer and 4 ppt in the bottom ice layer. The permittivity of the ice layers are given by the dielectric mixture of ice, air, and brine. The permittivity of ice is calculated following Mätzler and Wegmuller (1987) with the imaginary part given by Hufford (1991). The permittivity of brine is calculated following Stogryn and Desargant

(1985). The brine volume is calculated as expressed in Stogryn (1987). For first-year ice, the permittivity of ice and brine is calculated with a dielectric mixture model (Maxwell Garnett) assuming prolate spheroid inclusions with an axis fraction (i. e., the ratio of the semi-major to the semi-minor axis) of five to resemble brine pockets (Light et al. (2003) also treat brine pockets as prolate ellipsoids). For multiyear ice the effective permittivity is calculated based on effective-medium theory of Polder and van Santeen (1946) assuming spherical inclusions of air in ice.

The scattering mechanisms in ice are estimated by the improved Born approximation and depend on the ice type: for first-year ice small brine pockets are the dominant scatterers, while for multiyear ice air bubbles scatter the radiation following Tonboe (2010). Note that the parameterization for ice assumes scattering at spheres and calculates an effective permittivity (for FYI done assuming randomly-oriented needles), even though the dielectric mixture model assumes randomly-oriented ellipsoids for FYI. The assumed correlation lengths are taken from Rostosky et al. (2020) based on ice core data, where the FYI values are in agreement with values reported by Hallikainen and Winebrenner (1992).

Additional Model Parameters As our model is designed for the winter season, wetness (caused by meltwater in the ice or snowpack) is set to zero for all layers. Upper ocean salinity is of importance only for frequencies lower than the ones used in this study (Kilic et al., 2021). We use a value of 34 ppt and calculate the ocean permittivity and conductivity following Meissner and Wentz (2004).

We use the model without taking into account coherence effects. This is necessary to avoid oscillations due to coherent reflections at the parallel layers as soon as one layer gets smaller than 2 cm.

Additionally, the roughness of layer interfaces is not considered in our model. In general, we expect that the high frequencies (in this case at 89 GHz) are most challenging to model in the MEMLS_ice model. This is due to the small wavelength which can be of the order of, e. g., the brine inclusions or the interface roughness, so that other scattering mechanisms (e. g., geometrical optics) might come into play which are not yet parameterized.

Table 5.2: Model setup as input to MEMLS_ice: Values for the layer parameters layer thickness, d, correlation length, ζ, density, ρ, and salinity

	d (cm)		ζ (mm)		ρ (kg m^{-3})		salinity (ppt)	
	FYI	MYI	FYI	MYI	FYI	MYI	FYI	MYI
Snow	SND/3		0.13		314		0	
	SND/3		0.14		327		0	
	SND/6		0.22		250		0	
	SND/6		0.22		250		11.4	0
Sea ice	0.04	0.04	0.15	0.28	916	895	11.4	0.5
	0.21	0.21	0.15	0.28	916	895	9	0.5
	0.25	1.0	0.15	0.28	916	915	5	1.5
	0.4	1.0	0.15	0.28	916	915	5	3
	0.1	0.25	0.15	0.28	916	915	30	4

5.4 Forward Model Evaluation

5.4.1 Brightness Temperature Observations

In order to evaluate the forward model, we use MOSAiC observations from October to April as *ground truth* input to the model and compare the simulated brightness temperatures with satellite observations. Additionally, we simulate the uncertainty of the *ground truth* by running the model for each TB measurement 100 times, where the *ground truth* values are taken from respective normal distributions with standard deviations (representing spatial and/or temporal variability) given in Table 5.3. Figure 5.4 shows the time series of measured and modeled brightness temperatures at the lowest and highest frequency (6.9 GHz and 89 GHz), as well as their probability density distributions and differences. For the other frequencies the reader is referred to Figure 5.5 in the Appendix. The standard deviations of the 100 simulations are shown as shaded areas around the mean modeled TB in Figure 5.4. The temporal evolution is well represented in the modeled data. We note less agreement in the horizontal polarization, where ΔTB shows higher values and also the squared Pearson coefficient as a measure for the correlation (r^2) is lower (for example 0.61 compared to 0.92 for 6.9 GHz). As the satellite measures close to the Brewster angle, the surface reflection (mainly dependent on the difference of the refractive indices of surface and air) is stronger for horizontally-polarized TBs and this polarization is therefore more sensitive to changes in snow and ice properties which are not fully represented in our model. Thus, we expected less agreement for horizontal polarization.

In both polarizations, the differences between measurements and model are larger for the higher frequencies. The excellent agreement for vertically-polarized TB at 6.9 GHz is due to its high correlation with T_{si}. We also note changes over the season in the differences of modeled and measured TBs, especially at 89 GHz where ΔTB is, e. g., lower in March/April compared to November/December. One possible explanation is snow metamorphism: 89 GHz is very sensitive to the upper snow layer microstructure, suggesting that our model setup is more representative of a snowpack in the late winter season than at the beginning of winter.

Similar correlations between modeled and measured TB are observed when using the Round Robin Data Package dataset (Pedersen et al., 2021) as *ground truth*. Most parameters included in RRDP are used as given therein (SIC from the percentage of open water, SND, TWV, LWP, WSP). We set sea surface temperature (SST) to 273.15 K and make an assumption about MYIF, which is set to one if the sea ice thickness variable in RRDP is larger 1.5 m, else it is set to zero. We calculate T_{sa} from 2 m air temperature (T2m) in RRDP, and T_{si} is calculated from TBs at 6.9 GHz with the corresponding fit over MYIF (see Section 5.5).

The results of the comparison between modeled TBs and satellite TBs are summarized in the Appendix, Table C.1. Similar to the comparison using MOSAiC in situ data, we find high correlations between modeled and satellite TBs, which are decreasing with increasing frequency. Mean absolute error and bias are also again smaller for vertical polarization than for horizontal.

Due to the overall good agreement between simulations and observations, and because the observed biases show a seasonal dependence, we do not make a constant bias correction of the forward model. Some of the deviations from measurements, however, cannot be explained by the input uncertainties and are related to model (parameter) uncertainties.

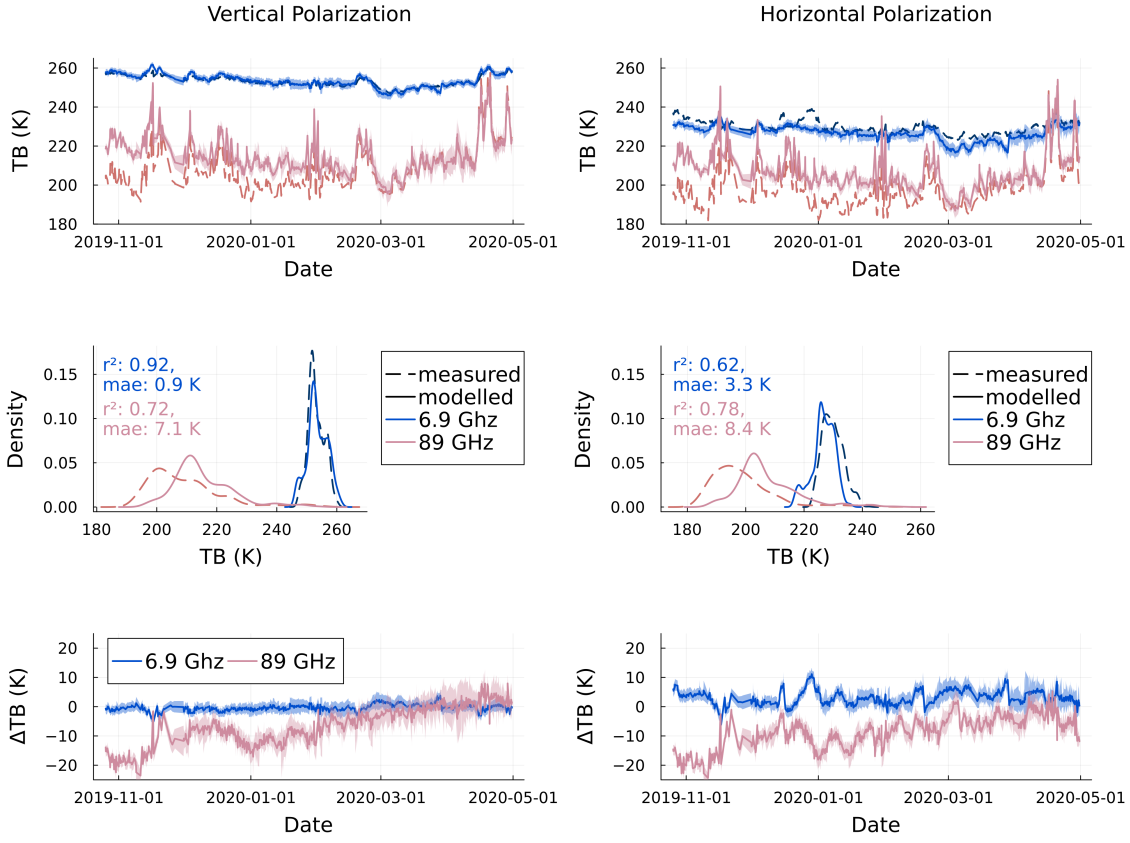

Figure 5.4: Modeled and measured brightness temperatures at 6.9 GHz and 89 GHz both vertically-polarized (left column) and horizontally-polarized (right column). First row shows satellite-based measurements of brightness temperature co-located to Polarstern (dashed lines) and modeled data using ground truth measurements as input (solid lines). The modeled data is given with a 1-σ uncertainty estimate derived from the ground truth uncertainties, see Table 5.3. In the center row, the distributions of modeled and measured brightness temperatures are plotted as probability density plots. Squared correlation coefficient (r^2) and mean absolute error (mae) are shown as annotations in the figure. The last row displays the difference between measured and modeled data, including uncertainty ribbon.

Table 5.3: *Ground truth* datasets used in the model evaluation and assumed variability for each parameter

Variable	Data source	Uncertainty estimate
SIC	classified synthetic-aperture radar (SAR) images (interpolated)*	1%
MYIF	classified SAR images (interpolated)*	5%
LWP+TWV	HATPRO radiometer (mean within ± 10 min)	temporal variability within ± 10 min
SST+WSP	R/V *Polarstern* (D-SHIP) (mean within ± 10 min)	temporal variability within ± 10 min
T_{sa}	surface IR thermometers** (mean within ± 20 min)	temporal (± 20 min) & spatial (four sensors) variability
SND+T_{si}	SIMBA (median of available daily-resampled buoys)	standard deviation of all buoys

* missing values replaced by mean.
** regression from T2m for cases with missing data.

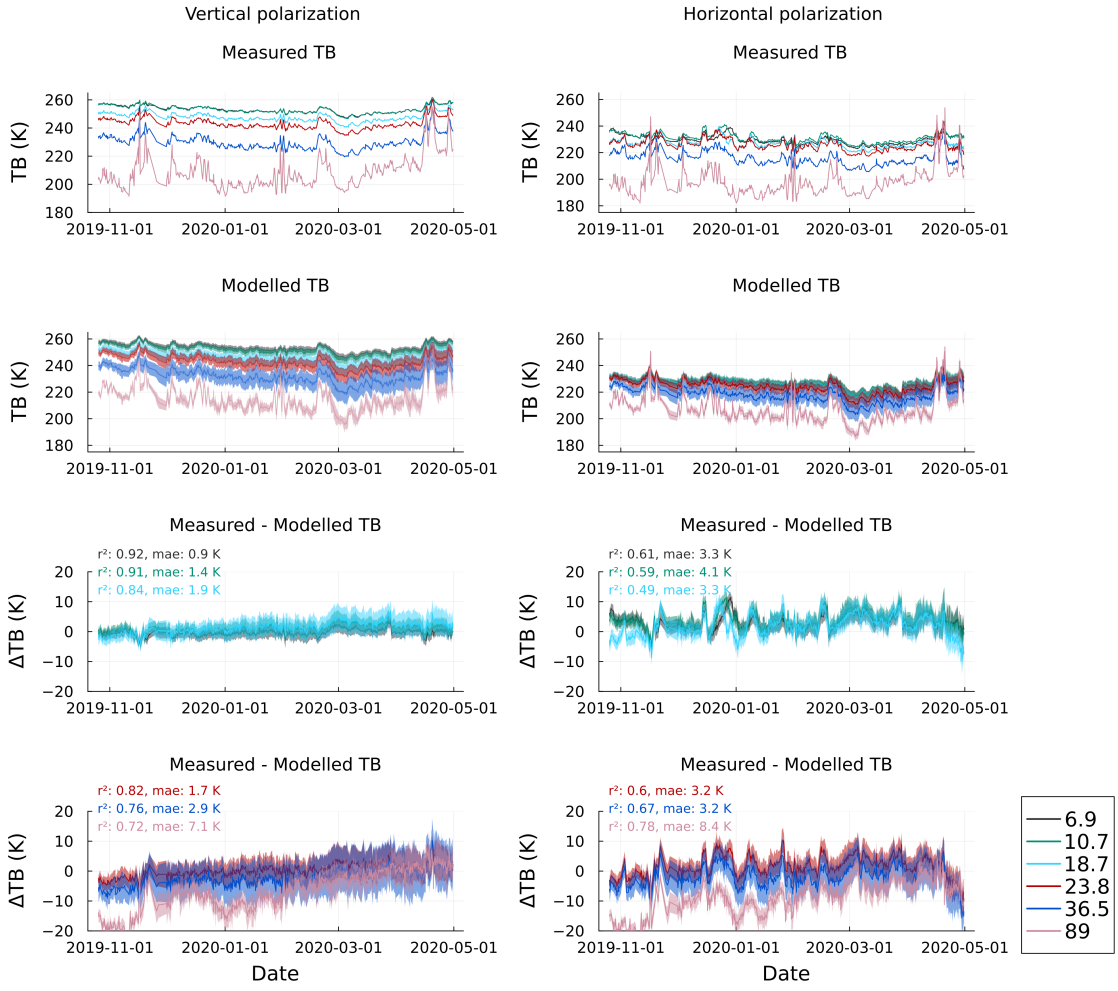

Figure 5.5: Time series of brightness temperatures both vertically-polarized (left column) and horizontally-polarized (right column): satellite-based measurements co-located to Polarstern (first row), modeled data using ground truth measurements as input (second) and the difference between measured and modeled data for the lower three frequencies (third row) and the higher three frequencies (fourth row). The modeled data is given with a 1-σ uncertainty estimate derived from the ground truth uncertainties, see Table 5.3.

5.4.2 Uncertainty Analysis: Effective Measurement Uncertainty $\mathbf{S}_e$

We now evaluate the uncertainties of the forward model further. The outcome will then serve as input to the inversion method (described in Chapter 2.2) for the satellite retrieval. One important quantity of the inversion method is the covariance matrix $\mathbf{S}_e$ which contains measurement but also model uncertainties. Following Maahn et al. (2020), we denote the forward model uncertainty as $\mathbf{S}_b$ and use an effective measurement uncertainty $\mathbf{S}_e = \mathbf{S}_y + \mathbf{S}_b$, where $\mathbf{S}_y$ accounts for the radiometric noise (NEΔT). We assume $\mathbf{S}_y$ to be 1 K for each frequency and polarization for $\mathbf{S}_y$ and no correlations. In order to get an estimation of the variability lost by fixing the model parameters like snow density and for evaluating the non-linearity of the model, we perform a sensitivity analysis to obtain $\mathbf{S}_e$. The effect on TB of certain parameters depends also on the retrieval parameters. Thus we scan the retrieval parameter space. For example, changes in ice salinity result in larger changes of computed TB if the ice temperatures are high. Therefore, we vary T_{sa} from 238 K to 270 K in steps of 1 K and snow depth from 0 cm to 40 cm in steps of 1 cm. The snow-ice interface temperature is chosen from a normal distribution with 1 K standard deviation around the value one obtains assuming thermal equilibrium (using ice and snow conductivities of $2.1\,\mathrm{W\,K^{-1}\,m^{-1}}$ and $0.31\,\mathrm{W\,K^{-1}\,m^{-1}}$, respectively). The analysis is done separately for first-year and multiyear ice.

We run 1000 simulations for each tuple of temperature, snow depth, and ice type, in which almost all layer parameters (listed in Table 5.2) are randomly chosen out of normal distributions that are truncated to constrain the parameter space to realistic values (Monte Carlo method). The standard deviation σ as well as upper and lower bound of these distributions can be found in Table 5.4. The mean values are the ones given in Table 5.2. We here focus on the surface emission model. Therefore, for estimating surface model uncertainties, downwelling brightness temperatures reflected at the surface are fixed to typical Arctic values for the six frequencies from 6.9 to 89 GHz ($T_D = (4, 5, 12, 22.5, 30, 70)K$). In the actual forward model and retrieval procedure downwelling brightness temperatures are calculated by the atmospheric model. The standard deviation of the resulting brightness temperatures is taken as a measure for the uncertainty that is introduced by fixing the parameters as described above.

With this method we obtain a diagonal covariance matrix $\mathbf{S}_b$. Note that, in principle, the uncertainties may be correlated, resulting in nonzero off-diagonal terms in $\mathbf{S}_e$ which would effect the weighting of the different TB channels in the cost function (Equation 2.37). Estimating these correlations is not straightforward, amongst others, a correlation may be conditioned on assumed values for other parameters, as discussed in, e. g., Cimini et al. (2018). For the time being, we therefore set the off-diagonal terms to zero, possibly introducing a bias.

The standard deviation of the TBs of all simulations (for all tuples of ice type, temperature, and snow depth) are plotted as violin plots in Figure 5.6 separated by ice type,

Table 5.4: Table with parameter ranges used in the simulations to estimate model uncertainty.Parameters are correlation length, ζ, density, ρ, salinity, and ice thickness d_{ice}. A single value means that this is used for all layers, while an array indicates different values for each layer starting from the upper layer. The snow salinity is not varied and for ice salinity only the upper two ice layers are varied

	Parameter	σ	lower bound	upper bound
Snow	ζ (mm)	0.06	0.05	0.35
	ρ (kg m^{-3})	[54,47,23]	180	420
Ice	salinity (only FYI) (ppt)	4.2	[0, 0]	[18, top layer value]
	d_{ice} (FYI/MYI) (m)	0.25/0.8	0.1/1.5	2.5/10
	ζ (FYI/MYI) (mm)	0.05	0.01	0.35
	ρ (FYI/MYI)(kg m^{-3})	35.7/23	800/800	975/975

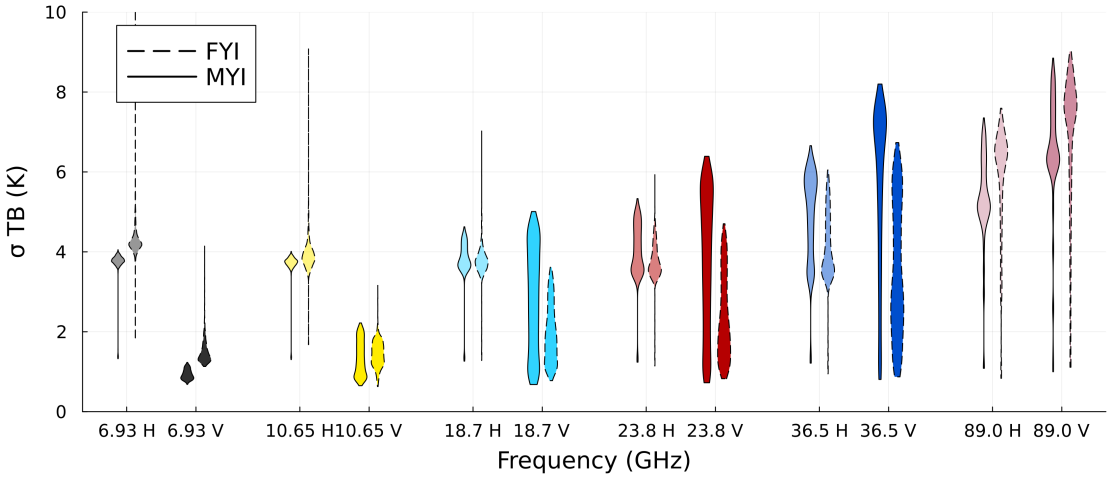

Figure 5.6: Sensitivity analysis for effective measurement covariance estimate. Shown are simulated standard deviations of 1000 simulations for each temperature and snow depth combination, separated by frequency, polarization and ice type. The violin plots show the 5th-95th percentile.

Table 5.5: Table with median of standard deviations (median σ) of simulated brightness temperatures taken together for the whole temperature and snow depth range and both ice types

Frequency (GHz)	Median σ (K) (H/V)
6.93	3.949/1.182
10.65	3.782/1.389
18.7	3.77/2.177
23.8	3.766/2.865
36.5	4.468/4.81
89.0	5.869/7.034

frequency and polarization. For each frequency, the median standard deviation (over both ice types) is listed in Table 5.5 and is used in the effective measurement covariance matrix $\mathbf{S}_e$ in the inversion method to include the model uncertainties as described above. We can see that for the low frequencies the uncertainty of modeled horizontally-polarized TB is higher than for vertically-polarized TB while it is the other way around for 36.5 GHz and 89 GHz. For the low frequencies, this was expected due to the Brewster effect.

In general, the uncertainty at vertically-polarized TB increases with frequency and is as high as 7 K for 89 GHz. Interestingly, the range of standard deviations is higher for vertically-polarized TBs. Depending on the frequency and polarization, different parameters are the dominant sources of uncertainty. For example, ice thickness and corresponding uncertainties of T_{si}, especially for large snow depth and high T_{sa} are important for vertical polarization and low frequencies, while snow density plays a major role for low-frequency horizontally-polarized TB. High frequencies like 89 GHz are especially sensitive to the snow correlation length. The interplay of parameter uncertainties is captured by our approach, for example, changes in salinity have a larger impact at high temperatures. In order to obtain reasonable results, a sensible choice of simulation ranges is key.

We observe about the same order of magnitude and frequency-dependence of the uncertainties compared to the mean differences of brightness temperatures modeled from ground truth vs. satellite measurements (described in the previous Section 5.4.1). Thus, the deviations between model and measurements can partly be attributed to the parameters of the model setup, i. e., better agreement could be obtained by adapting the model parameters accordingly and in a plausible range. We note however that the modeled uncertainties in this section for horizontally-polarized TB at 89 GHz are lower than the observed deviations. It is likely that additional model constraints play a role, which were not simulated here (e. g., scattering mechanisms, see next paragraph).

Additional Sources of Uncertainty The simulations serve both the understanding and identification of cases with higher uncertainty as well as giving a quantitative measure to adapt the effective error covariance matrix by including $\mathbf{S}_b$ so that it reflects the uncertainties of the model more accurately. However, it is important to keep in mind that not all restrictions of the model were simulated in this approach. There are additional sources of uncertainty. The most notable are:

- The number of layers (and thus the possibilities to resolve gradients of, e. g., temperature).
- The scattering mechanism, i. e., the parameterization of the scattering coefficient, as well as scattering anisotropy.
- The mixture model to calculate the effective permittivity of a composite material.

- Snow wetness which is important if temperatures are high (we consider freezing conditions only).
- Roughness of interfaces which we expect to have the largest effect on the highest frequency at 89 GHz.
- Uncertainties of the atmospheric model, which was not specifically developed for the polar atmosphere. Thus there are unknown model uncertainties. One known uncertainty is the cloud temperature which is now estimated to be half-way between the surface and freezing point temperature. From a simulation run of the MOSAiC time series with cloud temperatures one time fixed at $-30\,^{\circ}\mathrm{C}$ and one time at $10\,^{\circ}\mathrm{C}$ we conclude that the low frequencies have very low sensitivity to the cloud temperature. Here, we observe the largest effect for 89 GHz of the order of below 1 K.

5.5 Retrieval: A Priori Information

For the retrieval, the forward model that has now been introduced and evaluated is inverted using an optimal estimation method. The method is described in detail in Chapter 2.2 and the a priori information that is needed is introduced in the following.

A Priori State $\mathbf{x}_a$

As a priori state, we use climatological monthly data based on different datasets, all on a regular lat-lon grid of 0.25 degrees. In the retrieval, the values from the closest grid cell are chosen and linear interpolations between subsequent months are performed. For LWP, WSP, SST, SIC and TWV we use monthly mean values based on ERA5 reanalysis data from 1990-2019. From that data, we also obtain T2m that is then converted to T_{sa} by a seasonally varying regression given in Nielsen-Englyst et al. (2021). Snow depth (SND) a priori estimates are based on the merged Warren-AMSR2 climatology (Section 5.2.4). For multiyear ice fraction we use the multiyear ice satellite product based on microwave radiometer and scatterometer data (Section 5.2.3) and compute monthly averages for the years 2013-2022. The a priori snow-ice interface temperature of first-year ice is based on monthly data of vertically-polarized TB at 6.9 GHz (TB6V) from 2013-2022 of daily AMSR2 data, which is modified for multiyear ice according to an empirical fit (Equation 16 in Tonboe et al. (2011)). Using the a priori multiyear ice fraction, a weighted average of T_{si} is calculated. Due to different time spans (30 years of ERA5, but 10 years of TB6V), inconsistencies might arise. Thus, wherever T_{si} is below T_{sa}, we assume an isothermal snowpack with $T_{si} = T_{sa}$ as a priori estimate.

A Priori Covariance $\mathbf{S}_a$

For the time being, we assume no correlations yielding a diagonal covariance matrix. The values that we use are given in Table 5.6 in the last column. The values are based on Scarlat et al. (2017,0) and are chosen large enough for the new retrieval parameters to allow deviations from the a priori state.

Temporal Variability The current implementation assumes no temporal, for example seasonal, dependence of the variances and covariances. Future improvements of the method might be achieved by taking the seasonality of the variances into account. For example, water vapor has a low natural variability in winter that increases towards spring.

Correlations Currently, the method is biased towards no correlations between the geophysical parameters as the off-diagonal entries of $\mathbf{S}_a$ are set to zero. One major challenge when introducing correlations is their dependence on the actual state. For example, we expect higher correlations of temperature and water vapor over open ocean than over sea ice, where the amount of water that can evaporate is limited. Implementing this in the current optimization is not justified as we would introduce covariance matrices where the entries would differ for every iteration. This is of particular importance for the marginal ice zone.

Start guess

The start guess $\mathbf{x}_0$ is given by the a priori state vector, except for SIC, MYIF and T_{si}. The two ice parameters are computed using the NASA TEAM (Cavalieri et al., 1984,9) algorithm with tie points originally developed for SSMI sensors (Comiso et al., 1997) using the brightness temperatures at 36.5 GHz and 18.7 GHz. For T_{si} we apply the fit given in Equation 16 in Tonboe et al. (2011) using the vertically-polarized brightness temperature at 6.9 GHz as input.

Table 5.6: Source of a priori state x_a (from climatology) and a priori covariances given by standard deviation σ for all retrieval parameters

Parameter	x_a	σ
Sea ice concentration (SIC)	ERA5 climatology	20 %
Multiyear ice fraction (MYIF)	ASCAT/AMSR2 satellite product	20 %
Snow depth (SND)	merged Warren-AMSR2 climatology	0.2 m
Snow-ice interface temperature (T_{si})	(modified) AMSR2 TB6V climatology	8 K
Snow-air interface temperature (T_{sa})	Regression based on ERA5 climatology	10 K
Sea surface temperature (SST)	ERA5 climatology	6.93 K
Total water vapor (TWV)	ERA5 climatology	4.69 mm
Liquid water path (LWP)	ERA5 climatology	0.14 mm
Wind speed (WSP)	ERA5 climatology	$5\,\mathrm{m\,s^{-1}}$

5.6 Retrieval Evaluation

In this section we evaluate the retrieval output with the help of observational data. We start with an extensive comparison is performed using the MOSAiC datasets. Then, we focus on three of the four protagonists, SIC, SND, and LWP, and compare them to additional *ground truth* datasets. A special focus is put on water vapor, the fourth protagonist, in the next chapter where we use campaign and land station data for further evaluations. In a next step we analyze the Arctic-wide retrieval output. First, by looking at spatial patterns of the retrieval output parameters, their uncertainties and the differences between simulated and measured brightness temperatures for one day, and second we compare monthly data to reference products from other satellite retrievals or reanalysis for a qualitative assessment. Again, water vapor will not be treated here but instead in more depth in Chapter 6.

5.6.1 MOSAiC Expedition

When we apply the inversion method on the co-located satellite data during MOSAiC, we retrieve parameters as shown in Figure 5.7. For all cases, the convergence criterion is met. The degree of nonlinearity given by Equation 2.40 is close to unity, except for the warm air intrusions in April and in the end of April. The uncertainty estimate given by Equation 2.39 is shown as the 1-σ shaded area around the maximum a posteriori solution (blue line). It is clear that the method does not reproduce the a priori (shown as green line) in most cases, but instead converges to a different value (most drastically visible for snow depth). Most of the time, the observed values lie within the retrieval uncertainty. Notable is the sensitivity to LWP, where many events with high LWP are detected by the retrieval method.

The variability of T_{sa} is not captured well in the retrieval, and the values stay close to the a priori. This is likely due to the lower weights on the high frequencies (high values in the effective measurement covariance matrix $\mathbf{S}_e$) that are more sensitive to that parameter. On the other hand, due to the high weight on 6.9 GHz and strong correlation of this channel with T_{si}, the evolution of this quantity is well captured by the retrieval. The short-term fluctuations in retrieved snow depth are not realistic. The constraints on SND are rather loose so the method might use the snow depth parameter to counterbalance deviations in simulated and measured TB but overall, the retrieved snow depth is a better estimate than the a priori.

For total water vapor, the agreement is good. Special events like the two warm air intrusions in April 2020 (visible as peaks in the time series), described in Kirbus et al. (2023), are well represented in the retrieved data. Figure 5.8 shows the good correlation (squared Pearson coefficient: 0.7) and low bias ($0.18\,\mathrm{kg\,m^{-2}}$) between satellite retrieved values of total water vapor and the ship-based measurements. In comparison to the previ-

ously used version of the retrieval (using empirical emissivities (Scarlat et al., 2017)), we note a reduction of bias and increase of correlation (see Figure 5.1).

5.6.2 Sea Ice Concentration: Round Robin Data Package

Using the confirmed scenes of 100% SIC in the Round Robin Data Package (RRDP) (Section 5.2.5) from October-May (including observations from the predecessor AMSR-E sensor) shows that our retrieval method has an accuracy and precision similar to or even better than many other common sea ice concentration algorithms (Ivanova et al., 2015): we retrieve 100% SIC with a mean bias of 0.4% and a standard deviation of 1.5%. The sample size is 216,999. Note, however, that our method truncates SIC to 100% and does not allow SIC values $> 100\%$. That effects intercomparisons and evaluations of SIC products as discussed in Kern et al. (2019) and mentioned in this thesis in Section 4.1.2. For a fair comparison to other products, a systematic overestimation of our method would need to be checked. Using all available data from the dataset (years 2007–2019) including the melting season (without adapting the model or inversion method), we retrieve 100% SIC with a mean bias of 1% and a standard deviation of 3.8%, i. e., decreasing accuracy and precision compared to the winter only case. The sample size is 265,785.

The RRDP also contains confirmed scenes of ice-free ocean, i. e., 0% SIC. From October-May, we retrieve 0% SIC with a mean bias of 1.7% and a standard deviation of 2.5%. The sample size is 44,553. Using all available data from the dataset (year 2007–2019) North of 50°N, including the melting season, we retrieve 0% SIC with a mean bias of 1.5% and a standard deviation of 2.1%, i. e., increasing accuracy and precision compared to the winter only case. The sample size is 79,640.

5.6.3 Snow Depth: Operation Ice Bridge

Here, we use Operation Ice Bridge snow depth observations as contained in the RRDP. Note that the majority of flights is over multiyear ice. When we compare the probability density functions (PDFs) of retrieved and observed snow depth values in Figure 5.9, we observe a positive bias of around 6 cm for the retrieved snow depth. The width of the retrieved and observed snow depth PDFs are similar. The retrieved PDF, however, shows an indication of a bi-modal distribution not seen in the observations. The retrieved snow depth PDF shows a clear improvement over the a priori snow depth. The sample size is 530.

5.6.4 Liquid Water Path: Utqiaġvik Land Station

We extend the comparison of our cloud protagonist beyond the MOSAiC measurements using the LWP dataset from the ARM site in Utqiaġvik (see Section 5.2.6). We only take measurements that pass the quality check as good data and compare them to satellite

overpasses that we average within a 50 km radius. In order to account for the variability of LWP within the footprint we compare the spatially averaged retrieval data to 10-minute temporal averages of the ground-based observations.

The large number (over 15,500) of co-located data points enables a comparison of the distributions. Figure 5.10 shows the relation of observation and retrieval in a kernel density estimate plot. Most of the observations are over sea ice (high SIC). The mean bias is $-0.02\,\mathrm{kg\,m^{-2}}$ which is less than 10 %. However, we observe a low correlation of 0.2. The difference in the distributions is evident in Figure 5.11. While the observed LWP is a heavily tailed distribution that can be described by a lognormal or Weibull distribution (Huang et al., 2014), the distribution of the satellite observations are very different in the third and fourth moment (skew and kurtosis) and show larger values for LWP when the ground-based observations are actually very close to zero. Figure 5.12 reveals that this overestimation of LWP is especially pronounced in November and December, while in May the satellite retrieved values are lower than the ground-based observations.

We face again the *curse of remote sensing* because our satellite measurements are taken over the (frozen) ocean[1], while the ground-based measurements are taken over land and might not be representative of the satellite footprint. In future comparisons this uncertainty could be reduced by taking wind directions and related horizontal water vapor transport into account. For now it remains an open question to what extent the assumption of Gaussian PDFs in the inversion method (see Chapter 2) is a limiting factor in the retrieval of quantities like LWP whose distributions are not adequately described by Gaussians. Retrievals of liquid water path from space-based passive sensors in general still carry large uncertainties (Devasthale et al., 2020). The one presented here is no exception.

[1]that is, we use the land mask contained in the satellite product to mask out land observations.

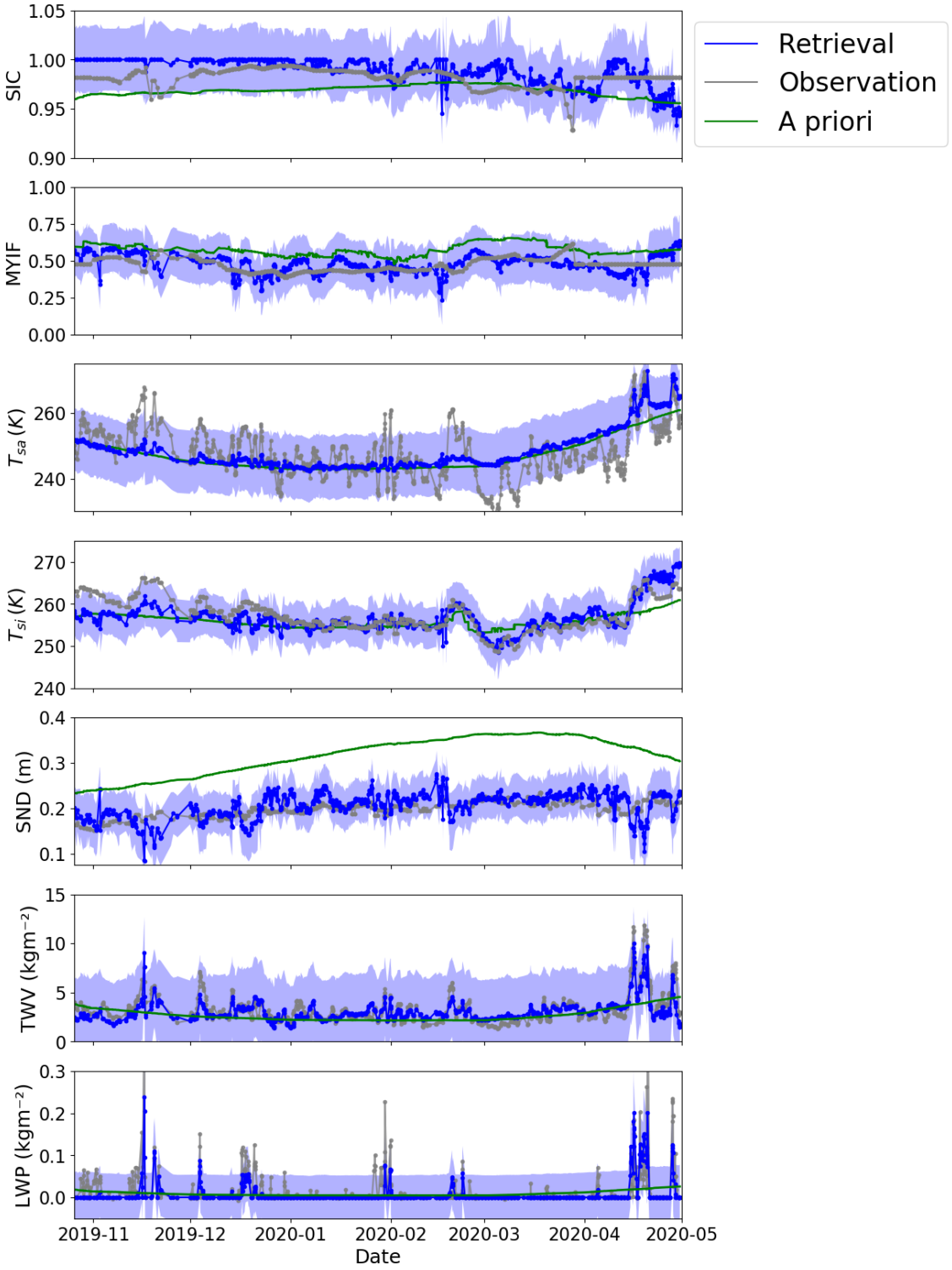

Figure 5.7: MOSAiC time series of retrieved parameters (blue) with their uncertainties (shaded areas), additionally the ground truth observations as described in Table 5.3 (grey line) and the a priori data (green line) is shown. Note that we do not display the full observational datasets, but only the part co-located with satellite measurements. The following seven quantities are displayed: SIC: sea ice concentration; MYIF: multiyear ice fraction; T_{sa}: snow-air interface temperature; T_{si}: snow-ice interface temperature; SND: snow depth; TWV: total water vapor; LWP: liquid water path.

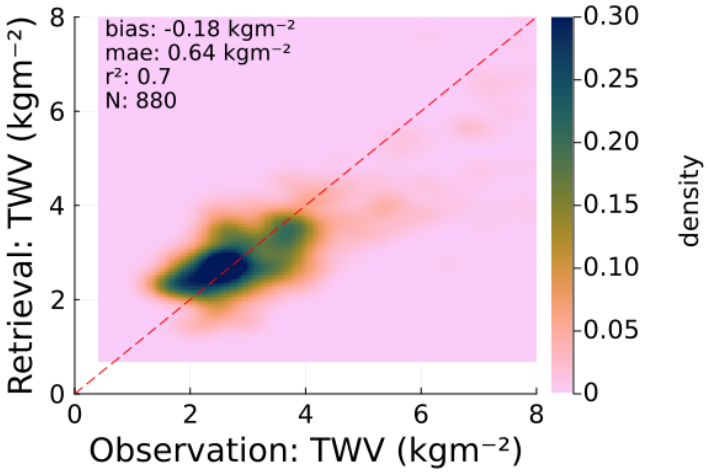

Figure 5.8: Scatter plot of retrieved total water vapor using the emission model vs. MOSAiC measurements from the co-located dataset. Included in the plot are bias, mean absolute error (mae) and the coefficient of determination given by the squared Pearson correlation coefficient, i. e., r^2.

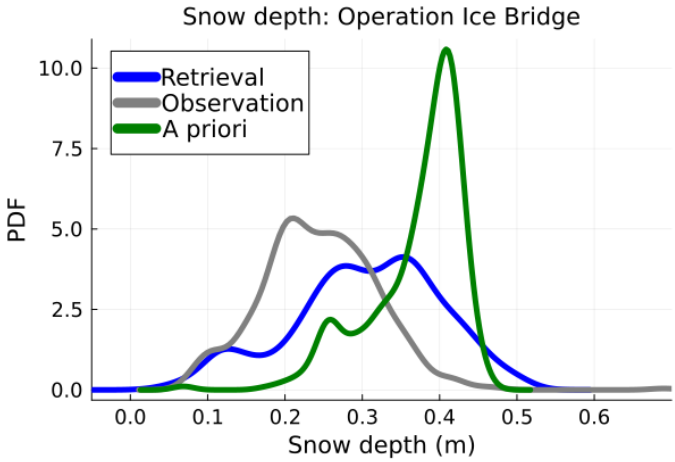

Figure 5.9: Density plot of snow depth data. Shown are observations from Operation Ice Bridge included in the Round Robin Data Package (grey), corresponding retrieved values (blue) and the a priori values used in the retrieval (green).

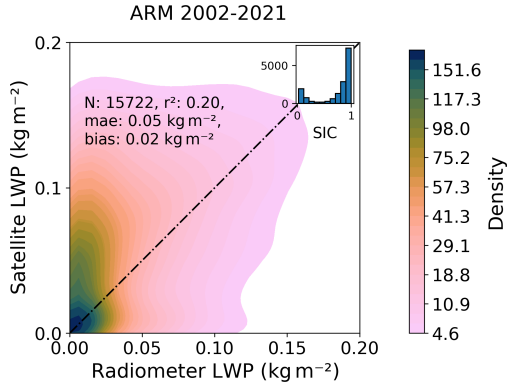

Figure 5.10: Kernel density estimate plot of ground-based observation of liquid water path (LWP) vs. co-located satellite retrieval of LWP at the Atmospheric Radiation Measurement (ARM) program site near Utqiaġvik. Inset is a histogram of the corresponding retrieved values for sea ice concentration (SIC).

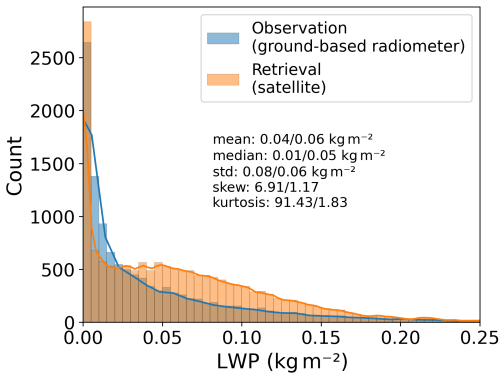

Figure 5.11: Histograms of all co-located observations of liquid water path (LWP) from the ground (blue, radiometer) and from space (orange) at the observation site near Utqiaġvik. Statistical parameters (mean, median, standard deviation, skewness, and kurtosis) are given in the annotation for the ground-based/satellite LWP distributions.

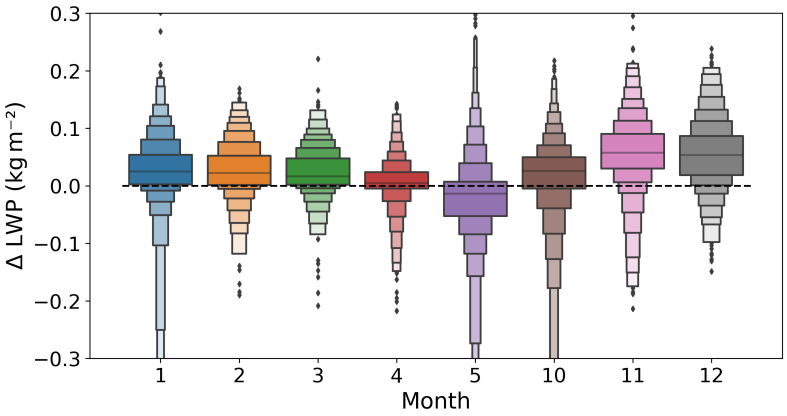

Figure 5.12: Letter-value plot of the difference between co-located satellite retrieval and ground-based observation of liquid water path (LWP) at the observation site near Utqiaġvik ordered by month. The line is displaying the median, and the data is grouped in boxes for each pair of adjacent letter values (Hofmann et al., 2017). The width of the boxes is proportional to the number of points in it.

5.6.5 Arctic-wide Retrieval Evaluation

Daily Arctic-wide Retrieval

We run the retrieval on satellite swath data of a whole day and the retrieval parameter are then resampled by Gaussian resampling using NSIDC's Polar Stereographic Projection (NSIDC, 2023) with a nominal gridded resolution of 12.5 km by 12.5 km to obtain maps on a pan-Arctic scale. One example for January 10, 2020 is shown in Figure 5.13, one for April 19, 2020 in Figure 5.14, the time when warm and moist air from the North Atlantic intruded into the central Arctic (Kirbus et al., 2023). The convergence rate is above 98%. The sea ice extent is well captured (compared to ERA5, see Figure C.1 in the Appendix).

The spatial distributions of multiyear ice fraction and snow depth are plausible, with higher values in the Canadian Arctic. The distribution of snow-air interface temperatures and snow-ice interface temperatures are within expected ranges.

Higher values of total water vapor and liquid water path over the open sea are observed as we can expect it. In some areas, the artificial gradients of TWV and LWP with respect to the ice type are still visible, but are a lot less pronounced than for the previously used version of the retrieval (see Figure 5.2). The warm and moist air intrusion on April 19, 2020 is also well seen in the retrieved elongated filament of high values of LWP and TWV. Some areas over first-year ice (e. g., Chukchi Sea around Bering Strait, Laptev Sea) exhibit higher values than the reanalysis ERA5 as discussed later in Section 5.6.5.

Spatial Distributions of Uncertainties

When we investigate the retrieval uncertainty given by $\hat{\mathbf{S}}$ (see Equation 2.39) with respect to water vapor (Figure 5.15) we see clearly higher uncertainties over the sea ice (middle), where the uncertainties over MYI are slightly lower than over FYI. Compared, however, to the a priori uncertainty of $4.69\,\mathrm{kg\,m^{-2}}$ we see an improvement also over ice, seen as values smaller than one in the ratio of retrieved to a priori uncertainty (Figure 5.15, right). Such tests help in the identification of areas of higher uncertainties, in this example the Russian Arctic with younger ice around 150°E.

The distribution of uncertainties of SIC, SND, and LWP are shown in the Appendix C.2. For SIC and LWP the retrieval uncertainties are again lowest over the open ocean, are only slightly higher over MYI and highest over FYI. For SND the retrieval uncertainties over ocean (where the retrieved SIC is below 15%) are masked out. Interestingly, there are areas (in this examples the Kara Sea) with very low retrieval SND uncertainties (below 5 cm). Overall the biggest improvement (lowest values in the ratio of retrieved to a priori uncertainty) is found for SIC. In the next section, the retrieval output will be compared to reference datasets, which will help to further estimate uncertainties.

Hitting the Boundary: Shortfall of the Retrieval

When investigating the Arctic-wide data, we found areas with very high snow depth (50 cm), see for example Appendix, Figure C.3, marked by a red rectangle. Here, the inversion method retrieves the upper limit of allowed snow depth. The deviations between modeled and measured TB, see Figure 5.16, reveal an overestimation of TB by the model in that area, especially in the higher frequency channels. This pattern is persistent over the whole month.

In order to compensate for high TB, the inversion method increases SND which decreases modeled TB. Because the variance of SND in the covariance matrix $\mathbf{S}_a$ is high ($0.04\,\mathrm{m}^2$), the method allows rather large deviations from the a priori SND. In the current implementation there is an upper bound of 50 cm for SND. When we increase this upper limit, even higher SND is retrieved and the overestimation of TB at 18.7 GHz and 23.8 GHz vanishes for the vertical polarization and decreases for the horizontal polarization at these frequencies as well as for both polarizations at 36.5 GHz (not shown).

The high SND areas also correspond to low values for the atmospheric variables (low TWV and LWP also decrease modeled TB).

The problem of the forward model to simulate the low observed TB suggests that it does not fully cover the range of sea and ice conditions leading to certain TB, possibly even beyond the parameter uncertainties discussed in Section 5.4.2. It is also possible that the inversion method fails to find the correct minimum of the cost function. For a small test sample of cases where the method retrieves these high values of SND, the degree of nonlinearity is, however, mostly close to unity and other optimization techniques (for example the Nelder-Mead method) did not find different minima for that test sample. More research is needed to improve the model and inversion setup which will be further discussed in Chapter 7.

For now, the retrieval runs where SND 'hits' the upper boundary are flagged as being more uncertain and are excluded from the following analyses. For daily gridded data on an Equal-Area Scalable Earth (EASE) grid with a spatial resolution of 25 km about 1.3% of the data is hereby removed on average. However, in certain years and months, this percentage is above 5%, namely in October to December 2002, in October to December 2004, February to April 2005 and October 2018. Further investigations of these particular time periods and areas may help to refine the search for possible reasons of the shortfall of the retrieval in these situations.

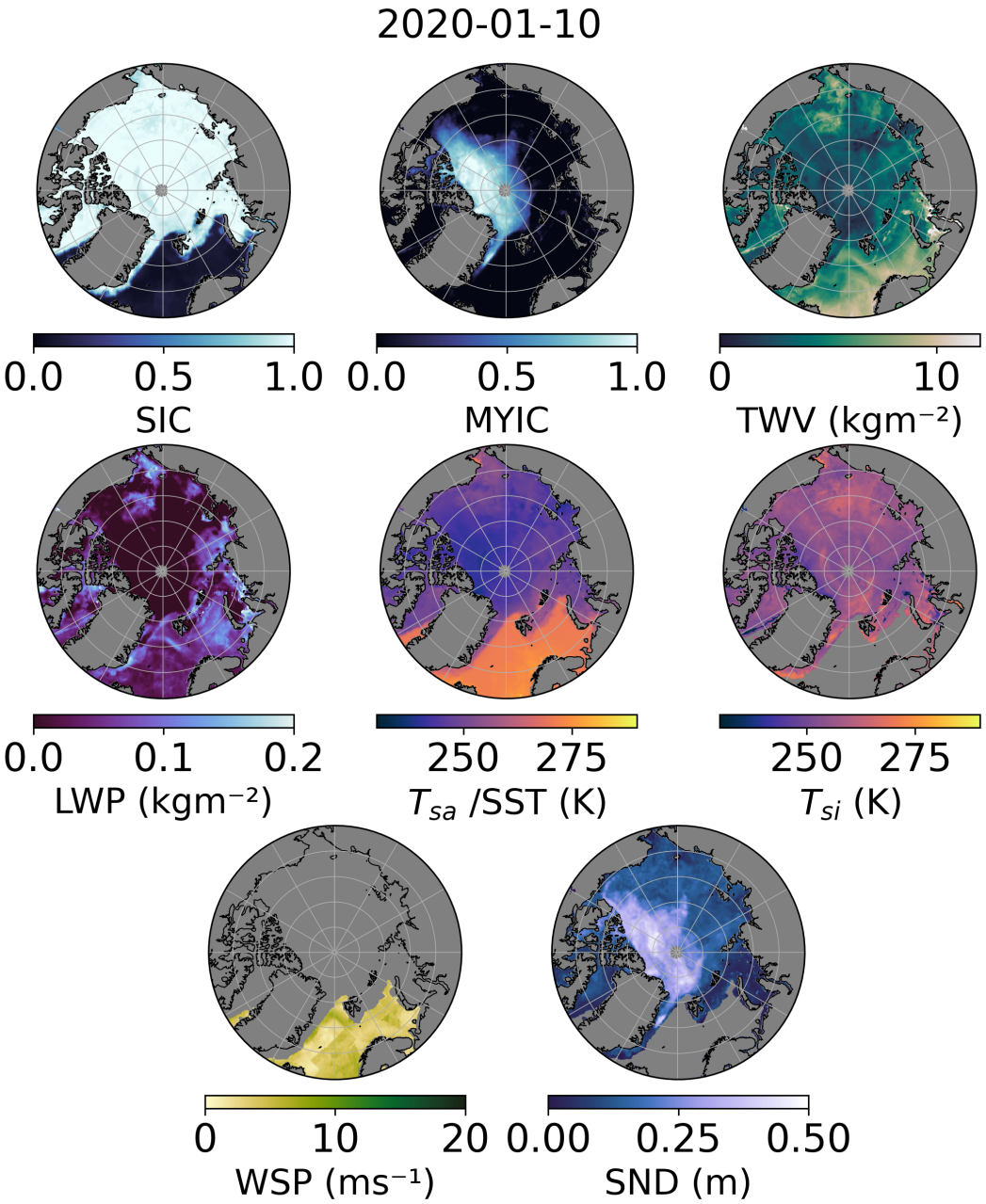

Figure 5.13: Retrieved parameters, gridded and resampled from daily AMSR2 swath data from January 10, 2020. Shown are sea ice concentration (SIC), multiyear ice concentration (MYIC) obtained by multiplying the multiyear ice fraction with SIC, total water vapor (TWV), liquid water path (LWP), the surface temperature as average (weighted by SIC) from the snow-air interface temperature T_{sa} over ice and the sea surface temperature (SST) over open water, the snow-ice interface temperature (T_{si}, shown only in areas where SIC > 15%), as well as wind speed (WSP, shown only in areas where SIC < 15%) and snow depth (SND, shown only in areas where SIC > 15%).

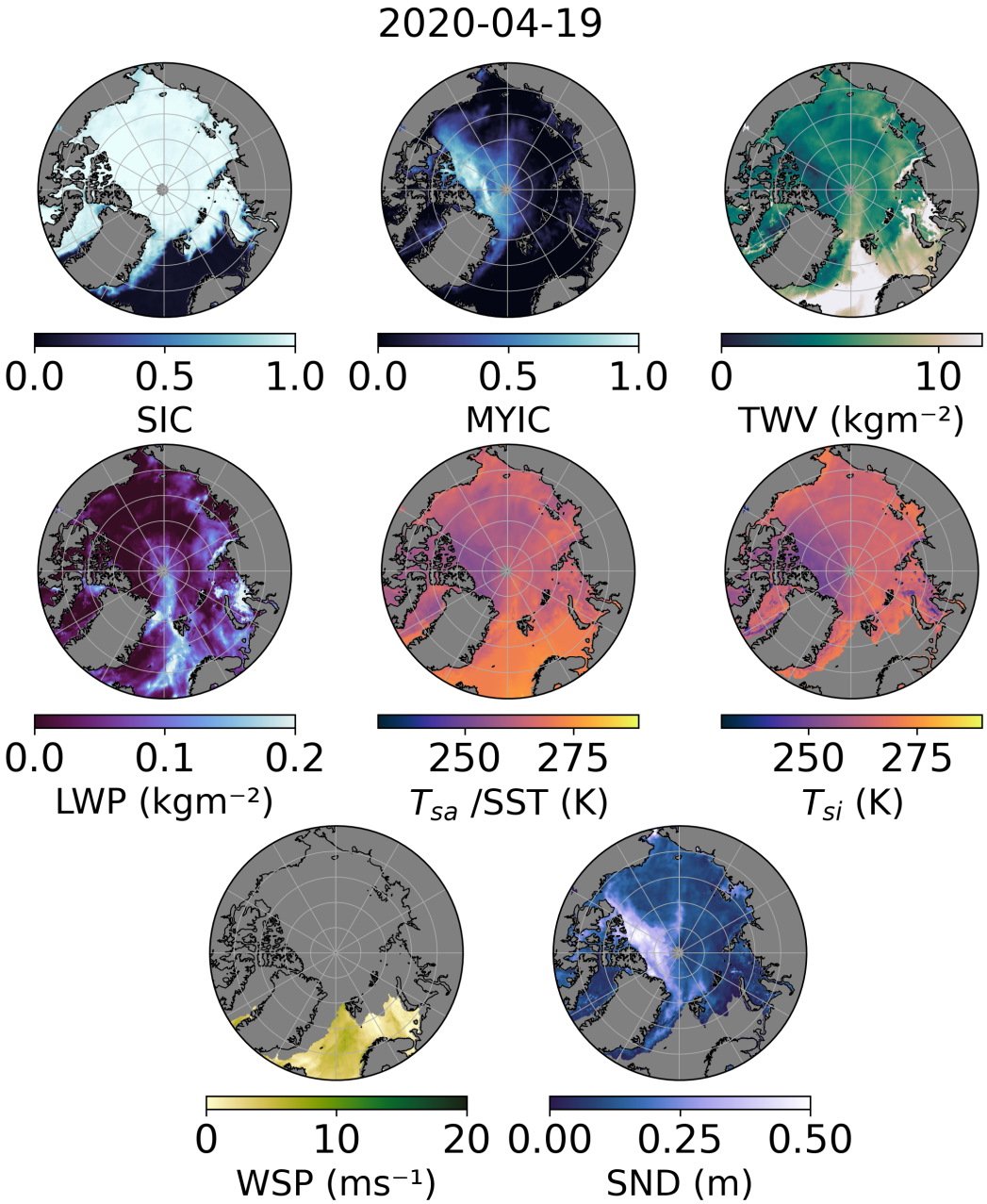

Figure 5.14: Retrieved parameters, gridded and resampled from daily swath data as in Figure 5.13 but from April 19, 2020.

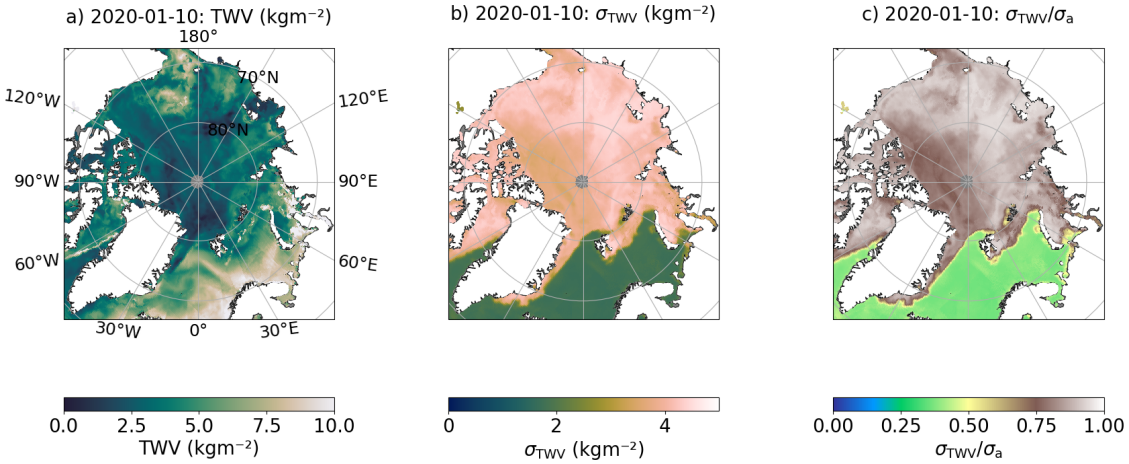

Figure 5.15: Daily gridded map of retrieved total water vapor (left) for January 10, 2020, retrieved uncertainties of TWV as one standard deviation (center) and the ratio of retrieved uncertainty to the a priori uncertainty (right).

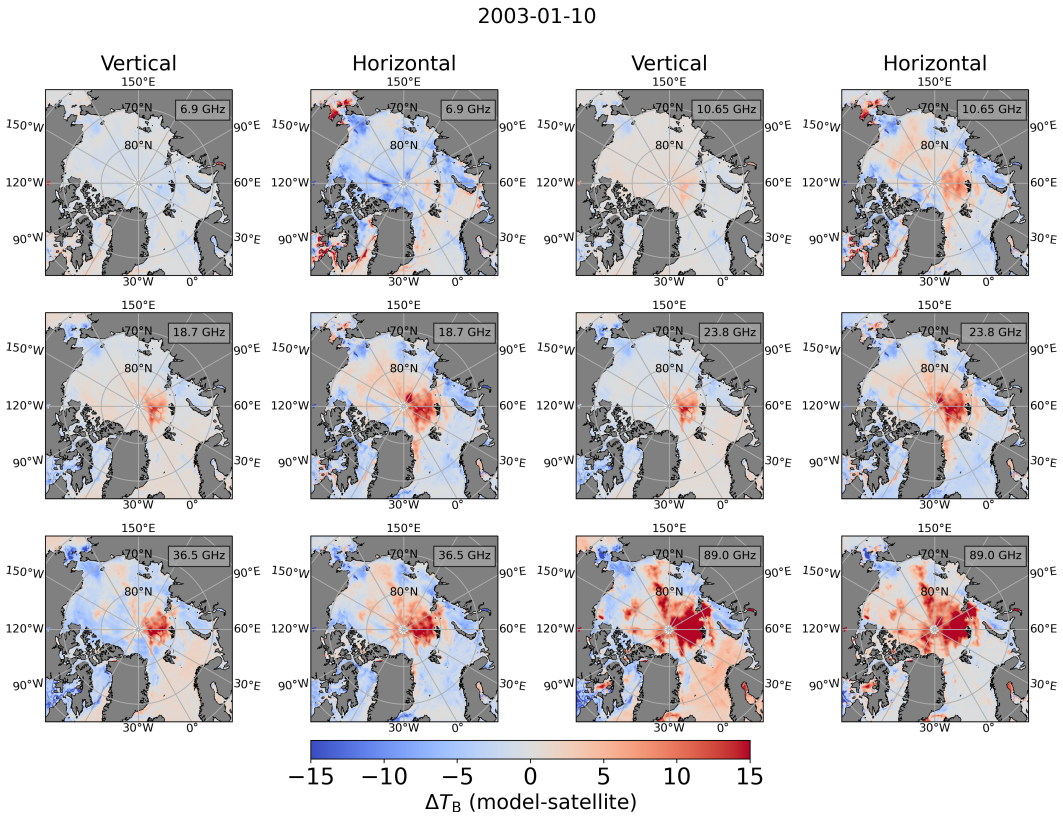

Figure 5.16: Daily gridded map of differences between modeled TB and measured TB

Sea Ice Concentration, Snow Depth, and Liquid Water Path: Pan-Arctic and Monthly

In this section we compare monthly maps of the retrieved parameters SIC, SND and LWP to reference datasets described below for each parameter. For each parameter we show the months October, January and April for the winter season 2018 – 2019[2]. Maps of retrieved MYIF, T_{si} and T_{sa} can be found in the Appendix C.5.

The maps are produced from averaging the daily data on an EASE grid with a spatial resolution of 25 km. The reference datasets are kept on their native grid for plotting but are resampled to the EASE grid for calculating mean biases. Note that the reference datasets themselves carry uncertainties, that, for example in the case of SND and LWP, are not even fully assessed yet. While we believe that analyzing differences between reference datasets and the multi-parameter retrieval output are a reasonable way to estimate uncertainties, we do not claim that the reference datasets are the *ground truth*.

For TWV a more extensive comparison and evaluation is performed in Chapter 6.

Sea Ice Concentration As reference dataset we use the ASI sea ice concentration product described in Chapter 4.1.2.

The comparison in Figure 5.17 shows spurious ice in the areas that are ice-free ocean in ASI and lower estimates of SIC in the high ice concentration regime. For the open ocean areas, averaged over grid cells with SIC less or equal to 15%, the retrieved SIC is between 6.3% (May) and 8.3% (January) higher than the ASI SIC with a low mean standard deviation of the residuals, $\sigma_{\text{res.}}$, of 1.4%. This is greater than the retrieval uncertainty (not shown), which ranges between 3.4% (December) and 4.1% (May). Here, we believe the ASI SIC product to be more reliable as we do not expect sea ice for example South of Svalbard or even Iceland in October. Stricter constraints, implemented in terms of lower variances of SIC in $\mathbf{S}_a$ (see Section 5.5), will likely improve the results. As this thesis focuses on the ice-covered ocean, refining the retrieval over open ocean will not be pursued further here.

Over sea ice, the differences are smaller but $\sigma_{\text{res.}}$ is larger. The retrieved SIC is, averaged over grid cells with SIC higher 15%, between 0.5% (bias October) and 1.8% (bias March) lower than the ASI SIC with a mean $\sigma_{\text{res.}}$ of 6.4%. Mean absolute deviations are in the range of 3.1% (January) to 7.1% (October). Average retrieval uncertainties range between 2.8% and 4.1%. Based on the comparison to ASI this uncertainty estimate should be raised to a more conservative estimate of the retrieval uncertainty of the order of at least 7%.

Snow As reference dataset for SND we use the snow depth product described by Kwok et al. (2020) and available via Kwok (2020). It is based on differencing satellite lidar

[2]This time period was picked because of the availability of the snow depth data.

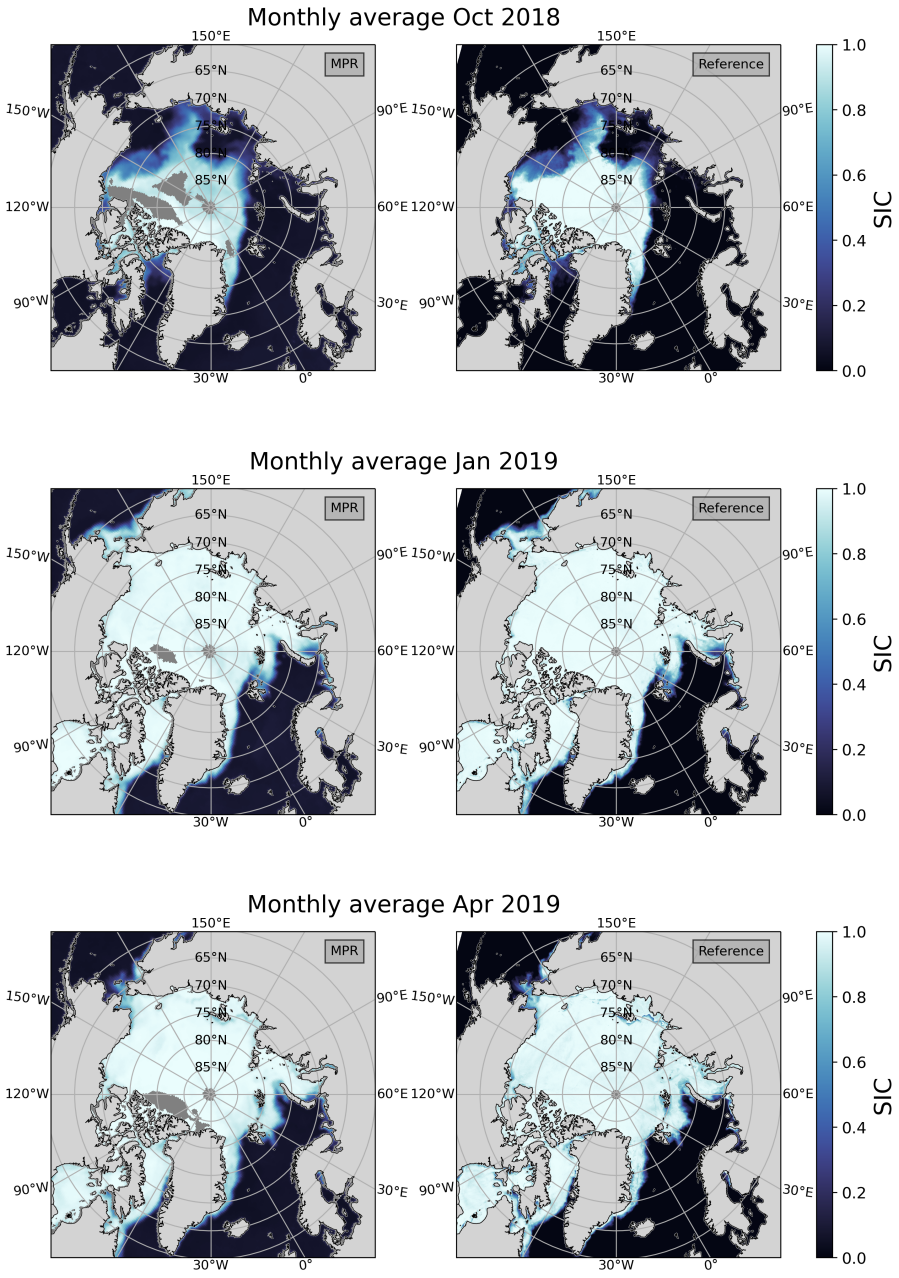

Figure 5.17: In comparison, maps of monthly average of sea ice concentration (SIC) from the multi-parameter retrieval (MPR, left) and from the reference ASI SIC satellite product (right).

(ICESat-2) and radar (CryoSat-2) freeboards and the available product is bounded by the gateways into the Pacific Ocean, the Canadian Arctic Archipelago, and the Greenland (Fram Strait) and Barents Seas. The two datasets are shown in Figure 5.18. While there is resemblance in spatial patterns between the two datasets, the retrieved SND is higher than the reference data, especially in October.

The mean absolute deviation in October is 12 cm with a large range of differences ($\sigma_{\text{res.}}$ yields 9 cm). In October, the average retrieval uncertainty, averaged over grid cells with SIC higher 15%, is highest amongst the months with 11 cm. The differences between the retrieved SND and the reference data decrease over the months. In January the retrieved SND is still higher than the reference but only by 6 cm (mean absolute error (mae)), and the spread also decreased to a $\sigma_{\text{res.}}$ of 6 cm. The values of the following months are similar. Also the retrieval uncertainty reduces to about 7 cm for all months other than October. This uncertainty estimate agrees with the comparison to the reference SND for January to March but should be raised to a more conservative estimate of the retrieval uncertainty of at least 10 cm for October to December.

We also note that the spatial distribution resembles the one from the MYIF, see previous paragraph. This is physically plausible as MYI is present from the beginning of the season and has more time to accumulate snow. However, some differences can be found, for example higher snow depth values around Wrangel Island (at 180°E between Chukchi and East Siberian Sea) in April that also appear in the reference data but not in the MYIF (see Section C.5).

Research is under way to evaluate the snow depth retrieval further and quantitatively.

Liquid Water Path From the European Centre for Medium-range Weather Forecasts (ECMWF) fifth generation reanalysis ERA5 (Hersbach et al., 2020) we use the total column cloud liquid water variable as reference. From the hourly reanalysis data we derive monthly averages shown in Figure 5.19.

Overall, both datasets show higher values of LWP over open ocean than over sea ice. The order of magnitude ($10^{-2}\,\mathrm{kg\,m^{-2}}$) of the retrieval and reanalysis is the same for all months but December, January, and February. In December, January and February, retrieved LWP is higher than the reanalysis over sea ice: mean December values over areas with retrieved SIC larger 15% are $0.052\,\mathrm{kg\,m^{-2}}$ in the retrieval but only $0.009\,\mathrm{kg\,m^{-2}}$ in the reanalysis. The standard deviation of LWP over sea ice is in general larger in the retrieval data than in the reanalysis data, in several months even by an order of magnitude (October, February, and March, $10^{-2}\,\mathrm{kg\,m^{-2}}$ versus $10^{-3}\,\mathrm{kg\,m^{-2}}$). Thus, considering monthly data, the retrieval LWP is spatially more heterogeneous over sea ice than the reanalysis. Over ocean, the retrieval is mostly higher than the reanalysis with a mean bias ranging between $0.033\,\mathrm{kg\,m^{-2}}$ (December) and $0.015\,\mathrm{kg\,m^{-2}}$ (February). The $\sigma_{\text{res.}}$ is about $0.013\,\mathrm{kg\,m^{-2}}$ for all months. Over ice, the deviations vary from month to month.

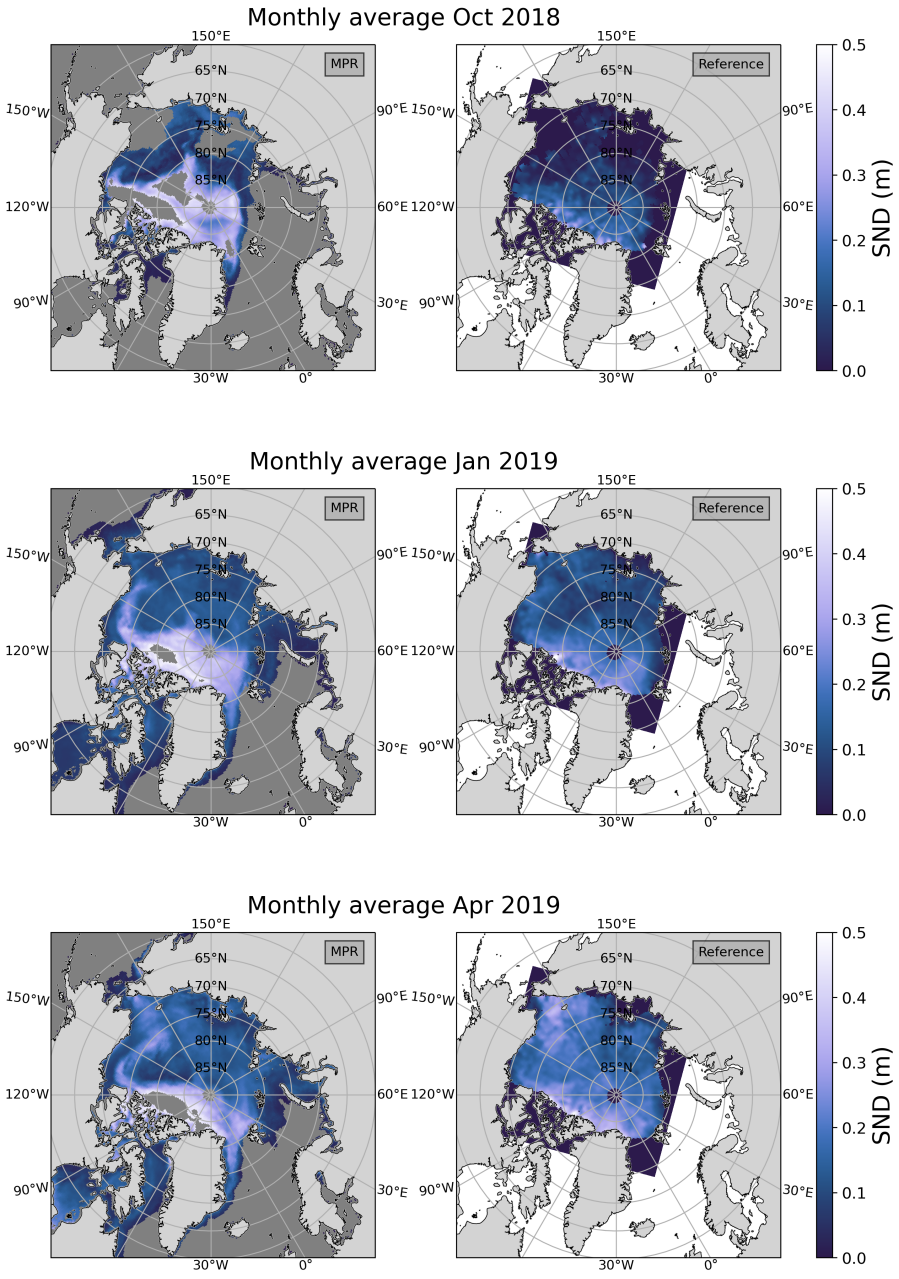

Figure 5.18: Maps of monthly average of retrieved snow depth (SND; left) from the multi-parameter retrieval (MPR) compared to the reference SND product based on lidar and radar satellite data.

While the retrieval is higher than the reanalysis in some areas (mostly over FYI or in the marginal ice zone (MIZ)) it is lower in other areas (mostly over MYI) in October and November (mean absolute deviations over sea ice are $0.051\,\mathrm{kg\,m^{-2}}$ and $0.047\,\mathrm{kg\,m^{-2}}$, respectively). In April the differences are smallest (mean absolute deviation of $0.015\,\mathrm{kg\,m^{-2}}$ with a $\sigma_{\mathrm{res.}}$ of $0.020\,\mathrm{kg\,m^{-2}}$) and in May the multi-parameter retrieval retrieves lower LWP values over ice than the reanalysis provides (mean bias of $-0.029\,\mathrm{kg\,m^{-2}}$).

Spatial differences are evident in the monthly averages in Figure 5.19 as well. For example, the sea ice edge shows very high LWP values in our retrieval in October. This is not visible in the reanalysis, indicating the MIZ or areas of ice growth might be challenging for our method. In some cases these areas might indeed contain high LWP because here the warm and moist air could be transported from the ocean onto colder sea ice where condensation takes place and clouds form. In January, a patch of suspiciously high LWP can be observed in the retrieved data around 80°N between 150°W and 180°W. High LWP is also observed in the Laptev Sea. Assuming that the true LWP is lower as indicated by the reanalysis, we hypothesize that the challenging surface conditions (for example young ice in the Laptev Sea) might affect the retrieval: If the sea ice is not sufficiently accurately modeled for the frequencies sensitive to the atmosphere then the method might account for differences in modeled and measured TB by changing the atmospheric LWP.

5.7 Summary and Conclusion

The combined atmosphere-snow-ice-ocean emission forward model together with optimal estimation is used in a multi-parameter retrieval of snow, ice and atmospheric parameters in the Arctic from satellite AMSR-E and AMSR2 microwave radiometer observations. Instead of correcting the satellite measurements for weather influences, we make use of the atmospheric information by using an integrated retrieval and retrieve both surface and atmospheric parameters. The surface part of the forward model requires four input variables, namely snow-air interface temperature T_{sa}, snow-ice interface temperature T_{si}, the ice type (either FYI or MYI), and snow depth. Data from the MOSAiC expedition provide valuable descriptions of the *ground truth* that can be used as model input. Despite simplifications regarding model parameters, we can simulate realistic values of brightness temperatures, and their variabilities, resembling the co-located satellite observations by using MOSAiC input data. To some extent, differences between forward model and observation can be explained by surface model parameter choices, like snow density or correlation length, as we can show in the simulation of the uncertainties of the model. In addition, in the MOSAiC case, we observe a seasonal dependence of the bias with better agreement towards spring.

The model is inverted using an optimal estimation method, which provides us with a physically consistent set of nine geophysical parameters and their uncertainties. These

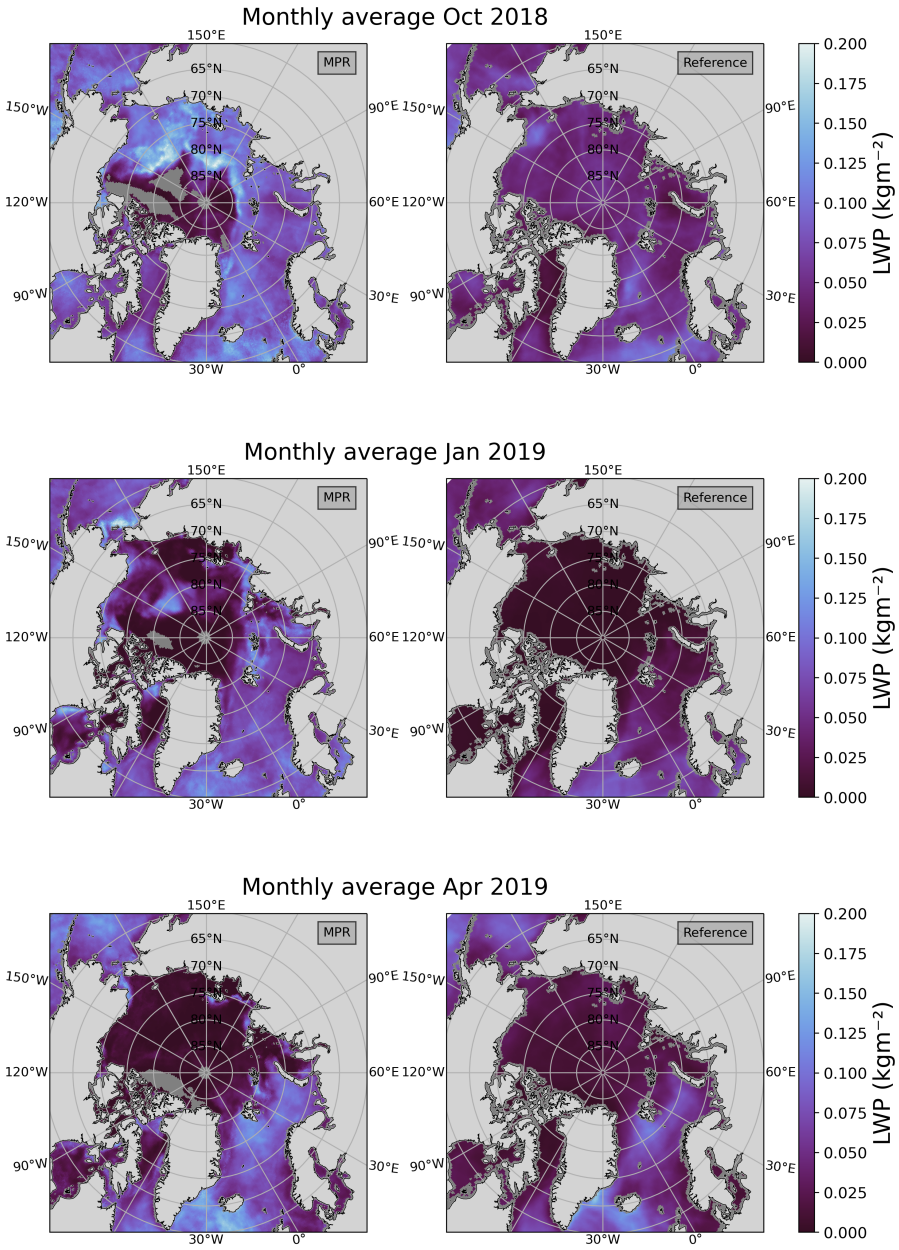

Figure 5.19: Maps of monthly average of retrieved liquid water path (LWP, left) from the multi-parameter retrieval (MPR) compared to the ERA5 reanalysis output (right).

parameters include the protagonists of this thesis: SIC, SND, LWP, and TWV. Although the degrees of freedom in the measurements are less than the number of retrieval parameters[3], they are mostly in agreement compared to MOSAiC observations. The model inversion by optimal estimation comes at acceptable computational costs, which enables daily retrievals using all available satellite observations. Spatial patterns as well as the seasonal development (Sections 5.6.1 and 5.6.5) of the retrieved parameters are plausible. This is now also true for the atmospheric parameters TWV and LWP in contrast to the previous model that used constant, empirical emissivities for sea ice. Evaluating the retrieval further is challenged by the sparse amount of available and suitable ground observations and the unknown accuracies of reference datasets such as reanalysis products. Based on the presented evaluations here, we conclude that the SIC retrieval performance is comparable to operational satellite products (Section 5.6.2 and 5.6.5) but small concentrations of spurious sea ice over open ocean are found. The retrieval of SND is satisfactory as comparisons against airborne data show (Section 5.6.3), but higher SND than in the satellite reference product are seen in the beginning of winter. We would like to emphasize the possibility of retrieving realistic values of LWP which has, to our knowledge, not been done successfully over sea ice so far by microwave radiometry. The comparison to the Mosaic data shows promising results as does the comparison to 20 years of ground-based station data (Section 5.6.4) which, however, also reveals weaknesses of the retrieval that require further analysis. LWP is overestimated in certain months and some areas are persistently featuring high values of LWP over weeks, which is likely due to the surface representation rather than actual atmospheric events. An extensive evaluation of TWV will follow in the next chapter.

The retrieval output contains the deviation between measured and modeled brightness temperatures as well as the retrieval uncertainties. The spatial distribution of these residuals for the different frequencies and of the uncertainties of the different retrieval parameters are useful tools to identify regions where the retrieval is challenged, for example over young ice (see Figure 5.15).

In summary, our improved method provides means to better monitor the Arctic from space in the months October to May. It now allows the analysis of long-term spatio-temporal winter trends for the time period of the AMSR-E and AMSR2 satellite sensors (starting 2002) as done for TWV in Chapter 6. Our sea ice-atmosphere-ocean multi-parameter retrieval has the advantage to provide a self-consistent set of retrieved parameters that can be analyzed jointly compared to single parameter retrievals as today common for most of the quantities we retrieve here.

[3]While the satellite radiometer measures at 12 channels (six frequencies, dual polarization), the number of independent measurements distinguishable from noise is lower than 12 as shown in Scarlat (2018)

Chapter 6

Focus Water Vapor

6.1 Water Vapor Retrieval: Evaluation and Comparison

The previous chapter contained a quantitative evaluation of the retrieval output using the Multidisciplinary drifting Observatory for the Study of Arctic Climate (MOSAiC) campaign data. Additionally, three of the four protagonists of this thesis (sea ice concentration (SIC), snow depth (SND) and liquid water path (LWP)) were further evaluated using reference datasets.In this chapter, we perform an evaluation of the retrieval of total water vapor (TWV). In order to evaluate the retrieved TWV we compile campaign and radiosonde station data and compare that data against the satellite product for the satellite sensors Advanced Microwave Scanning Radiometer - Earth Observing System (AMSR-E) and Advanced Microwave Scanning Radiometer 2 (AMSR2), see Table 5.1. In addition we compare the satellite retrieved data to the meteorological ECMWF Reanalysis v5 (ERA5). The curse of remote sensing (see Section 2.3) befalls us here as well. When trying to match satellite observations of large footprints on one hand and measurements that are almost pointlike on the other, we have both a spatial and temporal mismatch. Our co-location procedure usually contains a search radius and a time span before and after the start of the ground-based measurement. Only satellite observations within that time period and area are considered, averaged and then compared to the *ground truth*. Observations from warm air intrusions show that TWV can change by more than 100% within a few hours (Crewell et al., 2021). Thus a perfect agreement cannot be expected. Still, we believe this evaluation is necessary to extent the one from the MOSAiC campaign to other regions and ice types.

Another indication of a good retrieval performance is the capture of anomalous warm and moist air intrusions that deviate from the a priori background. This happened in April during the MOSAiC campaign (see previous Section), in March during the aircraft HALO-$(AC)^3$ campaign (Walbröl et al., 2023) and in July during the ATWAICE ship campaign. These events are depicted in the retrieved data; in case of the ATWAICE

campaign it happened when the ship was in the open ocean (about 50 km away from the ice edge).

6.1.1 Retrieval Evaluation with Campaign Data

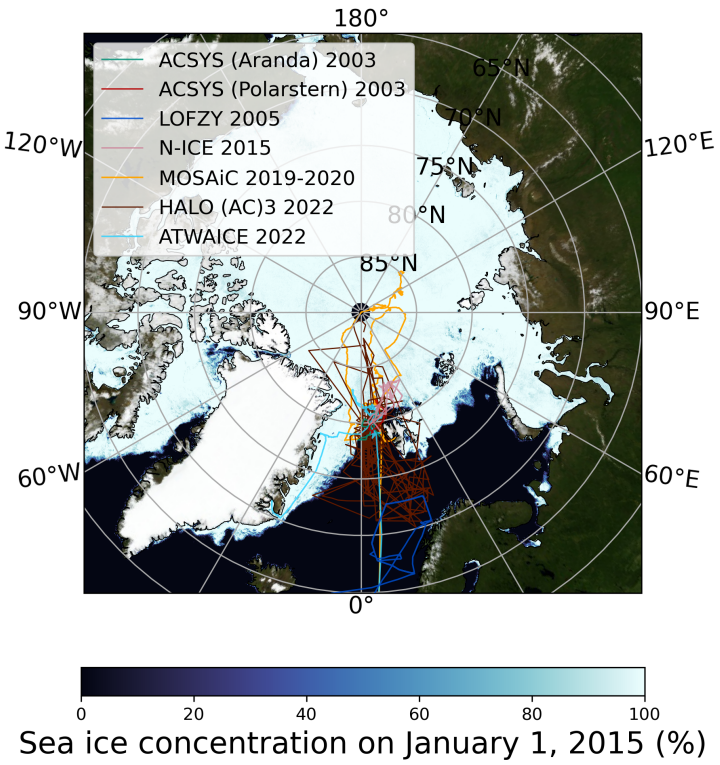

Figure 6.1: Location of campaign data used in the evaluation of the retrieved total water vapor. The map shows the daily sea ice concentration (SIC) from the operationally available ASI product (described in Section 4.1.3) on January 1, 2005.

Figure 6.1 shows where water vapor data was collected during campaigns which we use in the retrieval evaluation. Three different measurement techniques are used: dropsondes (HALO-(AC)^3), ship-based radiometers (ATWAICE) and radiosoundings (all other campaigns). Most of the data was collected in the Atlantic sector of the Arctic. We now discuss the results of the evaluation for each campaign, first the winter campaigns in chronological order starting with the most recent one and second the summer campaigns.

HALO-(AC)^3 2022 campaign data - dropsondes: The HALO-(AC)^3 campaign was an aircraft measurement program in the North Atlantic sector of the Arctic in March and April 2022. A synoptic overview of the environmental conditions during the campaign is given in Walbröl et al. (2023). Interestingly, the warm and moist air intrusions that occurred during that time (four independent events from March 12–20) even caused rainfall over sea ice northwest of Svalbard. Figure 6.2 shows retrieved TWV from two satellite

swathes coinciding with aircraft flights on March 12 and March 20. The moist air intrusion is visible on March 12 as high TWV and LWP values compared to the dry conditions on March 20.

For the TWV measurements by dropsondes (Mech et al., 2022) we co-locate satellite data using a search radius of 50 km and a maximum time difference of 30 min. The matched observations are shown in a scatter plot in Figure 6.2. Most of the observations are over open ocean according to the retrieved SIC (dark scatter points). The cases over sea ice (bright scatter points) are close to the one to one line. The overall correlation is high ($r^2 = 0.91$) and we observe a bias of $0.5\,\mathrm{kg\,m^{-2}}$.

MOSAiC 2019 – 2020 winter campaign data - radiometer: An extension of the comparison shown in the previous chapter is shown in Figure 6.3. The difference to the previous comparison (see Section 5.6.1) is the number of co-location events and the search radius. While we limited the previous comparison to overpasses where simultaneous *ground truth* measurements of all retrieval parameters were available, we now include all co-location events. Also we now average all satellite data within a radius of 50 km (only the closest observation was considered in the previous comparison) to be consistent with other comparisons in this chapter. The ground-based measurements are still averaged within ±10 minutes of the overpass time. The SIC was high during the entire time with 99% ± 1% (mean and standard deviation of retrieved SIC). Similar to before we conclude that the agreement is good (high correlation in terms of r^2 of 0.78 and low bias of $0.26\,\mathrm{kg\,m^{-2}}$). We can see that the distributions of TWV (Figure 6.3, right panel) agree well. Small deviations of the distribution are seen in a slightly higher stander deviation of the retrieved data.

N-ICE 2015 campaign data - radiosondes: We use radiosonde data from the Norwegian young sea ice cruise (N-ICE) 2015 which was conducted north of Svalbard in the Atlantic sector of the Arctic in thin, first-year sea ice from January to June 2015 (Hudson et al., 2017; Cohen et al., 2017). TWV is calculated from the radiosonde data using the saturation vapor pressure formulation by Hyland and Wexler (1983) and we restrict our analysis to January until May. The co-location was done by taking the satellite measurements within a distance of 50 km to the radiosonde launch position and a maximum time difference of 30 min to the start of the radiosonde launch. Figure 6.4 shows the agreement between total water vapor from radiosonde and satellite-derived TWV. The r^2 value is 0.55 and we observe a bias of $0.36\,\mathrm{kg\,m^{-2}}$. The sea ice during N-ICE 2015 was thin, young ice; during MOSAiC it was a second-year ice floe. Thus the good agreement between retrieved and observed TWV can be achieved for different surface conditions.

Field experiments ACSYS 2003 and LOFZY 2005 - radiosondes: Here, we use data from three campaigns collected by the Physical Meteorology Division of the Meteo-

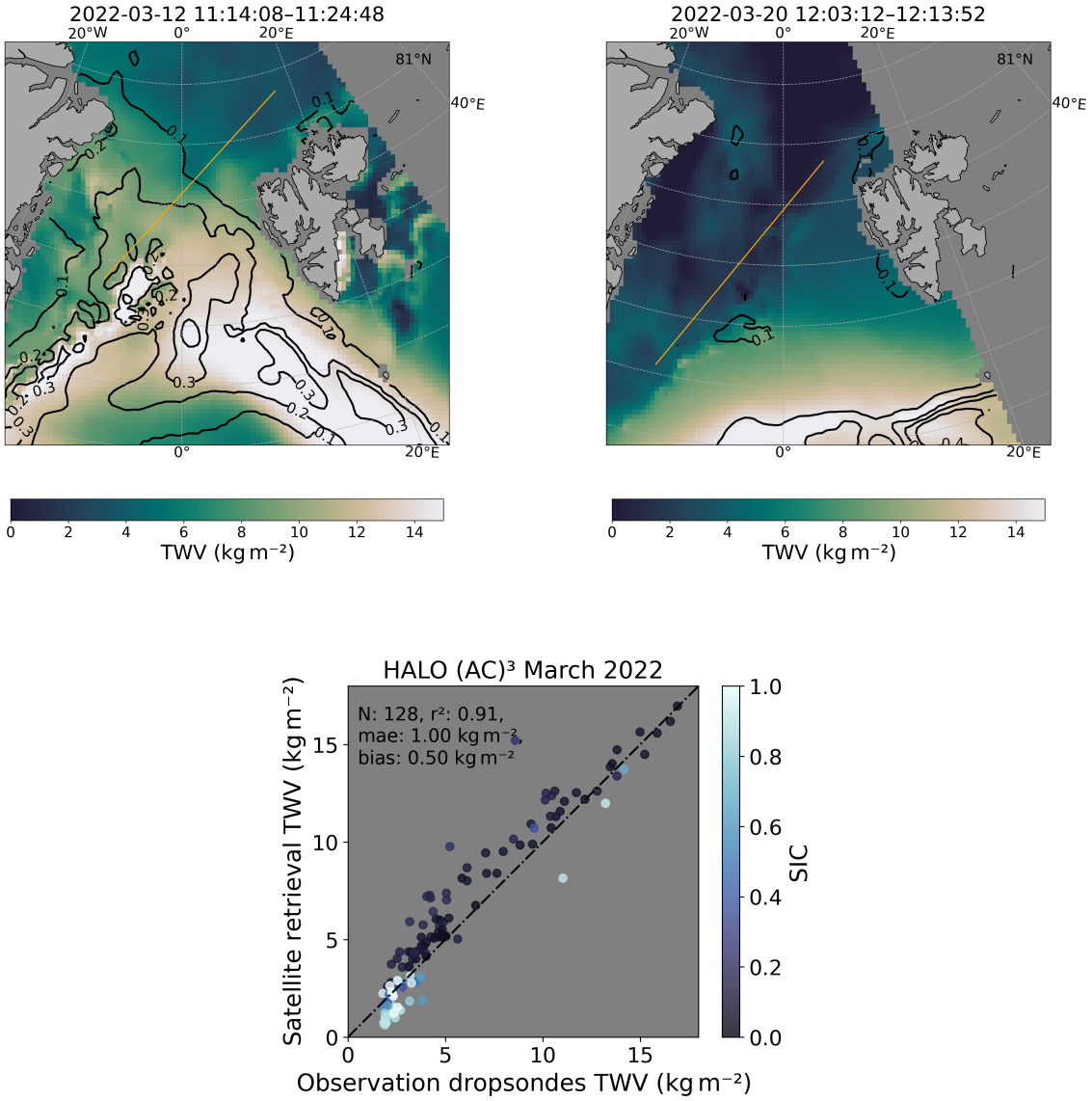

Figure 6.2: Top: Retrieved total water vapor (TWV) from one satellite swath over Fram strait, gridded on the EASE grid with a resolution of 12.5 km. On the left is the coast of Greenland and the island on the right is Svalbard. Left image shows data from March 12, 2022 during a warm air intrusion event, right image a swath from March 20, 2022. The retrieved liquid water path is shown as contour lines. The yellow line denotes the flight track of a coincident HALO-(AC)^3 campaign flight. Bottom: Scatter plot of retrieved total water vapor vs. dropsonde measurements from the HALO-(AC)^3 campaign 2022. Included in the plot are bias, mean absolute error (mae) and the coefficient of determination given by the square of the Pearson correlation coefficient r^2.

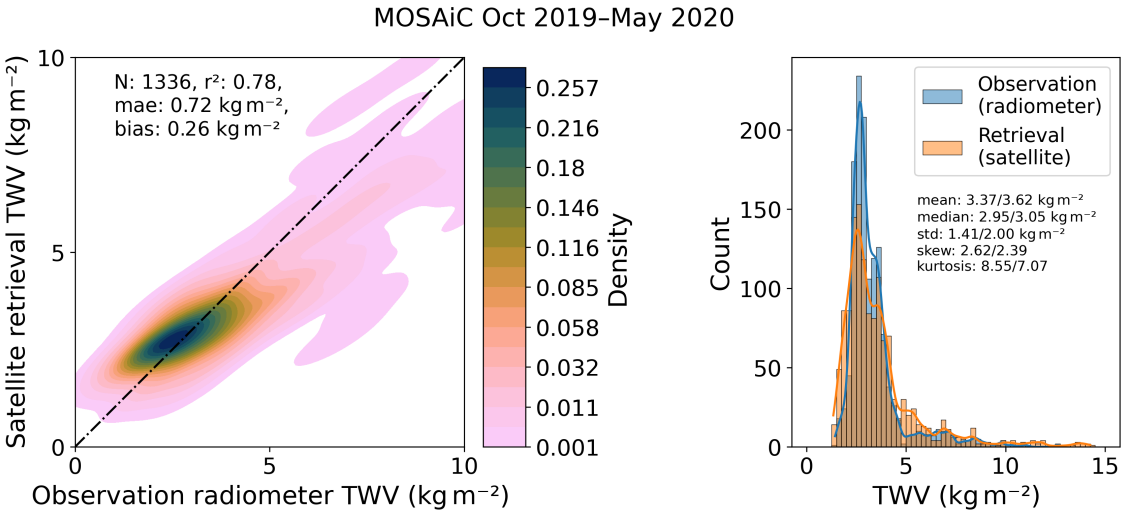

Figure 6.3: Left panel: Kernel density estimate plot of retrieved total water vapor (TWV) vs. radiometer measurements from the MOSAiC campaign during October 2019–May 2020. Included in the plot are bias, mean absolute error (mae) and the coefficient of determination given by the square of the Pearson correlation coefficient r^2. Right panel: Histograms of TWV from radiometer (blue) and from the retrieval (orange) of all matched observations. Annotated are the statistical parameters mean, median, standard deviation (std), skew and kurtosis for the ground-based observation (left value) and the satellite retrieval (right value).

rological Institute of the University of Hamburg:

(i) Arctic Climate System Study (ACSYS) 30.03.-21.04.2003 with R/V *Aranda*, Fram Strait (Brümmer et al., 2012a)

(ii) ACSYS 30.03.-21.04.2003 with R/V *Polarstern*, Fram Strait (Brümmer et al., 2012a)

(iii) LOFoten ZYklonen (LOFZY) 26.02.-19.03.2005 with R/V *Celtic Explorer*, Norwegian Sea (Brümmer et al., 2012b)

The data from the LOFZY campaign is independent, i. e., not used in weather forecast or renalyses schemes. Whether the ACSYS data was assimilated remains unfortunately unclear (personal communication with Gerd Müller, October 2023).

In case of no assimilation it is interesting to compare the performance of the satellite retrieval to the reanalysis. In most cases the radiosonde data is automatically assimilated and cannot be used for validating the reanalysis.

Along the lines of the comparison to the N-ICE 2015 data (last paragraph), the total water vapor is calculated from the radiosonde data using the saturation vapor pressure formulation by Hyland and Wexler (1983). We exclude soundings that did not reach altitudes higher 5 km (similar to requirements in Durre et al. (2009)).

The co-location was done by taking the satellite measurements within a distance of 50 km to the radiosonde launch position and a maximum time difference of 30 min to the

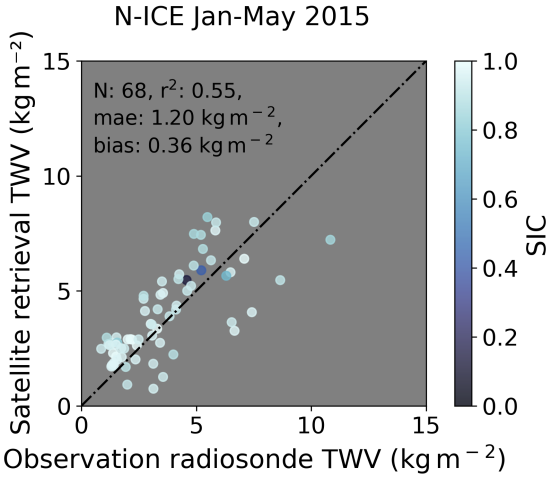

Figure 6.4: Scatter plot of retrieved total water vapor vs. measurements from the N-ICE campaign 2015. Included in the plot are bias, mean absolute error (mae) and the coefficient of determination given by the square of the Pearson correlation coefficient r^2.

start of the radiosonde launch. For the comparison to ERA5 reanalysis data, which is available on an hourly basis, we choose the ERA5 data from the grid cell closest to the radiosounding.

Figures 6.5a to 6.5c show the agreement between TWV from radiosoundings and satellite-derived TWV (left panels) or TWV from the reanalysis ERA5 (right panels). For the two datasets from the ACSYS campaign (Figures 6.5a and 6.5b), the r^2 value is 0.84 in both cases and we observe negative biases between $-0.78\,\mathrm{kg\,m^{-2}}$ to $-0.88\,\mathrm{kg\,m^{-2}}$. The co-located data to R/V *Aranda* corresponds to intermediate SIC conditions, while the one to R/V *Polarstern* corresponds to high values of SIC. In both cases the reanalysis performs better. Note that the number of data points is higher for the reanalysis and that we do not know whether the soundings were assimilated into the reanalysis. The field campaigns were in close proximity to Ny-Ålesund, Svalbard. Radiosoundings from there are regularly assimilated into ERA5. Assuming a spatial correlation between TWV at Ny-Ålesund and at the ship position, the high agreement of reanalysis and ship-based observations is not surprising, even if the ship data was not assimilated.

In case of the LOFZY campaign (Figure 6.5c), the r^2 value is high (0.9) and we observe a small negative bias ($-0.31\,\mathrm{kg\,m^{-2}}$). SIC is well below 0.2. Here, the reanalysis performance is comparable which also holds when reducing the reanalysis data to a smaller subset matching the size of the satellite data.

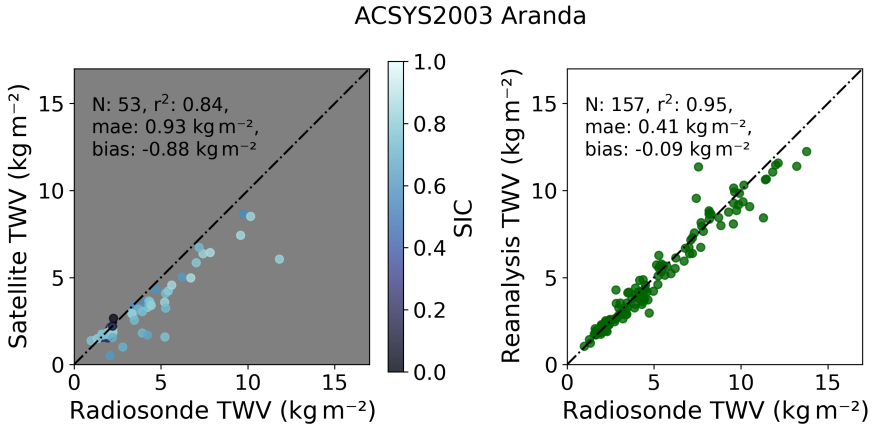

(a) ACSYS campaign 2003 from R/V Aranda.

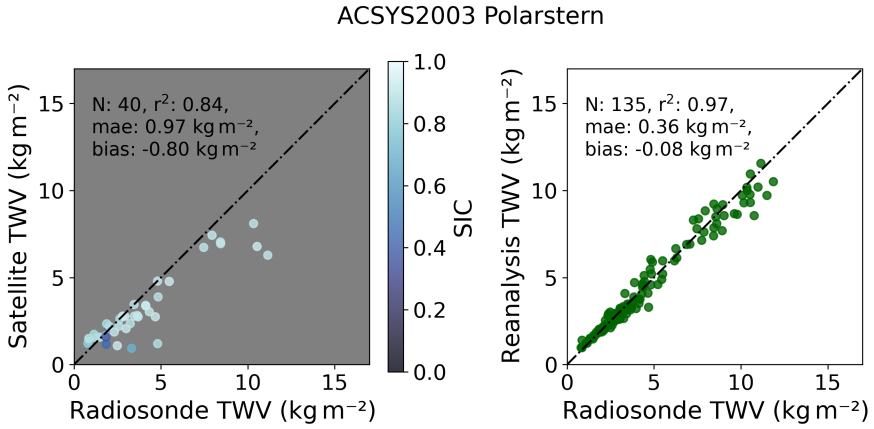

(b) ACSYS campaign 2003 from R/V Polarstern.

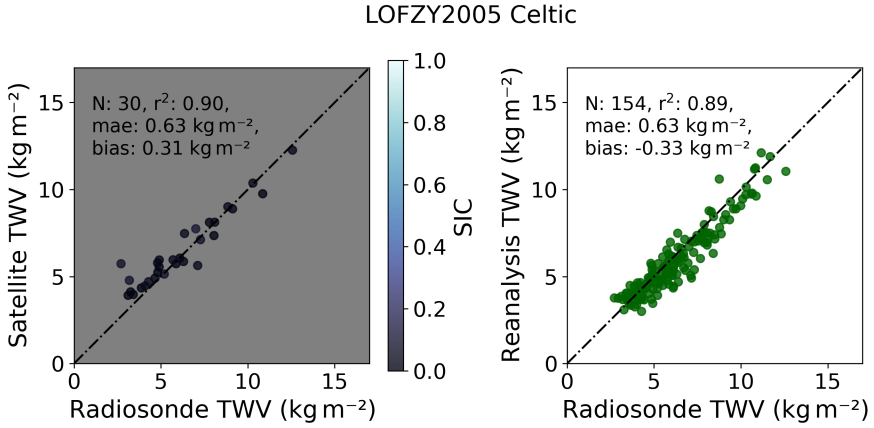

(c) LOFZY campaign 2005 from R/V Celtic Explorer.

Figure 6.5: Scatter plot of retrieved total water vapor vs. radiosonde measurements during the different campaigns. Included in the plot are bias, mean absolute error (mae) and the coefficient of determination given by the square of the Pearson correlation coefficient r^2.

Retrieval performance in summer - radiometer during MOSAiC 2020 and ATWAICE 2022: So far, we have focused our analysis on winter campaigns during the non-melting season. Here, we want to briefly explore the retrieval performance in summer. During the ATlantic WAter pathways to the ICE in the Nansen Basin and Fram Strait (ATWAICE) campaign, described in Chapter 3, water vapor was measured from the ship-based radiometer Humidity and Temperature Profiler (HATPRO). For every satellite overpass we average within 50 km. The ground-based measurements are averaged to 10 minute intervals. The time series of TWV is shown in the Appendix, Figure D.1, while there is no satellite overpass during the peak of the warm air intrusion around July 18, higher values around the maximum are depicted in the retrieved data.

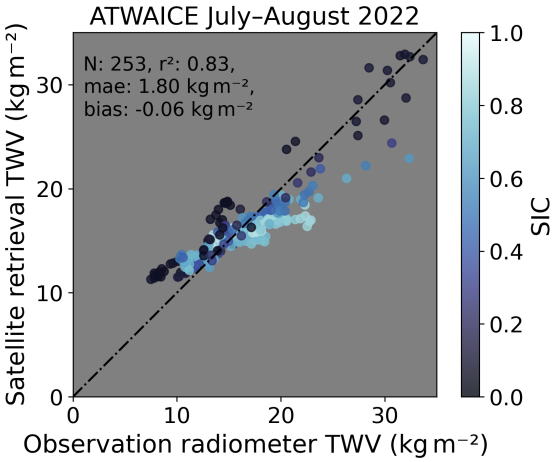

Figure 6.6: Scatter plot of retrieved total water vapor vs. radiometer measurements from the ATWAICE campaign 2022. For every overpass, the retrieval data was averaged within a 50 km radius. Included in the plot are bias, mean absolute error (mae) and the coefficient of determination given by the square of the Pearson correlation coefficient r^2.

Figure 6.6 shows the agreement between TWV from radiometer and satellite-derived TWV during the ATWAICE campaign. The r^2 value is 0.83 and we observe a low bias of ($-0.06\,\mathrm{kg\,m^{-2}}$). SIC was varying between 0 and 100% as the ship was transecting the marginal ice zone. Cases over ice only (SIC $> 85\%$, reducing the sample size to 17) yield a correlation of $r^2 = 0.91$ and a bias of $-0.38\,\mathrm{kg\,m^{-2}}$ (not shown).

The MOSAiC summer data from the HATPRO radiometer is co-located to satellite retrieved data by taking the satellite overpasses within a distance of 50 km to the ship position. The ground-based measurements are averaged within $\pm$ 10 minutes of the overpass time. Figure 6.7 shows the agreement between TWV from radiometer and satellite-derived TWV during the MOSAiC campaign. We were mostly observing SIC higher 50%. The r^2 value is 0.76 and we observe a low bias of $0.88\,\mathrm{kg\,m^{-2}}$. However the distributions reveal differences (Figure 6.7, right panel). Especially the bi-modal nature of the distribution of the ground-based observations (peaks around $9\,\mathrm{kg\,m^{-2}}$ and $15\,\mathrm{kg\,m^{-2}}$) is not visible in the satellite retrieval.

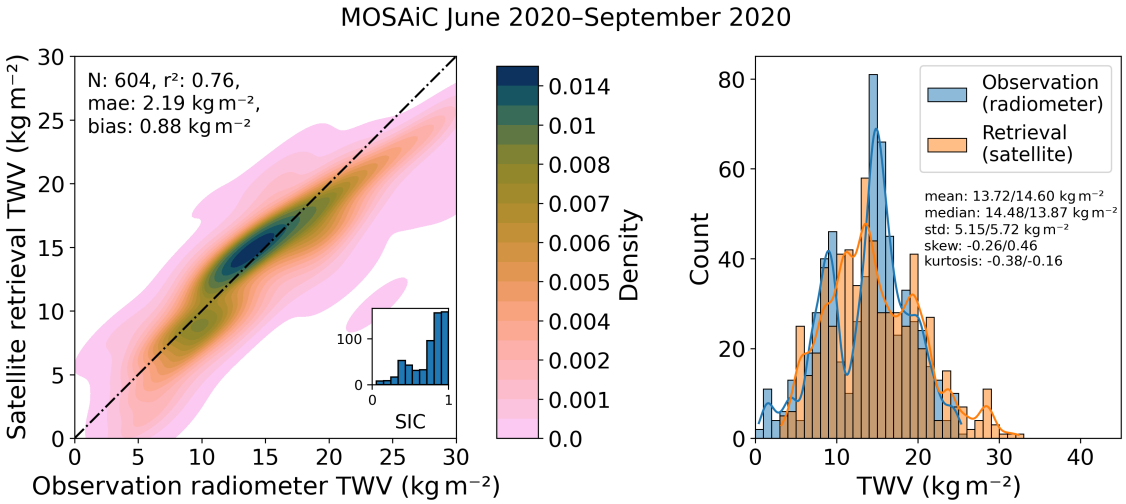

Figure 6.7: Left panel: Kernel density estimate plot of retrieved total water vapor (TWV) vs. radiometer measurements from the MOSAiC campaign during June–September 2020. Included in the plot are bias, mean absolute error (mae) and the coefficient of determination given by the square of the Pearson correlation coefficient r^2. Right panel: Histograms of TWV from radiometer (blue) and from the retrieval (orange) of all matched observations. Annotated are the statistical parameters mean, median, standard deviation (std), skew and kurtosis for the ground-based observation (left value) and the satellite retrieval (right value).

Based on these two campaigns we conclude that the retrieval performance in summer is promising and that it is worthwhile to investigate the potential of this satellite retrieval in the summer months further.

6.1.2 Retrieval Evaluation with Radiosoundings from Land Stations

The Integrated Global Radiosonde Archive (IGRA) contains worldwide radiosonde observations (Durre et al., 2006,0). The archive also provides derived products such as integrated water vapor (precipitable water). It is calculated following Durre et al. (2009). We use Version 2.2 of the data and choose only Arctic stations that were close to the coast in order to obtain retrieval data, which is only available over ocean (land data is masked out). The chosen stations are listed in Table 6.1.

The co-location was done by taking the satellite measurements that are within a distance of 50 km to the radiosonde launch position and have a maximum time difference of 120 min to the start of the radiosonde launch. We allow larger temporal deviations here than in the previous comparisons to campaign data to obtain a large number of co-location events. This enables a comparison of water vapor *distributions*.

In the following we therefore do not go into details on single sites, discussing for example orographic effects or comparability of the quality of radiosondes, but focus on the statistical parameters instead.

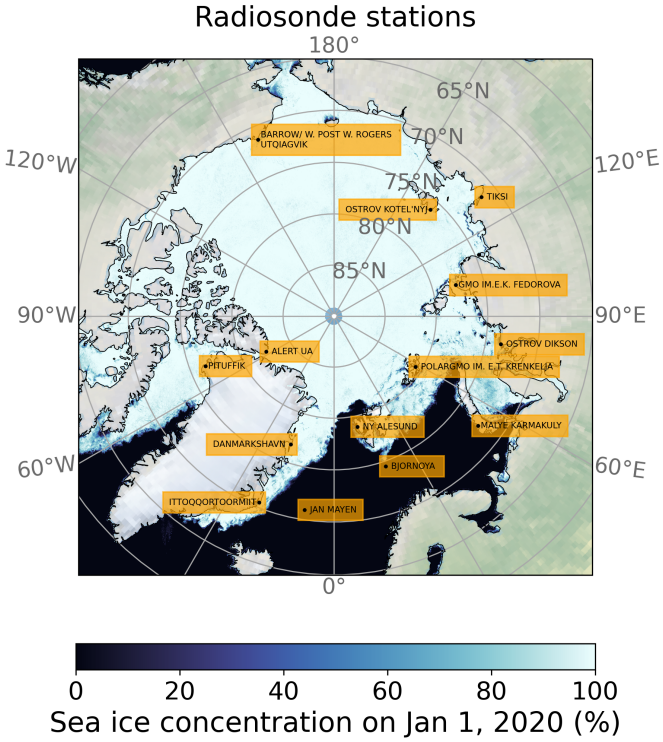

Figure 6.8: Map of radiosonde stations used in the retrieval evaluation.

Table 6.1: Summary of land stations sorted by name. When there is at least one month with measurements in a year, it is listed in the column *available time span*.

Name	IGRA station ID	Geolocation (latitude (°N), longitude(°E))	Available time spans	Average soundings per day
Alert	CAM00071082	82.5, -62.3333	1950–1971, 1973,1980–2023	1.87
Barrow/W. Post W. Rogers	USM00070026	71.2889, -156.7833	1948–2023	1.97
Bjornoya	SVM00001028	74.5039, 19.0011	1957–2023	1.92
Danmarkshaven	GLM00004320	76.7694,-18.6681	1950–1953, 1955–1970, 1973–2023	1.69
Gmo Im. E. K. Fedorova	RSM00020292	77.7131, 104.2919	1950–1970, 1972–1997, 2008–2023	1.81
Ittoqqortoormiit	GLM00004339	70.5, -21.97	1946–1948, 1981–2023	1.82
Jan Mayen	JNM00001001	70.9397, -8.6678	1949–2023	1.83
Malye Karmakuly	RSM00020744	72.3667,52.7	1950–1961, 1967–2023	1.66
Ny-Ålesund II	SVM00001004	78.9233, 11.9222	1992–2023	1.15
Ostrov Dikson	RSM00020674	73.5136, 80.4064	1950–1963, 1965–1971, 1973–2023	1.64
Ostrov Kotel'Nyj	RSM00021432	76.0, 137.8667	1955–1963, 1965–2000, 2010–2023	1.89
Pituffik[a]	GLM00004202	76.533, -68.75	1946–1971, 1973–2006	2.15
Polargmo Im. E. T. Krenkelja	RSM00020046	80.6264, 58.0589	1957–1963, 1965–1997, 2007–2023	2.02
Tiksi	RSM00021824	871.5833, 128.9167	1950–1963, 1965–2023	1.78

[a]The stations Pittufik and Polargmo Im. E. T. Krenkelja are too close to land to achieve co-location within a search radius of 50 km but the station data will be used in the next chapter and is therefore included in Table 6.1.

Exemplary, we show the results of the comparison of satellite-derived TWV and ground-based observation for four selected land stations in Figures 6.9 to Figures 6.12. The other sites are shown in the Appendix D.2. Because of the high number of coinciding overpasses we show the data as kernel density plot (left panels), illustrating correlations and deviations; and the distributions as histograms (right panels), illustrating how the statistical parameters (mean, median, standard deviation, skewness, and kurtosis) of satellite retrieval and ground-based measurements agree. In addition, the retrieved SIC is shown in the left panel as histogram. For sites with little sea ice such as Jan Mayen, Ny-Ålesund and Malye Karmakuly, Figures 6.9, D.2 and D.3, the agreement is excellent in terms of correlation (r^2 values of 0.94, 0.93 and 0.85, respectively) and in the shape of the distributions (skew, kurtosis). However we do observe a positive bias of up to $1.12\,\mathrm{kg\,m^{-2}}$. We observe correlation values between 0.50 and 0.75 for the sites with high sea ice concentration (Figures 6.10 to 6.12 and Appendix D.2), positive biases (between $0.23\,\mathrm{kg\,m^{-2}}$ and $2.28\,\mathrm{kg\,m^{-2}}$) and an overall good agreement in the distribution shape. The agreement in the statistical parameters is comparable to the sites over open ocean; especially in terms of the standard deviations of the distributions the agreement is good, see for example the site Gmo Im. E. K. Fedorova [1], Figure 6.11. The medians can differ by up to $2.5\,\mathrm{kg\,m^{-2}}$ (Figure D.7) but for the sites Alert, Danmarkshaven, Gmo Im. E. K. Fedorov and Tiksi that difference is below $1\,\mathrm{kg\,m^{-2}}$.

[1] Russian abbreviation, stands for Hydrometeorological observatory named after Evgeny Konstantinovich Fedorov.

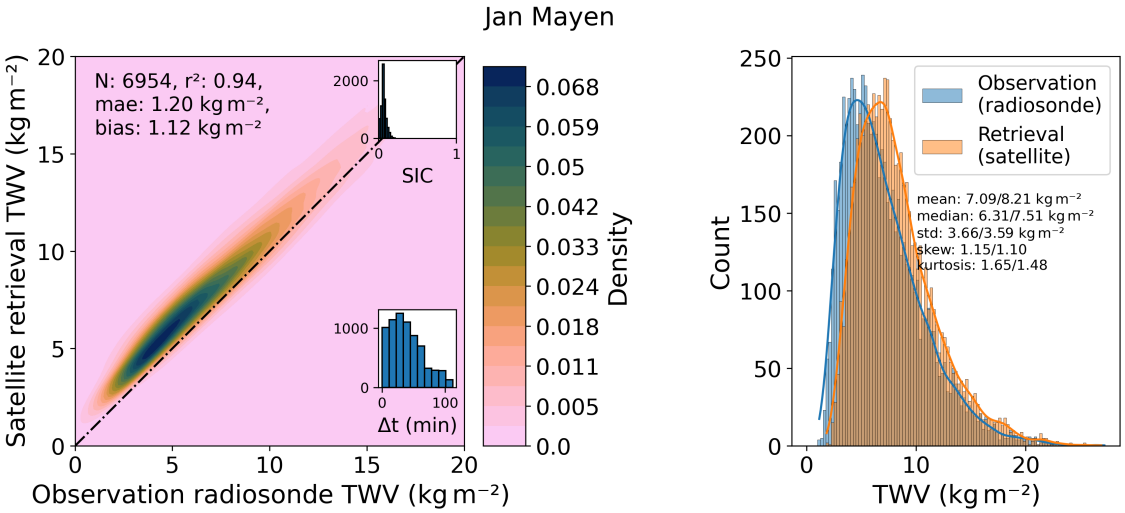

Figure 6.9: Total water vapor (TWV) from the radiosonde land station Jan Mayen in the Greenland Sea compared to co-located satellite retrievals of TWV (average of data within up to 2 hours after launch and within 50 km). Left panel: Kernel density estimate plot of all co-located values. Inset axes show histograms of co-located sea ice concentration (SIC) from the same satellite retrieval and of the time difference (Δt) between the satellite overpass and the sounding. Annotated in the plot are the number of matched observations, N, the square of the Pearson correlation coefficient, r^2, the mean absolute error, mae, and the bias. Right panel: Histograms of TWV from radiosounding (blue) and from the retrieval (orange) of all matched observations. Annotated are the statistical parameters mean, median, standard deviation (std), skew and kurtosis for the ground-based observation (left value) and the satellite retrieval (right value).

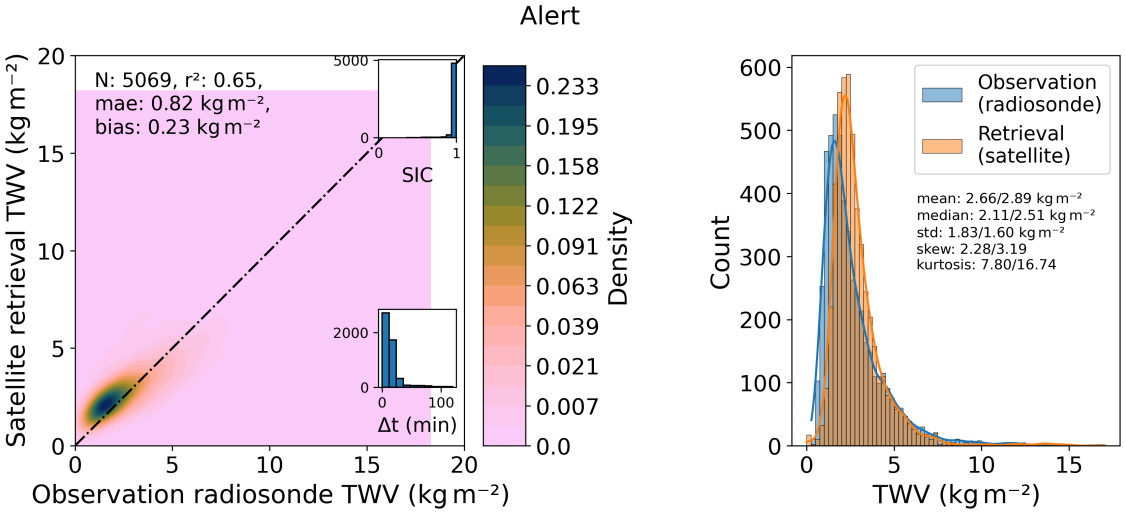

Figure 6.10: As Figure 6.9 but for the site Alert on Ellesmere Island, Nunavut.

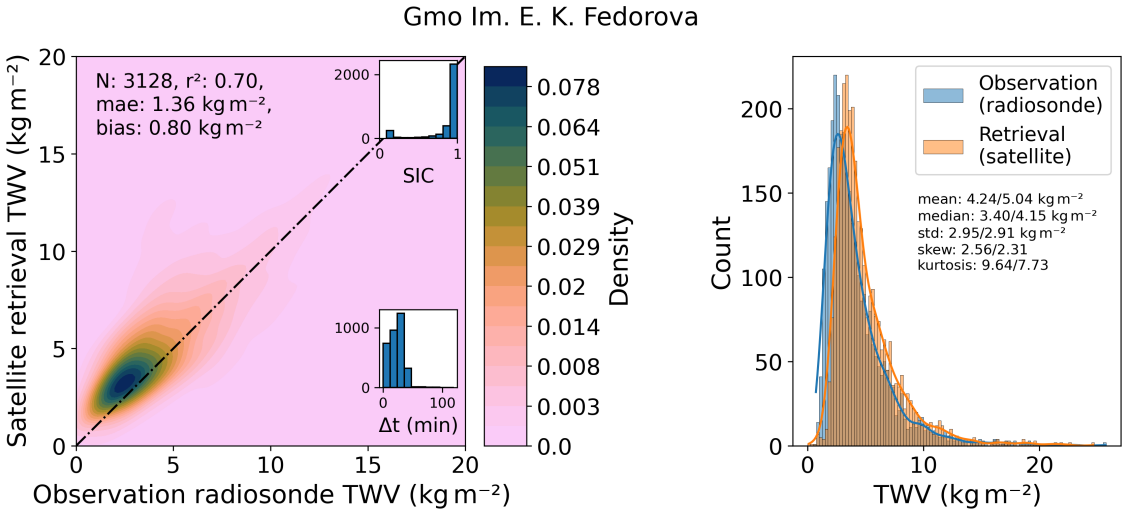

Figure 6.11: As Figure 6.9 but for the site Gmo Im. E. K. Fedorova at Cape Chelyuskin, south of Severnaya Zemlya archipelago between Kara and Laptev Sea.

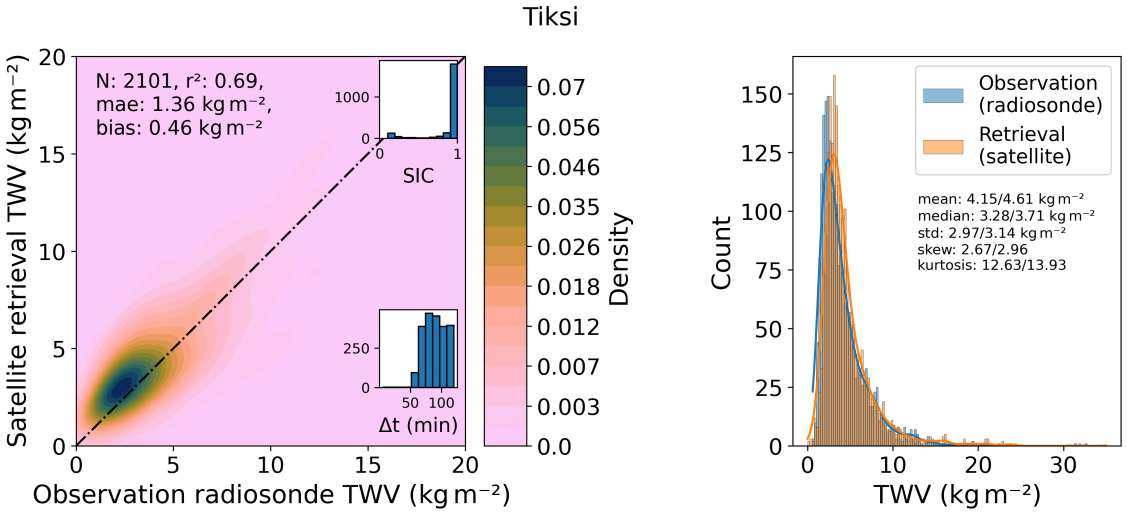

Figure 6.12: As Figure 6.9 but for the site Tiksi on the shore of the Laptev Sea, southeast of the delta of the Lena River.

6.1.3 Comparison to Reanalysis ERA5 Data

ERA5 and many numerical weather prediction models currently do not directly assimilate brightness temperature (TB) from passive microwave radiometers over sea ice because of the high uncertainties of the ice and snow emissions. Studies suggest that this could improve performances (Scott et al., 2012). As mentioned before, radiosoundings are usually assimilated in reanalyses, assessing the performance of the ERA5 in the Arctic is therefore not straightforward and accuracies of the reanalysis products are not well known (Persson and Vihma, 2017). That means that when comparing the retrieval to ERA5, differences are not necessarily an indicator of insufficient retrieval performance of the satellite product. Agreements however can increase confidence in findings based on either product. In addition the comparison may give hints on where to improve the retrieval algorithm (or may even point out issues of the reanalysis).

In order to compare the retrieval against the reanalysis ERA5, we first resample the retrieved TWV based on satellite swath data to the 0.25° grid using Gaussian resampling with a radius of 12.5 km and a σ of 5 km to obtain daily data. We then compare the monthly averages of this gridded data product and the reanalysis in Figure 6.13 for the winter season 2019–2020. Spatial differences are evident and differences change over the season. Over open ocean, the differences between TWV from the retrieval and the reanalysis vary little. The retrieval TWV is higher than the reanalysis (about 1.4 $\mathrm{kg\,m^{-2}}$). Over the multiyear ice (MYI), on the other hand, we observe that the retrieval is lower than the reanalysis in October (up to 3 $\mathrm{kg\,m^{-2}}$). This difference is decreasing and eventually even changes sign in some areas towards April. In May, the retrieval TWV is then again lower than the reanalysis in most areas over MYI. Over first-year ice, a different behavior is visible: the retrieved values are higher than the reanalysis (dark red areas in Figure 6.13) in November. Here, the differences decrease towards April and eventually change sign, resulting in negative differences in May for both first and multiyear ice areas. The patterns are similar for the winter season 2003–2004, shown in Figure 6.14, where the retrieval is based on satellite data from the sensor AMSR-E. Here, the retrieval over multiyear ice is in principal lower than the reanalysis, strongest in October, and it is higher than the reanalysis over first-year ice. Over ocean, the retrieval TWV is only slightly higher than the reanalysis (about 0.6 $\mathrm{kg\,m^{-2}}$), this difference hardly changes from month to month. Differences between the sensors are less evident in the central Arctic but there is a clear distinction between the data based on the AMSR-E and on the AMSR2 sensor in areas with more open ocean.

In the following we constrain the comparison to the ice-covered ocean by using the ERA5 land mask on both datasets as well as the ERA5 sea ice concentration variable to mask out all data where the daily mean SIC is below 15% for at least half of the days in the corresponding month. A comparison of the monthly mean values of all the ice covered grid cells is shown in Figure 6.15 for October 2019–May 2020 (AMSR2) and in Figure 6.16

for October 2003–May 2004 (AMSR-E). We note some interesting features of the reanalysis: in both seasons there are several modes visible in the histograms, corresponding to different months. Also, very low values (less than $0.34\,\mathrm{kg\,m^{-2}}$ for daily data and less than $1.28\,\mathrm{kg\,m^{-2}}$ for monthly data for October 2019–May 2020) are not observed. The modes are less distinct in the satellite retrieval but can also be identified. The distribution from the satellite retrieval shows lower values and a larger variability of TWV. In terms of means and medians, satellite retrieval and reanalysis differ by less than $0.6\,\mathrm{kg\,m^{-2}}$.

Over open ocean (see Appendix D.10 and D.9) the correlation is high and similarly to the land stations that are close to open ocean (see last paragraph) we observe a small positive bias. In fact, this bias is larger for the AMSR2 ($1.33\,\mathrm{kg\,m^{-2}}$) than for the AMSR-E ($0.47\,\mathrm{kg\,m^{-2}}$) time period. This hints at sensor intercalibration issues and will need to be taken into account in the next Section.

6.1.4 Summary

Overall, the comparisons against data from five winter campaigns over sea ice demonstrates that the retrieval performance varies but is satisfying overall. Values for the squared correlation coefficient r^2 range between 0.55 and 0.91 with biases that can be negative (up to $-0.88\,\mathrm{kg\,m^{-2}}$) or positive (up to $0.50\,\mathrm{kg\,m^{-2}}$). Comparisons against data from land stations, measured over sea ice, reveal that the distributions of TWV are similar, which is a requirement for statistical analyses of the TWV data. Mean absolute deviations range between $0.82\,\mathrm{kg\,m^{-2}}$ to $2.55\,\mathrm{kg\,m^{-2}}$. The retrieval uncertainty over ice, given by $\hat{\mathbf{S}}$, see Section 5.6.5, is on the order of $3\,\mathrm{kg\,m^{-2}}$ to $4\,\mathrm{kg\,m^{-2}}$ and thus even higher than these deviations. Based on the results of this chapter, the actual uncertainty of the retrieved TWV over sea ice may in fact be lower and we estimate it to be about $2\,\mathrm{kg\,m^{-2}}$.

Over open ocean, the agreement between retrieval and ground-based measurements is excellent (r^2 values above 0.8) and similar to the performance of the reanalysis ERA5 (based on the the comparison against data from the LOFZY campaign which was not assimilated). The retrieval uncertainty over open ocean is about $1.8\,\mathrm{kg\,m^{-2}}$. Taking all comparisons of this chapter into account this is a reasonable estimate for the uncertainty over open ocean.

Comparison to the reanalysis ERA5 show that mean absolute deviations over sea ice between October and May are about $1\,\mathrm{kg\,m^{-2}}$ but that these differences vary from month to month. In several months these differences are also correlated to the ice type. In addition we see a systematic bias between AMSR-E and AMSR2 which is particular evident over open ocean areas.

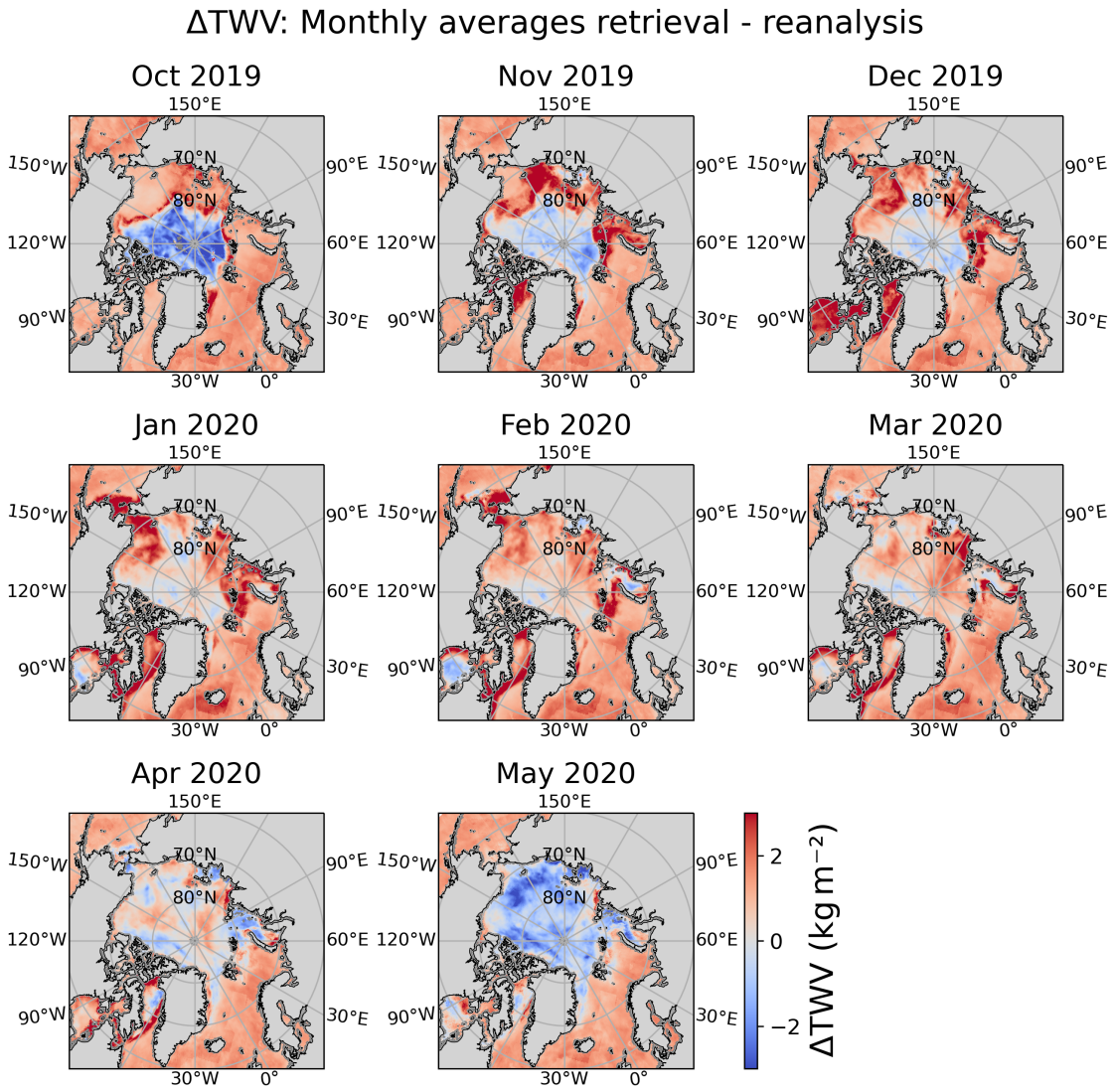

Figure 6.13: Differences in monthly mean values of total water vapor (TWV) between the meteorological reanalysis ERA5 and the retrieval for the winter season October 2019 to May 2020.

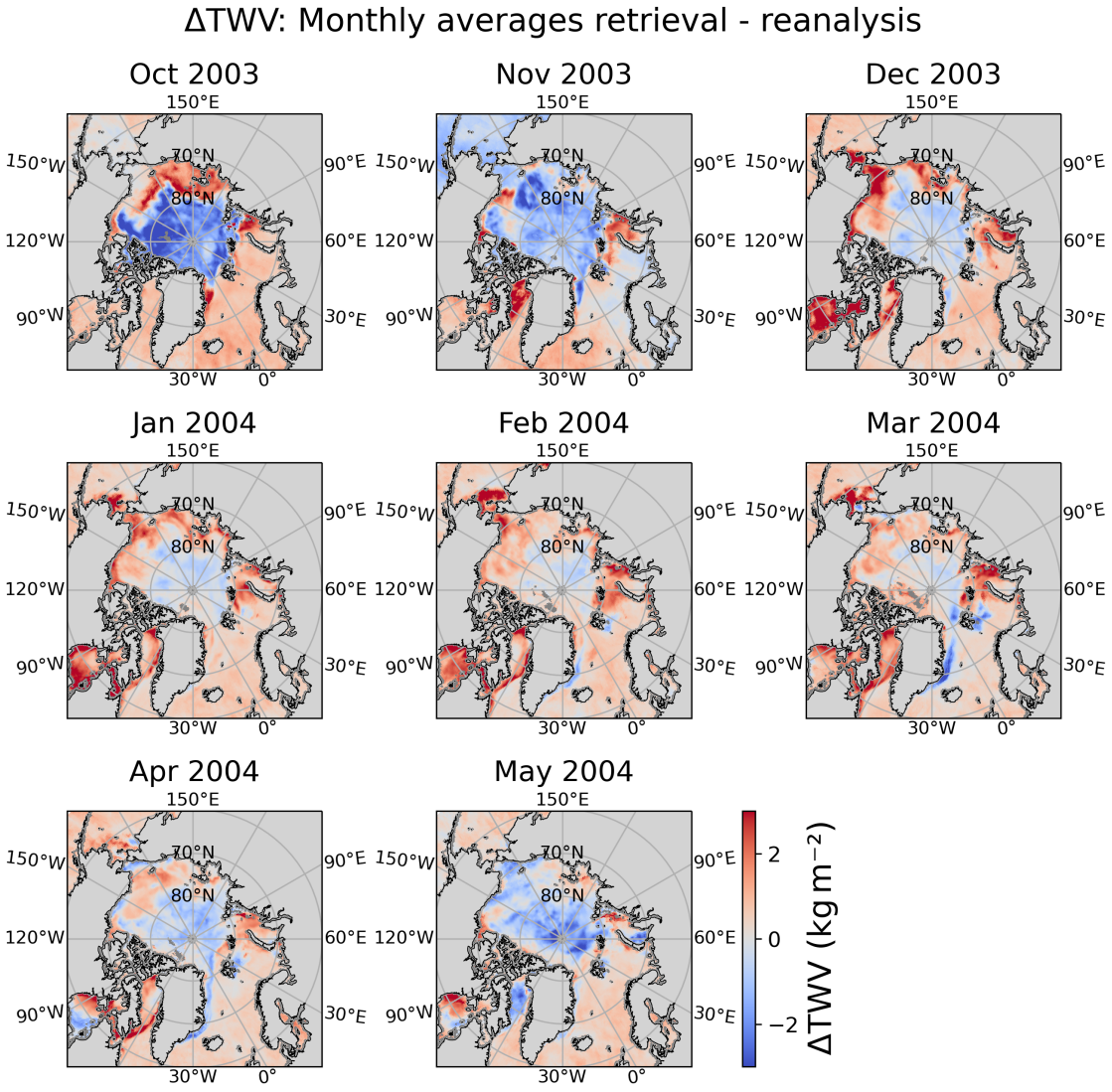

Figure 6.14: Same as Figure 6.13 but for the winter season October 2003 to May 2004.

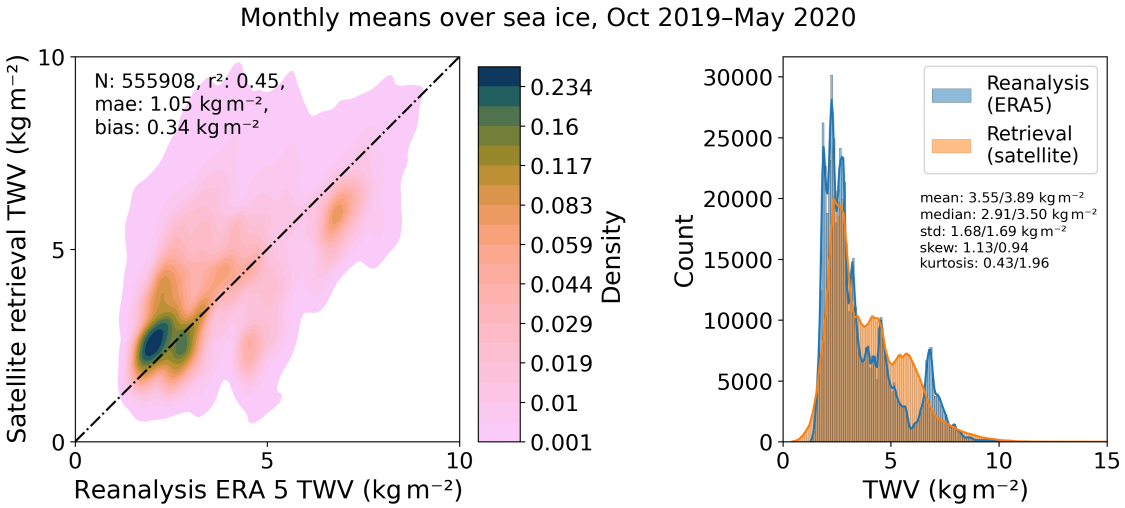

Figure 6.15: Monthly mean values of total water vapor (TWV) from the reanalysis ERA5 compared to satellite retrievals of TWV from October 2019–May 2020. Only sea ice covered grid cells are considered. Left panel: Kernel density estimate plot of all values. Annotated in the plot are the number of observations, N, the square of the Pearson correlation coefficient, r^2, the mean absolute error, mae, and the bias. Right panel: Histograms of TWV from reanalysis (blue) and from the retrieval (orange) of observations. Annotated are the statistical parameters mean, median, standard deviation (std), skew and kurtosis for the reanalysis (left value) and the satellite retrieval (right value).

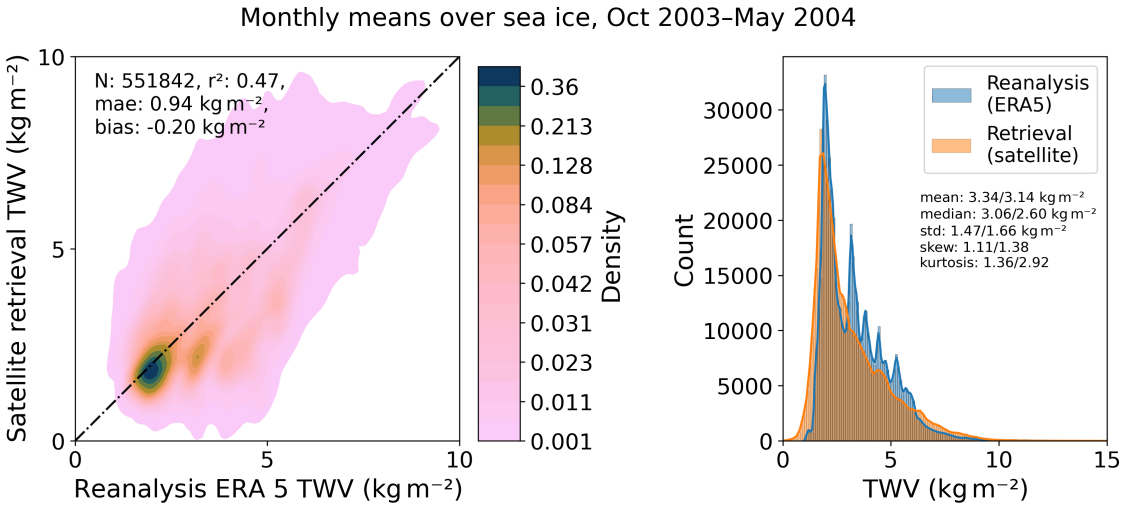

Figure 6.16: As Figure 6.15 but for October 2003–May 2004 (satellite sensor AMSR-E).

6.2 Trends and Variability of Arctic Water Vapor

6.2.1 Introduction

Total water vapor (TWV) generally increased in the Northern Hemisphere over the last decades as observed in radiosonde observations (Durre et al., 2009; Ross and Elliott, 1996). In terms of trends and variability of water vapor in the Arctic, a comprehensive picture has not yet emerged. First existing studies' insights from local Arctic sites, reanalysis and satellite data are summarized. Then we present results based on the satellite retrieval which was evaluated in the previous section.

Total water vapor trends and variability can be assessed at Arctic sites from radiosoundings or using Global Navigation Satellite System (GNSS) data. Maturilli and Kayser (2016) used the homogenized radiosonde record at Ny-Ålesund from 1993 – 2016 and found a moistening trend in winter (December, January and February) of $83 \pm 122 \times 10^{-3}\,\mathrm{kg\,m^{-2}}$ per year. Tomasi et al. (2020) analyzed monthly mean values of TWV obtained radiosonde measurements for the years 2001 – 2015 from 14 Arctic stations. They found variabilities in terms of standard deviation of $0.7\,\mathrm{kg\,m^{-2}}$ to $2.5\,\mathrm{kg\,m^{-2}}$ in winter months. Half the stations exhibit slightly decreasing values of TWV at rates on the order of $0.03\,\mathrm{kg\,m^{-2}}$ per year, for the other half TWV is increasing at rates on the order of $0.06\,\mathrm{kg\,m^{-2}}$ per year. Negusini et al. (2021) analyzed water vapor from GNSS stations for over 20 years and provided local trends as well. Those partly differ from the ones derived from radiosonde data at the same site (even in sign). Both positive (close to the Atlantic Ocean) and negative (Greenland and North America) trends were found using the GNSS data. Overall, however, sites at high latitudes show no significant trend. Rinke et al. (2019) took into account seasonal dependencies and found positive trends in May – October and negative trends in late winter when averaging TWV trends based on radiosoundings from the IGRA (see Section 6.1.2) of Arctic sites north of 65°N.

Atmospheric reanalyses, combining model output with available observations, are known to be less accurate in data-sparse regions such as the Arctic (Persson and Vihma, 2017) but they have the advantage of a high temporal resolution and an Arctic-wide coverage. Several issues of reanalysis products in the Arctic have been found, including a warm bias of air and surface temperature over Arctic sea ice in (Wang et al., 2019) and an imbalance between precipitation and evaporation (no hydrological balance) (Persson and Vihma, 2017).

Rinke et al. (2019) analyzed four different reanalysis products and concluded that, while there is an overall agreement of a general robust moistening, there are significant differences in terms of trend magnitude especially in the summer months where differences are larger than $0.05\,\mathrm{kg\,m^{-2}}$ per year. Based on the median of the four reanalyses, the monthly moistening for October – May is mostly below $0.04\,\mathrm{kg\,m^{-2}}$. The moistening

trend in the Arctic was also found based on reanalysis data (ERA-Interim) by Parracho et al. (2018) who also noticed the strong interannual variability in winter. Finally, satellite products can provide additional insights. While six different satellite products have been systematically assessed by Crewell et al. (2021) for summer, and differences of up to 30% in monthly TWV in the central Arctic have been found, little is known about the performances of these products (at least those operational without sunlight) in wintertime. Boisvert and Stroeve (2015) analyzed monthly data from the Atmospheric Infrared Sounder (AIRS) between 2003 and 2013. This satellite data reveal that the Arctic has become wetter: TWV trends are mostly positive in winter and there is a large spatial variability from month to month.

Altogether we find that the observation periods and considered temporal (or spatial) averages differ in the presented studies, hindering intercomparisons between them. This might explain some of the apparent discrepancies between them, e. g., in terms of TWV trends. On the other hand TWV changes vary depending on the time of the year and region that is of interest as well as on the investigated time period. Clearly, the overall picture of Arctic TWV and its spatiotemporal trends and variabilities is not complete, not even for the most recent decades.

Data: Water Vapor Satellite Product We now study the TWV satellite dataset from the multi-parameter retrieval that was evaluated against *ground truth* data in the previous section. This dataset comprises the retrieval from two different sensors that are listed in Table 5.1: AMSR-E (until 2011) and AMSR2 (launched 2012). We use the AMSR2 data as provided by JAXA and not converted brightness temperatures based on, e. g., Meier and Ivanoff (2017), that is, the sensor data we are analyzing is not intercalibrated. A possible change between the years prior and after 2011 could thus be attributed to sensor differences rather than actual (climatological) trends. We did apply the retrieval on calibrated brightness temperatures as well but observed differences between the sensors prevailed (see Appendix E.1). Because of the non-linearity of our retrieval method we cannot apply common methods to intercalibrate the satellite product by matching it to the reanalysis (e. g., Double-Differencing Method, Chander et al. (2013)). We therefore use piece-wise linear regressions when analyzing trends. Due to higher uncertainties in the presence of melt ponds that are not properly accounted for in our forward model, we restrict the following analysis to the non-melting season from October to May.

Despite these limitations we now aim to answer the questions, where and by how much the Arctic moistened or dried during the last twenty years according to the satellite observations. We first look at variability to identify regions of higher and lower variability.

6.2.2 Spatiotemporal Variability

In the following we use the daily resampled satellite product in the EASE projection of 25 $\times$ 25 km^2. The Gaussian resampling method uses a maximum number of neighbors of 12, a search radius of 12.5 km and a sigma of 5 km that is chosen as half the sampling interval of the swath data.

For the winter months December, January and February we calculate mean values per grid cell as well as standard deviations that are then averaged over the whole available time span (2002 – 2023). Separating the dataset by sensor yields similar results (not shown). The resulting mean winter state is shown in Figure 6.17a) while b) shows the mean winter variability in terms of standard deviation of TWV (σ_{TWV}). The mean winter TWV is higher over open ocean with 5.7 $\mathrm{kg\,m^{-2}}$ to 13.5 $\mathrm{kg\,m^{-2}}$ (5th – 95th percentile) than over sea ice with 2.1 $\mathrm{kg\,m^{-2}}$ to 7.2 $\mathrm{kg\,m^{-2}}$ (5th – 95th percentile) and a median value of 3.79 $\mathrm{kg\,m^{-2}}$. Here, the open ocean is defined as the area with mean winter SIC smaller 15%. The order of magnitude of the variability fits to the range of values documented by Tomasi et al. (2020), who reported values between 0.7 $\mathrm{kg\,m^{-2}}$ to 2.5 $\mathrm{kg\,m^{-2}}$ based on radiosonde station data. It is evident that the variability is also higher where values of TWV are higher, which is most notably the case over the open ocean or in areas of lower SIC such as the Barents Sea. The lower variability of TWV over high SIC areas is depicted in Figure 6.18.

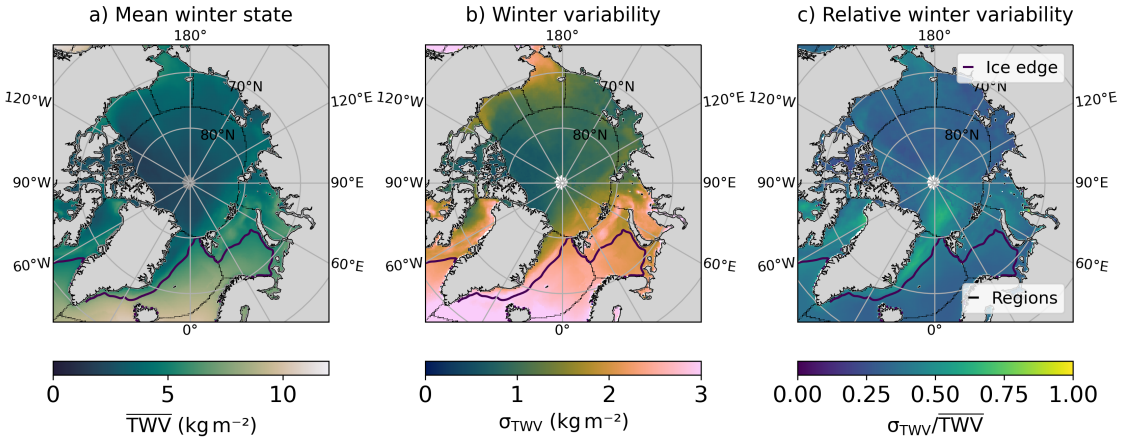

Figure 6.17: Mean winter state of total water vapor (TWV) for December, January and February averaged over 2002 – 2023 (a). Panel (b) shows the standard deviation giving the winter variability of TWV for the same time period (December – February, averaged over 2002 – 2023). Panel c) shows the relative variability. The mean ice edge (from the retrieved sea ice concentration at 15%) and the Arctic regions are outlined as well.

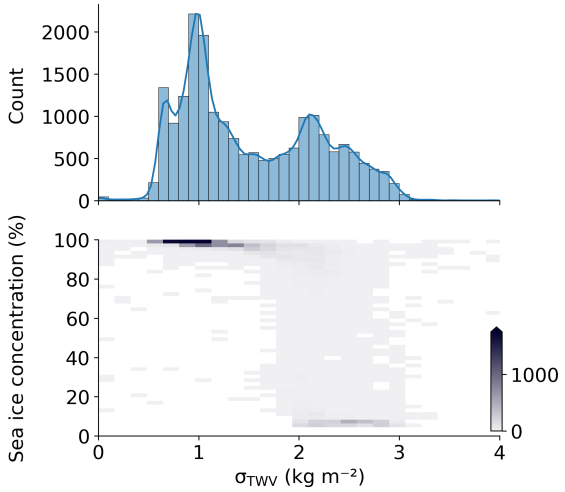

Figure 6.18: 2D histogram of the standard deviation of total water vapor (σ_{TWV}), indicating its winter variability over December, January and February, and the sea ice concentration (SIC). All data above 66.5°N, excluding land areas, is shown.

6.2.3 Regional Time Series

Figure 6.19: Definitions of Arctic Regions from the National Snow and Ice Data Center (NSIDC) (Meier and Stewart, 2023).

In order to compare regional time series for the Arctic regions shown in Figure 6.19 to reanalysis we resample the reanalysis data (ERA5) onto daily grids in the EASE projection of $25 \times 25\,\mathrm{km}^2$ to match the satellite product. Here, the Gaussian resampling method uses a maximum number of neighbors of 12, a search radius of 25 km and a sigma of 5 km.

We derive regional and monthly averages based on the regions outlined above (excluding land regions) for the satellite product, referred to as retrieval in the following, and the reanalysis. First, we calculate daily regional averages and derive monthly mean values from this regional data. Due to the shortcoming of the retrieval described in Section 5.6.5 some values are excluded and daily regional averages are only included when at least two third of the area contains valid data. In order to derive monthly means, at least 20 days need to have valid data.

TWV Winter Time Series The time series for four selected regions, Central Arctic, Barents Sea, Beaufort Sea and Laptev Sea, are shown in Figure 6.20. Note the different spatial extents of the regions ranging from $4.566 \times 10^6\,\mathrm{km}^2$ (Central Arctic), $1.542 \times 10^6\,\mathrm{km}^2$ (Barents Sea) and $0.692 \times 10^6\,\mathrm{km}^2$ (Beaufort Sea) to $0.495 \times 10^6\,\mathrm{km}^2$ (Laptev Sea). All numerical values reported in the following are from the retrieval.

For all regions TWV is at the maximum in the transition season (either October or May). In the Central Arctic, the maximum is found in May (both in reanalysis and retrieval) between $4.5\,\mathrm{kg\,m}^{-2}$ to $6.0\,\mathrm{kg\,m}^{-2}$. The month of the minimum varies from year

to year (both in reanalysis and retrieval) and is as low as $1.6\,\mathrm{kg\,m^{-2}}$ in 2003. In March or April TWV increases again every year. The month-to-month variability from December to March, given by the difference between maximum and minimum value in these months, is less than $0.73\,\mathrm{kg\,m^{-2}}$.

The other regions show a similar seasonal dependence but the absolute TWV values, their range and month-to-month variability are higher. The maximum of TWV is found in either May or October (both in reanalysis and retrieval) and lies between $7.2\,\mathrm{kg\,m^{-2}}$ to $11.6\,\mathrm{kg\,m^{-2}}$ for the Barents Sea, between $6.2\,\mathrm{kg\,m^{-2}}$ to $8.0\,\mathrm{kg\,m^{-2}}$ for the Laptev Sea and between $6.3\,\mathrm{kg\,m^{-2}}$ to $8.2\,\mathrm{kg\,m^{-2}}$ for the Beaufort Sea. The month of the minimum also varies from year to year (both in reanalysis and retrieval) and is as low as $3.4\,\mathrm{kg\,m^{-2}}$ in the Barents Sea in January 2003, $2.5\,\mathrm{kg\,m^{-2}}$ in the Laptev Sea in January 2023 and $2.7\,\mathrm{kg\,m^{-2}}$ in the Beaufort Sea in February 2004.

The month-to-month variability from December to March strongly varies from year to year: it lies between $0.3\,\mathrm{kg\,m^{-2}}$ to $2.8\,\mathrm{kg\,m^{-2}}$ for the Barents Sea, $0.3\,\mathrm{kg\,m^{-2}}$ to $2.1\,\mathrm{kg\,m^{-2}}$ for the Laptev Sea and $0.2\,\mathrm{kg\,m^{-2}}$ to $1.6\,\mathrm{kg\,m^{-2}}$ for the Beaufort Sea.

Comparison to Reanalysis Within the TWV time series differences to the reanalysis are visible. They have partly been discussed in Section 6.1.3. We can see that the differences vary from year to year and from month to month (see also Appendix, Figure E.3). In the Laptev and Beaufort Sea the retrieval reports higher values than the reanalysis (about $1\,\mathrm{kg\,m^{-2}}$ with maximum differences up to $3.6\,\mathrm{kg\,m^{-2}}$ in November). In the Central Arctic differences are smaller and average out ($0.05\,\mathrm{kg\,m^{-2}}$) because of mostly negative differences in the beginning and end of the non-melting season and positive differences in between. Monthly differences however can be as large as $-1.8\,\mathrm{kg\,m^{-2}}$ in October 2004. In the Barents Sea the difference is systematically higher during the AMSR2 time period (about $1.4\,\mathrm{kg\,m^{-2}}$) compared to the AMSR-E period ($0.6\,\mathrm{kg\,m^{-2}}$). Because of the sensor differences, especially evident in the Barents Sea data, we consider two independent time series in the following section.

SIC Winter Time Series The corresponding time series of SIC is shown in the Appendix, Figure E.2. Except for the Barents Sea, SIC is high ($> 90\%$) in all years for the months November to March with little year-to-year variability. In the Barents Sea SIC is lower ($< 60\%$) and the year-to-year variability to variability is high, with a minimum in 2004 (below 30% in both reanalysis and retrieval).

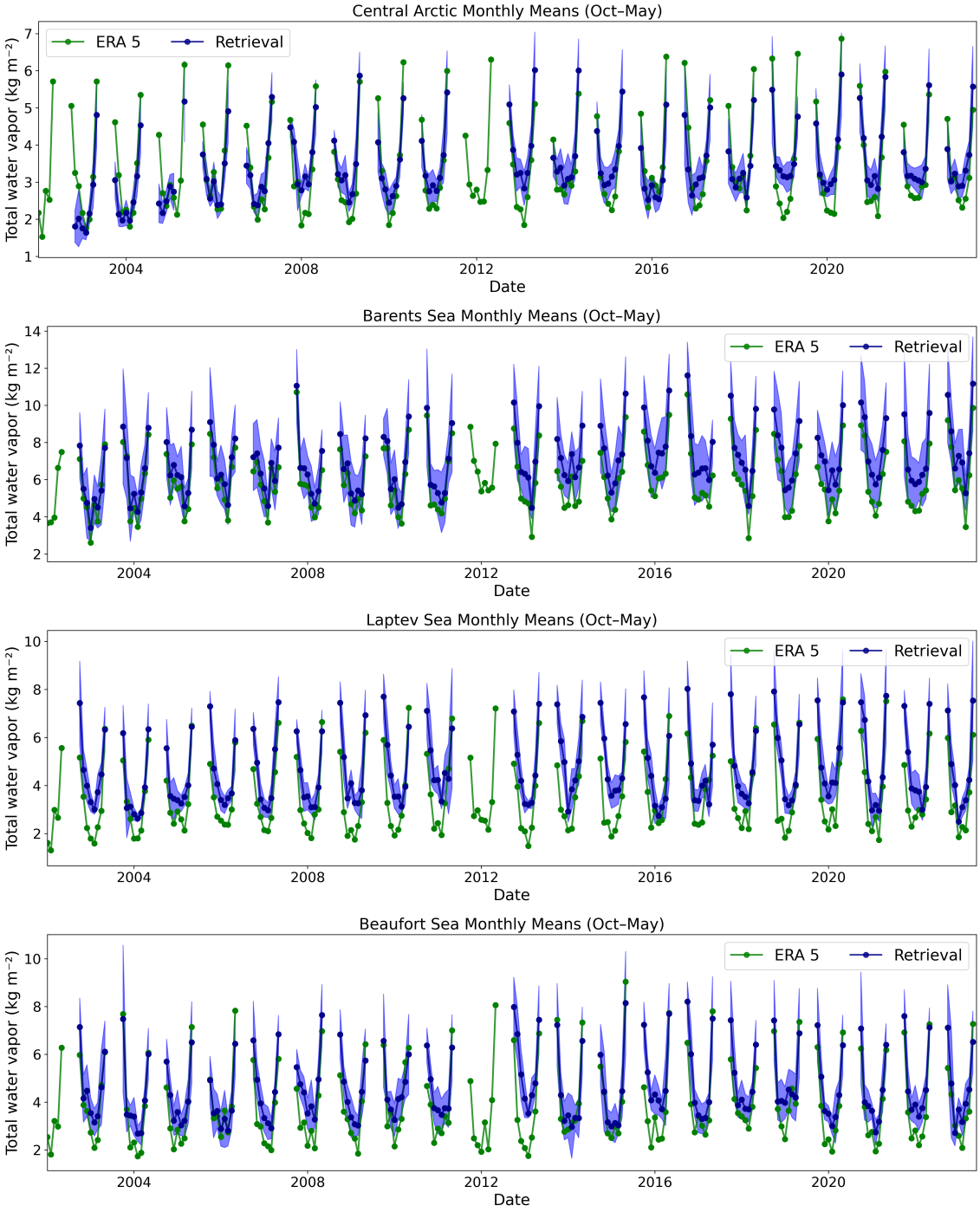

Figure 6.20: Regional time series of monthly total water vapor (TWV) from 2002 – 2023 for October to May from the satellite retrieval (blue) and the ERA5 reanalysis (green), averaged over the central Arctic (first panel), the Barents Sea (second panel), the Laptev Sea (third panel) and the Beaufort Sea (fourth panel). Blue shading indicates the temporal variability of the retrieval TWV given by the monthly standard deviation per grid cell averaged over the respective region.

6.2.4 Changes in Arctic Total Water Vapor

As a first order approximation of changes in Arctic TWV we use the satellite time series of gridded monthly data and obtain a rate of change from a fitted linear least-squares regression of each grid cell over the AMSR-E and AMSR2 time period separately. The regression is calculated using SciPy (Virtanen et al., 2020) and the p-value is calculated for a hypothesis test whose null hypothesis is that the slope is zero. This approach follows Boisvert and Stroeve (2015), enabling a comparison against their results in the next section. However we are aware of the unresolved debate about the use of p-values to determine statistical significance (Ambaum, 2010; Shepherd, 2021). Frailties include that p-values depend on sample size, for example, if we use daily data instead of monthly data we get lower p-values but the values for the slope remain the same (not shown). High p-values in our case mean that the null hypothesis cannot be rejected but that does not automatically discard trends other than zero.

The trends[2] in terms of the slope of the regression are shown in Figure 6.21 for November, January and March. Note that per grid cell a maximum of only $n = 9$ data points is available for the AMSR-E time period ($n = 11$ for AMSR2). As additional measure of the robustness of the derived slope we also calculate linear regressions for $n-1$ points, leaving each year out once. The standard deviation of the hereby calculated slopes, called σ_{slope}, serves as additional uncertainty metric shown in the Appendix, Figure E.4. In addition we use a linear least-squares regression over the same time periods to derive trends for the monthly averaged radiosonde land station data (introduced in Section 6.1.2), shown as well in Figure 6.21 in the circles (only for stations with at least 5 years of available data within the respective periods). Radiosonde trends with p-values smaller than 0.05 are shown with a bold outline.

For all months the changes are stronger and show more often small p-values between 2002 – 2011 than between 2012 – 2023. In some regions, the trends also have different signs in the two time spans. We note the patchiness of the trends over sea ice that can partly be attributed to less data points in certain areas. Overall there is agreement between these trends and the ones based on the radiosonde land station data, shown as circles in Figure 6.21, but the trends based on ground-based data also differ in several cases from the surrounding satellite grid cells (even in sign).

November Of the three selected months shown in Figure 6.21, the highest values of the slope are found in November between 2002 and 2011. Here, the atmosphere over ice got moister overall (red areas) but regional differences exist: the strongest positive (up to $0.7\,\mathrm{kgm^{-2}/year}$) changes are observed for the Laptev Sea, the Northern area of the Kara Sea and for parts of the Central Arctic between 90°W and 180°W. For these

[2]Note that this term is not to be confused with climatological trends for which our time span is too short.

regions, relative uncertainties of the trend are below 20%. Negative changes are seen for the ice-covered East Greenland Sea and the Southern area of the Kara Sea. σ_{slope} over sea ice is on average 0.05 kgm^{-2}/year (0.04 kgm^{-2}/year) for 2002 – 2011 (2012 – 2023) and lower than the observed changes in most areas.However, there are areas in the Central Arctic and the East Siberian Sea with high σ_{slope} above 0.1 kgm^{-2}/year for 2002 – 2011. For the time period of 2012 – 2023 the atmosphere got drier above the Beaufort Sea and large parts of the Central Arctic and moister above the East Greenland Sea and North-East of Greenland. Both increasing and decreasing TWV are observed over the ice-free Pacific between 2002 and 2011 and decreasing TWV between 2012 to 2023. Over the ice free Atlantic east of 45°W the atmosphere got drier between 2002 and 2011 and moister between 2012 to 2023.

January Several patches of positive trends are seen in parts of the Central Arctic between 135°W and 180°W and in the Laptev and Kara Sea in January for the time period 2002 – 2011. This trend pattern is also observed between 2012 – 2023 although trend magnitude values are smaller. For these areas σ_{slope} is lower than the observed trends and over sea ice σ_{slope} is on average 0.04 kgm^{-2}/year (0.03 kgm^{-2}/year) for 2002 – 2011 (2012 – 2023). However there are areas in the Barents Sea with high σ_{slope} above 0.1 kgm^{-2}/year for 2002 – 2011. During the time span 2012 – 2023 we additionally observe decreasing TWV in the East Greenland Sea close to the ice edge and in some parts of the Eastern Central Arctic which is less pronounced for 2002 – 2011. Both decreasing TWV are observed over the ice-free Pacific between 2002 and 2011 and mostly increasing TWV between 2012 to 2023. We see a moistening in the ice-free North Atlantic Ocean in January between 2002 and 2011 but decreasing TWV between 2012 and 2023, consistent with trends derived based on data from the radiosonde station on Jan-Mayen.

March In March large areas of the Central Arctic show positive trends between 2002 – 2011 which are around 0.13 kgm^{-2}/year. The atmosphere over the ice-free North Atlantic got drier which is in agreement with radiosonde data. Again trend values, both negative and positive, are small. Decreasing TWV are observed over the ice-free Pacific between 2002 and 2011 and increasing TWV between 2012 to 2023. Over the ice free Atlantic the atmosphere got drier between 2002 and 2011 and shows hardly any change between 2012 to 2023. Over sea ice σ_{slope} is on average 0.04 kgm^{-2}/year (0.03 kgm^{-2}/year) for 2002 – 2011 (2012 – 2023).

Winter Trends The derived trends from the satellite dataset need to be handled with care. First, our forward model consists of an idealized sea ice and snow setup that does not include climatological changes of model parameters which could translate into changes of the retrieval parameters. Examples could be changes in the sea ice thickness or a possibly

changing percentage of refrozen melt ponds that would alter the emission characteristics of the surface. Thus it is possible that the forward model setup is more representative of a snow and ice pack at the beginning of the AMSR time series than of what one would find now (or vice versa), and it may be the case that this introduces a bias in the retrieved TWV.

Second, we are only looking at short time spans of about a decade. As described above, the trends vary with the observed decade, per month and per region. The question posed above, where and by how much the Arctic moistened or dried, thus requires a careful refining by including the specific time period and time of the year that is of interest. This is also true when one wants to compare these trend values to the results from other studies, like the ones presented in the introduction or as done in the next section. Only the area 75°N – 85°N, 135°W – 180°W shows a moistening in all three shown months and in both time spans with p-values smaller 0.05. Here, we can speak of an overall robust moistening. Based on both available literature discussed above and on the physical relation between increasing air temperatures (as observed in the Arctic) and water vapor given by the Clausius-Clapeyron relation[3], this is reasonable. But the main conclusion from this investigation is that the spatiotemporal variability of trends is high and needs to be taking into consideration when analyzing TWV changes.

[3]The Clausius-Clapeyron equation relates the saturation vapor pressure of water to air temperature and results in about 7% increase in TWV per degree warming assuming 100% relative humidity.

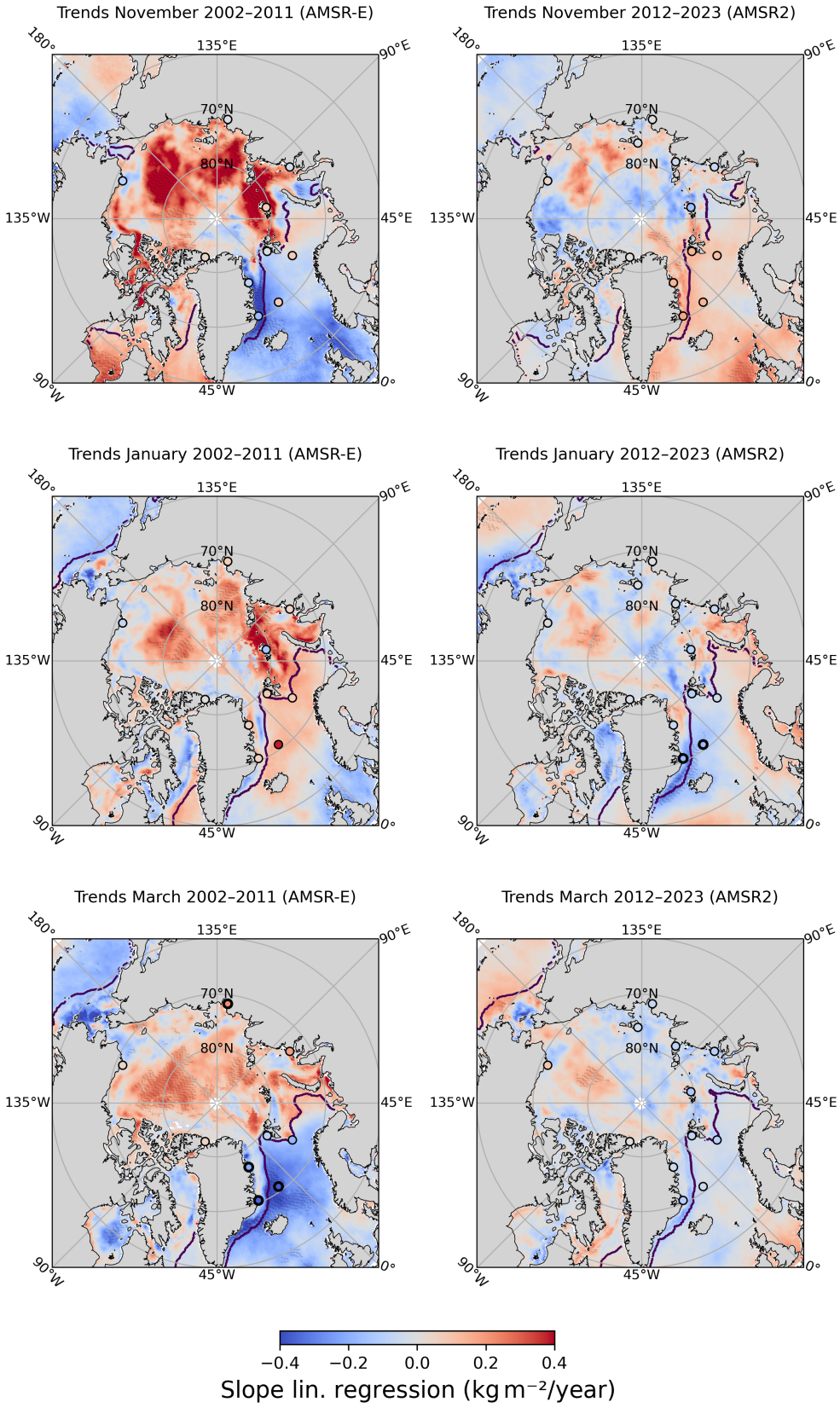

Figure 6.21: Changes in total water vapor (TWV) from the slope of a linear regression over monthly data from the AMSR-E time period (2002 – 2011, left panels) and the AMSR2 time period (2012 – 2023, right panels). Changes over the same time from radiosonde-derived TWV are shown in the circles. Thick circle outlines and stippling indicate changes that are significant at the 95th percentile. The purple line indicates the mean sea ice edge for the corresponding time spans.

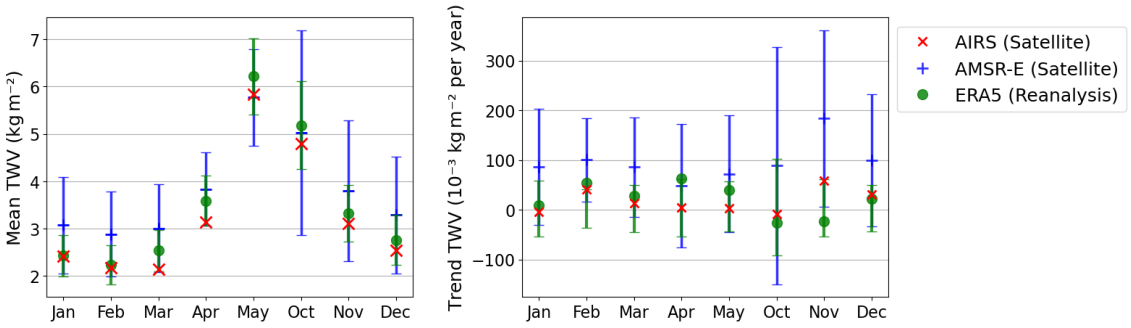

Figure 6.22: Mean values of total water vapor (TWV, left panel) and trends (from a linear regression, right panel) over 2003 – 2013 (AIRS), values from Boisvert and Stroeve (2015) and 2002 – 2011 (AMSR-E, ERA5). The area considered here encompassed the Arctic regions Central Arctic, the Canadian Archipelago, Beaufort Sea, Chukchi Sea, East Siberian Sea, Laptev Sea and Kara Sea, excluding land areas. The standard deviation derived from spatial averaging is shown as error bars.

Comparison to AIRS Satellite and Reanalysis Data As stated in the last section, the atmospheric water vapor trends vary spatially and from month to month. Boisvert and Stroeve (2015) provide monthly values for TWV trends for a large region encompassing the Central Arctic, the Canadian Archipelago, Beaufort Sea, Chukchi Sea, East Siberian Sea, Laptev Sea and Kara Sea from 2003 – 2013. In order to compare our derived mean TWV and trends to the values given in Boisvert and Stroeve (2015), derived from the infrared sounder AIRS, we also compute these regional averages for the satellite product (for the AMSR-E period) and the reanalysis ERA5[4], shown in Figure 6.22. The time spans are slightly different due to the availability of the AMSR-E data. Note the large spatial variability, especially for the AMSR-E satellite product, denoted by the error bars, indicating that this representation of trends falls short in describing the complexity of Arctic TWV trends. However, we can still compare the datasets here: the seasonal cycle of TWV (left panel in Figure 6.22) is evident in all datasets with higher values in May and October and the minimum in February. Reanalysis and AIRS agree very well in January and February while our satellite product is higher (about $1\,\mathrm{kg\,m^{-2}}$). Similar observations can be made in November and December. In May and October the reanalysis product is higher than both AIRS and our satellite data. In terms of trends (right panel), the differences between the three datasets are more pronounced, and are highest in November when the trends range from $-0.023\,\mathrm{kgm^{-2}}$/year (ERA5) to $0.183\,\mathrm{kgm^{-2}}$/year (AMSR-E satellite product) . While our satellite product shows positive trends in all months, the reanalysis data gives a negative trend in October and November. AIRS shows a negative trend in January and October but not in November and gives the lowest absolute trends compared to the other two datasets in all months except for November. To some extent the trends of the two satellite datasets are correlated, with both datasets providing higher

[4]Trends of the reanalysis data are obtained the same way as for the multi-parameter retrieval output dataset described in the previous section.

values in November, December and February than in the other months. The correlation with respect to the reanalysis is lower for both datasets.

We can learn from this comparison that the differences between satellite and reanalysis and between different satellite products are too large on this pan-Arctic scale to allow for confident statements regarding the magnitude of changes within one decade. But although the magnitudes vary, the different datasets do agree on the sign in most months, yielding an overall moistening. However, as we have seen in the previous section, trends can strongly vary from decade to decade. Additional intercomparisons of satellite products are needed as well as longer time periods in order to arrive at robust statements. Also, meaningful conclusions should be drawn on regional levels instead of Arctic-wide averages.

6.2.5 Outlook: Water Vapor Feedback

As outlook we like to explore how this new dataset can provide insights into the water vapor feedback. We hypothesize that three major regimes are prevailing in the Arctic, sketched in Figure 6.23. The first case is the one of low SIC where moisture is available and increasing temperatures will increase atmospheric TWV according to the Clausius-Clapeyron relation, i. e., about 7-9% increase in TWV per degree warming at 100% relative humidity[5]. In the second case SIC is high and the relative humidity is not saturated because there is no moisture source. The increase in atmospheric TWV with increasing temperatures will be less than what is predicted by Clausius-Clapeyron. In the third case SIC is high as well, but increasing temperatures increase atmospheric TWV according to the Clausius-Clapeyron relation because moisture is available from other, remote sources, e. g.,from meridional transport. As first example we show relationships between regional and monthly averages of the logarithm of the retrieved TWV, as well as SIC, presented in Section 6.2.3, and the 2-m monthly temperature anomalies from ERA5 for the same regions in Figure 6.24. As an illustration, we show data for January for three regions, the Barents Sea (left panel), the Beaufort Sea (center) and the East Siberian Sea (right). In the case of the Barents Sea, SIC is mostly below 50% and strongly and positively correlated with the 2 m air temperature (T2m) anomalies. ln(TWV) shows a strong positive correlation as well and an increase of about 5% per degree warming, thus this case is corresponding to the first, hypothesized regime. In the case of the Beaufort Sea, SIC is high and not correlated with the 2-m temperature anomalies. ln(TWV) is correlated neither, thus this case is corresponding to the second, hypothesized regime. In the case of the East Siberian Sea, SIC is high and not correlated with the 2-m temperature anomalies. ln(TWV) however is correlated to the 2-m temperature anomalies and increases by about 5% per degree warming, thus this case corresponding to the third, hypothesized regime. These are preliminary results. More cases and months need to be studied and methods to identify potential remote moisture sources need to be applied, e. g. using backward trajectories of air masses. Also, the presented relationships between SIC, TWV and T2m need to be verified using other satellite products. Further, the question needs to be answered whether temperature at other heights are more appropriate than T2m because of moisture inversions. Here, we merely want to illustrate the potential of deriving such relationships. They can help in understanding the water vapor feedback. Because we expect a decrease of SIC with rising Arctic temperatures, the rate at which TWV increases, and thus the strength of the water vapor feedback, can change as well, possibly depending on the region (or regime). Using the satellite data we may identify regions where we expect an accelerated change of TWV with decreasing SIC, and, consequently, an enhanced water vapor feedback.

[5]The upper limit of the increase given by the Clausius-Clapeyron relation is higher at low temperatures following the approximation given in Bolton (1980).

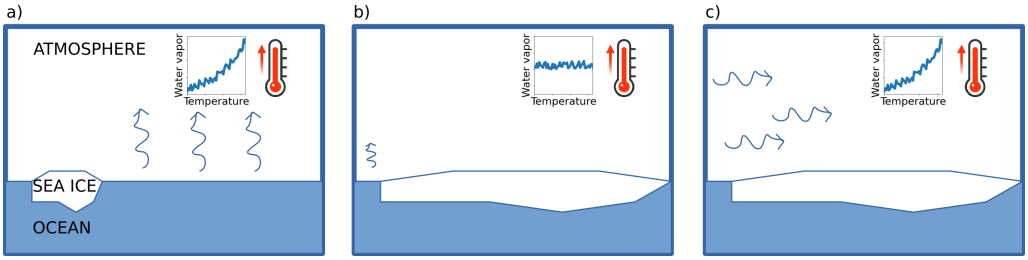

Figure 6.23: Hypothesized regimes of relationships between atmospheric total water vapor (TWV) and temperature. a) low sea ice concentration (SIC), high moisture availability, high correlation between temperature and TWV, b) high SIC, low moisture availability, low correlation between temperature and TWV, c) high SIC, high moisture availability, high correlation between temperature and TWV.

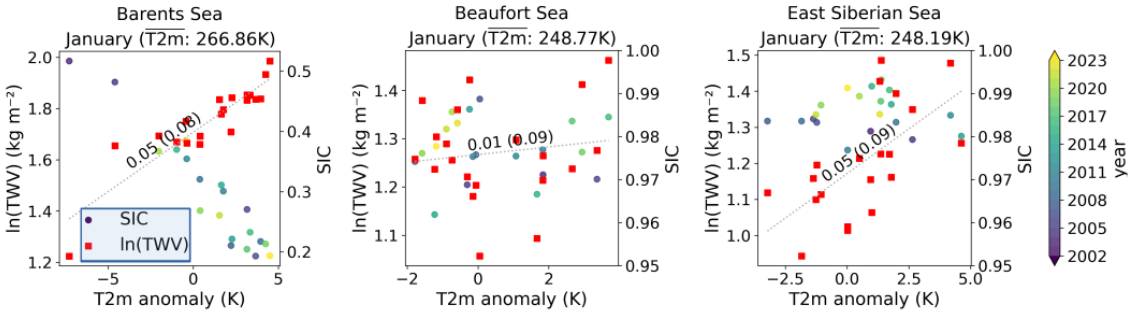

Figure 6.24: Scatter plots of regional and monthly averages of the logarithm of retrieved total water vapor (ln(TWV), red squares) against the monthly 2 m temperature (T2m) anomalies from ERA5 for the same regions for January. Circles show the sea ice concentration (SIC) compared against the T2m anomalies with colors denoting the year. Selected regions are the Barents Sea (left), the Beaufort Sea (center) and the East Siberian Sea (right). A linear least-square fit of ln(TWV) against T2m anomaly is shown as dotted line, where the number indicates the slope and the number in brackets the upper limit of the slope given by the Clausius-Clapeyron relation.

Chapter 7

Conclusions and Outlook

The protagonists of this thesis are sea ice, snow, atmospheric water vapor, cloud liquid water. We use their microwave emission and scattering properties to unravel the Arctic atmosphere and snow-covered sea ice. At the heart of this work lies the development of an improved forward model and multi-parameter retrieval method and its evaluation with a focus on atmospheric water vapor. In contrast to many single-parameter retrievals, the multi-parameter retrieval uses all frequency channels and polarizations and, thus, aims to fully exploit the information content available from the satellite measurements. In this thesis, atmospheric contributions are not considered as noise as done in sea ice concentration (SIC) retrievals but instead the method takes advantage of the information about liquid water path (LWP) and total water vapor (TWV) contained in the signal. Because it is not tuned to a specific geophysical parameter the multi-parameter retrieval may not be as accurate or precise as a single-parameter retrieval on one hand but on the other hand it provides a consistent set of parameters, enabling simultaneous analyses of several parameters. For the multi-parameter retrieval to be successful, the surface emissions need to be well represented in the forward model. For this we have studied the concept of surface emissivity, performed measurements of surface emissions, and related surface emission changes to changes in satellite SIC retrievals before we improved and evaluated the multi-parameter retrieval. The summary and conclusions presented here are structured according to the different chapters because the thesis covers these various dimensions. Main achievements are listed at the beginning of this chapter and are additionally highlighted in bold fonts in the text. Further research directions with regard to the multi-parameter retrieval method are considered in the second section.

7.1 Summary and Conclusions

The most important achievements of this thesis are:

I. Measurements of summer Arctic sea ice emissivities in the marginal ice zone.

II. An analysis of the effects of warm air intrusions on satellite sea ice concentration retrievals in a case study.

III. Improvements of a multi-parameter satellite retrieval using a microwave emission model of the Arctic snow and sea ice.

IV. An assessment of the performance of this retrieval with a focus on atmospheric total water vapor.

Snow, sea ice, atmospheric water vapor and cloud liquid water are the main players in the microwave regime. These protagonists and their role in Arctic amplification are introduced in Chapter 1, including the quantities they are measured in which are assessed in this thesis: SIC, snow depth (SND), TWV and LWP. The fundamentals of microwave remote sensing and the inverse method for the satellite retrieval are outlined in Chapter 2. A brief discourse about some inherent uncertainties of remote sensing and the ambiguity of a *ground truth* is included.

The ability of sea ice to emit electromagnetic radiation is often described by the emissivity which is measured in field studies and used in satellite retrievals. Seemingly straightforward, the concept of sea ice emissivity actually requires a nuanced analysis and is reviewed in Chapter 3. **We underline the importance of intrinsic assumptions when deriving the quantity emissivity and state under which conditions the resulting emissivities are more (or less) prone to these assumptions.** Chapter 3 also includes a literature review of measurements of Arctic sea ice emissivity and summarizes the therein used assumptions. Measurements of sea ice brightness temperatures (TBs) and emissivities from platforms other than satellites are rare. So in summer 2022 we set sail on the research vessel *Polarstern* to the marginal ice zone in Fram Strait. During that cruise we observed ice and ocean surface emissions at frequencies from 22 to 243 GHz with a ship-based instrumental setup using a novel mirror construction to switch between atmospheric and surface observations flexibly. Chapter 3.2 describes the measurement design and how emissivities are estimated, and summarizes the results: **In the summer marginal ice zone a clear distinction between open ocean and sea ice is found at frequencies between** 22 GHz **to** 31 GHz**, vertical polarization, and a large variability of ice emissivities is found at** 243 GHz**, horizontal polarization.**

We then bridge between surface emissions and satellite retrievals and analyze how the emissions of the snow-covered sea ice can change due to atmospheric events and how that subsequently impacts satellite retrievals of SIC in a case study in Chapter 4. The

presented case study is about two warm air intrusion events in April 2020 during the Multidisciplinary drifting Observatory for the Study of Arctic Climate (MOSAiC) expedition and combines satellite and in-situ observations as well as model results. **We find that the changes in surface emissions, which we attribute to large-scale surface glazing, are relevant for several SIC retrieval algorithms.**

The strong influence of the surface emissions on satellite retrieval (uncertainties) motivates Chapter 5, the heart of this thesis: **a physical model of the microwave emissions of sea ice and snow is incorporated into a satellite retrieval.** The forward model maps geophysical parameters to top-of-atmosphere TBs. **For the surface component of the forward model we establish an idealized layered snow and ice pack using literature data of snow and ice parameters such as density or salinity.** This new model extends the forward model used in previous works in a way that (empirical) surface emissivities, whose limitations have been mentioned above, are no longer needed. Because snow depth is included as new parameter, changes in TB related to this parameter can be simulated and **snow depth can be retrieved.**

To answer whether this model can simulate realistic (ranges of) TBs we need *ground truth* input parameters. Fortunately, we have the unique and extensive datasets acquired during the MOSAiC expedition as *ground truth* and can evaluate the new forward model against co-located satellite TBs between 6.9 GHz to 89 GHz that are measured by the satellite sensor AMSR2 since 2012 and have been measured by its predecessor AMSR-E from 2002 – 2012.

The model represents the temporal evolution and variability of TB from October to April well and the agreement is found to be especially good for the low-frequency, vertically-polarized TBs. For the higher frequencies at vertical polarization, especially for 89 GHz, the bias between model and satellite decreases from October to April, possibly related to snow metamorphism: our model setup could be more representative of a snowpack in the late winter season than at the beginning of winter.

Because of the Brewster effect, horizontally polarized TBs are more sensitive to changes in snow and ice properties which are not fully represented in our model. As expected, the agreement between model and satellite is indeed lower at this polarization.

As described above, the snow and ice model setup is idealized and each snow and ice layer has fixed internal parameters like correlation length or density based on literature and campaign data. The impact of the parameter choices on the simulated TBs depends on the interplay of the parameters and on the state (described by snow depth, temperature and ice type). **The uncertainties of the forward model are estimated using a Monte Carlo-like method.** The results of this uncertainty analysis exhibit about the same order of magnitude and frequency-dependence as the TB difference between model and satellite described above. **The majority of the deviations between model and satellite can therefore be explained by the model parameter choices.** For 89 GHz, horizontal

polarization, however, we find indications that not all sources of uncertainty are accounted for (e. g., scattering mechanisms).

The retrieval method, inversion by optimal estimation, is a Bayesian approach and provides consistent sets of nine retrieval parameters and their uncertainties, namely TWV, LWP, SIC, multiyear ice fraction, snow-ice interface temperature, snow-air interface temperature, sea surface temperature and wind speed (the latter two only over open water). The uncertainties from the Monte Carlo analysis are used as weights (in terms of the covariance matrix in the optimal estimation scheme) in the retrieval. As the method is limited with regard to independent measurements, a priori information about the state is needed and used in the inversion as constraints. Here, we use climatologies projected on an Arctic-wide grid to provide seasonally varying a priori data for each grid cell.

To investigate whether the new forward model improves the retrieval, the retrieval output is evaluated against the MOSAiC *ground truth*. For most points in time, the *ground truth* values lie within the retrieval uncertainty. The retrieved values, except for the snow-air interface temperature, differ from the a priori, i. e., the retrieval does not reproduce the a priori but provides additional information.

For the non-melting season (October to May), our four protagonists are evaluated further using additional campaign and station data and are compared against reference datasets, such as other satellite products or atmospheric reanalysis data. In summary, we find for SIC, SND, and LWP:

- **An excellent agreement for SIC in comparison to a reference dataset** containing scenes of 0% and 100% ice concentration. Good agreement, but spurious ice in open water areas is found compared to a reference satellite dataset. Because the deviations between the two satellite datasets are larger than the retrieval uncertainty we conclude to increase the retrieval uncertainty to 7%.

- **A promising SND retrieval**. Reference data is sparse but a comparison to airborne campaign data reveals a clear improvement compared to the climatological priori. Spatial patterns are as expected and for the late winter in good agreement with the reference satellite product. For the beginning of the freezing season, however, retrieved uncertainties are very high (15 cm in October, corresponding to relative uncertainties higher than 100%) and deviations to the reference product are high and show a high spatial variability.

- **Too high retrieval of LWP** in a comparison encompassing 20 years to ground-based station data. While the order of magnitude and the spatial patterns of LWP are comparable to reanalysis data, some areas are persistently featuring higher values likely due to the surface representation rather than actual atmospheric events. The MOSAiC data however shows that the method is sensitive to changes in LWP which motivates future studies.

We find cases with no true convergence in which the method retrieves the upper boundary of snow depth and flag this data as being highly uncertain. This is currently one of the main limitations of the method: **under certain conditions low TBs are observed by the satellite radiometer that the forward model fails to simulate.** While this affects usually only 1.3% of the daily data on average, in certain years and months this percentage is above 5%. The reasons for this shortfall need further research.

Chapter 6 centers around TWV. **The agreement between our dataset and campaign as well as radiosonde station data is convincing. Performance substantially improves compared to the previous version of the retrieval. We can compare TWV distributions and find satisfactory agreement in terms of the statistical parameters** such as mean and standard deviation because the radiosonde station datasets are large. Comparisons to the reanalysis ERA5 reveal differences between the retrieval from sensor AMSR-E and AMSR2. Additionally, we find that differences between our dataset and the reanalysis vary regionally, showing a dependence on the ice type, and from month to month.

The second part of Chapter 6 is an **investigation of spatiotemporal variabilities and trends of TWV based on our new satellite retrieval dataset spanning the years from 2002 to 2023.** In the winter months December to February, the atmosphere over the ice-covered Arctic Ocean is dry (for most areas below $4\,\mathrm{kg\,m^{-2}}$). Using the standard deviation over these months as measure of the variability of TWV we identified regions of higher and lower variability over sea ice. It lies between $0.5\,\mathrm{kg\,m^{-2}}$ to $2.5\,\mathrm{kg\,m^{-2}}$ and is higher in the regions closer to the ice edge. Over open ocean the variability is between $2.0\,\mathrm{kg\,m^{-2}}$ to $3.1\,\mathrm{kg\,m^{-2}}$. Spatially averaged time series of TWV reveal similarities and differences in TWV between the different Arctic regions and between our satellite retrieval and the reanalysis ERA5. The seasonal cycle is evident in all regions with maximum values in either October or May. As expected, the Central Arctic is the driest region and the Barents Sea, being not fully ice-covered, has a moister atmosphere and larger month-to-month variability. Using a straightforward measure of changes by taking the slope of a linear regression as metric, we investigate whether a region has become drier or wetter over the satellite time span. Because of the sensor differences revealed by comparisons to reanalysis data, we consider the time period of 2002–2011 (AMSR-E) and 2012–2023 (AMSR2) independently. For the first time span we additionally compare the changes of the new dataset with reanalysis data and another satellite product from the infrared sounder AIRS (Chapter 6.2).

In the AMSR-E period, the mean pan-Arctic TWV from our satellite retrieval is higher than the reanalysis and Atmospheric Infrared Sounder (AIRS) data for the months November to April. In terms of derived trends, our satellite data shows the strongest moistening in all months of the order of $0.05\,\mathrm{kg\,m^{-2}}$ to $1.8\,\mathrm{kg\,m^{-2}}$ per year. However, the main conclusion from this investigation is that **the spatiotemporal variability of trends is high**

and needs to be considered when analyzing TWV changes. As described above, we see an advantage in the possibilities of simultaneous analyses of several parameters, e. g., correlating sea ice loss and total water vapor change, a direction in research already taken in Chapter 6.2.5. We consider this mostly an advantage. However, there might be cases when changes in certain parameters obscure changes in others, e. g., are we observing actual changes in LWP or rather changes in surface conditions: this will be important for future works.

7.2 Outlook: Further Method Development

While working on the forward model and retrieval method, many ideas and suggestions evolved on how to improve the retrieval. Not all of them could be implemented, but they shall be collected here, for the sake of future researchers who may build upon our work. We also mention our suggested first steps for each aspect. We start with the forward model itself.

Forward Model In general, Monte Carlo-like methods may be used to find the most relevant forward model parameters and to focus the improvement on those. One major goal here is to achieve simulations of low TB as observed in certain areas over multiyear ice (MYI). Currently, too high snow depth and possibly too low TWV are retrieved in these areas. Aspects regarding the improvement of the forward model are:

- Forward model parameter choices - surface: the surface model contains many fixed model parameters. To some extent their influence on the modeled brightness temperatures is illustrated by the uncertainty analysis in Section 5.4.2. Some of the surface model parameters, e. g., the snow correlation length, could be adapted in the future using more accurate in situ data. Others, like ice thickness or snow density, might be parameterized as a function of, e. g., time, as they vary over the season. Here, the first step could be a thorough analysis of the MOSAiC SnowMicroPen (SMP) measurements to learn more about the correlation lengths and density of snow and their temporal evolution.

- Forward model parameters choices - atmosphere: like the surface model, the atmospheric model contains many fixed model parameters. Uncertainties of those atmospheric parameters could be estimated using other models like PAMTRA (Mech et al., 2020) in an inter-model comparison, which could be performed as a first step for typical Arctic conditions.

- Forward model parameterizations: All microwave emission models include a multitude of model choices. These include the calculation of the effective permittivity

of a dielectric mixture, the micro-structure representation or the solver of the radiative transfer equations. Inter-comparing MEMLS_ice and SMRT is a first step that could be taken to validate model choices. The SMRT model has an active community and includes even more model choices than the current implementation of MEMLS_ice[1].

- Forward model assumptions and limits: Only recently the SMRT model was evaluated for frequencies higher than 89 GHz for snow (Wivell et al., 2023). This is an interesting finding because, technically, concepts like the effective permittivity of a mixture imply that the wavelength is large with respect to the inclusions in the mixture. Exploring the (theoretical) limits of the parameterizations used in the forward model also for sea ice is a necessary next step, especially when frequencies higher than 89 GHz (upcoming satellite missions) will be considered. Also, scattering in the atmosphere is neglected. Scattering-allowing models like PAMTRA can be used to test this assumption for 89 GHz which is closest to the assumed limits of negligible scattering in microwave remote sensing. The assumption is certainly no longer true for a precipitating atmosphere, which, if the Arctic is transitioning to a rain-dominated regime as some studies suggest, might become more and more relevant. A first step is to introduce a quality flag tailored towards detecting rain.

- Surface and interface roughness: In order to treat surface roughness correctly in our model we need both realistic forward model parameter choices and a parameterization. What is the roughness of snow on sea ice at relevant length scales? How about the roughness at interfaces such as the snow-ice interface? How can we take into account the size of a satellite footprint, e. g., tilted surfaces? What are the limitations in our parameterizations when wavelength and roughness parameters are of the same order of magnitude? The first question may be answered in a first step using the data from a rapid photogrammetric method that was used during MOSAiC and ATWAICE campaigns to measure surface roughness.

Inversion Method Besides the forward model, the inversion method itself may be improved in various ways:

- A priori covariance: Work is underway to evaluate the impact of using both temporally varying variances (e. g. a lower variance of TWV in winter than in spring as derived from reanalysis) and correlations. Here, the state dependence of the correlations (e. g., different correlations of TWV and surface temperature depending on SIC) is a major challenge.

[1] Alas, it is currently too slow to be used in inversion method for large satellite datasets.

- Temporal and spatial correlations: currently, each satellite footprint is evaluated independently of its surrounding observations and of the observations of the same area at an earlier point in time. However, these observations are likely correlated. The amount by which a parameter can change from, e. g., one day to the next is more or less probable. Also, certain parameters are likely spatially correlated, although the correlation length scale might be small, as for snow depth and sea ice thickness (below 100 m (Itkin et al., 2023) or even unknown) and strong gradients do exist as well, especially in the marginal ice zone. It is feasible to include this information in the cost function by, e. g., punishing strong deviations from the average surroundings. This needs of course some care in order to avoid a bias and to still include true outliers, such as polynyas.

- Optimization scheme: currently the Levenberg-Marquardt method is used to minimize the cost function. The modular code setup that is now implemented allows exchanging this optimization scheme against others, e. g., statistical methods. In a first test they most often converged to the same solution but at higher computational cost, though they could be of interest for specific cases that are known to be challenging (e. g., the ice edge).

- Non-Gaussian probability density functions (PDFs): the method assumes that the retrieval parameter distributions are described by Gaussians. If the actual PDF is known one may transform this quantity to one which then is normally distributed. For example, if we would find out the LWP is best described by a log-normal distribution we may instead use the parameter exp(LWP) in our forward model.

- Positivity: similarly to the argument above we may consider transformations enforcing positivity of certain parameters like TWV or SIC.

- Spatial resolution: currently, the method uses the brightness temperature product resampled to the lowest spatial resolution. Techniques exist (e. g., Ludwig et al. (2020)) to merge finer and coarser resolution datasets in order to enhance the spatial resolution. These possibilities should be exploited in the future. Some of the discrepancies between in situ measurements and retrieval parameters can likely be attributed to the footprint size, see 2.3. It would be interesting to see whether higher resolution products would increase accuracy and precision.

- Dealing with uncertainties: We saw in Chapter 4 how ice layers on the snow, caused by warm air intrusions, influence satellite retrievals. As a first step, detection algorithms may be implemented to detect possible rain on snow events or warm air intrusions in order to set quality flags in the final satellite product that indicate higher uncertainties. The same holds for a precipitating atmosphere.

Extension to Summer Months In principle, the surface model does not account for melting conditions (like snow wetness or melt pond formation). Analysis of the summer data (Section 6.1.1) indicates that the method can still provide information about TWV. Here, optical retrievals (and more in situ data) are available and more studies need to follow to analyze summer data. It is worth testing whether changing the snow wetness model parameter can improve the results.

Extension in Frequency Space Finally, we want to point out the potential of combining our modular retrieval setup (Chapter 2.2) with upcoming satellite missions, like the Arctic Weather Satellite or the Copernicus Imaging Microwave Radiometry (CIMR). Our retrieval setup is modular, making it possible to extend it to more frequency channels. On one end of the spectrum this has already been demonstrated for a lower frequency observations (L-Band, i. e., 1.4 GHz, Scarlat et al. (2020)). The WALSEMA measurements presented in Chapter 3 on the other end may serve as a reference when incorporating the higher frequency channel at 243 GHz in the forward surface model. For the atmospheric part, the current model which neglects scattering can not be used but it can readily be exchanged against other atmospheric models.

Appendices

Appendix A

Angle of Transmission

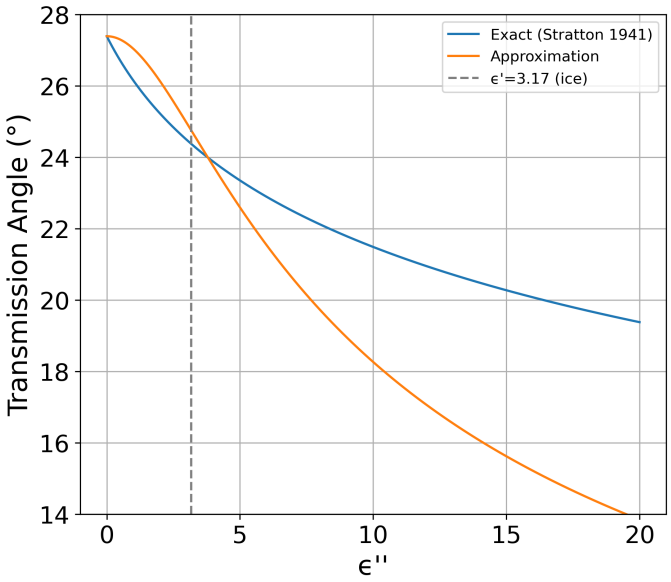

Figure A.1: Angle of transmission (θ_2) for radiation entering medium 2 from air (i. e., with permittivity $\epsilon_1 = 1$ and refractive index n_1) under an incidence angle of θ_1=55° depending on the imaginary part of the permittivity of medium 2 given by $\epsilon_2 = \epsilon' - i\epsilon''$ with $\epsilon' = 3.17$ (and refractive index n_2). Shown is the exact formulation following Stratton (1941) (orange line) and the approximation using $\theta_2 = \sin^{-1}(\sin\theta_1 \frac{n_1}{\mathrm{Re}(n_2)})$ (blue line).

Appendix B

MOSAiC Expedition Case Study

B.1 Site Perspective: Ground-based Radiometry

We focus on two microwave radiometers deployed during Multidisciplinary drifting Observatory for the Study of Arctic Climate (MOSAiC) observing the surface at 6.9 GHz, 10.7 GHz, 19 GHz and 89 GHz at horizontal and vertical polarization, similar to AMSR2. The radiometers made observations at incident angles between 35° and 75°. In this study, we show values observed at 45° (6.9 GHz) and 55° (19 GHz and 89 GHz). For this incident angle, the field of view (FOV) of the radiometers is around 6 m for 19 GHz and 89 GHz and 11 m (H-Pol) to 14 m (V-Pol) for 6.9 GHz. Details are provided in the supplemental Text S1 and Table B.1. Due to increased snow accumulation in front of the instruments after the warm air intrusions, the snow was much deeper around the ground-based radiometers compared to the surrounding MOSAiC floe. Especially during and after the second warm air intrusion, deep snow drifts formed in the FOV of some radiometers (Text S2, Figures B.3 and B.4).

B.1.1 Brightness Temperatures from Ground-based Radiometers

The brightness temperatures of the ground-based radiometers between April 15 and 21 are summarized in Figure B.1. All data shown in this figure is smoothed applying a running mean with a one hour window. The analyzed period can be divided into four phases. The gray shaded areas indicate the phases of the warm air intrusions with high TWV (see Figure 4.1) and high temperatures. The first phase is the period from April 15 to April 16, noon. In this period the first warm air intrusion hit the MOSAiC site. 2 m air temperatures are rising from −12°C to −2°C. Increased wind speed and (wet) snowfall led to changes of the snow cover. At, e. g., 6.9 GHz horizontal polarization (Figure B.1 (b)), fluctuations during the peak of the first warm air intrusion indicate here that surface properties in the FOV of the radiometer changed and that there might be already some low amount of liquid water building in the uppermost layer of the snowpack. However, these fluctuations

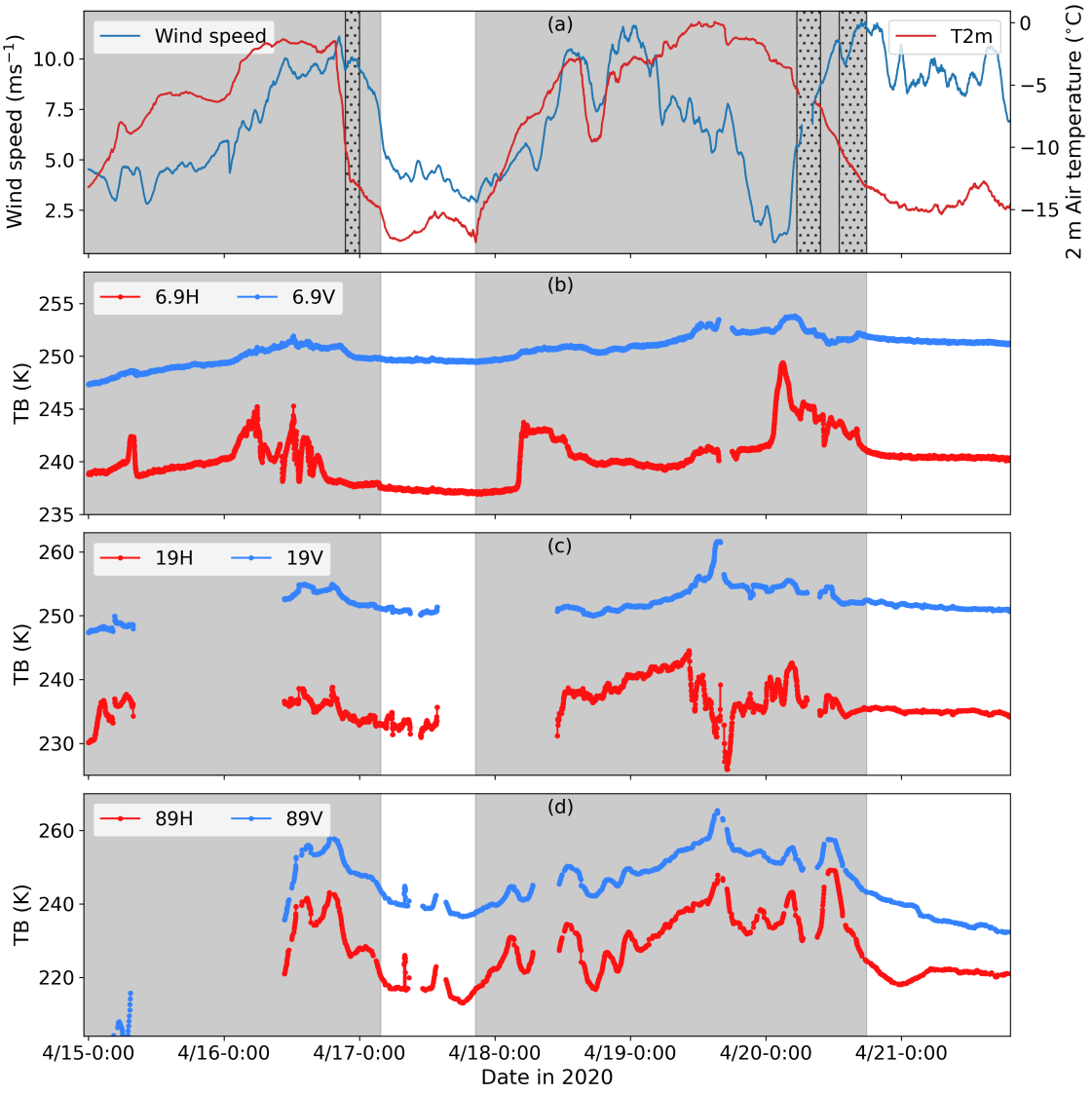

Figure B.1: Meteorological conditions and brightness temperatures observed by the ground-based radiometers during the events. (a) 2 m air temperature (T2m) and 10 m wind speed during the warm air intrusions. In addition, three major snowfall events are highlighted (see Figure 4.1). Rows (b) – (d): Observed brightness temperatures for vertical (V) and horizontal (H) polarizations for 6.9 GHz, 19 GHz, and 89 GHz, respectively. Background shading indicate the four different phases for cloudy (gray) and clear sky (white) conditions.

can also be caused by snow dune wandering through the FOV of the radiometer. At 19 GHz horizontal polarization, no such fluctuations are visible. These measurements were taken several meters apart from the 6.9 GHz observations and thus the snow conditions could have been very different during the first storm event. While the average brightness temperature at lower frequencies (6.9 to 19 GHz) is only slightly increasing, a strong increase can be found at 89 GHz (Figure B.1 (d)), indicating that mainly the temperature of the upper snow layer changed (89 GHz has the lowest penetration depth), which is consistent with Figure 4.5.

The second phase, between April 17 and April 18 is marked by a rapid cooling below −15 °C, clear sky and calm conditions. Brightness temperatures at all frequencies are stable during this phase with a slight cooling at 19 GHz and a strong drop in brightness temperature at 89 GHz.

The third phase marks the second, stronger warm air intrusion where the 2 m air temperature reached 0 °C. Strong changes for horizontally-polarized TB at all frequencies indicate changes in the snow surface due to snow fall and drift as well as accumulation and possible formation of liquid water in the snow. However, during this period, increased snow accumulation around the instruments complicate the interpretation of the data at the remote sensing site as the exact timings of snow dune formation are unknown.

Of special interest is the fourth phase, the period right after the second warming event, where a strong decline in brightness temperatures is observed at higher frequencies. At 89 GHz, brightness temperatures at both polarization start decreasing around April 20, 11:00. After 14:00 and until 18:00, brightness temperatures at horizontal polarization decrease much faster than at vertical polarization, leading to an increase in polarization difference similarly to what was observed from the satellites (Figure 4.4). We note that the start of this pronounced decrease coincides with a snowfall event, indicating that there could have been snow dune formations. However, in the case of snow drift through the FOV of the radiometer, we would expect higher temporal variability at H-pol. Instead, brightness temperatures decrease in an almost monotonic way.

At the lower frequencies, this drop in TB H is less pronounced. In contrast to the satellite observations, the PD(89) of the ground-based observations recovers after less than one day and thus much faster than the satellite measurements. A likely explanation is the accumulation of snow in front of the ground-based radiometers, which does not occur on the satellite scale. This already highlights the need of auxiliary data when using ground-based measurements to interpret satellite data due to the local snow conditions. Unlike the snow drifts that accumulated in front of the instruments, most of the level ice on the floe-scale did not experience accumulation during this event.

B.1.2 Model Experiment On-ice Site: Simulation of a Glaze Ice Layer

Similar to the simulations of the SnowMicroPen (SMP) profiles (Section 4.1.3), we perform an experiment with simulating the effect of a glaze ice layer in the FOV of the radiometers. In the model, the glaze ice layer is approximated by a thin, radiometrically flat ice layer (≤ 1.6 mm) at top of the snowpack. The setup is chosen such that the model can reproduce the observed PD changes from the ground-based radiometer at 6.9 GHz and 89 GHz during phase 4, i. e., the clear sky phase after the second warm air intrusion (fourth phase in Figure B.1). As discussed earlier, during this phase, the increase in PD at 89 GHz cannot be explained by cloud forcing and is most likely due to the formation of a glaze ice layer in the FOV of the radiometer.

For the experiment we simulate an ice layer that starts developing at April 20 at around 14:00 and grows up to 1.6 mm until 20:00. After that we allow a layer of new snow to accumulate on top of this ice layer in order to reproduce the decrease in PD(89) from April 21 at 03:00 onward. We know of the increased snow accumulation in front of the instruments due to snow drift formation as wind speed was high during this period (Figure B.1), however the exact timing of new snow accumulations remains a unknown. The reflectance data from the terrestrial laser scanner (TLS) scan on April 22 shows that a glaze ice layer is not visible anymore in the FOV of the radiometers by this date. Figure B.2 shows the observed and simulated brightness temperatures between April 20 14:00 and April 21 08:00. With this set-up it is possible to reproduce the observed increase of polarization difference at 89 GHz indicating that indeed the formation of a glaze ice layer likely explains the strong increase in observed PD 89.

In summary, the temporal development of microwave brightness temperatures measured by the on-ice radiometers and especially their polarization difference can be explained if a thin glaze ice layer is added in the microwave emission model. Such a glaze layer actually was observed in the field. The effect of the glaze ice layer is larger at higher frequencies and mainly affect the polarization difference.

B.1.3 Supplemental Text S1 - Ground-based Radiometer Observations

We focus on two microwave radiometers deployed during MOSAiC observing the surface at frequencies ranging from 6.9 GHz to 89 GHz, similar to AMSR2. Details are provided in Table B.1. They were installed next to each other on the ice facing the same area but the footprints do not overlap (see Figure B.5). The low-frequency system of HUTRAD (Helsinki University of Technology Radiometer) (Hallikainen et al., 1996; Colliander et al., 2007; Lemmetyinen et al., 2009) measures at three frequencies at 6.825, 10.65 and 18.7 GHz, at two orthogonal polarizations H and V. During MOSAiC, HUTRAD had a sampling rate of 1 s, the dataset used here was averaged to 1-minute temporal resolution in order to decrease fluctuations. HUTRAD was observing at a fixed incident angle of

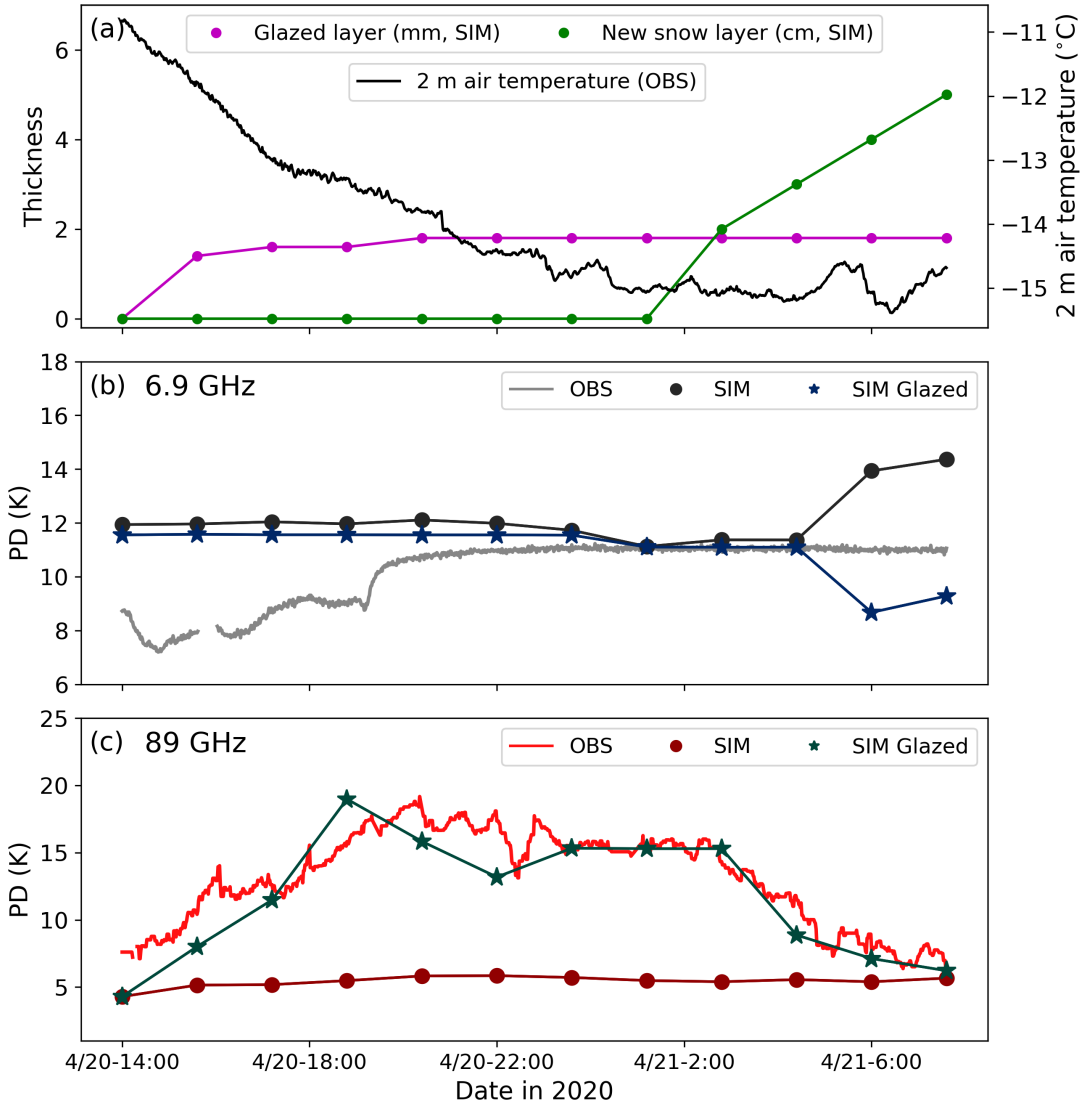

Figure B.2: Model experiment adding a glaze ice layer on top of the snowpack. The model experiment covers parts of phase 4 after the second warm air intrusion (see Figure B.1). Panel (a) shows the observed 2 m air temperature. In addition the glaze and snow layer setup used for the simulations (SIM) is shown. Panel (b) and (c) show the observed (OBS) and simulated (SIM) brightness temperatures for PD 6.9 (b) and PD 89 (c). (SIM) refers to the simulations without and (SIM Glazed) to the simulations with the glaze layer included in the model setup.

Table B.1: HUTRAD and SBR radiometric properties: Shown are frequency (GHz), polarization P, radiometric bandwidth BW (MHz) and sensitivity (K), incidence angle θ (degree), field of view (FOV) given by the half power beam width (degree) and the FOV on the ground (cm) based on an instrument height of 0.8 m (HUTRAD) and 1.1 m (SBR)

	HUTRAD				SBR	
Frequency (GHz)	6.9		10.7		19	89
Polarization	H	V	H	V	H/V	H/V
Bandwidth (MHz)	310	310	120	120	1000	4000
Sensitivity (K)	0.09	0.11	0.24	0.22	0.04	0.08
θ (°)	45	45	45	45	55	55
Field of View (°)	11.2	14.8	6.6	9.1	6	5.88
Field of View (cm)	22 × 32	30 × 42	13 × 19	18 × 26	20 × 35	20 × 35

45°. With an instrument height of 0.8 m the largest footprint size (at vertically-polarized 6.9 GHz) is 30 cm × 42 cm. The radiometer was deployed at a fixed location during the whole period investigated. The uncertainty (i.e., 2× standard deviation) of the calibrated brightness temperature is estimated to be around 3 K. The internal temperature control of the 18.7 GHz receiver failed early on in the MOSAiC campaign, which made measurements unstable and unusable for our investigation. The surfaced-based radiometer from University of Manitoba (SBR) observes at 19, 37 and 89 GHz (Radiometrics, 2004). Radiometric properties are provided in Table B.1; for more detailed specifications see Table 1 in Derksen et al. (2012). The SBR was measuring in scanning-mode with incident angles varying from 40° to 70° in 5° steps. The sampling rate varies between 1 s and 5 s. For this study, we only used the measurements at 55°, as most data were collected at this angle. The footprint size is about 20 cm × 35 cm (assuming 1.1 m instrument height). Similar to HUTRAD the SBR data are resampled to 1-minute temporal resolution. The uncertainty of the observations at 89 GHz is similar to the lower frequencies (6 K for horizontally and 5 K for vertically polarized TB). Unfortunately, during leg 3, the 37 GHz receiver was not functioning. As the 18.7 GHz horizontally polarized channel from HUTRAD was unstable during our period of interest, we used the data from SBR which measures at 19 GHz. During the first warming event some values from SBR (between two calibrations) had to be removed because they showed unrealistic fluctuations. Corrupted scans and data points with clearly non-physical values were filtered out manually for Figure B.1. Figure B.5 illustrates the formation of snow dunes in front of the radiometers that further increase the local (intra- and inter-footprint) variability of the snow conditions.

B.1.4 Supplemental Text S2 - Glaze Layer Observations

Figure B.3 shows the TLS reflectance for April 17 and April 22. Glaze ice areas have low TLS reflectance (dark purple colors) in the near-IR due to increased absorption and specular reflections. On April 17, only a few patchy glaze ice areas are present (for example the dark purple patch in the upper right) and none are within the instruments' footprints.

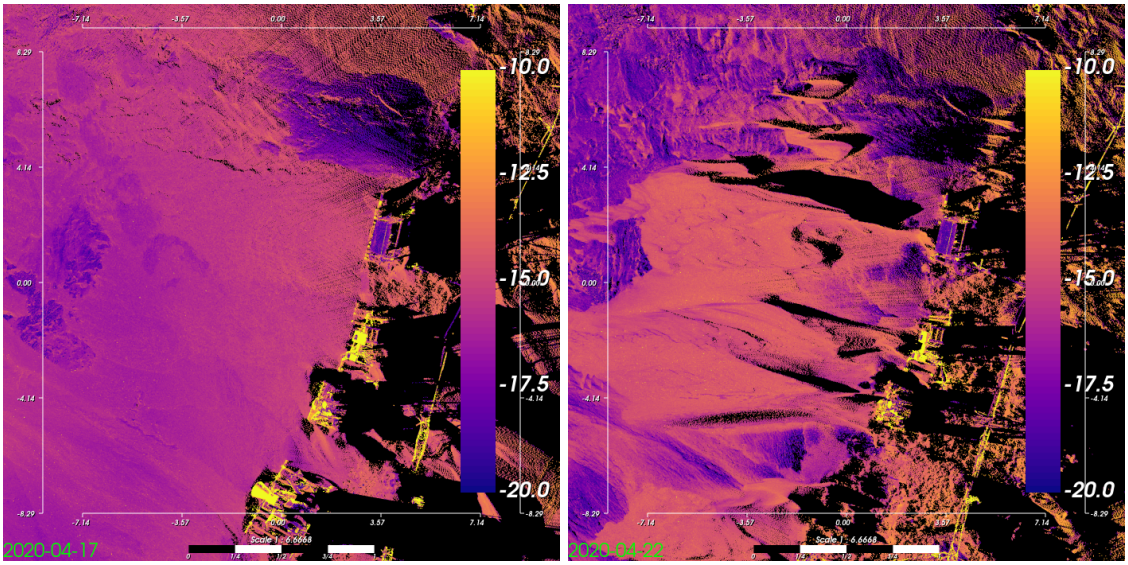

Figure B.3: Terrestrial Laser Scanning (TLS) reflectance near the HUTRAD and SBR instruments. Glaze snow surfaces are on April 17 (left) and April 22 (right). Scale bars are in meters.

On April 22, widespread glazing was observed on unaltered snow surfaces (upper portion of figure). However, the snow drifts that formed in the instruments' footprints were not glazed. The glazing was also evident from visual observations. Figure B.4 shows the glaze snow surfaces observed on April 22 at the remote sensing site (Figure B.4, left). The snow in front of the radiometers is freshly accumulated. Also on pictures from the panorama camera mounted on *Polarstern*, the glazing was visible at April 22 (Figure B.4, right).

B.1.5 Supplemental Text S3 - MEMLS_ice Initialization

MEMLS_ice is a microwave emission model for layered snow and ice to simulate the upwelling brightness temperatures of a snow-ice system in the microwave regime, based on its dielectric properties. The model needs several snow and ice properties as input data. For the snow, most of these properties like density, exponential correlation length or temperature can be obtained from SnowMicroPen and snow pit samples, while some parameters like snow wetness or interface roughness have to be assumed. The roughness is modelled by the modification of the interface reflectivity following Choudhury et al. (1979). In principle, a glaze layer can lead to coherent reflections in the microwave regime. However, as we do not have enough information about the thickness and uniformity of that ice layer, we do not calculate coherent reflections in our modelling of the glaze layer. Note that coherence is in principle implemented in MEMLS but deactivated for our purposes.

During the warm air intrusion events, one ice core sample was taken at April 17 in the vicinity (approximately within 100 m) of the remote sensing site. We use this ice core as first guess for the sea ice properties and then slightly varied the salinity and density profiles to obtain brightness temperatures at 6.9 GHz that are similar to the ground-based

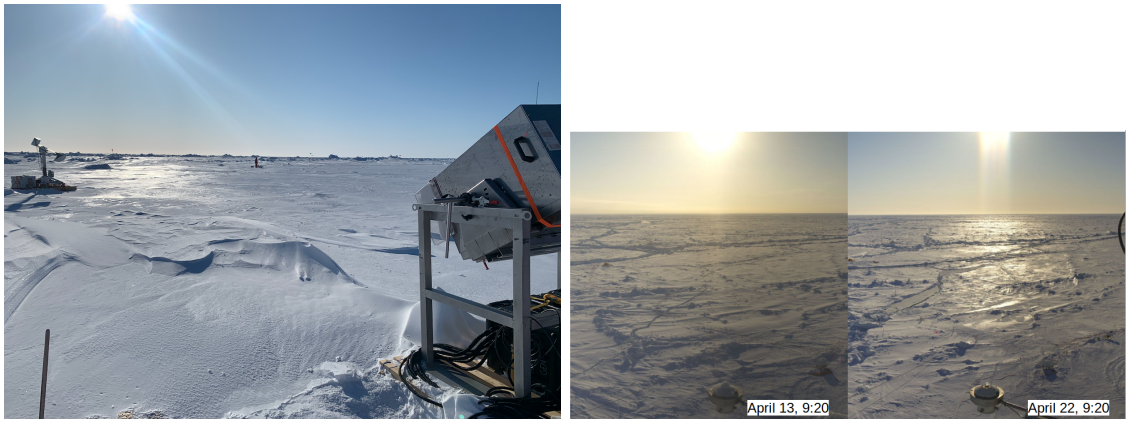

Figure B.4: Visual observations of the glazing. Left: Image from April 22 at the remote sensing site (photo: Lars Kaleschke). Right: panorama image from Panomax webcam onboard Polarstern (https://www.mosaic-panorama.org/) from April 13 and April 22.

radiometer observations before the warm air intrusion. For all layers, the deviations from the ice core samples are less than 1 ppt for salinity and less than $50\,\mathrm{kg\,m^{-3}}$ for the density. Also note that the Central Observatory was on second-year ice (with a low amount of salinity in the upper layers) at the beginning of the expedition in 2019 but that there was new ice formation during the winter. On the satellite footprint scale a mixture of second- (dominating) and first-year ice prevailed. Except for the ice temperature, for which a linear fit is used between the snow/ice and ice/ocean interface temperatures, the ice profile properties are kept constant for the whole time series. Since the warm air intrusions were short-term events and the temperature at the snow-ice interface only changed slightly, this assumption is valid. Table B.2 shows the initialization profile for April 08 07:40 based on the SMP profile S49M2235 (Macfarlane et al., 2021) for 6.9 GHz. Density and SSA were provided in the SMP data. The exponential correlation length was derived from snow density and SSA measurements following Mätzler (2002). At the microwaves frequencies investigated here, only the upper ice layer is relevant due to the high absorption in the ice. Therefore, only the upper 40 cm of the ice are shown (bottom five rows in Table B.2). The model was initialized with 2 m thick ice. Thus there is no influence from the ocean below. The downwelling sky temperature is calculated with the radiative transfer model PAMTRA (Mech et al., 2020) using the HATPRO TWV and LWP data as well as profiles from radiosondes launched during MOSAiC.

Note that the snow height from the SMP profiles was usually lower than the snow in the field of view of the radiometers due to enhanced snow accumulation. The TLS scan data provides accurate relative differences of snow height. In order to obtain absolute values, we used the measurement of the maximum snow dune height with a ruler stick on April 22, namely 90 cm as reference point. The acquired snow depths are in agreement with other manual ruler stick measurements of snow height performed close to the radiometer footprints. Table B.3 shows the snow height at the different sensors from TLS scans from

Table B.2: Initialization profile for the MEMLS_ice simulation for April 08 07:40 for 6.9 GHz. Shown are the parameters: layer thickness LT (cm), temperature T (K), sensity ρ (kg m^{-3}), exponential correlation length pc (mm), wetness W, salinity S (ppt), interface roughness R (mm). Parameters used for fitting the simulations are shown in *italics*. The downwelling sky temperature at 6.9 GHz is 6.1 K

Depth	LT	T	ρ	pc	W	S	R
0	2.1	250.1	269.8	0.292	0	0	0
2.1	3.3	250.9	374.6	0.344	0	0	0
5.4	4.0	251.9	311.5	0.298	0	0	0
9.4	2.8	252.5	299.0	0.271	0	0	0
12.2	2.0	252.8	287.7	0.271	0	0	0
14.2	3.0	253.0	287.7	0.271	0	0	0
17.2	2.1	252.9	312.8	0.299	0	0	0
19.3	3.0	252.8	264.6	0.203	0	0	0
22.3	8	253.0	*880*	*0.450*	0	*3.08*	*2.20*
30.3	8	253.5	*880*	*0.450*	0	*2.93*	0
38.3	8	253.2	*880*	*0.450*	0	*2.80*	0
46.3	8	253.4	*880*	*0.450*	0	*2.66*	0
54.3	8	253.6	*880*	*0.450*	0	*2.50*	0

Table B.3: Average snow height (cm) in the FOV of the different channels (GHz) at April 17 and April 22

Date	6.9	10.7	19	89
April 17	48	46	45	44
April 22	48	53	46	71

April 17 and April 22. Figure B.5 shows the surface elevation at April 22 based on a TLS scan. In addition, the FOV of the different frequencies of the ground-based radiometers is shown. High snow dunes were forming during the second warm air intrusion in front of the radiometers.

B.1.6 Supplemental Text S4 - SMP-based Modelling

Figure B.6 shows the simulated brightness temperatures at different frequencies for the time period before the warming events (April 08 to April 15, blue) and after the warming events (April 21 to April 27, red). For the simulations, the SMP profiles were averaged to layers of at least 2 cm thickness. To maintain the layering in the snowpack, snow type classifications provided by Kaltenborn et al. (2022) were used for the initial step. Strong changes in simulated brightness temperatures are visible at all frequencies. At 6.9 GHz and 19 GHz, brightness temperatures are higher after the warming events caused by a generally higher snowpack temperature. In contrast, at 37 GHz, increased scattering due to snow metamorphism leads to a decrease of brightness temperatures. Note that no glaze layer was used in these simulations.

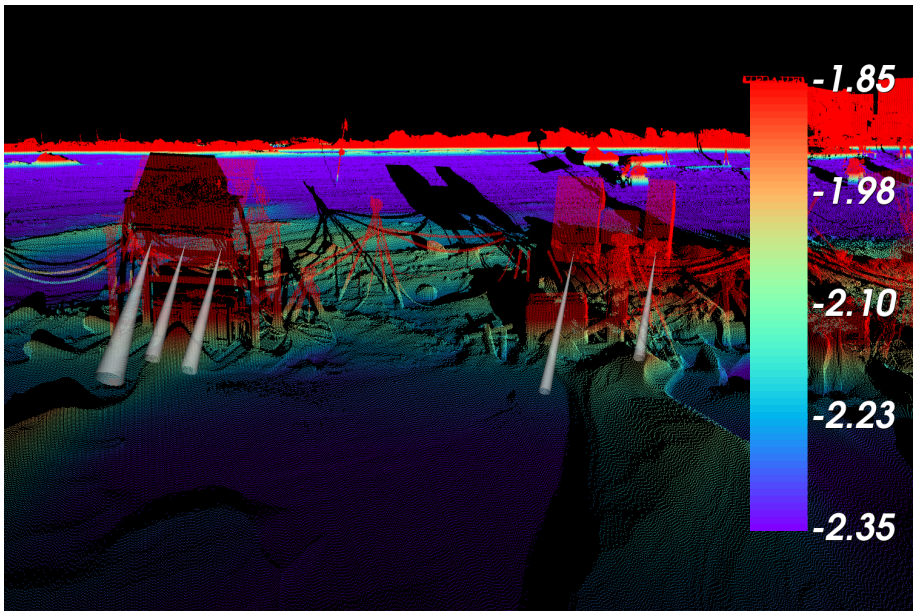

Figure B.5: TLS surface height with respect to the laser scanner (height: 2.5 m) from April 22. The cones indicate the viewing direction if the different sensors. From left to right: HUTRAD frequencies (GHz): 10.7, 18.7 (not used), 6.9, SBR frequencies (GHz): 19, 89.

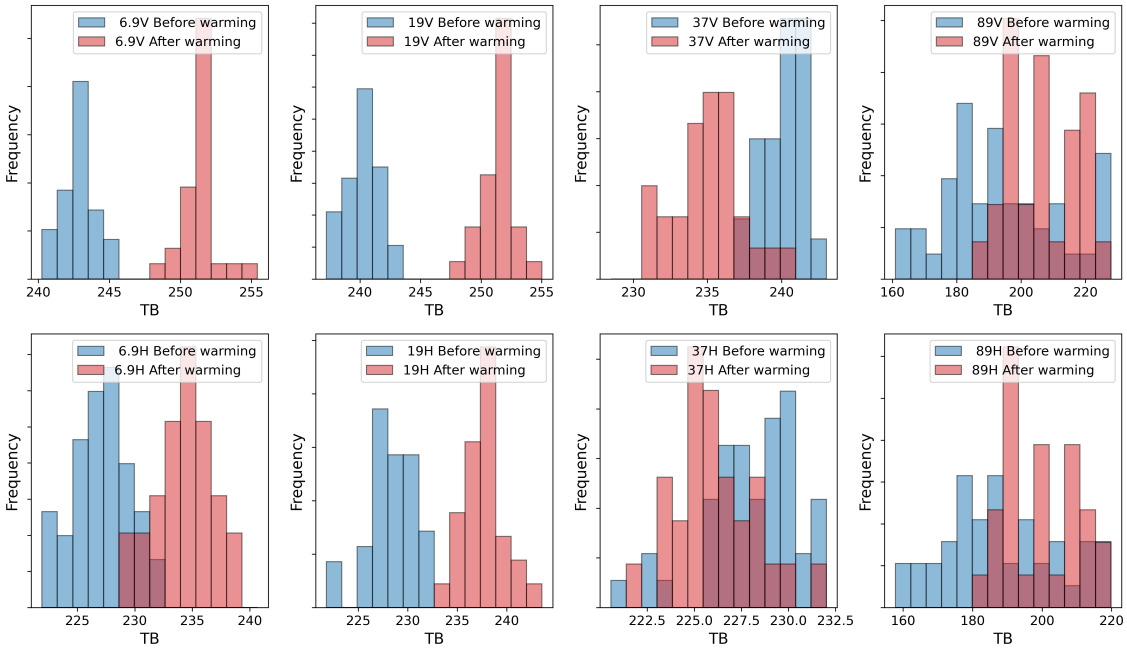

Figure B.6: Simulated brightness temperature from SnowMicroPen (SMP) profiles. The data are split into the periods from April 08 to April 15 (blue) and April 21 to April 27 (red).

Appendix C

Multi-parameter Retrieval

C.1 Brightness Temperature Comparison: RRDP

Table C.1: Results from the evaluation of the forward model performance using RRDP data as input. From the RRDP, *ground truth* data is taken as input for the forward model. The simulated TBs are compared to the corresponding satellite measured TBs included in the RRDP and mean absolute error (mae), bias and r^2 are listed in this Table. The total number of data points is 530 (for each frequency)

Frequency/Polarization	mae	bias	r^2
6.9 V	1.15	1.00	0.93
6.9 H	4.80	-4.53	0.43
10.7 V	1.50	1.05	0.88
10.7 H	5.45	-5.10	0.49
18.7 V	3.30	1.16	0.66
18.7 H	5.08	-3.60	0.52
23.8 V	4.68	0.92	0.60
23.8 H	5.46	-1.84	0.55
36.5 V	7.09	-1.39	0.54
36.5 H	7.16	-0.85	0.51
89.0 V	5.83	-2.62	0.55
89.0 H	6.25	0.88	0.52

C.2 Sea Ice Extent

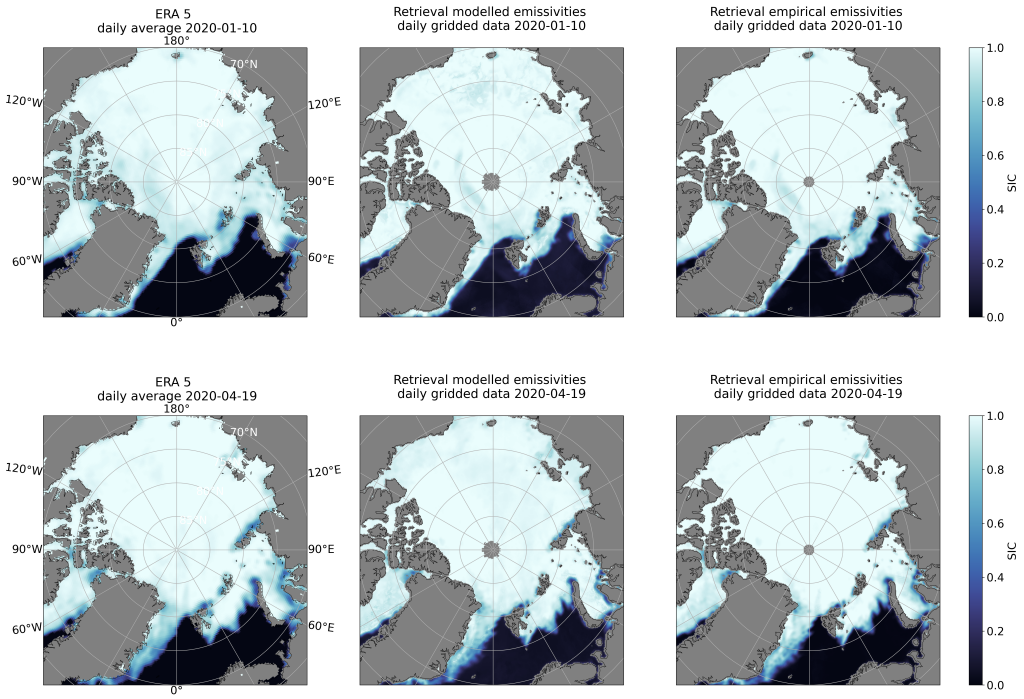

Figure C.1: Sea ice concentration on January 10, 2020 (top row) and April 19, 2020 (bottom row) from ERA 5 (left), the retrieval using modeled emissivities (center) and the previous version using empirical emissivities (right).

C.3 Uncertainties

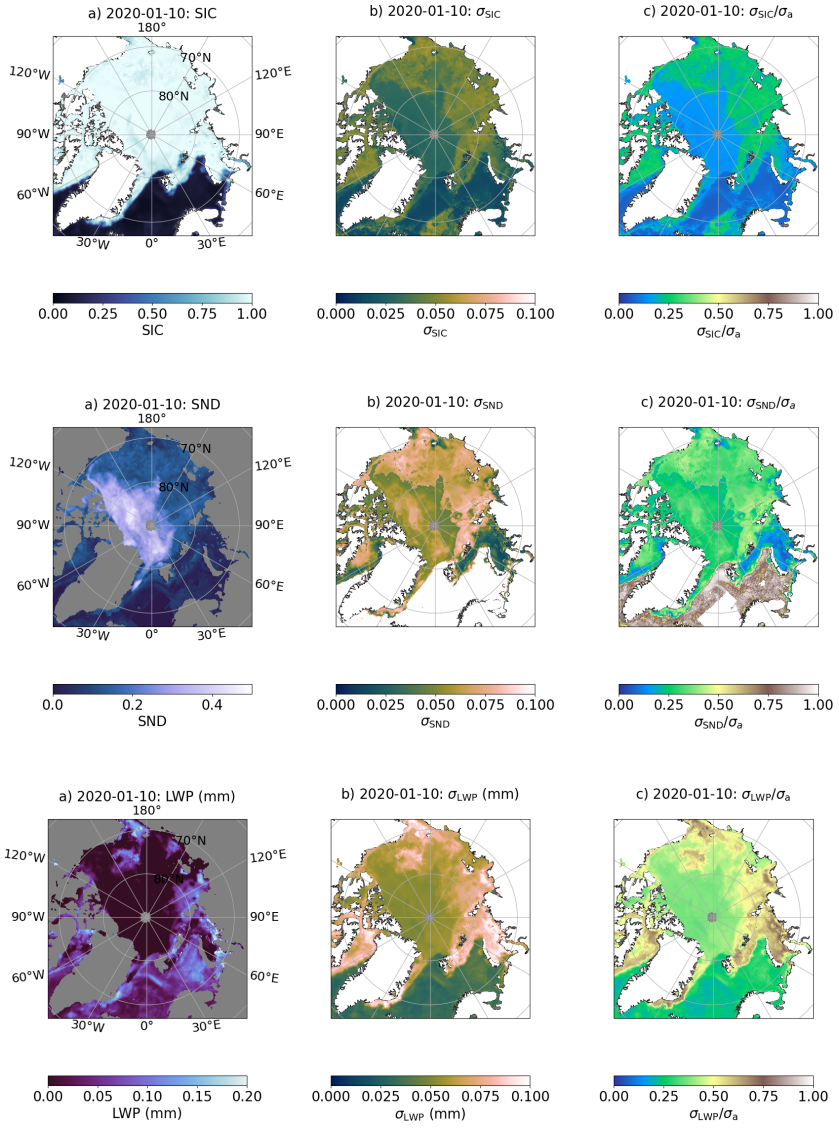

Figure C.2: First row (i): Daily gridded map of retrieved sea ice concentration (SIC, left) for January 10th, 2020, retrieved uncertainties of SIC as one standard deviation (center) and the ratio of retrieved uncertainty to the a priori uncertainty (right). Second (ii) and third (iii) row: same as first row but for snow depth (SND) and liquid water path (LWP).

C.4 Shortfall of the Retrieval

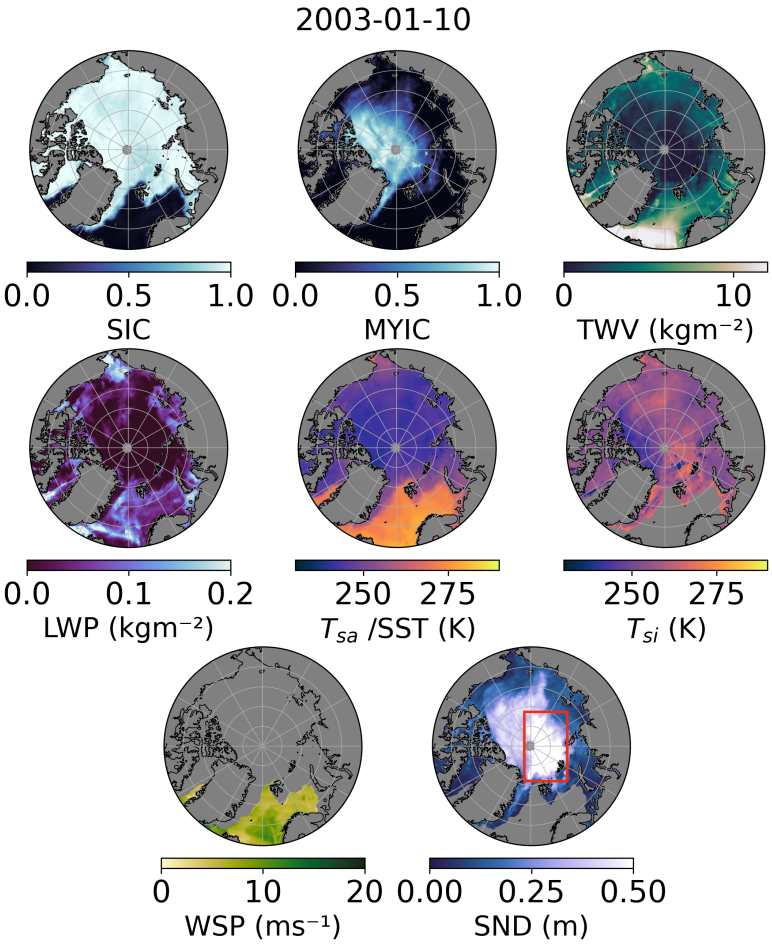

Figure C.3: Retrieved parameters, gridded and resampled from daily AMSR2 swath data from January 10th, 2003. Shown are sea ice concentration (SIC), multiyear ice concentration (MYIC) obtained by multiplying the multiyear ice fraction with SIC, total water vapor (TWV), and liquid water path (LWP), as well as the surface temperature as average (weighted by SIC) from the snow-air interface temperature T_{sa} over ice and the sea surface temperature (SST) over open water, the snow-ice interface temperature (T_{si}, shown only in areas where SIC $>$ 15%), wind speed (WSP, shown only in areas where SIC $<$ 15%) and snow depth (SND, shown only in areas where SIC $>$ 15%). The area with very high snow depth (50 cm is indicated by a red rectangle in the SND map.

C.5 Monthly Maps

C.5.1 Multiyear Ice Fraction

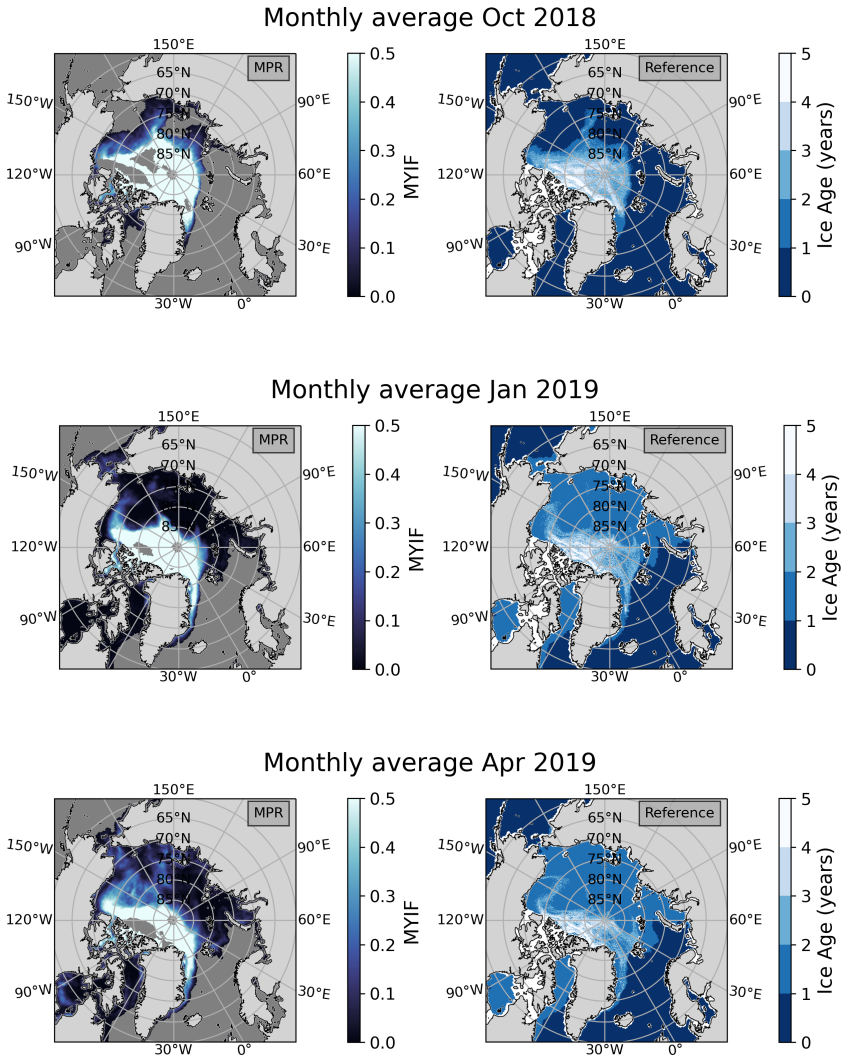

Figure C.4: Maps of monthly average of retrieved multiyear ice fraction (MYIF, left) from the multi-parameter retrieval (MPR) compared to the reference sea ice age product, Version 4, provided as weekly estimates by the National Snow and Ice Data Center (NSIDC) based on satellite-derived sea ice extent and sea ice motion (Tschudi et al., 2019).

C.5.2 Surface and Interface Temperature

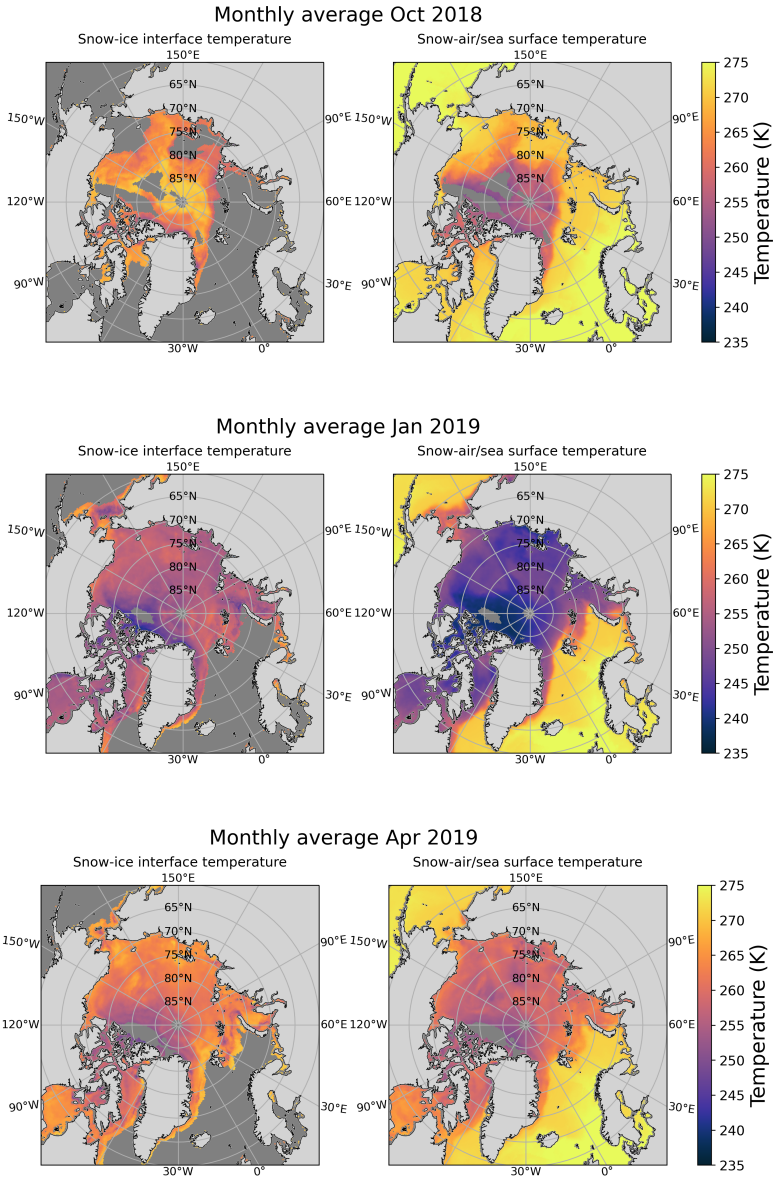

Figure C.5: Maps of monthly average of retrieved snow-ice interface temperature (T_{si}, left, only displayed where monthly mean sea ice concentration is higher than 15%) and a retrieved surface temperature given by the average of the snow-air interface temperature (T_{sa}) and the sea surface temperature (SST) weighted by the retrieved sea ice concentration.

Appendix D

Water Vapor Retrieval Evaluation

D.1 Evaluation with Observational Data from ATWAICE

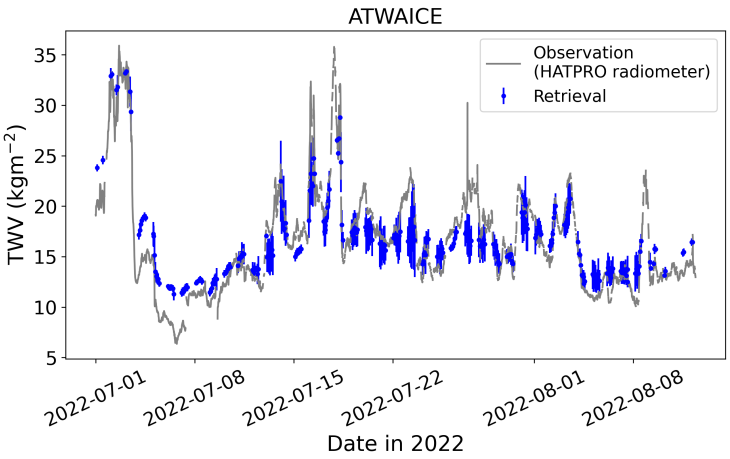

Figure D.1: Time series of retrieved total water vapor (TWV, blue) and radiometer measurements (grey, resampled to 10 minutes) from the ATWAICE campaign 2022. For every overpass, the retrieval data was averaged within a 50 km radius, the spatial variability within that radius is shown as error bar (given by the standard deviation).

D.2 Land Stations: Radiosondes

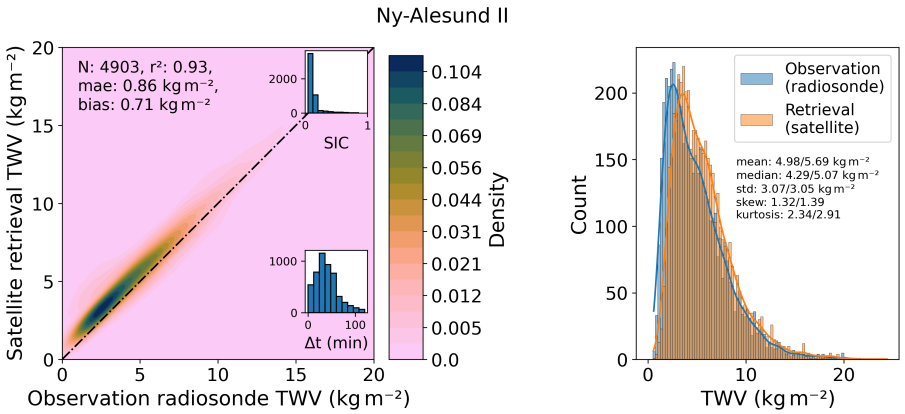

Figure D.2: As Figure 6.9 but for the site Ny-Ålesund at the west coast of Spitsbergen, Greenland Sea.

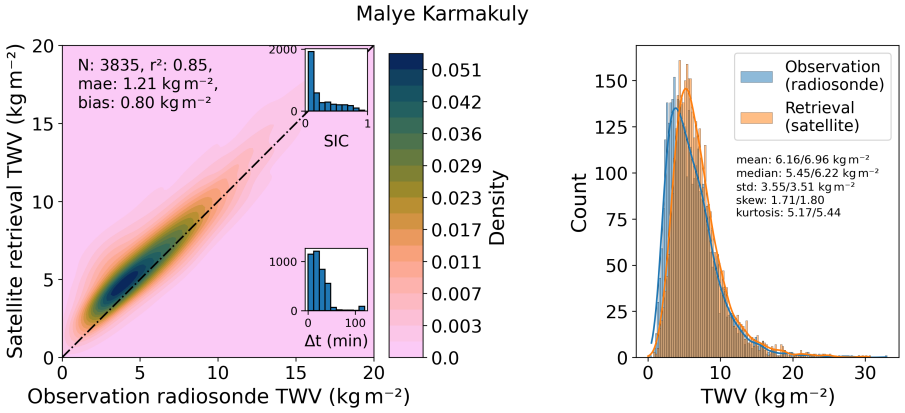

Figure D.3: As Figure 6.9 but for the site Malye Karmakuly at the west coast of Novaya Zemlya, an island between Barents and Kara Sea.

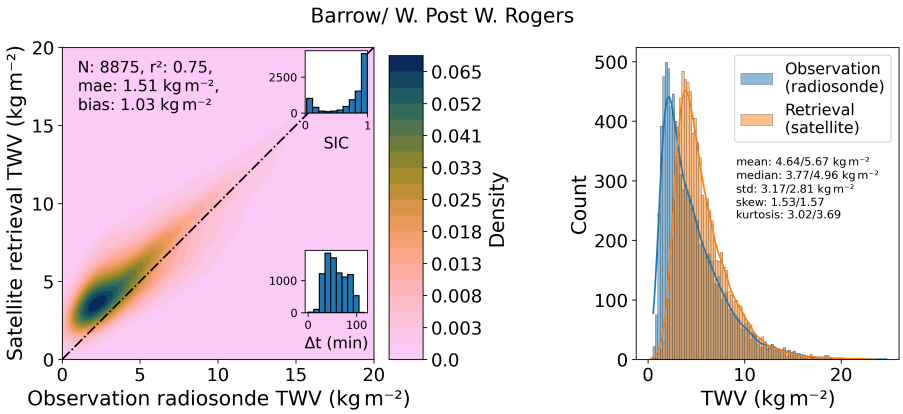

Figure D.4: As Figure 6.9 but for the site Utqiaġvik, formerly known as Barrow, Alaska at the coast to the Beaufort Sea/Chukchi Sea.

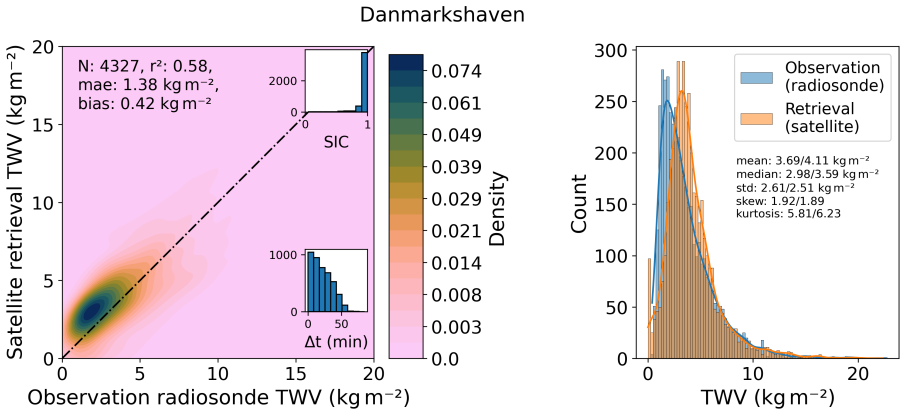

Figure D.5: As Figure 6.9 but for the site Danmarkshaven, at the east coast of Greenland (Greenland Sea).

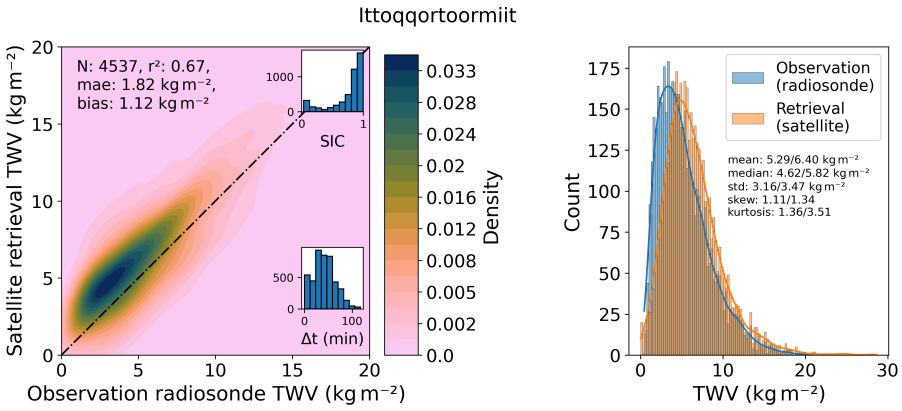

Figure D.6: As Figure 6.9 but for the site Ittoqqortoormiit, at the east coast of Greenland (Greenland Sea).

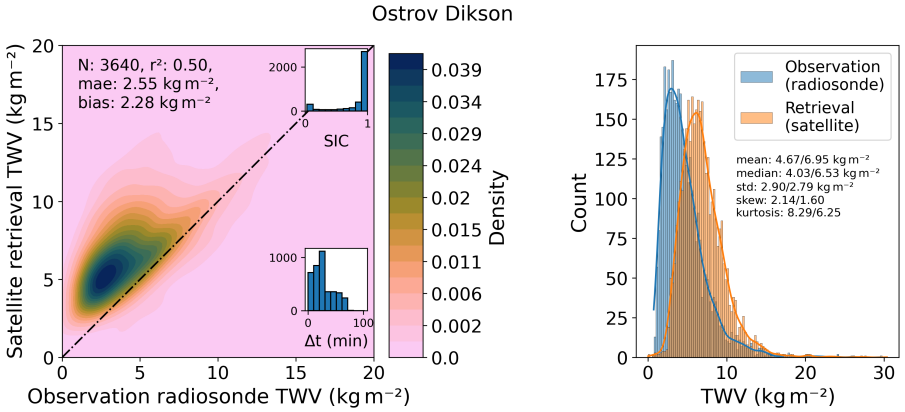

Figure D.7: As Figure 6.9 but for the site Ostrov Dikson on an island in the Kara Sea near the mouth of the Yenisei River.

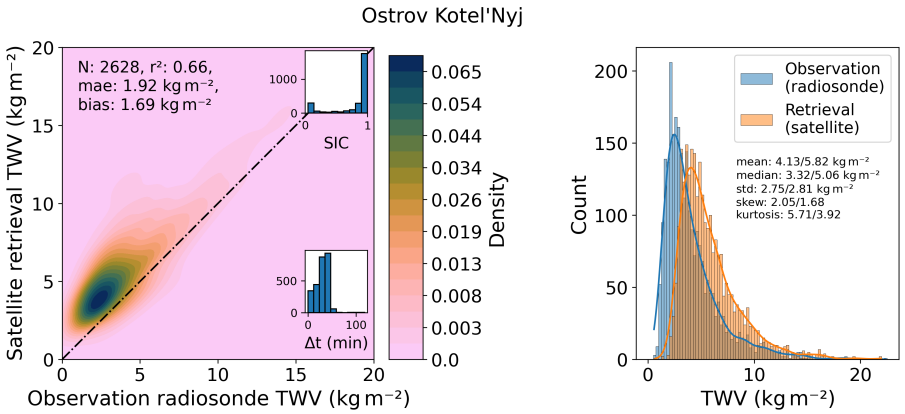

Figure D.8: As Figure 6.9 but for the site Ostrov Kotel'Nyj situated on the New Siberian Islands between the Laptev Sea and the East Siberian Sea.

D.3 Comparison against Reanalysis

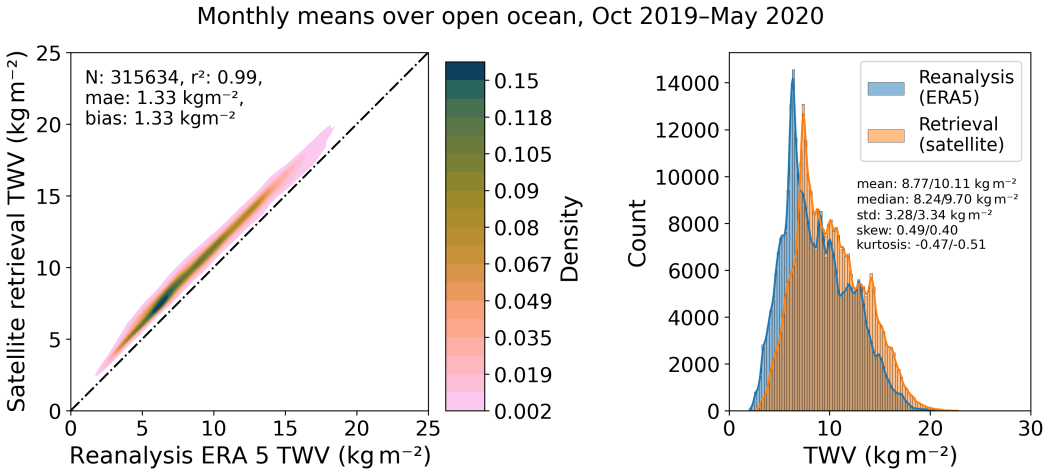

Figure D.9: Monthly mean values of total water vapor (TWV) from the reanalysis ERA5 compared to satellite retrievals from October 2019 – May 2020. Only open ocean grid cells are considered. Left panel: Kernel density estimate plot of all values. Annotated in the plot are the number of observations, N, the square of the Pearson correlation coefficient, r^2, the mean absolute error, mae, and the bias. Right panel: Histograms of TWV from reanalysis (blue) and from the retrieval (orange). Annotated are the statistical parameters mean, median, standard deviation (std), skew and kurtosis for the reanalysis (left value) and the satellite retrieval (right value).

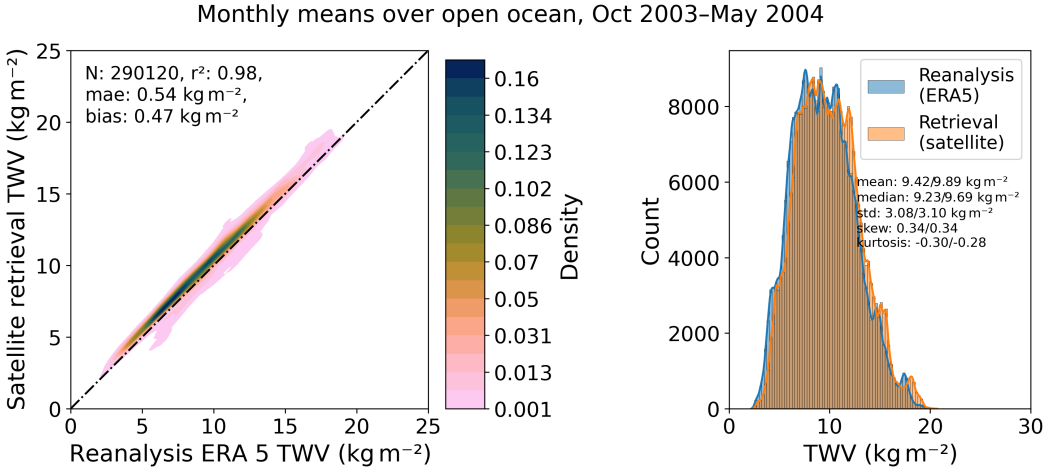

Figure D.10: As Figure D.9 but for October 2003 – May 2004.

Appendix E

Water Vapor: Time series and Changes

E.1 Sensor Differences

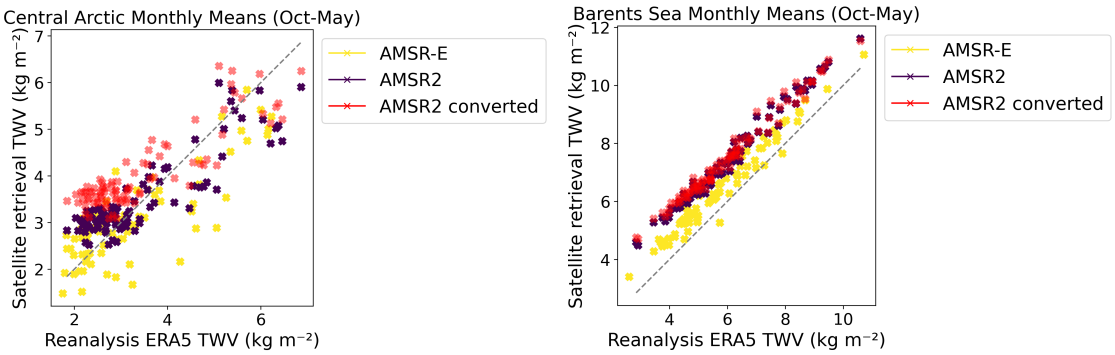

Figure E.1: Scatter plot of regional and monthly mean values of total water vapor (TWV) for the Central Arctic (left) and Barents Sea (right) from reanalysis ERA 5 and satellite retrieval. Colors denote the satellite sensor, either AMSR-E (2002-2011; yellow), AMSR2 (2012-2023; purple) or brightness temperatures from AMSR2 converted to AMSR-E equivalent brightness temperatures (AMSR2 converted, red; following Meier and Ivanoff (2017)).

E.2 Regional Time Series

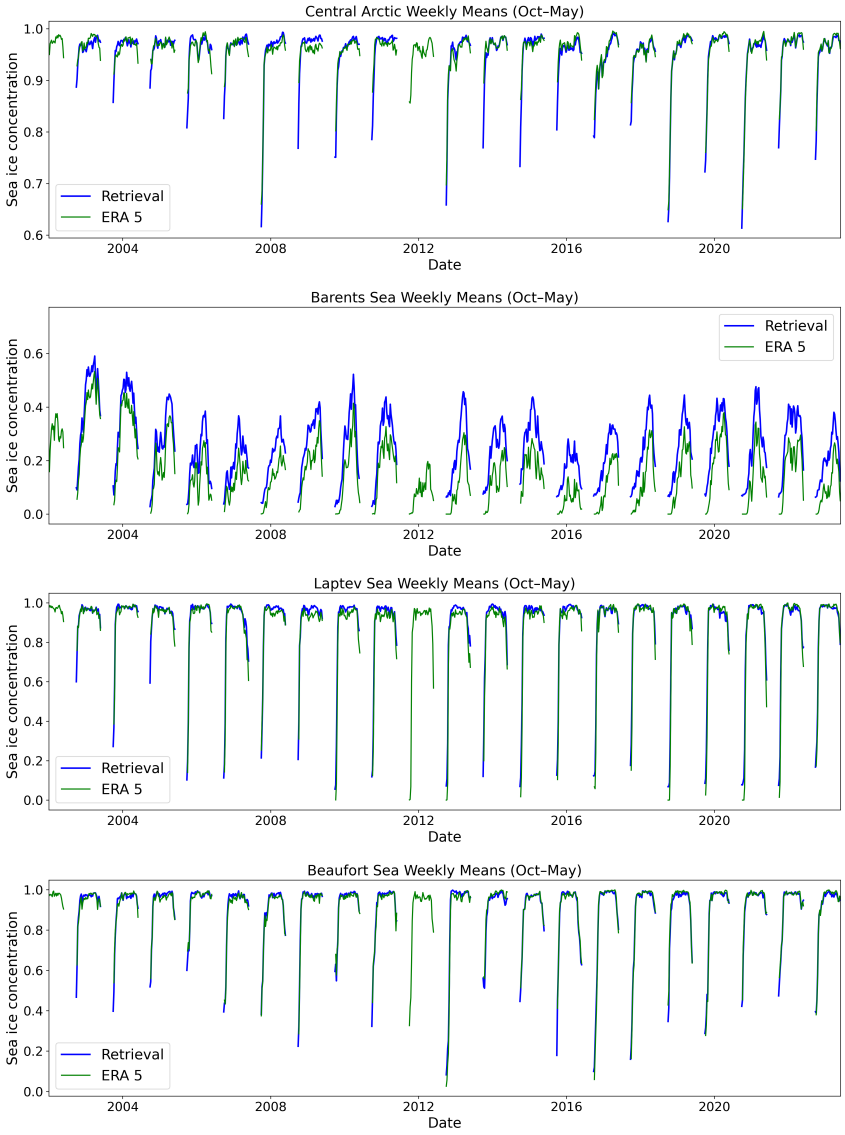

Figure E.2: Regional time series of weekly sea ice concentration (SIC) from 2002 – 2023 for October to May from the satellite retrieval (blue) and the ERA5 reanalysis (green), averaged over the central Arctic (first panel), the Barents Sea (second panel), the Laptev Sea (third panel) and the Beaufort Sea (fourth panel). Blue shading indicates the temporal variability of the retrieval SIC given by the weekly standard deviation per grid cell averaged over the respective region.

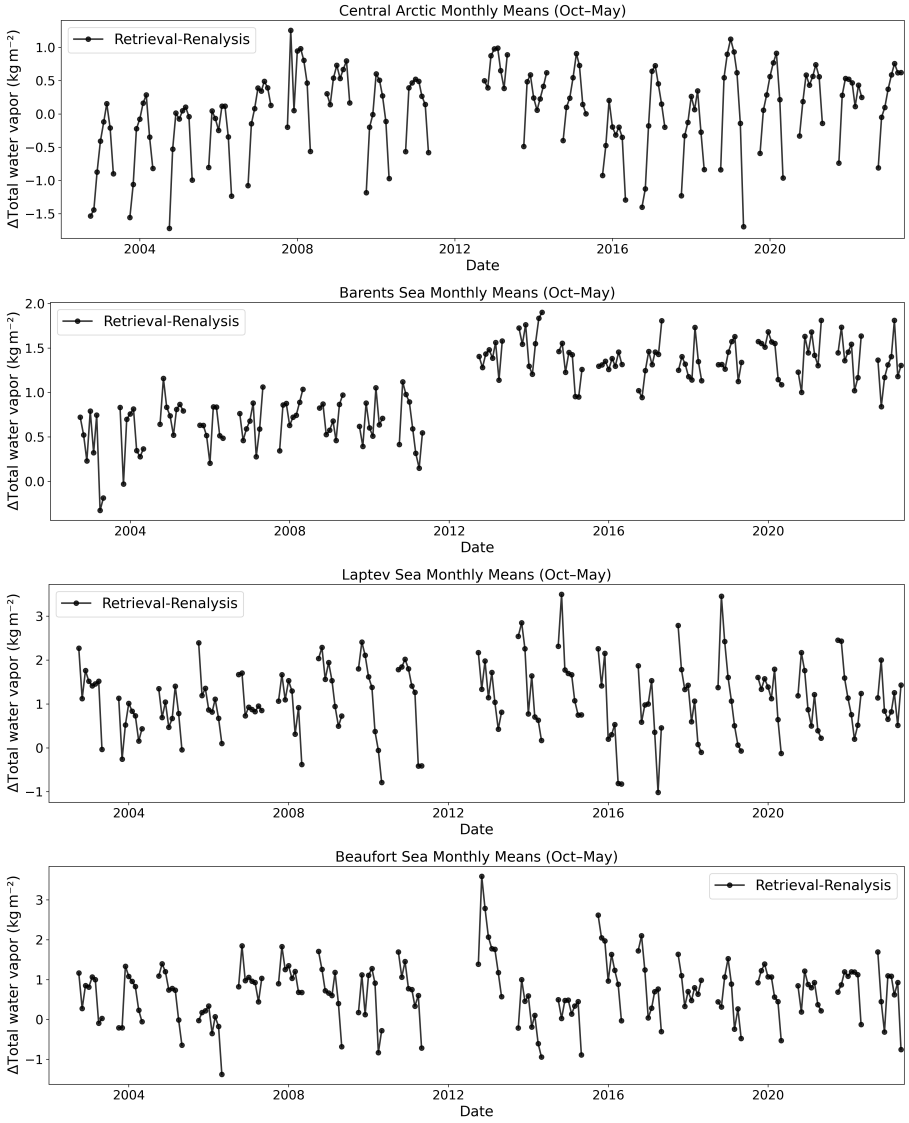

Figure E.3: Regional time series of monthly differences in total water vapor (TWV) between the satellite retrieval and the reanalysis ERA5 from 2002 – 2023 for October to May, averaged over the central Arctic (first panel), the Barents Sea (second panel), the Laptev Sea (third panel) and the Beaufort Sea (fourth panel).

E.3 Trend Uncertainties

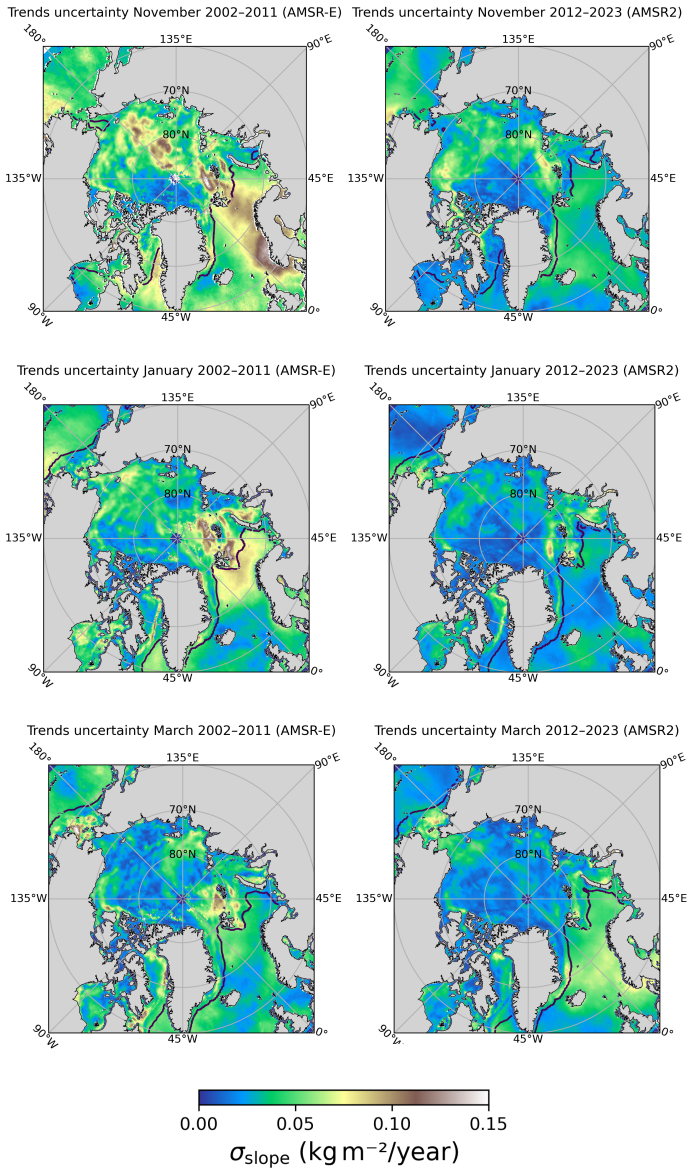

Figure E.4: Uncertainties of the slope (σ_{slope}, with the slope values shown in Figure 6.21) of a linear regression over monthly data from the AMSR-E time period (2002 – 2011, left panels) and the AMSR2 time period (2012 – 2023, right panels). The purple line indicates the mean sea ice edge for the corresponding time spans.

Bibliography

Alexandrov, V., S. Sandven, J. Wahlin, and O. M. Johannessen (2010). The relation between sea ice thickness and freeboard in the Arctic. *The Cryosphere*, 4(3): pp. 373–380. doi:10.5194/tc-4-373-2010.

Ambaum, M. H. P. (2010). Significance tests in climate science. *Journal of Climate*, 23(22): pp. 5927–5932. doi:10.1175/2010JCLI3746.1.

Andersen, S., R. Tonboe, L. Kaleschke, G. Heygster, and L. T. Pedersen (2007). Intercomparison of passive microwave sea ice concentration retrievals over the high-concentration Arctic sea ice. *Journal of Geophysical Research*, 112(C8): p. C08004. doi:10.1029/2006JC003543.

Andersen, S., R. Tonboe, S. Kern, and H. Schyberg (2006). Improved retrieval of sea ice total concentration from spaceborne passive microwave observations using numerical weather prediction model fields: An intercomparison of nine algorithms. *Remote Sensing of Environment*, 104(4): pp. 374–392. doi:10.1016/j.rse.2006.05.013.

Arrhenius, S. (1896). On the emission of carbonic acid in the air upon the temperature of the ground. *Philosoph. Magazine and J. Science*, 41 (5): pp. 237–276.

Ashcroft, P. and F. J. Wentz (2019). AMSR-E/Aqua L2A global swath spatially-resampled brightness temperatures, version 4. doi:10.5067/YL62FUZLAJUT. [Dataset].

Aue, L., T. Vihma, P. Uotila, and A. Rinke (2022). New insights into cyclone impacts on sea ice in the Atlantic sector of the Arctic Ocean in winter. *Geophysical Research Letters*, 49(22): p. e2022GL100051. doi:10.1029/2022GL100051.

Barber, D. G., S. P. Reddan, and E. F. LeDrew (1995). Statistical characterization of the geophysical and electrical properties of snow on landfast first-year sea ice. *Journal of Geophysical Research*, 100(C2): p. 2673. doi:10.1029/94JC02200.

Barry, R. G. and T. Y. Gan (2021). *The Global Cryosphere: Past, Present and Future*. Cambridge university press, Cambridge New York, 2nd edition. ISBN 978-1-108-48755-9 978-1-108-72058-8 978-1-108-76726-2.

Bartelt, P. and M. Lehning (2002). A physical SNOWPACK model for the Swiss avalanche warning: Part I: numerical model. *Cold Regions Science and Technology*, 35(3): pp. 123–145. doi:10.1016/S0165-232X(02)00074-5.

Basharinov, A. E., A. S. Gurvich, S. T. Egorov, V. I. Zhukov, A. A. Kurskaya, L. I. Malafeev, D. T. Matveev, A. S. Mikhailov, and A. M. Shutko (1971). Results of observation of the thermal radio emission of the earth's surface in an experiment on the cosmos-243 satellite. *Kosmicheskie Issledovania*, 9: p. 268.

Ben-Reuven, A. (1965). Transition from resonant to nonresonant line shape in microwave absorption. *Physical Review Letters*, 14(10): pp. 349–351. doi:10.1103/PhysRevLett.14.349.

Bezanson, J., A. Edelman, S. Karpinski, and V. B. Shah (2017). Julia: A fresh approach to numerical computing. *SIAM Review*, 59(1): pp. 65–98. doi:10.1137/141000671.

Bluyssen, H., A. Dymanus, and J. Verhoeven (1967). Hyperfine structure of H2O and HDSe by beam-maser spectroscopy. *Physics Letters A*, 24(9): pp. 482–483. doi:10.1016/0375-9601(67)90154-5.

Boisvert, L. N. and J. C. Stroeve (2015). The Arctic is becoming warmer and wetter as revealed by the Atmospheric Infrared Sounder. *Geophysical Research Letters*, 42(11): pp. 4439–4446. doi:10.1002/2015GL063775.

Boisvert, L. N., D. L. Wu, and C.-L. Shie (2015). Increasing evaporation amounts seen in the Arctic between 2003 and 2013 from AIRS data. *Journal of Geophysical Research: Atmospheres*, 120(14): pp. 6865–6881. doi:10.1002/2015JD023258.

Bolton, D. (1980). The computation of equivalent potential temperature. *Monthly Weather Review*, 108(7): pp. 1046–1053. doi:10.1175/1520-0493(1980)108<1046:TCOEPT>2.0.CO;2.

Born, M. and E. Wolf (2019). *Principles of Optics: 60th Anniversary Edition*. Cambridge University Press, 7 edition. doi:10.1017/9781108769914.

Brodzik, M. J., B. Billingsley, T. Haran, B. Raup, and M. H. Savoie (2012). EASE-Grid 2.0: Incremental but significant improvements for earth-gridded data sets. *ISPRS International Journal of Geo-Information*, 1(1): pp. 32–45. doi:10.3390/ijgi1010032.

Brümmer, B., J. Launiainen, G. Müller, A. Kirchgaessner, and C. Wetzel (2012a). ACSYS 2003 - Arctic Atmospheric Boundary Layer and Sea Ice Interaction Study north of Spitsbergen: meteorological measurements of the research aircraft Falcon, 11 autonomous ice buoys and radiosoundings at the research vessels Aranda and Polarstern. doi:10.1594/WDCC/UNI_HH_MI_ACSYS2003. [Dataset].

Brümmer, B., G. Müller, D. Schröder, and C. Wetzel (2012b). LOFZY 2005 - Field Experiment on Cyclones over the Norwegian Sea: meteorological measurements of the research aircraft Falcon, 23 autonomous water buoys and radiosoundings at the research vessel Celtic Explorer. doi:10.1594/WDCC/UNI_HH_MI_LOFZY2005. [Dataset].

Callen, H. B. and T. A. Welton (1951). Irreversibility and generalized noise. *Physical Review*, 83(1): pp. 34–40. doi:10.1103/PhysRev.83.34.

Cavalieri, D. J., P. Gloersen, and W. J. Campbell (1984). Determination of sea ice parameters with the NIMBUS 7 SMMR. *Journal of Geophysical Research: Atmospheres*, 89(D4): pp. 5355–5369. doi:10.1029/JD089iD04p05355.

Cavalieri, D. J., C. L. Parkinson, P. Gloersen, and H. J. Zwally (1997). Arctic and Antarctic sea ice concentrations from multichannel passive-microwave satellite data sets: October 1978-september 1995 user's guide.

Chander, G., T. J. Hewison, N. Fox, X. Wu, X. Xiong, and W. J. Blackwell (2013). Overview of intercalibration of satellite instruments. *IEEE Transactions on Geoscience and Remote Sensing*, 51(3): pp. 1056–1080. doi:10.1109/TGRS.2012.2228654.

Chandrasekhar, S. (1950). *Radiative transfer*. Dover books on physics. Oxford University Press, Oxford. ISBN 978-0-486-60590-6.

Chen, K. S., T.-D. Wu, L. Tsang, Q. Li, J. Shi, and A. K. Fung (2003). Emission of rough surfaces calculated by the integral equation method with comparison to three-dimensional moment method simulations. *IEEE Transactions on Geoscience and Remote Sensing*, 41(1): pp. 90–101. doi:10.1109/TGRS.2002.807587.

Choudhury, B. J., T. J. Schmugge, A. Chang, and R. W. Newton (1979). Effect of surface roughness on the microwave emission from soils. *Journal of Geophysical Research*, 84(C9): p. 5699. doi:10.1029/JC084iC09p05699.

Cimini, D., P. W. Rosenkranz, M. Y. Tretyakov, M. A. Koshelev, and F. Romano (2018). Uncertainty of atmospheric microwave absorption model: impact on ground-based radiometer simulations and retrievals. *Atmospheric Chemistry and Physics*, 18(20): pp. 15231–15259. doi:10.5194/acp-18-15231-2018.

Clemens-Sewall, D., M. Parno, D. Perovich, C. Polashenski, and I. A. Raphael (2022a). FlakeOut: A geometric approach to remove wind-blown snow from terrestrial laser scans. *Cold Regions Science and Technology*, 201: p. 103611. doi:10.1016/j.coldregions.2022.103611.

Clemens-Sewall, D., C. Polashenski, I. Raphael, D. Perovich, S. Fons, P. Itkin, M. Jaggi, A. Jutila, A. Macfarlane, I. Matero, M. Oggier, D. Wagner, R. Visser, T. Olufson,

M. Radenz, C. Schönning, J. Hansen, M. Votvik, E. Brossier, and S. Svavarsdottir (2022b). High-resolution repeat topography of drifting ice floes in the Arctic Ocean from terrestrial laser scanning collected on the Multidisciplinary drifting Observatory for the Study of Arctic Climate Expedition. doi:10.18739/A26688K9D. [Dataset].

Clemens-Sewall, D., C. M. Polashenski, M. M. Frey, C. J. Cox, M. A. Granskog, A. Macfarlane, S. Fons, J. Schmale, J. K. Hutchings, L. von Albedyll, S. Arndt, M. Schneebeli, and D. Perovich (2023). Snow loss into leads in Arctic sea ice: Minimal in typical wintertime conditions, but high during a warm and windy snowfall event. preprint, Preprints. doi:10.22541/essoar.167751637.76975855/v1.

Cohen, J., X. Zhang, J. Francis, T. Jung, R. Kwok, J. Overland, T. J. Ballinger, U. S. Bhatt, H. W. Chen, D. Coumou, S. Feldstein, H. Gu, D. Handorf, G. Henderson, M. Ionita, M. Kretschmer, F. Laliberte, S. Lee, H. W. Linderholm, W. Maslowski, Y. Peings, K. Pfeiffer, I. Rigor, T. Semmler, J. Stroeve, P. C. Taylor, S. Vavrus, T. Vihma, S. Wang, M. Wendisch, Y. Wu, and J. Yoon (2020). Divergent consensuses on Arctic amplification influence on midlatitude severe winter weather. *Nature Climate Change*, 10(1): pp. 20–29. doi:10.1038/s41558-019-0662-y.

Cohen, L., S. R. Hudson, V. P. Walden, R. M. Graham, and M. A. Granskog (2017). Meteorological conditions in a thinner arctic sea ice regime from winter to summer during the norwegian young sea ice expedition (n-ice2015). *Journal of Geophysical Research: Atmospheres*, 122(14): pp. 7235–7259. doi:10.1002/2016JD026034.

Colbeck, S. C. (1983). Theory of metamorphism of dry snow. *Journal of Geophysical Research: Oceans*, 88(C9): pp. 5475–5482. doi:10.1029/JC088iC09p05475.

Colliander, A., J. Lahtinen, S. Tauriainen, J. Pihlflyckt, J. Lemmetyinen, and M. Hallikainen (2007). Sensitivity of airborne 36,5-GHz polarimetric radiometer's wind-speed measurement to incidence angle. *IEEE Transactions on Geoscience and Remote Sensing*, 45(7): pp. 2122–2129.

Colman, R. and B. J. Soden (2021). Water vapor and lapse rate feedbacks in the climate system. *Reviews of Modern Physics*, 93(4): p. 045002. doi:10.1103/RevModPhys.93.045002.

Comiso, J. C. (1983). Sea ice effective microwave emissivities from satellite passive microwave and infrared observations. *Journal of Geophysical Research*, 88(C12): p. 7686. doi:10.1029/JC088iC12p07686.

Comiso, J. C. (1986). Characteristics of Arctic winter sea ice from satellite multispectral microwave observations. *Journal of Geophysical Research*, 91(C1): p. 975. doi:10.1029/JC091iC01p00975.

Comiso, J. C., D. J. Cavalieri, C. L. Parkinson, and P. Gloersen (1997). Passive microwave algorithms for sea ice concentration: A comparison of two techniques. *Remote Sensing of Environment*, 60(3): pp. 357–384. doi:10.1016/S0034-4257(96)00220-9.

Comiso, J. C., R. A. Gersten, L. V. Stock, J. Turner, G. J. Perez, and K. Cho (2017). Positive trend in the Antarctic sea ice cover and associated changes in surface temperature. *Journal of Climate*, 30(6): pp. 2251–2267. doi:10.1175/JCLI-D-16-0408.1.

Comiso, J. C. and D. K. Hall (2014). Climate trends in the Arctic as observed from space. *WIREs Climate Change*, 5(3): pp. 389–409. doi:10.1002/wcc.277.

Cox, C., M. Gallagher, M. Shupe, O. Persson, B. Blomquist, A. Grachev, L. Riihimaki, M. Kutchenreiter, V. Morris, A. Solomon, I. Brooks, D. Costa, D. Gottas, J. Hutchings, J. Osborn, S. Morris, A. Preusser, and T. Uttal (2023a). Met City meteorological and surface flux measurements (Level 3 Final), Multidisciplinary Drifting Observatory for the Study of Arctic Climate (MOSAiC), central Arctic, October 2019 - September 2020. doi:10.18739/A2PV6B83F. [Dataset].

Cox, C., M. Gallagher, M. Shupe, O. Persson, A. Grachev, A. Solomon, T. Ayers, D. Costa, J. Hutchings, J. Leach, S. Morris, J. Osborn, S. Pezoa, and T. Uttal (2023b). Atmospheric Surface Flux Station #30 measurements (Level 3 Final), Multidisciplinary Drifting Observatory for the Study of Arctic Climate (MOSAiC), central Arctic, October 2019 - September 2020. doi:10.18739/A2FF3M18K. [Dataset].

Cox, C., M. Gallagher, M. Shupe, O. Persson, A. Grachev, A. Solomon, T. Ayers, D. Costa, J. Hutchings, J. Leach, S. Morris, J. Osborn, S. Pezoa, and T. Uttal (2023c). Atmospheric Surface Flux Station #40 measurements (Level 3 Final), Multidisciplinary Drifting Observatory for the Study of Arctic Climate (MOSAiC), central Arctic, October 2019 - September 2020. doi:10.18739/A25X25F0P. [Dataset].

Cox, C., M. Gallagher, M. Shupe, O. Persson, A. Grachev, A. Solomon, T. Ayers, D. Costa, J. Hutchings, J. Leach, S. Morris, J. Osborn, S. Pezoa, and T. Uttal (2023d). Atmospheric Surface Flux Station #50 measurements (Level 3 Final), Multidisciplinary Drifting Observatory for the Study of Arctic Climate (MOSAiC), central Arctic, October 2019 - September 2020. doi:10.18739/A2XD0R00S. [Dataset].

Cox, C., M. Gallagher, M. Shupe, O. Persson, A. Solomon, B. Blomquist, I. Brooks, D. Costa, D. Gottas, J. Hutchings, J. Osborn, S. Morris, A. Preusser, and T. Uttal (2021). 10-meter (m) meteorological flux tower measurements (Level 1 Raw), Multidisciplinary Drifting Observatory for the Study of Arctic Climate (MOSAiC), central Arctic, october 2019 - september 2020. doi:10.18739/A2VM42Z5F. [Dataset].

Cox, G. F. N. and W. F. Weeks (1974). Salinity variations in sea ice. *Journal of Glaciology*, 13(67): pp. 109–120. doi:10.3189/S0022143000023418.

Crewell, S., K. Ebell, P. Konjari, M. Mech, T. Nomokonova, A. Radovan, D. Strack, A. M. Triana-Gómez, S. Noël, R. Scarlat, G. Spreen, M. Maturilli, A. Rinke, I. Gorodetskaya, C. Viceto, T. August, and M. Schröder (2021). A systematic assessment of water vapor products in the Arctic: from instantaneous measurements to monthly means. *Atmospheric Measurement Techniques*, 14(7): pp. 4829–4856. doi:10.5194/amt-14-4829-2021.

Crocker, G. (1992). Observations of the snowcover on sea ice in the Gulf of Bothnia. *International Journal of Remote Sensing*, 13(13): pp. 2433–2445. doi:10.1080/01431169208904280.

Dada, L., H. Angot, I. Beck, A. Baccarini, L. L. J. Quéléver, M. Boyer, T. Laurila, Z. Brasseur, G. Jozef, G. de Boer, M. D. Shupe, S. Henning, S. Bucci, M. Dütsch, A. Stohl, T. Petäjä, K. R. Daellenbach, T. Jokinen, and J. Schmale (2022). A central Arctic extreme aerosol event triggered by a warm air-mass intrusion. *Nature Communications*, 13(1): p. 5290. doi:10.1038/s41467-022-32872-2.

Debye, P. J. W. (1929). *Polar molecules*. The Chemical Catalog Company, Inc. New York, New York.

Deems, J. S., T. H. Painter, and D. C. Finnegan (2013). Lidar measurement of snow depth: a review. *Journal of Glaciology*, 59(215): pp. 467–479. doi:10.3189/2013JoG12J154.

Denoth, A. (1980). The pendular-funicular liquid transition in snow. *Journal of Glaciology*, 25(91): pp. 93–98. doi:10.3189/S0022143000010315.

Derksen, C., P. Toose, J. Lemmetyinen, J. Pulliainen, A. Langlois, N. Rutter, and M. Fuller (2012). Evaluation of passive microwave brightness temperature simulations and snow water equivalent retrievals through a winter season. *Remote Sensing of Environment*, 117: pp. 236–248. doi:10.1016/j.rse.2011.09.021.

Devasthale, A., J. Sedlar, M. Tjernström, and A. Kokhanovsky (2020). A climatological overview of arctic clouds. In Kokhanovsky, A. and C. Tomasi (editors), *Physics and Chemistry of the Arctic Atmosphere*, Springer Polar Sciences, pp. 331–360. Springer International Publishing, Cham. ISBN 978-3-030-33566-3. doi:10.1007/978-3-030-33566-3_5.

Donlon, C. (2020). Copernicus Imaging Microwave Radiometer (CIMR) Mission Requirements Document. Technical report, European Space Agency, Noordwijk, The Netherlands.

Durre, I., R. S. Vose, and D. B. Wuertz (2006). Overview of the Integrated Global Radiosonde Archive. *Journal of Climate*, 19(1): pp. 53–68. doi:10.1175/JCLI3594.1.

Durre, I., C. N. Williams Jr., X. Yin, and R. S. Vose (2009). Radiosonde-based trends in precipitable water over the Northern Hemisphere: An update. *Journal of Geophysical Research: Atmospheres*, 114(D5). doi:10.1029/2008JD010989.

Durre, I., X. Yin, R. S. Vose, S. Applequist, and J. Arnfield (2018). Enhancing the data coverage in the Integrated Global Radiosonde Archive. *Journal of Atmospheric and Oceanic Technology*, 35(9): pp. 1753–1770. doi:10.1175/JTECH-D-17-0223.1.

Ebell, K., T. Nomokonova, M. Maturilli, and C. Ritter (2020). Radiative effect of clouds at Ny-Ålesund, Svalbard, as inferred from ground-based remote sensing observations. *Journal of Applied Meteorology and Climatology*, 59(1): pp. 3–22. doi:10.1175/JAMC-D-19-0080.1.

Ehrenfest, P. (1911). Welche Züge der Lichtquantenhypothese spielen in der Theorie der Wärmestrahlung eine wesentliche Rolle? *Annalen der Physik*, 341(11): pp. 91–118.

Emslie, A. G. and J. R. Aronson (1973). Spectral reflectance and emittance of particulate materials. 1: Theory. *Applied Optics*, 12(11): pp. 2563–2572. doi:10.1364/AO.12.002563.

Eppler, D. T., L. D. Farmer, A. W. Lohanick, M. R. Anderson, D. J. Cavalieri, J. Comiso, P. Gloersen, C. Garrity, T. C. Grenfell, M. Hallikainen, J. A. Maslanik, C. MäTzler, R. A. Melloh, I. Rubinstein, and C. T. Swift (1992). Passive microwave signatures of sea ice. In *Microwave Remote Sensing of Sea Ice*, chapter 4, pp. 47–71. American Geophysical Union (AGU). ISBN 978-1-118-66395-0. doi:10.1029/GM068p0047.

EUMETSAT Ocean and Sea Ice Satellite Application Facility (2017). *Global sea ice concentration interim climate data record 2016-onwards (v2.0, 2017), OSI-430-b.* (Data extracted from OSI SAF FTP server/EUMETSAT Data Center: April 2020, Northern Hemisphere). Accessed September 7, 2021.

Fierz, C., R. L. Armstrong, Y. Durand, P. Etchevers, E. Greene, D. M. McClung, K. Nishimura, P. K. Satyawali, and S. A. Sokratov (2009). The international classification for seasonal snow on the ground. Technical Report 83, UNESCO-IHP, Paris.

Fox-Kemper, B., H. T. Hewitt, C. Xiao, G. Aðalgeirsdóttir, S. S. Drijfhout, T. L. Edwards, N. R. Golledge, M. Hemer, R. E. Kopp, G. Krinner, A. Mix, D. Notz, S. Nowicki, I. S. Nurhati, L. Ruiz, J.-B. Sallée, A. B. A. Slangen, and Y. Yu (2021). Ocean, cryosphere and sea level change. In Masson-Delmotte, V., P. Zhai, A. Pirani, S. L. Connors, C. Péan, S. Berger, N. Caud, Y. Chen, L. Goldfarb, M. I. Gomis, M. Huang, K. Leitzell, E. Lonnoy, J. B. R. Matthews, T. K. Maycock, T. Waterfield, O. Yelekçi, R. Yu, and a. B. Zhoue (editors), *In Climate Change 2021: The Physical Science Basis. Contribution of Working Group I to the Sixth Assessment Report of the Intergovernmental Panel on Climate Change*. Cambridge University Press. doi:10.1017/9781009157896.011.

Fritz, M., J. E. Vonk, and H. Lantuit (2017). Collapsing Arctic coastlines. *Nature Climate Change*, 7(1): pp. 6–7. doi:10.1038/nclimate3188.

Fuhrhop, R., T. C. Grenfell, G. Heygster, K.-P. Johnsen, P. Schlüssel, M. Schrader, and C. Simmer (1998). A combined radiative transfer model for sea ice, open ocean, and atmosphere. *Radio Science*, 33(2): pp. 303–316. doi:10.1029/97RS03020.

Gallo, P., K. Amann-Winkel, C. A. Angell, M. A. Anisimov, F. Caupin, C. Chakravarty, E. Lascaris, T. Loerting, A. Z. Panagiotopoulos, J. Russo, J. A. Sellberg, H. E. Stanley, H. Tanaka, C. Vega, L. Xu, and L. G. M. Pettersson (2016). Water: A tale of two liquids. *Chemical Reviews*, 116(13): pp. 7463–7500. doi:10.1021/acs.chemrev.5b00750.

Garnett, J. C. M. and J. Larmor (1904). XII. Colours in metal glasses and in metallic films. *Philosophical Transactions of the Royal Society of London. Series A, Containing Papers of a Mathematical or Physical Character*, 203(359-371): pp. 385–420. doi:10.1098/rsta.1904.0024.

Garnett, J. C. M. and J. Larmor (1906). VII. Colours in metal glasses, in metallic films, and in metallic solutions.—ii. *Philosophical Transactions of the Royal Society of London. Series A, Containing Papers of a Mathematical or Physical Character*, 205(387-401): pp. 237–288. doi:10.1098/rsta.1906.0007.

Geldsetzer, T., A. Langlois, and J. Yackel (2009). Dielectric properties of brine-wetted snow on first-year sea ice. *Cold Regions Science and Technology*, 58(1-2): pp. 47–56. doi:10.1016/j.coldregions.2009.03.009.

Ghatak, D. and J. Miller (2013). Implications for Arctic amplification of changes in the strength of the water vapor feedback. *J. Geophys. Res. Atmos.*, 118(14): pp. 7569–7578. doi:10.1002/jgrd.50578.

Gimmestad, G. G. and D. W. Roberts (2023). Particles in the atmosphere. In *Lidar Engineering: Introduction to Basic Principles*, p. 65–112. Cambridge University Press. doi:10.1017/9781139014106.006.

Gloersen, P., W. Nordberg, T. J. Schmugge, T. T. Wilheit, and W. J. Campbell (1973). Microwave signatures of first-year and multiyear sea ice. *Journal of Geophysical Research (1896-1977)*, 78(18): pp. 3564–3572. doi:10.1029/JC078i018p03564.

Goldstein, H. (1951). Attenuation by condensed water. In Kerr, D. E. (editor), *Propagation of short radio waves*, pp. 671–692. McGraw-Hill, New York.

Goosse, H., J. E. Kay, K. C. Armour, A. Bodas-Salcedo, H. Chepfer, D. Docquier, A. Jonko, P. J. Kushner, O. Lecomte, F. Massonnet, H.-S. Park, F. Pithan, G. Svensson, and M. Vancoppenolle (2018). Quantifying climate feedbacks in polar regions. *Nature Communications*, 9(1): p. 1919. doi:10.1038/s41467-018-04173-0.

Graham, R. M., L. Cohen, A. A. Petty, L. N. Boisvert, A. Rinke, S. R. Hudson, M. Nicolaus, and M. A. Granskog (2017). Increasing frequency and duration of Arctic winter warming events. *Geophysical Research Letters*, 44(13): pp. 6974–6983. doi:10.1002/2017GL073395.

Gray, A., R. Hawkins, C. Livingstone, L. Arsenault, and W. Johnstone (1982). Simultaneous scatterometer and radiometer measurements of sea-ice microwave signatures. *IEEE Journal of Oceanic Engineering*, 7(1): pp. 20–32. doi:10.1109/JOE.1982.1145506.

Grenfell, T. (1986). Surface-based passive microwave observations of sea ice in the Bering and Greenland Seas. *IEEE Transactions on Geoscience and Remote Sensing*, GE-24(3): pp. 378–382. doi:10.1109/TGRS.1986.289595.

Grenfell, T. and J. Comiso (1986). Multifrequency passive microwave observations of first-year sea ice grown in a tank. *IEEE Transactions on Geoscience and Remote Sensing*, GE-24(6): pp. 826–831. doi:10.1109/TGRS.1986.289696.

Grenfell, T. C. (1992). Surface-based passive microwave studies of multiyear sea ice. *Journal of Geophysical Research*, 97(C3): p. 3485. doi:10.1029/91JC02651.

Grenfell, T. C. and A. W. Lohanick (1985). Temporal variations of the microwave signatures of sea ice during the late spring and early summer near Mould Bay NWT. *Journal of Geophysical Research: Oceans*, 90(C3): pp. 5063–5074. doi:10.1029/JC090iC03p05063.

Grenfell, T. C. and J. Putkonen (2008). A method for the detection of the severe rain-on-snow event on Banks Island, October 2003, using passive microwave remote sensing. *Water Resources Research*, 44(3). doi:10.1029/2007WR005929.

Guo, W., P. Itkin, S. Singha, A. P. Doulgeris, M. Johansson, and G. Spreen (2023). Sea ice classification of TerraSAR-X ScanSAR images for the MOSAiC expedition incorporating per-class incidence angle dependency of image texture. *The Cryosphere*, 17(3): pp. 1279–1297. doi:10.5194/tc-17-1279-2023.

Haggerty, J. A. and J. A. Curry (2001). Variability of sea ice emissivity estimated from airborne passive microwave measurements during FIRE SHEBA. *Journal of Geophysical Research: Atmospheres*, 106(D14): pp. 15265–15277. doi:10.1029/2000JD900485.

Hallikainen, M., M. Kemppinen, K. Rautiainen, J. Pihlflyckt, J. Lahtinen, T. Tirri, I. Mononen, and T. Auer (1996). Airborne 14-channel microwave radiometer HUTRAD. In *IGARSS '96. 1996 International Geoscience and Remote Sensing Symposium*, volume 4, pp. 2285–2287. IEEE, Lincoln, NE, USA. ISBN 978-0-7803-3068-9. doi:10.1109/IGARSS.1996.516963.

Hallikainen, M., F. Ulaby, and M. Abdelrazik (1986). Dielectric properties of snow in the 3 to 37 GHz range. *IEEE Transactions on Antennas and Propagation*, 34(11): pp. 1329–1340. doi:10.1109/TAP.1986.1143757.

Hallikainen, M. and D. P. Winebrenner (1992). The physical basis for sea ice remote sensing. In Carsey, F. D. (editor), *Geophysical Monograph Series*, volume 68, pp. 29–46. American Geophysical Union, Washington, D. C. ISBN 978-0-87590-033-9. doi:10.1029/GM068p0029.

Hao, M., Y. Luo, Y. Lin, Z. Zhao, L. Wang, and J. Huang (2019). Contribution of atmospheric moisture transport to winter Arctic warming. *International Journal of Climatology*, 39(5): pp. 2697–2710. doi:10.1002/joc.5982.

Harlow, R. C. (2009). Millimeter microwave emissivities and effective temperatures of snow-covered surfaces: Evidence for Lambertian surface scattering. *IEEE Transactions on Geoscience and Remote Sensing*, 47(7): pp. 1957–1970. doi:10.1109/TGRS.2008.2011893.

Harlow, R. C. (2011). Sea ice emissivities and effective temperatures at MHS frequencies: An analysis of airborne microwave data measured during two Arctic campaigns. *IEEE Transactions on Geoscience and Remote Sensing*, 49(4): pp. 1223–1237. doi:10.1109/TGRS.2010.2051555.

Henderson, G. R., B. S. Barrett, L. J. Wachowicz, K. S. Mattingly, J. R. Preece, and T. L. Mote (2021). Local and remote atmospheric circulation drivers of Arctic change: A review. *Frontiers in Earth Science*, 9: p. 709896. doi:10.3389/feart.2021.709896.

Hendricks, S. and S. Paul (2022). Product User Guide & Algorithm Specification: AWI CryoSat-2 Sea Ice Thickness (version 2.5). doi:10.5281/ZENODO.7416200.

Herrmannsdörfer, L., M. Müller, M. D. Shupe, and P. Rostosky (2023). Surface temperature comparison of the Arctic winter MOSAiC observations, ERA5 reanalysis, and MODIS satellite retrieval. *Elementa: Science of the Anthropocene*, 11(1): p. 00085. doi:10.1525/elementa.2022.00085.

Hersbach, H., B. Bell, P. Berrisford, S. Hirahara, A. Horányi, J. Muñoz-Sabater, J. Nicolas, C. Peubey, R. Radu, D. Schepers, A. Simmons, C. Soci, S. Abdalla, X. Abellan, G. Balsamo, P. Bechtold, G. Biavati, J. Bidlot, M. Bonavita, G. Chiara, P. Dahlgren, D. Dee, M. Diamantakis, R. Dragani, J. Flemming, R. Forbes, M. Fuentes, A. Geer, L. Haimberger, S. Healy, R. J. Hogan, E. Hólm, M. Janisková, S. Keeley, P. Laloyaux, P. Lopez, C. Lupu, G. Radnoti, P. Rosnay, I. Rozum, F. Vamborg, S. Villaume, and J.-N. Thépaut (2020). The ERA5 global reanalysis. *Quarterly Journal of the Royal Meteorological Society*, 146(730): pp. 1999–2049. doi:10.1002/qj.3803.

Hewison, T. and S. English (1999). Airborne retrievals of snow and ice surface emissivity at millimeter wavelengths. *IEEE Transactions on Geoscience and Remote Sensing*, 37(4): pp. 1871–1879. doi:10.1109/36.774700.

Hewison, T., N. Selbach, G. Heygster, J. Taylor, and A. McGrath (2002). Airborne measurements of Arctic sea ice, glacier and snow emissivity at 24-183 GHz. In *IEEE International Geoscience and Remote Sensing Symposium*, volume 5, pp. 2851–2855. IEEE, Toronto, Ont., Canada. ISBN 978-0-7803-7536-9. doi:10.1109/IGARSS.2002.1026797.

Hill, V., M. Ardyna, S. H. Lee, and D. E. Varela (2018). Decadal trends in phytoplankton production in the Pacific Arctic Region from 1950 to 2012. *Deep Sea Research Part II: Topical Studies in Oceanography*, 152: pp. 82–94. doi:10.1016/j.dsr2.2016.12.015.

Hoese, D., M. Raspaud, P. Lahtinen, W. Roberts, Lavergne, Stickler Bot, G. Holl, S. Finkensieper, G. Ghiggi, A. Dybbroe, X. Zhang, M. Itkin, A. Meraner, BENR0, A. Valentino, Nina, L. Ø. Rasmussen, L. Clementi, M. Valgur, D. Rykov, A. Brammer, B. Couwenberg, B. Raml, B. Hawkins, F. Pinault, M. Savoie, Storpipfugl, and Owenlittlejohns (2023). pytroll/pyresample: Version 1.27.1 (2023/06/21). Zenodo. doi:10.5281/ZENODO.8065154. [Software].

Hofmann, H., H. Wickham, and K. Kafadar (2017). Letter-value plots: Boxplots for large data. *Journal of Computational and Graphical Statistics*, 26(3): pp. 469–477. doi:10.1080/10618600.2017.1305277.

Hollinger, J. P., B. E. Troy Jr, R. O. Ramseier, K. W. Asmus, M. F. Hartman, and C. A. Luther (1984). Microwave emission from high Arctic sea ice during freeze-up. *Journal of Geophysical Research: Oceans*, 89(C5): pp. 8104–8122. doi:10.1029/JC089iC05p08104.

Howell, J. R., M. P. Mengüç, K. J. Daun, and R. Siegel (2021). *Thermal radiation heat transfer*. CRC Press, Boca Raton, seventh edition edition. ISBN 978-0-367-34707-9.

Huang, D., E. Campos, and Y. Liu (2014). Statistical characteristics of cloud variability. part 1: Retrieved cloud liquid water path at three ARM sites. *Journal of Geophysical Research: Atmospheres*, 119(18): pp. 10,813–10,828. doi:10.1002/2014JD022001.

Hudson, S. R., L. Cohen, M. Kayser, M. Maturilli, J.-H. Kim, S.-J. Park, W. Moon, and M. A. Granskog (2017). N-ICE2015 atmospheric profiles from radiosondes. doi:10.21334/NPOLAR.2017.216DF9B3. [Dataset].

Hufford, G. (1991). A model for the complex permittivity of ice at frequencies below 1 THz. *International Journal of Infrared and Millimeter Waves*, 12(7): pp. 677–682. doi:10.1007/BF01008898.

Huntemann, M., G. Heygster, L. Kaleschke, T. Krumpen, M. Mäkynen, and M. Drusch (2014). Empirical sea ice thickness retrieval during the freeze up period from SMOS high incident angle observations. *Cryosphere*, 8: pp. 439–451. doi:10.5194/tc-8-439-2014.

Hutchings, J., J. Delamere, and P. Heil (2020). *The Ice Watch Manual*.

Hwang, B. J., J. K. Ehn, D. G. Barber, R. Galley, and T. C. Grenfell (2007). Investigations of newly formed sea ice in the Cape Bathurst polynya: 2. Microwave emission. *Journal of Geophysical Research*, 112(C5): p. C05003. doi:10.1029/2006JC003703.

Hyland, R. and A. Wexler (1983). Formulations for the thermodynamic properties of the saturated phases of H2O from 173.15 to 473.15 K. *Ashrae Transactions*.

Intergovernmental Panel on Climate Change (2023). *Climate Change 2021 – The Physical Science Basis: Working Group I Contribution to the Sixth Assessment Report of the Intergovernmental Panel on Climate Change*. Cambridge University Press, 1 edition. ISBN 978-1-00-915789-6. doi:10.1017/9781009157896.

Itkin, P., S. Hendricks, M. Webster, L. von Albedyll, S. Arndt, D. Divine, M. Jaggi, M. Oggier, I. Raphael, R. Ricker, J. Rohde, M. Schneebeli, and G. E. Liston (2023). Sea ice and snow characteristics from year-long transects at the MOSAiC Central Observatory. *Elementa: Science of the Anthropocene*, 11(1): p. 00048. doi:10.1525/elementa.2022.00048.

Ivanova, N., L. T. Pedersen, R. T. Tonboe, S. Kern, G. Heygster, T. Lavergne, A. Sørensen, R. Saldo, G. Dybkjær, L. Brucker, and M. Shokr (2015). Inter-comparison and evaluation of sea ice algorithms: towards further identification of challenges and optimal approach using passive microwave observations. *The Cryosphere*, 9(5): pp. 1797–1817. doi:10.5194/tc-9-1797-2015.

Jutila, A., S. Hendricks, R. Ricker, L. von Albedyll, T. Krumpen, and C. Haas (2022). Retrieval and parameterisation of sea-ice bulk density from airborne multi-sensor measurements. *The Cryosphere*, 16(1): pp. 259–275. doi:10.5194/tc-16-259-2022.

Kaleschke, L., C. Lüpkes, T. Vihma, J. Haarpaintner, A. Bochert, J. Hartmann, and G. Heygster (2001). SSM/I sea ice remote sensing for mesoscale ocean-atmosphere interaction analysis. *Canadian Journal of Remote Sensing*, 27(5): pp. 526–537. doi:10.1080/07038992.2001.10854892.

Kaltenborn, J., A. R. Macfarlane, V. Clay, and M. Schneebeli (2022). Automatic classification and segmentation of Snow Micro Penetrometer profiles with machine learning algorithms. preprint, Cryosphere. doi:10.5194/egusphere-2022-938.

Kang, E.-J., B.-J. Sohn, R. T. Tonboe, Y.-C. Noh, I.-H. Kwon, S.-W. Kim, M. Maturilli, H.-C. Kim, and C. Liu (2023). Explicitly determined sea ice emissivity and emission

temperature over the Arctic for surface-sensitive microwave channels. *Quarterly Journal of the Royal Meteorological Society*, 149(754): pp. 2011–2030. doi:10.1002/qj.4492.

Kanzow, T. (2023). The expedition PS131 of the research vessel POLARSTERN to the Fram Strait in 2022. In Bornemann, H. and S. A. Sawadkuhi (editors), *Berichte zur Polar- und Meeresforschung = Reports on polar and marine research*, volume 770. Alfred-Wegener-Institut Helmholtz-Zentrum für Polar- und Meeresforschung, Bremerhaven. doi:10.57738/BzPM_0770_2023.

Kay, J. E., T. L'Ecuyer, H. Chepfer, N. Loeb, A. Morrison, and G. Cesana (2016). Recent advances in Arctic cloud and climate research. *Current Climate Change Reports*, 2(4): pp. 159–169. doi:10.1007/s40641-016-0051-9.

Kern, S., T. Lavergne, D. Notz, L. T. Pedersen, R. T. Tonboe, R. Saldo, and A. M. Sørensen (2019). Satellite passive microwave sea-ice concentration data set intercomparison: closed ice and ship-based observations. *The Cryosphere*, 13(12): pp. 3261–3307. doi:10.5194/tc-13-3261-2019.

Kern, S., T. Lavergne, L. T. Pedersen, R. T. Tonboe, L. Bell, M. Meyer, and L. Zeigermann (2022). Satellite passive microwave sea-ice concentration data set intercomparison using Landsat data. *The Cryosphere*, 16(1): pp. 349–378. doi:10.5194/tc-16-349-2022.

Kerner, E. H. (1956). The electrical conductivity of composite media. *Proceedings of the Physical Society. Section B*, 69(8): p. 802. doi:10.1088/0370-1301/69/8/304.

Kiehl, J. T. and K. E. Trenberth (1997). Earth's annual global mean energy budget. *Bulletin of the American Meteorological Society*, 78(2): pp. 197–208. doi:10.1175/1520-0477(1997)078<0197:EAGMEB>2.0.CO;2.

Kilic, L., C. Prigent, C. Jimenez, and C. Donlon (2021). Technical note: A sensitivity analysis from 1 to 40 GHz for observing the Arctic Ocean with the Copernicus Imaging Microwave Radiometer. *Ocean Science*, 17(2): pp. 455–461. doi:10.5194/os-17-455-2021.

Kim, Y.-H., S.-K. Min, N. P. Gillett, D. Notz, and E. Malinina (2023). Observationally-constrained projections of an ice-free Arctic even under a low emission scenario. *Nature Communications*, 14(1): p. 3139. doi:10.1038/s41467-023-38511-8.

King, J., S. Howell, M. Brady, P. Toose, C. Derksen, C. Haas, and J. Beckers (2020). Local-scale variability of snow density on Arctic sea ice. *The Cryosphere*, 14(12): pp. 4323–4339. doi:10.5194/tc-14-4323-2020.

Kirbus, B., S. Tiedeck, A. Camplani, J. Chylik, S. Crewell, S. Dahlke, K. Ebell, I. Gorodetskaya, H. Griesche, D. Handorf, I. Höschel, M. Lauer, R. Neggers, J. Rückert, M. D.

Shupe, G. Spreen, A. Walbröl, M. Wendisch, and A. Rinke (2023). Surface impacts and associated mechanisms of a moisture intrusion into the Arctic observed in mid-April 2020 during MOSAiC. *Frontiers in Earth Science*, 11: p. 1147848. doi:10.3389/feart.2023.1147848.

Kirchhoff, G. (1860). Ueber das Verhältniss zwischen dem Emissionsvermögen und dem Absorptionsvermögen der Körper für Wärme und Licht. *Annalen der Physik und Chemie*, 185(2): pp. 275–301. doi:10.1002/andp.18601850205.

Klein, L. and C. T. Swift (1977). An improved model for the dielectric constant of sea water at microwave frequencies. *IEEE Journal of Oceanic Engineering*, 2: pp. 104–111. doi:10.1109/JOE.1977.1145319.

Knust, R. (2017). Polar research and supply vessel POLARSTERN operated by the Alfred-Wegener-Institute. *Journal of large-scale research facilities JLSRF*, 3: p. A119. doi:10.17815/jlsrf-3-163.

Kortum, K., S. Singha, and G. Spreen (2022). Robust multiseasonal ice classification from high-resolution X-Band SAR. *IEEE Transactions on Geoscience and Remote Sensing*, 60: pp. 1–12. doi:10.1109/TGRS.2022.3144731.

Kwok, R. (2020). Arctic Ocean sea ice snow depth and ice thickness. doi:10.1594/PANGAEA.914565. [Dataset].

Kwok, R., G. F. Cunningham, M. Wensnahan, I. Rigor, H. J. Zwally, and D. Yi (2009). Thinning and volume loss of the Arctic Ocean sea ice cover: 2003–2008. *Journal of Geophysical Research: Oceans*, 114(C7). doi:10.1029/2009JC005312.

Kwok, R., S. Kacimi, M. Webster, N. Kurtz, and A. Petty (2020). Arctic snow depth and sea ice thickness from ICESat-2 and CryoSat-2 freeboards: A first examination. *Journal of Geophysical Research: Oceans*, 125(3). doi:10.1029/2019JC016008.

Lainema, M. and J. Nurminem (2009). *A history of Arctic exploration: discovery, adventure and endurance at the top of the world*. Conway, London New York. ISBN 978-1-84486-069-2.

Landrum, L. and M. M. Holland (2020). Extremes become routine in an emerging new Arctic. *Nature Climate Change*, 10(12): pp. 1108–1115. doi:10.1038/s41558-020-0892-z.

Lavergne, T., A. M. Sørensen, S. Kern, R. Tonboe, D. Notz, S. Aaboe, L. Bell, G. Dybkjær, S. Eastwood, C. Gabarro, G. Heygster, M. A. Killie, M. Brandt Kreiner, J. Lavelle, R. Saldo, S. Sandven, and L. T. Pedersen (2019). Version 2 of the EUMETSAT OSI SAF and ESA CCI sea-ice concentration climate data records. *The Cryosphere*, 13(1): pp. 49–78. doi:10.5194/tc-13-49-2019.

Lehning, M., P. Bartelt, B. Brown, and C. Fierz (2002a). A physical SNOWPACK model for the Swiss avalanche warning: Part III: meteorological forcing, thin layer formation and evaluation. *Cold Regions Science and Technology*, 35(3): pp. 169–184. doi:10.1016/S0165-232X(02)00072-1.

Lehning, M., P. Bartelt, B. Brown, C. Fierz, and P. Satyawali (2002b). A physical SNOWPACK model for the Swiss avalanche warning: Part II. snow microstructure. *Cold Regions Science and Technology*, 35(3): pp. 147–167. doi:10.1016/S0165-232X(02)00073-3.

Lei, R., B. Cheng, M. Hoppmann, and G. Zuo (2021). Snow depth and sea ice thickness derived from the measurements of SIMBA buoys deployed in the Arctic Ocean during the Legs 1a, 1, and 3 of the MOSAiC campaign in 2019-2020. doi:10.1594/PANGAEA.938244. [Dataset].

Leinss, S., H. Löwe, M. Proksch, J. Lemmetyinen, A. Wiesmann, and I. Hajnsek (2016). Anisotropy of seasonal snow measured by polarimetric phase differences in radar time series. *The Cryosphere*, 10(4): pp. 1771–1797. doi:10.5194/tc-10-1771-2016.

Lemmetyinen, J., C. Derksen, J. Pulliainen, W. Strapp, P. Toose, A. Walker, S. Tauriainen, J. Pihlflyckt, J.-P. Karna, and M. Hallikainen (2009). A comparison of airborne microwave brightness temperatures and snowpack properties across the boreal forests of Finland and Western Canada. *IEEE Transactions on Geoscience and Remote Sensing*, 47(3): pp. 965–978. doi:10.1109/TGRS.2008.2006358.

Levine, X. J., I. Cvijanovic, P. Ortega, M. G. Donat, and E. Tourigny (2021). Atmospheric feedback explains disparate climate response to regional Arctic sea-ice loss. *npj Climate and Atmospheric Science*, 4(1): pp. 1–8. doi:10.1038/s41612-021-00183-w.

Liebe, H. J. (1985). An updated model for millimeter wave propagation in moist air. *Radio Science*, 20(5): pp. 1069–1089. doi:10.1029/RS020i005p01069.

Light, B., G. A. Maykut, and T. C. Grenfell (2003). Effects of temperature on the microstructure of first-year Arctic sea ice. *Journal of Geophysical Research: Oceans*, 108(C2): pp. n/a–n/a. doi:10.1029/2001JC000887.

Liu, G. and J. A. Curry (2003). Observation and interpretation of microwave cloud signatures over the Arctic Ocean during winter. *Journal of Applied Meteorology*, 42(1): pp. 51–64. doi:10.1175/1520-0450(2003)042<0051:OAIOMC>2.0.CO;2.

Livingstone, C., R. Onstott, L. Arsenault, A. Gray, and K. Singh (1987a). Microwave sea-ice signatures near the onset of melt. *IEEE Transactions on Geoscience and Remote Sensing*, GE-25(2): pp. 174–187. doi:10.1109/TGRS.1987.289816.

Livingstone, C. E., R. K. Hawkins, A. L. Gray, L. Drapier Arsenault, K. Okamoto, T. L. Wilkinson, and D. Pearson (1983). The CCRS/SURSAT Active-Passive Experiment 1978-1980: The microwave signatures of sea ice.

Livingstone, C. E., K. P. Singh, and A. L. Gray (1987b). Seasonal and regional variations of active/passive microwave signatures of sea ice. *IEEE Transactions on Geoscience and Remote Sensing*, GE-25(2): pp. 159–173. doi:10.1109/TGRS.1987.289815.

Lohanick, A. W. (1993). Microwave brightness temperatures of laboratory-grown undeformed first-year ice with an evolving snow cover. *Journal of Geophysical Research: Oceans*, 98(C3): pp. 4667–4674. doi:10.1029/92JC02756.

Long, C. N., J. M. Sabburg, J. Calbó, and D. Pagès (2006). Retrieving cloud characteristics from ground-based daytime color all-sky images. *Journal of Atmospheric and Oceanic Technology*, 23(5): pp. 633–652. doi:10.1175/JTECH1875.1.

Lu, J., R. Scarlat, G. Heygster, and G. Spreen (2022). Reducing weather influences on an 89 GHz sea ice concentration algorithm in the Arctic using retrievals from an optimal estimation method. *Journal of Geophysical Research: Oceans*, 127(9): p. e2019JC015912. doi:10.1029/2019JC015912.

Lubin, D. and R. Massom (2005). *Polar remote sensing*. Springer, Berlin : New York, 1st ed edition. ISBN 978-3-540-43097-1 978-3-540-26101-8.

Ludwig, V., G. Spreen, and L. T. Pedersen (2020). Evaluation of a new merged sea-ice concentration dataset at 1 km resolution from thermal infrared and passive microwave satellite data in the Arctic. *Remote Sensing*, 12(19): p. 3183. doi:10.3390/rs12193183.

Łupikasza, E. B. and K. Cielecka-Nowak (2020). Changing probabilities of days with snow and rain in the Atlantic Sector of the Arctic under the current warming trend. *Journal of Climate*, 33(7): pp. 2509–2532. doi:10.1175/JCLI-D-19-0384.1.

Maahn, M., D. D. Turner, U. Löhnert, D. J. Posselt, K. Ebell, G. G. Mace, and J. M. Comstock (2020). Optimal estimation retrievals and their uncertainties: What every atmospheric scientist should know. *Bulletin of the American Meteorological Society*, 101(9): pp. E1512–E1523. doi:10.1175/BAMS-D-19-0027.1.

Macfarlane, A. R., M. Schneebeli, R. Dadic, D. N. Wagner, S. Arndt, D. Clemens-Sewall, S. Hämmerle, H.-R. Hannula, M. Jaggi, N. Kolabutin, D. Krampe, M. Lehning, I. Matero, M. Nicolaus, M. Oggier, R. Pirazzini, C. Polashenski, I. Raphael, J. Regnery, E. Shimanchuck, M. M. Smith, and A. Tavri (2021). Snowpit SnowMicroPen (SMP) force profiles collected during the MOSAiC expedition. doi:10.1594/PANGAEA.935554. [Dataset].

Maeda, T., Y. Taniguchi, and K. Imaoka (2016). GCOM-W1 AMSR2 Level 1R product: Dataset of brightness temperature modified using the antenna pattern matching technique. *IEEE Transactions on Geoscience and Remote Sensing*, 54(2): pp. 770–782. doi:10.1109/TGRS.2015.2465170.

Manabe, S. and R. T. Wetherald (1967). Thermal equilibrium of the atmosphere with a given distribution of relative humidity. *Journal of the Atmospheric Sciences*, 24(3): pp. 241–259. doi:10.1175/1520-0469(1967)024<0241:TEOTAW>2.0.CO;2.

Maslanik, J. A., C. Fowler, J. Stroeve, S. Drobot, J. Zwally, D. Yi, and W. Emery (2007). A younger, thinner Arctic ice cover: Increased potential for rapid, extensive sea-ice loss. *Geophysical Research Letters*, 34(24): p. L24501. doi:10.1029/2007GL032043.

Mathew, N., G. Heygster, and C. Melsheimer (2009). Surface emissivity of the Arctic sea ice at AMSR-E frequencies. *IEEE Transactions on Geoscience and Remote Sensing*, 47(12): pp. 4115–4124. doi:10.1109/TGRS.2009.2023667.

Mathew, N., G. Heygster, C. Melsheimer, and L. Kaleschke (2008). Surface emissivity of Arctic sea ice at AMSU window frequencies. *IEEE Transactions on Geoscience and Remote Sensing*, 46(8): pp. 2298–2306. doi:10.1109/TGRS.2008.916630.

Mathews, N. (2007). *Retrieval of Surface Emissivity of Sea Ice and Temperature Profiles over Sea Ice from Passive Microwave Radiometers.* Ph.D. thesis, University of Bremen.

Maturilli, M., D. J. Holdridge, S. Dahlke, J. Graeser, A. Sommerfeld, R. Jaiser, H. Deckelmann, and A. Schulz (2021). Initial radiosonde data from 2019-10 to 2020-09 during project MOSAiC. doi:10.1594/PANGAEA.928656. [Dataset. Accessed March 30, 2021].

Maturilli, M. and M. Kayser (2016). Arctic warming, moisture increase and circulation changes observed in the Ny-Ålesund homogenized radiosonde record. *Theoretical and Applied Climatology*. doi:10.1007/s00704-016-1864-0.

Mätzler, C. (1998). Improved Born approximation for scattering of radiation in a granular medium. *Journal of Applied Physics*, 83(11): pp. 6111–6117. doi:10.1063/1.367496.

Mätzler, C. (2002). Relation between grain-size and correlation length of snow. *Journal of Glaciology*, 48(162): pp. 461–466. doi:10.3189/172756502781831287.

Mätzler, C. (2005). On the determination of surface emissivity from satellite observations. *IEEE Geoscience and Remote Sensing Letters*, 2(2): pp. 160–163. doi:10.1109/LGRS.2004.842448.

Mätzler, C., R. Ramseier, and E. Svendsen (1984). Polarization effects in seaice signatures. *IEEE Journal of Oceanic Engineering*, 9(5): pp. 333–338. doi:10.1109/JOE.1984.1145646.

Mätzler, C. and U. Wegmuller (1987). Dielectric properties of freshwater ice at microwave frequencies. *Journal of Physics D: Applied Physics*, 20(12): pp. 1623–1630. doi:10.1088/0022-3727/20/12/013.

Mätzler, C. and A. Wiesmann (1999). Extension of the Microwave Emission Model of Layered Snowpacks to coarse-grained snow. *Remote Sensing of Environment*, 70(3): pp. 317–325. doi:10.1016/S0034-4257(99)00047-4.

Maykut, G. A. (1986). The surface heat and mass balance. In Untersteiner, N. (editor), *The Geophysics of Sea Ice*, pp. 395–463. Springer US, Boston, MA. ISBN 978-1-4899-5352-0. doi:10.1007/978-1-4899-5352-0_6.

McCrystall, M. R., J. Stroeve, M. Serreze, B. C. Forbes, and J. A. Screen (2021). New climate models reveal faster and larger increases in Arctic precipitation than previously projected. *Nature Communications*, 12(1): p. 6765. doi:10.1038/s41467-021-27031-y.

Mchedlishvili, A., C. Lüpkes, A. Petty, M. Tsamados, and G. Spreen (2023). New estimates of pan-Arctic sea ice–atmosphere neutral drag coefficients from ICESat-2 elevation data. *The Cryosphere*, 17(9): pp. 4103–4131. doi:10.5194/tc-17-4103-2023.

Mech, M., L.-L. Kliesch, A. Anhäuser, T. Rose, P. Kollias, and S. Crewell (2019). Microwave Radar/radiometer for Arctic Clouds (MiRAC): first insights from the ACLOUD campaign. *Atmospheric Measurement Techniques*, 12(9): pp. 5019–5037. doi:10.5194/amt-12-5019-2019.

Mech, M., M. Maahn, S. Kneifel, D. Ori, E. Orlandi, P. Kollias, V. Schemann, and S. Crewell (2020). PAMTRA 1.0: the Passive and Active Microwave radiative TRAnsfer tool for simulating radiometer and radar measurements of the cloudy atmosphere. *Geoscientific Model Development*, 13(9): pp. 4229–4251. doi:10.5194/gmd-13-4229-2020.

Mech, M., N. Risse, G. Marrollo, and D. Paul (2022). ac3airborne. Zenodo. doi:10.5281/ZENODO.7305586. [Dataset and Software].

Meier, W., F. Fetterer, A. Windnagel, and S. Stewart (2021). NOAA/NSIDC climate data record of passive microwave sea ice concentration, version 4. doi:10.7265/EFMZ-2T65. [Dataset].

Meier, W. and J. Stroeve (2022). An updated assessment of the changing Arctic sea ice cover. *Oceanography*. doi:10.5670/oceanog.2022.114.

Meier, W. N. and A. Ivanoff (2017). Intercalibration of AMSR2 NASA Team 2 Algorithm sea ice concentrations with AMSR-E slow rotation data. *IEEE Journal of Selected Topics in Applied Earth Observations and Remote Sensing*, 10(9): pp. 3923–3933. doi:10.1109/JSTARS.2017.2719624.

Meier, W. N., A. Petty, S. Hendricks, D. Perovich, S. Farrell, M. Webster, D. Divine, S. Gerland, L. Kaleschke, R. Ricker, and X. Tian-Kunze (2022). Arctic Report Card 2022: Sea Ice. Technical report, Global Ocean Monitoring and Observing (U.S.).

Meier, W. N. and J. S. Stewart (2023). NSIDC Land, Ocean, Coast, Ice, and Sea Ice Region Masks. Technical Report NSIDC Special Report 25, National Snow and Ice Data Center, Boulder CO, USA.

Meissner, T. and F. Wentz (2004). The complex dielectric constant of pure and sea water from microwave satellite observations. *IEEE Transactions on Geoscience and Remote Sensing*, 42(9): pp. 1836–1849. doi:10.1109/TGRS.2004.831888.

Meissner, T. and F. J. Wentz (2012). The emissivity of the ocean surface between 6 and 90 GHz over a large range of wind speeds and Earth incidence angles. *IEEE Transactions on Geoscience and Remote Sensing*, 50(8): pp. 3004–3026. doi:10.1109/TGRS.2011.2179662.

Melsheimer, C. (2019). *ASI Version 5 Sea Ice Concentration User Guide*. Institute of Environmental Physics, University of Bremen.

Melsheimer, C., G. Heygster, and L. T. Pedersen (2008). Integrated retrieval of surface and atmospheric parameters over the Arctic from AMSR-E satellite microwave radiometer data using inverse methods. In *IGARSS 2008 - 2008 IEEE International Geoscience and Remote Sensing Symposium*, volume 4, pp. IV – 986–IV – 989. doi:10.1109/IGARSS.2008.4779890.

Merkouriadi, I., B. Cheng, S. R. Hudson, and M. A. Granskog (2020). Effect of frequent winter warming events (storms) and snow on sea-ice growth – a case from the Atlantic sector of the Arctic Ocean during the N-ICE2015 campaign. *Annals of Glaciology*, 61(82): pp. 164–170. doi:10.1017/aog.2020.25.

Merkouriadi, I., J.-C. Gallet, R. M. Graham, G. E. Liston, C. Polashenski, A. Rösel, and S. Gerland (2017). Winter snow conditions on Arctic sea ice north of Svalbard during the Norwegian young sea ICE (N-ICE2015) expedition. *Journal of Geophysical Research: Atmospheres*, 122(20): pp. 10,837–10,854. doi:10.1002/2017JD026753.

Mie, G. (1908). Beiträge zur Optik trüber Medien, speziell kolloidaler Metallösungen. *Annalen der Physik*, 330(3): pp. 377–445. doi:10.1002/andp.19083300302.

Montpetit, B., A. Royer, A. Roy, A. Langlois, and C. Derksen (2013). Snow microwave emission modeling of ice lenses within a snowpack using the Microwave Emission Model for Layered Snowpacks. *IEEE Transactions on Geoscience and Remote Sensing*, 51(9): pp. 4705–4717. doi:10.1109/TGRS.2013.2250509.

Murashkin, D., G. Spreen, M. Huntemann, and W. Dierking (2018). Method for detection of leads from Sentinel-1 SAR images. *Ann. Glaciol.*, 59(76pt2): pp. 124–136. doi:10.1017/aog.2018.6.

Nakawo, M. and N. K. Sinha (1981). Growth rate and salinity profile of first-year sea ice in the high Arctic. *Journal of Glaciology*, 27(96): pp. 315–330. doi:10.3189/S0022143000015409.

Nandan, V., T. Geldsetzer, J. Yackel, M. Mahmud, R. Scharien, S. Howell, J. King, R. Ricker, and B. Else (2017). Effect of snow salinity on CryoSat-2 Arctic first-year sea ice freeboard measurements: Sea ice brine-snow effect on cryosat-2. *Geophysical Research Letters*, 44(20): pp. 10,419–10,426. doi:10.1002/2017GL074506.

Nansen, F. (1897). *Farthest North*. Modern Library, New York, reprint 1968 edition. ISBN 978-0-375-75472-2.

Negusini, M., B. H. Petkov, V. Tornatore, S. Barindelli, L. Martelli, P. Sarti, and C. Tomasi (2021). Water vapour assessment using GNSS and radiosondes over polar regions and estimation of climatological trends from long-term time series analysis. *Remote Sensing*, 13(23): p. 4871. doi:10.3390/rs13234871.

Nicolaus, M., A. Jutila, I. Raphael, and M. Hoppmann (2021). Snow height on sea ice, meteorological conditions and drift of sea ice from autonomous measurements from buoy 2020S99, deployed during MOSAiC 2019/20. doi:10.1594/PANGAEA.936227. [Dataset].

Nicolaus, M., D. K. Perovich, G. Spreen, M. A. Granskog, L. von Albedyll, M. Angelopoulos, P. Anhaus, S. Arndt, H. J. Belter, V. Bessonov, G. Birnbaum, J. Brauchle, R. Calmer, E. Cardellach, B. Cheng, D. Clemens-Sewall, R. Dadic, E. Damm, G. de Boer, O. Demir, K. Dethloff, D. V. Divine, A. A. Fong, S. Fons, M. M. Frey, N. Fuchs, C. Gabarró, S. Gerland, H. F. Goessling, R. Gradinger, J. Haapala, C. Haas, J. Hamilton, H.-R. Hannula, S. Hendricks, A. Herber, C. Heuzé, M. Hoppmann, K. V. Høyland, M. Huntemann, J. K. Hutchings, B. Hwang, P. Itkin, H.-W. Jacobi, M. Jaggi, A. Jutila, L. Kaleschke, C. Katlein, N. Kolabutin, D. Krampe, S. S. Kristensen, T. Krumpen, N. Kurtz, A. Lampert, B. A. Lange, R. Lei, B. Light, F. Linhardt, G. E. Liston, B. Loose, A. R. Macfarlane, M. Mahmud, I. O. Matero, S. Maus, A. Morgenstern, R. Naderpour, V. Nandan, A. Niubom, M. Oggier, N. Oppelt, F. Pätzold, C. Perron, T. Petrovsky, R. Pirazzini, C. Polashenski, B. Rabe, I. A. Raphael, J. Regnery, M. Rex, R. Ricker, K. Riemann-Campe, A. Rinke, J. Rohde, E. Salganik, R. K. Scharien, M. Schiller, M. Schneebeli, M. Semmling, E. Shimanchuk, M. D. Shupe, M. M. Smith, V. Smolyanitsky, V. Sokolov, T. Stanton, J. Stroeve, L. Thielke, A. Timofeeva, R. T. Tonboe, A. Tavri, M. Tsamados, D. N. Wagner, D. Watkins, M. Webster, and M. Wendisch

(2022). Overview of the MOSAiC expedition: Snow and sea ice. *Elem Sci Anth*, 10(1): p. 000046. doi:10.1525/elementa.2021.000046.

Niehaus, H., G. Spreen, G. Birnbaum, L. Istomina, E. Jäkel, F. Linhardt, N. Neckel, N. Fuchs, M. Nicolaus, T. Sperzel, R. Tao, M. Webster, and N. Wright (2023). Sea ice melt pond fraction derived from Sentinel-2 data: Along the MOSAiC drift and Arctic-wide. *Geophysical Research Letters*, 50(5): p. e2022GL102102. doi:10.1029/2022GL102102.

Nielsen-Englyst, P., J. L. Høyer, K. S. Madsen, R. T. Tonboe, G. Dybkjær, and S. Skarpalezos (2021). Deriving Arctic 2 m air temperatures over snow and ice from satellite surface temperature measurements. *The Cryosphere*, 15(7): pp. 3035–3057. doi:10.5194/tc-15-3035-2021.

Nomokonova, T., K. Ebell, U. Löhnert, M. Maturilli, C. Ritter, and E. O'Connor (2019). Statistics on clouds and their relation to thermodynamic conditions at Ny-Ålesund using ground-based sensor synergy. *Atmospheric Chemistry and Physics*, 19(6): pp. 4105–4126. doi:10.5194/acp-19-4105-2019.

NORSEX, G. (1983). Norwegian remote sensing experiment in a marginal ice zone. *Science*, 220(4599): pp. 781–787. doi:10.1126/science.220.4599.781.

NSIDC (2023). A guide to NSIDC's polar stereographic projection. https://nsidc.org/data/user-resources/help-center/guide-nsidcs-polar-stereographic-projection. [Website].

Nyquist, H. (1928). Thermal agitation of electric charge in conductors. *Physical Review*, 32(1): pp. 110–113. doi:10.1103/PhysRev.32.110.

Oelke, C. (1997). Atmospheric signatures in sea-ice concentration estimates from passive microwaves: Modelled and observed. *International Journal of Remote Sensing*, 18(5): pp. 1113–1136. doi:10.1080/014311697218601.

Onstott, R. G., T. C. Grenfell, C. Mätzler, C. A. Luther, and E. A. Svendsen (1987). Evolution of microwave sea ice signatures during early summer and midsummer in the marginal ice zone. *Journal of Geophysical Research*, 92(C7): p. 6825. doi:10.1029/JC092iC07p06825.

Parracho, A. C., O. Bock, and S. Bastin (2018). Global IWV trends and variability in atmospheric reanalyses and GPS observations. *Atmospheric Chemistry and Physics*, 18(22): pp. 16213–16237. doi:10.5194/acp-18-16213-2018.

Pedersen, L. T., R. Saldo, N. Ivanova, S. Kern, G. Heygster, R. Tonboe, M. Huntemann, B. Ozsoy, F. Ardhuin, and L. Kaleschke (2021). Reference dataset for sea ice concentration. doi:10.6084/M9.FIGSHARE.6626549.V7. [Dataset].

Perovich, D. K. (2017). Sea ice and sunlight. In Thomas, D. N. (editor), *Sea Ice*, pp. 110–137. John Wiley & Sons, Ltd. ISBN 978-1-118-77837-1. doi:10.1002/9781118778371.ch4.

Perovich, D. K., C. S. Roesler, and W. S. Pegau (1998). Variability in Arctic sea ice optical properties. *Journal of Geophysical Research: Oceans*, 103(C1): pp. 1193–1208. doi:10.1029/97JC01614.

Persson, O. and T. Vihma (2017). The atmosphere over sea ice. In *Sea Ice*, pp. 160–196. John Wiley & Sons, Ltd. ISBN 978-1-118-77837-1. doi:10.1002/9781118778371.ch6.

Petrich, C. and H. Eicken (2017). Overview of sea ice growth and properties. In *Sea Ice*, chapter 1, pp. 1–41. John Wiley & Sons, Ltd. ISBN 978-1-118-77837-1. doi:10.1002/9781118778371.ch1.

Petty, G. W. (2006). *A first course in atmospheric radiation*. Sundog Pub, Madison, Wis, 2nd edition. ISBN 978-0-9729033-1-8.

Picard, G., L. Brucker, A. Roy, F. Dupont, M. Fily, A. Royer, and C. Harlow (2013). Simulation of the microwave emission of multi-layered snowpacks using the Dense Media Radiative transfer theory: the DMRT-ML model. *Geoscientific Model Development*, 6(4): pp. 1061–1078. doi:10.5194/gmd-6-1061-2013.

Picard, G., H. Löwe, and C. Mätzler (2022). Brief communication: A continuous formulation of microwave scattering from fresh snow to bubbly ice from first principles. *The Cryosphere*, 16(9): pp. 3861–3866. doi:10.5194/tc-16-3861-2022.

Picard, G., M. Sandells, and H. Löwe (2018). SMRT: an active–passive microwave radiative transfer model for snow with multiple microstructure and scattering formulations (v1.0). *Geoscientific Model Development*, 11(7): pp. 2763–2788. doi:10.5194/gmd-11-2763-2018.

Pithan, F., G. Svensson, R. Caballero, D. Chechin, T. Cronin, A. Ekman, R. A. J. Neggers, M. Shupe, A. Solomon, M. Tjernstroem, and M. Wendisch (2018). Role of air-mass transformations in exchange between the Arctic and mid-latitudes. *Nat. Geosci.*, 11: pp. 805–812. doi:10.1038/s41561-018-0234-1.

Polder, D. and J. van Santeen (1946). The effective permeability of mixtures of solids. *Physica*, 12(5): pp. 257–271. doi:10.1016/S0031-8914(46)80066-1.

Post, E., R. B. Alley, T. R. Christensen, M. Macias-Fauria, B. C. Forbes, M. N. Gooseff, A. Iler, J. T. Kerby, K. L. Laidre, M. E. Mann, J. Olofsson, J. C. Stroeve, F. Ulmer, R. A. Virginia, and M. Wang (2019). The polar regions in a 2°C warmer world. *Science Advances*, 5(12): p. eaaw9883. doi:10.1126/sciadv.aaw9883.

Proksch, M., H. Löwe, and M. Schneebeli (2015). Density, specific surface area, and correlation length of snow measured by high-resolution penetrometry. *Journal of Geophysical Research: Earth Surface*, 120(2): pp. 346–362. doi:10.1002/2014JF003266.

Rabe, B., C. Heuzé, J. Regnery, Y. Aksenov, J. Allerholt, M. Athanase, Y. Bai, C. Basque, D. Bauch, T. M. Baumann, D. Chen, S. T. Cole, L. Craw, A. Davies, E. Damm, K. Dethloff, D. V. Divine, F. Doglioni, F. Ebert, Y.-C. Fang, I. Fer, A. A. Fong, R. Gradinger, M. A. Granskog, R. Graupner, C. Haas, H. He, Y. He, M. Hoppmann, M. Janout, D. Kadko, T. Kanzow, S. Karam, Y. Kawaguchi, Z. Koenig, B. Kong, R. A. Krishfield, T. Krumpen, D. Kuhlmey, I. Kuznetsov, M. Lan, G. Laukert, R. Lei, T. Li, S. Torres-Valdés, L. Lin, L. Lin, H. Liu, N. Liu, B. Loose, X. Ma, R. McKay, M. Mallet, R. D. C. Mallett, W. Maslowski, C. Mertens, V. Mohrholz, M. Muilwijk, M. Nicolaus, J. K. O'Brien, D. Perovich, J. Ren, M. Rex, N. Ribeiro, A. Rinke, J. Schaffer, I. Schuffenhauer, K. Schulz, M. D. Shupe, W. Shaw, V. Sokolov, A. Sommerfeld, G. Spreen, T. Stanton, M. Stephens, J. Su, N. Sukhikh, A. Sundfjord, K. Thomisch, S. Tippenhauer, J. M. Toole, M. Vredenborg, M. Walter, H. Wang, L. Wang, Y. Wang, M. Wendisch, J. Zhao, M. Zhou, and J. Zhu (2022). Overview of the MOSAiC expedition: Physical oceanography. *Elem Sci Anth*, 10(1): p. 00062. doi:10.1525/elementa.2021.00062.

Radiometrics (2004). AC1900 19 GHz, AC3700 37 GHz, and AC8900 89 GHz dual polarization radiometers. *Radiometric Corporation*.

Rees, A., J. Lemmetyinen, C. Derksen, J. Pulliainen, and M. English (2010). Observed and modelled effects of ice lens formation on passive microwave brightness temperatures over snow covered tundra. *Remote Sensing of Environment*, 114(1): pp. 116–126. doi:10.1016/j.rse.2009.08.013.

Revels, J., M. Lubin, and T. Papamarkou (2016). Forward-mode automatic differentiation in Julia. *arXiv:1607.07892 [cs.MS]*.

Ridley, J. K., E. W. Blockley, and M. A. Ringer (2023). Arctic sea ice causes seasonal differences in the response of Arctic water vapor to climate warming in the CMIP6 Model, HadGEM3-GC3.1. *Geophysical Research Letters*, 50(13): p. e2022GL102541. doi:10.1029/2022GL102541.

Rinke, A., J. J. Cassano, E. N. Cassano, R. Jaiser, and D. Handorf (2021). Meteorological conditions during the MOSAiC expedition: Normal or anomalous? *Elementa: Science of the Anthropocene*, 9(1). doi:10.1525/elementa.2021.00023.

Rinke, A., M. Maturilli, R. M. Graham, H. Matthes, D. Handorf, L. Cohen, S. R. Hudson, and J. C. Moore (2017). Extreme cyclone events in the Arctic: Wintertime variability and trends. *Environmental Research Letters*, 12(9): p. 094006. doi:10.1088/1748-9326/aa7def.

Rinke, A., B. Segger, S. Crewell, M. Maturilli, T. Naakka, T. Nygård, T. Vihma, F. Alshawaf, G. Dick, J. Wickert, and J. Keller (2019). Trends of vertically integrated water vapor over the Arctic during 1979–2016: Consistent moistening all over? *Journal of Climate*, 32(18): pp. 6097–6116. doi:10.1175/JCLI-D-19-0092.1.

Risse, N., Mario Mech, C. Prigent, Gunnar Spreen, and S. Crewell (2024). Assessing the sea ice microwave emissivity up to submillimeter waves from airborne and satellite observations. In preparation for submission.

Rodgers, C. D. (2000). *Inverse Methods for Atmospheric Sounding: Theory and Practice*. WORLD SCIENTIFIC. ISBN 978-981-02-2740-1 978-981-281-371-8. doi:10.1142/3171.

Rose, T., S. Crewell, U. Löhnert, and C. Simmer (2005). A network suitable microwave radiometer for operational monitoring of the cloudy atmosphere. *Atmospheric Research*, 75(3): pp. 183–200. doi:10.1016/j.atmosres.2004.12.005.

Rosenkranz, P. (2017). Line-by-line microwave radiative transfer (non-scattering). Remote Sensing Code Library. doi:10.21982/M81013. [Computer Code].

Ross, R. J. and W. P. Elliott (1996). Tropospheric water vapor climatology and trends over North America: 1973–93. *Journal of Climate*, 9(12): pp. 3561–3574. doi:10.1175/1520-0442(1996)009<3561:TWVCAT>2.0.CO;2.

Rostosky, P. and G. Spreen (2023). Relevance of warm air intrusions for Arctic satellite sea ice concentration time series. *The Cryosphere*, 17(9): pp. 3867–3881. doi:10.5194/tc-17-3867-2023.

Rostosky, P., G. Spreen, S. L. Farrell, T. Frost, G. Heygster, and C. Melsheimer (2018). Snow depth retrieval on Arctic sea ice from passive microwave radiometers—improvements and extensions to multiyear ice using lower frequencies. *Journal of Geophysical Research: Oceans*, 123(10): pp. 7120–7138. doi:10.1029/2018JC014028.

Rostosky, P., G. Spreen, S. Gerland, M. Huntemann, and M. Mech (2020). Modeling the microwave emission of snow on Arctic sea ice for estimating the uncertainty of satellite retrievals. *Journal of Geophysical Research: Oceans*, 125(3). doi:10.1029/2019JC015465.

Rückert, J. E. (2023). Satellite-based measurements of brightness temperatures (AMSR2 sensor) colocated to MOSAiC ground measurements. doi:10.5281/ZENODO.8144560. [Dataset].

Rückert, J. E., M. Huntemann, R. T. Tonboe, and G. Spreen (2023a). Modeling snow and ice microwave emissions in the Arctic for a multi-parameter retrieval of surface and atmospheric variables from microwave radiometer satellite data. *Earth and Space Science*, 10(10): p. e2023EA003177. doi:10.1029/2023EA003177.

Rückert, J. E., P. Rostosky, M. Huntemann, D. Clemens-Sewall, K. Ebell, L. Kaleschke, J. Lemmetyinen, A. R. Macfarlane, R. Naderpour, J. Stroeve, A. Walbröl, and G. Spreen (2023b). Sea ice concentration satellite retrievals influenced by surface changes due to warm air intrusions: A case study from the MOSAiC expedition. *Elementa: Science of the Anthropocene*, 11(1): p. 00039. doi:10.1525/elementa.2023.00039.

Rückert, J. E., A. Walbröl, H. Niehaus, and G. Spreen (2023c). Sea ice density and salinity profiles measured during RV POLARSTERN cruise PS131. doi:10.1594/PANGAEA .961670. [Dataset].

Rückert, J. E., A. Walbröl, N. Risse, P. Krobot, R. Haseneder-Lind, M. Mech, K. Ebell, and G. Spreen (2023d). Measuring microwave sea ice and ocean brightness temperature and emissivity between 22 and 243 GHz by ship-based radiometers with rotatable mirrors. Paper submitted for publication to Annals of Glaciology.

Rückert, J. E., A. Walbröl, and G. Spreen (2023e). Sea ice temperature profiles measured during RV POLARSTERN cruise PS131. doi:10.1594/PANGAEA.961656. [Dataset].

Scambos, T., M. Frezzotti, T. Haran, J. Bohlander, J. Lenaerts, M. Van Den Broeke, K. Jezek, D. Long, S. Urbini, K. Farness, T. Neumann, M. Albert, and J.-G. Winther (2012). Extent of low-accumulation 'wind glaze' areas on the East Antarctic plateau: implications for continental ice mass balance. *Journal of Glaciology*, 58(210): pp. 633–647. doi:10.3189/2012JoG11J232.

Scarlat, R. (2018). *Improving an optimal estimation algorithm for surface and atmospheric parameter retrieval using passive microwave data in the Arctic*. Ph.D. thesis, University of Bremen, Bremen.

Scarlat, R. C., G. Heygster, and L. T. Pedersen (2017). Experiences with an optimal estimation algorithm for surface and atmospheric parameter retrieval from passive microwave data in the Arctic. *IEEE Journal of Selected Topics in Applied Earth Observations and Remote Sensing*, 10(9): pp. 3934–3947. doi:10.1109/JSTARS.2017.2739858.

Scarlat, R. C., G. Spreen, G. Heygster, M. Huntemann, C. Paţilea, L. T. Pedersen, and R. Saldo (2020). Sea ice and atmospheric parameter retrieval from satellite microwave radiometers: Synergy of AMSR2 and SMOS compared with the CIMR candidate mission. *Journal of Geophysical Research: Oceans*, 125(3). doi:10.1029/2019JC015749.

Schmithüsen, H., A. Raeke, and J. Kieser (2021a). Meteorological observations during POLARSTERN cruise PS122/1. doi:10.1594/PANGAEA.935263. [Dataset].

Schmithüsen, H., C. Rohleder, and R. Hausen (2021b). Meteorological observations during POLARSTERN cruise PS122/3. doi:10.1594/PANGAEA.935265. [Dataset].

Schmithüsen, H., S. Schröter, and J. Wenzel (2021c). Meteorological observations during POLARSTERN cruise PS122/2. doi:10.1594/PANGAEA.935264. [Dataset].

Schneising, O., M. Buchwitz, M. Reuter, H. Bovensmann, J. P. Burrows, T. Borsdorff, N. M. Deutscher, D. G. Feist, D. W. T. Griffith, F. Hase, C. Hermans, L. T. Iraci, R. Kivi, J. Landgraf, I. Morino, J. Notholt, C. Petri, D. F. Pollard, S. Roche, K. Shiomi, K. Strong, R. Sussmann, V. A. Velazco, T. Warneke, and D. Wunch (2019). A scientific algorithm to simultaneously retrieve carbon monoxide and methane from TROPOMI onboard Sentinel-5 Precursor. *Atmospheric Measurement Techniques*, 12(12): pp. 6771–6802. doi:10.5194/amt-12-6771-2019.

Schreiber, E. A. P. and M. C. Serreze (2020). Impacts of synoptic-scale cyclones on Arctic sea-ice concentration: a systematic analysis. *Annals of Glaciology*, 61(82): pp. 139–153. doi:10.1017/aog.2020.23.

Scott, K. A., M. Buehner, A. Caya, and T. Carrieres (2012). Direct assimilation of AMSR-E brightness temperatures for estimating sea ice concentration. *Monthly Weather Review*, 140(3): pp. 997–1013. doi:10.1175/MWR-D-11-00014.1.

Screen, J. A. (2021). An ice-free Arctic: what could it mean for European weather? *Weather*, 76(10): pp. 327–328. doi:10.1002/wea.4069.

Screen, J. A. and I. Simmonds (2010). The central role of diminishing sea ice in recent Arctic temperature amplification. *Nature*, 464(7293): pp. 1334–1337. doi:10.1038/nature09051.

Semmler, T., R. McGrath, and S. Wang (2012). The impact of Arctic sea ice on the Arctic energy budget and on the climate of the Northern mid-latitudes. *Climate Dynamics*, 39(11): pp. 2675–2694. doi:10.1007/s00382-012-1353-9.

Serreze, M. C. and R. G. Barry (2011). Processes and impacts of Arctic amplification: A research synthesis. *Global and Planetary Change*, 77(1-2): pp. 85–96. doi:10.1016/j.gloplacha.2011.03.004.

Serreze, M. C. and J. A. Francis (2006). The Arctic amplification debate. *Climatic Change*, 76(3): pp. 241–264. doi:10.1007/s10584-005-9017-y.

Sharkov, E. A. (2003). *Passive microwave remote sensing of the Earth: physical foundations*. Springer-Praxis books in geophysical sciences. Springer Berlin, Heidelberg, Berlin; New York : Chichester, UK. ISBN 978-3-540-43946-2.

Shepherd, A., E. Ivins, E. Rignot, B. Smith, M. van den Broeke, I. Velicogna, P. Whitehouse, K. Briggs, I. Joughin, G. Krinner, S. Nowicki, T. Payne, T. Scambos, N. Schlegel, G. A, C. Agosta, A. Ahlstrøm, G. Babonis, V. R. Barletta, A. A. Bjørk, A. Blazquez,

J. Bonin, W. Colgan, B. Csatho, R. Cullather, M. E. Engdahl, D. Felikson, X. Fettweis, R. Forsberg, A. E. Hogg, H. Gallee, A. Gardner, L. Gilbert, N. Gourmelen, A. Groh, B. Gunter, E. Hanna, C. Harig, V. Helm, A. Horvath, M. Horwath, S. Khan, K. K. Kjeldsen, H. Konrad, P. L. Langen, B. Lecavalier, B. Loomis, S. Luthcke, M. McMillan, D. Melini, S. Mernild, Y. Mohajerani, P. Moore, R. Mottram, J. Mouginot, G. Moyano, A. Muir, T. Nagler, G. Nield, J. Nilsson, B. Noël, I. Otosaka, M. E. Pattle, W. R. Peltier, N. Pie, R. Rietbroek, H. Rott, L. Sandberg Sørensen, I. Sasgen, H. Save, B. Scheuchl, E. Schrama, L. Schröder, K.-W. Seo, S. B. Simonsen, T. Slater, G. Spada, T. Sutterley, M. Talpe, L. Tarasov, W. J. van de Berg, W. van der Wal, M. van Wessem, B. D. Vishwakarma, D. Wiese, D. Wilton, T. Wagner, B. Wouters, J. Wuite, and The IMBIE Team (2020). Mass balance of the Greenland Ice Sheet from 1992 to 2018. *Nature*, 579(7798): pp. 233–239. doi:10.1038/s41586-019-1855-2.

Shepherd, T. G. (2021). Bringing physical reasoning into statistical practice in climate-change science. *Climatic Change*, 169(1-2): p. 2. doi:10.1007/s10584-021-03226-6.

Shi, Y. (2019). Atmospheric Radiation Measurement (ARM) user facility. doi:10.5439/1507725. Surface Meteorological Instrumentation (PWD). 2019-10-11 to 2020-10-01, ARM Mobile Facility (MOS) MOSAIC (Drifting Obs - Study of Arctic Climate); AMF2 (M1). Compiled by Y. Shi. ARM Data Center. [Dataset. Accessed November 7, 2022].

Shine, K. P., I. V. Ptashnik, and G. Rädel (2012). The water vapour continuum: Brief history and recent developments. *Surveys in Geophysics*, 33(3-4): pp. 535–555. doi:10.1007/s10712-011-9170-y.

Shokr, M., K. Asmus, and T. A. Agnew (2009). Microwave emission observations from artificial thin sea ice: The ice-tank experiment. *IEEE Transactions on Geoscience and Remote Sensing*, 47(1): pp. 325–338. doi:10.1109/TGRS.2008.2005585.

Shokr, M. E. and N. K. Sinha (1994). Arctic sea ice microstructure observations relevant to microwave scattering. *Arctic*, 47(3): pp. 265–279. doi:10.14430/arctic1297.

Shupe, M. D., M. Rex, B. Blomquist, P. O. G. Persson, J. Schmale, T. Uttal, D. Althausen, H. Angot, S. Archer, L. Bariteau, I. Beck, J. Bilberry, S. Bucci, C. Buck, M. Boyer, Z. Brasseur, I. M. Brooks, R. Calmer, J. Cassano, V. Castro, D. Chu, D. Costa, C. J. Cox, J. Creamean, S. Crewell, S. Dahlke, E. Damm, G. de Boer, H. Deckelmann, K. Dethloff, M. Dütsch, K. Ebell, A. Ehrlich, J. Ellis, R. Engelmann, A. A. Fong, M. M. Frey, M. R. Gallagher, L. Ganzeveld, R. Gradinger, J. Graeser, V. Greenamyer, H. Griesche, S. Griffiths, J. Hamilton, G. Heinemann, D. Helmig, A. Herber, C. Heuzé, J. Hofer, T. Houchens, D. Howard, J. Inoue, H.-W. Jacobi, R. Jaiser, T. Jokinen, O. Jourdan, G. Jozef, W. King, A. Kirchgaessner, M. Klingebiel, M. Krassovski, T. Krumpen, A. Lampert, W. Landing, T. Laurila, D. Lawrence,

M. Lonardi, B. Loose, C. Lüpkes, M. Maahn, A. Macke, W. Maslowski, C. Marsay, M. Maturilli, M. Mech, S. Morris, M. Moser, M. Nicolaus, P. Ortega, J. Osborn, F. Pätzold, D. K. Perovich, T. Petäjä, C. Pilz, R. Pirazzini, K. Posman, H. Powers, K. A. Pratt, A. Preußer, L. Quéléver, M. Radenz, B. Rabe, A. Rinke, T. Sachs, A. Schulz, H. Siebert, T. Silva, A. Solomon, A. Sommerfeld, G. Spreen, M. Stephens, A. Stohl, G. Svensson, J. Uin, J. Viegas, C. Voigt, P. von der Gathen, B. Wehner, J. M. Welker, M. Wendisch, M. Werner, Z. Xie, and F. Yue (2022). Overview of the MOSAiC expedition: Atmosphere. *Elem Sci Anth*, 10(1): p. 00060. doi:10.1525/elementa.2021.00060.

Sikora, M., V. V. Pitulko, V. C. Sousa, M. E. Allentoft, L. Vinner, S. Rasmussen, A. Margaryan, P. de Barros Damgaard, C. de la Fuente, G. Renaud, M. A. Yang, Q. Fu, I. Dupanloup, K. Giampoudakis, D. Nogués-Bravo, C. Rahbek, G. Kroonen, M. Peyrot, H. McColl, S. V. Vasilyev, E. Veselovskaya, M. Gerasimova, E. Y. Pavlova, V. G. Chasnyk, P. A. Nikolskiy, A. V. Gromov, V. I. Khartanovich, V. Moiseyev, P. S. Grebenyuk, A. Y. Fedorchenko, A. I. Lebedintsev, S. B. Slobodin, B. A. Malyarchuk, R. Martiniano, M. Meldgaard, L. Arppe, J. U. Palo, T. Sundell, K. Mannermaa, M. Putkonen, V. Alexandersen, C. Primeau, N. Baimukhanov, R. S. Malhi, K.-G. Sjögren, K. Kristiansen, A. Wessman, A. Sajantila, M. M. Lahr, R. Durbin, R. Nielsen, D. J. Meltzer, L. Excoffier, and E. Willerslev (2019). The population history of northeastern Siberia since the Pleistocene. *Nature*, 570(7760): pp. 182–188. doi:10.1038/s41586-019-1279-z.

Smith, D. M. (1996). Extraction of winter total sea-ice concentration in the Greenland and Barents Seas from SSM/I data. *International Journal of Remote Sensing*, 17(13): pp. 2625–2646. doi:10.1080/01431169608949096.

Smith, M. M., B. Light, A. R. Macfarlane, D. K. Perovich, M. M. Holland, and M. D. Shupe (2022). Sensitivity of the Arctic sea ice cover to the summer surface scattering layer. *Geophysical Research Letters*, 49(9): p. e2022GL098349. doi:10.1029/2022GL098349.

Spreen, G., L. Kaleschke, and G. Heygster (2008). Sea ice remote sensing using AMSR-E 89-GHz channels. *Journal of Geophysical Research*, 113(C2): p. C02S03. doi:10.1029/2005JC003384.

Stevens, B. and S. Bony (2013). Water in the atmosphere. *Physics Today*, 66(6): pp. 29–34. doi:10.1063/PT.3.2009.

Stogryn, A. (1971). Equations for calculating the dielectric constant of saline water (correspondence). *IEEE Transactions on Microwave Theory and Techniques*, 19(8): pp. 733–736. doi:10.1109/TMTT.1971.1127617.

Stogryn, A. (1987). An analysis of the tensor dielectric constant of sea ice at microwave frequencies. *IEEE Transactions on Geoscience and Remote Sensing*, GE-25(2): pp. 147–158. doi:10.1109/TGRS.1987.289814.

Stogryn, A. and G. Desargant (1985). The dielectric properties of brine in sea ice at microwave frequencies. *IEEE Transactions on Antennas and Propagation*, 33(5): pp. 523–532. doi:10.1109/TAP.1985.1143610.

Stratton, J. A. (1941). Boundary-value problems. In *Electromagnetic theory*, chapter IX, pp. 482–600. McGraw-Hill, New York. ISBN 0470131535.

Stroeve, J., V. Nandan, R. Willatt, R. Dadic, P. Rostosky, M. Gallagher, R. Mallett, A. Barrett, S. Hendricks, R. Tonboe, M. McCrystall, M. Serreze, L. Thielke, G. Spreen, T. Newman, J. Yackel, R. Ricker, M. Tsamados, A. Macfarlane, H.-R. Hannula, and M. Schneebeli (2022). Rain on snow (ROS) understudied in sea ice remote sensing: a multi-sensor analysis of ROS during MOSAiC (Multidisciplinary drifting Observatory for the Study of Arctic Climate). *The Cryosphere*, 16(10): pp. 4223–4250. doi:10.5194/tc-16-4223-2022.

Sturm, M., J. Holmgren, M. König, and K. Morris (1997). The thermal conductivity of seasonal snow. *Journal of Glaciology*, 43(143): pp. 26–41. doi:10.3189/S0022143000002781.

Sturm, M. and R. A. Massom (2017). Snow in the sea ice system: friend or foe? In *Sea Ice*, chapter 3, pp. 65–109. John Wiley & Sons, Ltd. ISBN 978-1-118-77837-1. doi:10.1002/9781118778371.ch3.

Svendsen, E., C. Mätzler, and T. C. Grenfell (1987). A model for retrieving total sea ice concentration from a spaceborne dual-polarized passive microwave instrument operating near 90 ghz. *International Journal of Remote Sensing*, 8(10): pp. 1479–1487. doi:10.1080/01431168708954790.

Taylor, P. C., R. C. Boeke, L. N. Boisvert, N. Feldl, M. Henry, Y. Huang, P. L. Langen, W. Liu, F. Pithan, S. A. Sejas, and I. Tan (2022). Process drivers, inter-model spread, and the path forward: A review of amplified Arctic warming. *Frontiers in Earth Science*, 9: p. 758361. doi:10.3389/feart.2021.758361.

Thielke, L. (2023). *Winter sea ice characteristics in the central Arctic from thermal infrared imaging*. Ph.D. thesis, University of Bremen. doi:10.26092/elib/2305.

Thielke, L., M. Huntemann, and G. Spreen (2022). Lead classification maps from helicopter-borne surface temperatures during the mosaic expedition. doi:10.1594/PANGAEA.951569. [Dataset].

Tiuri, M., A. Sihvola, E. Nyfors, and M. Hallikaiken (1984). The complex dielectric constant of snow at microwave frequencies. *IEEE Journal of Oceanic Engineering*, 9(5): pp. 377–382. doi:10.1109/JOE.1984.1145645.

Tjernström, M., M. D. Shupe, I. M. Brooks, P. O. G. Persson, J. Prytherch, D. J. Salisbury, J. Sedlar, P. Achtert, B. J. Brooks, P. E. Johnston, G. Sotiropoulou, and D. Wolfe (2015). Warm-air advection, air mass transformation and fog causes rapid ice melt. *Geophysical Research Letters*, 42(13): pp. 5594–5602. doi:10.1002/2015GL064373.

Tomasi, C., B. H. Petkov, O. Drofa, and M. Mazzola (2020). Thermodynamics of the Arctic atmosphere. In Kokhanovsky, A. and C. Tomasi (editors), *Physics and Chemistry of the Arctic Atmosphere*, pp. 53–152. Springer International Publishing, Cham. ISBN 978-3-030-33566-3. doi:10.1007/978-3-030-33566-3_2.

Tonboe, R. T. (2010). The simulated sea ice thermal microwave emission at window and sounding frequencies. *Tellus A*, 62(3): pp. 333–344. doi:10.1111/j.1600-0870.2010.00434.x.

Tonboe, R. T., S. Andersen, and L. Toudal (2003). Anomalous winter sea ice backscatter and brightness temperatures. Technical report, Danish Meteorological Institute, Copenhagen.

Tonboe, R. T., Andersen, S, Toudal, L, and Heygster, G (2006). Sea ice emission modelling. In *Thermal Microwave Radiation-Applications for Remote Sensing*, volume 52, pp. 382–400. Institution of Engineering and Technology.

Tonboe, R. T., G. Dybkjær, and J. L. Høyer (2011). Simulations of the snow covered sea ice surface temperature and microwave effective temperature. *Tellus A: Dynamic Meteorology and Oceanography*, 63(5): p. 1028. doi:10.1111/j.1600-0870.2011.00530.x.

Torquato, S. and J. Kim (2021). Nonlocal effective electromagnetic wave characteristics of composite media: Beyond the quasistatic regime. *Physical Review X*, 11(2): p. 021002. doi:10.1103/PhysRevX.11.021002.

Triana-Gómez, A. M., G. Heygster, C. Melsheimer, and G. Spreen (2019). Improved water vapour retrieval from AMSU-B/MHS in polar regions. *Atmospheric Measurement Techniques Discussions*, pp. 1–24. doi:10.5194/amt-2019-253.

Troitsky, A. V., A. M. Osharin, A. V. Korolev, and J. W. Strapp (2003). Polarization of thermal microwave atmospheric radiation due to scattering by ice particles in clouds. *Journal of the Atmospheric Sciences*, 60(13): pp. 1608–1620. doi:10.1175/1520-0469(2003)60<1608:POTMAR>2.0.CO;2.

Troy, B. E., J. P. Hollinger, R. M. Lerner, and M. M. Wisler (1981). Measurement of the microwave properties of sea ice at 90 GHz and lower frequencies. *Journal of Geophysical Research*, 86(C5): p. 4283. doi:10.1029/JC086iC05p04283.

Tsang, L. and J. A. Kong (2008). Multiple scattering of electromagnetic waves by random distributions of discrete scatterers with coherent potential and quantum mechanical formalism. *Journal of Applied Physics*, 51(7): pp. 3465–3485. doi:10.1063/1.328200.

Tsang, L. and J. A. Kong (editors) (2009). *Scattering of electromagnetic waves: numerical simulations*. Wiley series in remote sensing. Wiley, New York, NY Weinheim, nachdr. edition. ISBN 978-0-471-38800-5.

Tsang, L., J. A. Kong, and K.-H. Ding (2000). Characteristics of discrete scatterers and rough surfaces. In *Scattering of Electromagnetic Waves: Theories and Applications*, chapter 4, pp. 167–197. John Wiley & Sons, Ltd. ISBN 978-0-471-22428-0. doi:10.1002/0471224286.ch4.

Tsang, L., S. Tan, X. Xu, and K.-H. Ding (2016). Scattering and emission models for microwave remote sensing of snow using numerical solutions of Maxwell equations. In *2016 IEEE international geoscience and remote sensing symposium (IGARSS)*, pp. 7050–7052. doi:10.1109/IGARSS.2016.7730838.

Tschudi, M., W. M. Meier, J. S. Stewart, C. Fowler, and J. Maslanik. (2019). EASE-Grid sea ice age, version 4. doi:10.5067/UTAV7490FEPB. [Dataset].

Tucker, W. B., D. K. Perovich, A. J. Gow, W. F. Weeks, and M. R. Drinkwater (1992). Physical properties of sea ice relevant to remote sensing. In Carsey, F. D. (editor), *Geophysical Monograph Series*, volume 68, pp. 9–28. American Geophysical Union, Washington, D. C. ISBN 978-0-87590-033-9. doi:10.1029/GM068p0009.

Tucker III, W. B., T. C. Grenfell, R. G. Onstott, D. K. Perovich, A. J. Gow, R. A. Snuchman, and L. L. Sutherland (1991). Microwave and physical properties of sea ice in the winter marginal ice zone. *Journal of Geophysical Research: Oceans*, 96(C3): pp. 4573–4587. doi:10.1029/90JC02269.

Turner, D. D., S. A. Clough, J. C. Liljegren, E. E. Clothiaux, K. E. Cady-Pereira, and K. L. Gaustad (2007). Retrieving liquid water path and precipitable water vapor from the Atmospheric Radiation Measurement (ARM) microwave radiometers. *IEEE Transactions on Geoscience and Remote Sensing*, 45(11): pp. 3680–3690. doi:10.1109/TGRS.2007.903703.

Ulaby, F. and D. Long (2014). *Microwave Radar and Radiometric Remote Sensing*. University of Michigan Press. ISBN 978-0-472-11935-6. doi:10.3998/0472119356.

Union of Concerned Scientists (2023). UCS Satellite Database. [Website. Retrieved from https://www.ucsusa.org/resources/satellite-database October 1, 2023].

Valkonen, E., J. Cassano, and E. Cassano (2021). Arctic cyclones and their interactions with the declining sea ice: A recent climatology. *Journal of Geophysical Research: Atmospheres*, 126(12). doi:10.1029/2020JD034366.

van Huissteden, J. (2020). Introduction. In van Huissteden, J. (editor), *Thawing Permafrost: Permafrost Carbon in a Warming Arctic*, pp. 1–50. Springer International Publishing, Cham. ISBN 978-3-030-31379-1. doi:10.1007/978-3-030-31379-1_1.

Van Vleck, J. H. and V. F. Weisskopf (1945). On the shape of collision-broadened lines. *Reviews of Modern Physics*, 17(2-3): pp. 227–236. doi:10.1103/RevModPhys.17.227.

Vihma, T., J. Screen, M. Tjernström, B. Newton, X. Zhang, V. Popova, C. Deser, M. Holland, and T. Prowse (2016). The atmospheric role in the Arctic water cycle: A review on processes, past and future changes, and their impacts. *Journal of Geophysical Research: Biogeosciences*, 121(3): pp. 586–620. doi:10.1002/2015JG003132.

Virtanen, P., R. Gommers, T. E. Oliphant, M. Haberland, T. Reddy, D. Cournapeau, E. Burovski, P. Peterson, W. Weckesser, J. Bright, S. J. van der Walt, M. Brett, J. Wilson, K. J. Millman, N. Mayorov, A. R. J. Nelson, E. Jones, R. Kern, E. Larson, C. J. Carey, İ. Polat, Y. Feng, E. W. Moore, J. VanderPlas, D. Laxalde, J. Perktold, R. Cimrman, I. Henriksen, E. A. Quintero, C. R. Harris, A. M. Archibald, A. H. Ribeiro, F. Pedregosa, P. van Mulbregt, and SciPy 1.0 Contributors (2020). Scipy 1.0: Fundamental algorithms for scientific computing in python. *Nature Methods*, 17: pp. 261–272. doi:10.1038/s41592-019-0686-2.

Wagner, D. N., M. D. Shupe, C. Cox, O. G. Persson, T. Uttal, M. M. Frey, A. Kirchgaessner, M. Schneebeli, M. Jaggi, A. R. Macfarlane, P. Itkin, S. Arndt, S. Hendricks, D. Krampe, M. Nicolaus, R. Ricker, J. Regnery, N. Kolabutin, E. Shimanshuck, M. Oggier, I. Raphael, J. Stroeve, and M. Lehning (2022). Snowfall and snow accumulation during the MOSAiC winter and spring seasons. *The Cryosphere*, 16(6): pp. 2373–2402. doi:10.5194/tc-16-2373-2022.

Walbröl, A., S. Crewell, R. Engelmann, E. Orlandi, H. Griesche, M. Radenz, J. Hofer, D. Althausen, M. Maturilli, and K. Ebell (2022). Atmospheric temperature, water vapour and liquid water path from two microwave radiometers during MOSAiC. *Scientific Data*, 9(1): p. 534. doi:10.1038/s41597-022-01504-1.

Walbröl, A., J. Michaelis, S. Becker, H. Dorff, I. Gorodetskaya, B. Kirbus, M. Lauer, N. Maherndl, M. Maturilli, J. Mayer, H. Müller, R. A. J. Neggers, F. M. Paulus, J. Röttenbacher, J. E. Rückert, I. Schirmacher, N. Slättberg, A. Ehrlich, M. Wendisch, and S. Crewell (2023). Environmental conditions in the North Atlantic sector of the Arctic during the HALO–$(AC)^3$ campaign. *EGUsphere*, 2023: pp. 1–48. doi:10.5194/egusphere-2023-668. [preprint].

Wang, C., R. M. Graham, K. Wang, S. Gerland, and M. A. Granskog (2019). Comparison of ERA5 and ERA-Interim near-surface air temperature, snowfall and precipitation over Arctic sea ice: effects on sea ice thermodynamics and evolution. *The Cryosphere*, 13(6): pp. 1661–1679. doi:10.5194/tc-13-1661-2019.

Wang, D., C. Prigent, L. Kilic, S. Fox, C. Harlow, C. Jimenez, F. Aires, C. Grassotti, and F. Karbou (2017). Surface emissivity at microwaves to millimeter waves over polar regions: Parameterization and evaluation with aircraft experiments. *Journal of Atmospheric and Oceanic Technology*, 34(5): pp. 1039–1059. doi:10.1175/JTECH-D-16-0188.1.

Warren, S. G., I. G. Rigor, N. Untersteiner, V. F. Radionov, N. N. Bryazgin, Y. I. Aleksandrov, and R. Colony (1999). Snow depth on Arctic sea ice. *Journal of Climate*, 12(6): pp. 1814–1829. doi:10.1175/1520-0442(1999)012<1814:SDOASI>2.0.CO;2.

Waters, J. (1976). Absorption and emission by atmospheric gases. In Meeks, M. (editor), *Astrophysics*, volume 12 of *Methods in Experimental Physics*, pp. 142–176. Academic Press. ISBN 978-0-12-475952-7. doi:10.1016/S0076-695X(08)60684-5.

Weeks, W. and O. Lee (1962). The salinity distribution in young sea-ice. *ARCTIC*, 15(2): pp. 92–108. doi:10.14430/arctic3562.

Wendisch, M., M. Brückner, J. Burrows, S. Crewell, K. Dethloff, K. Ebell, C. Lüpkes, A. Macke, J. Notholt, J. Quaas, A. Rinke, and I. Tegen (2017). Understanding causes and effects of rapid warming in the Arctic. *Eos*. doi:10.1029/2017EO064803.

Wendisch, M., M. Brückner, S. Crewell, A. Ehrlich, J. Notholt, C. Lüpkes, A. Macke, J. P. Burrows, A. Rinke, J. Quaas, M. Maturilli, V. Schemann, M. D. Shupe, E. F. Akansu, C. Barrientos-Velasco, K. Bärfuss, A.-M. Blechschmidt, K. Block, I. Bougoudis, H. Bozem, C. Böckmann, A. Bracher, H. Bresson, L. Bretschneider, M. Buschmann, D. G. Chechin, J. Chylik, S. Dahlke, H. Deneke, K. Dethloff, T. Donth, W. Dorn, R. Dupuy, K. Ebell, U. Egerer, R. Engelmann, O. Eppers, R. Gerdes, R. Gierens, I. V. Gorodetskaya, M. Gottschalk, H. Griesche, V. M. Gryanik, D. Handorf, B. Harm-Altstädter, J. Hartmann, M. Hartmann, B. Heinold, A. Herber, H. Herrmann, G. Heygster, I. Höschel, Z. Hofmann, J. Hölemann, A. Hünerbein, S. Jafariserajehlou, E. Jäkel, C. Jacobi, M. Janout, F. Jansen, O. Jourdan, Z. Jurányi, H. Kalesse-Los, T. Kanzow, R. Käthner, L. L. Kliesch, M. Klingebiel, E. M. Knudsen, T. Kovács, W. Körtke, D. Krampe, J. Kretzschmar, D. Kreyling, B. Kulla, D. Kunkel, A. Lampert, M. Lauer, L. Lelli, A. von Lerber, O. Linke, U. Löhnert, M. Lonardi, S. N. Losa, M. Losch, M. Maahn, M. Mech, L. Mei, S. Mertes, E. Metzner, D. Mewes, J. Michaelis, G. Mioche, M. Moser, K. Nakoudi, R. Neggers, R. Neuber, T. Nomokonova, J. Oelker, I. Papakonstantinou-Presvelou, F. Pätzold, V. Pefanis, C. Pohl, M. van Pinxteren,

A. Radovan, M. Rhein, M. Rex, A. Richter, N. Risse, C. Ritter, P. Rostosky, V. V. Rozanov, E. R. Donoso, P. Saavedra Garfias, M. Salzmann, J. Schacht, M. Schäfer, J. Schneider, N. Schnierstein, P. Seifert, S. Seo, H. Siebert, M. A. Soppa, G. Spreen, I. S. Stachlewska, J. Stapf, F. Stratmann, I. Tegen, C. Viceto, C. Voigt, M. Vountas, A. Walbröl, M. Walter, B. Wehner, H. Wex, S. Willmes, M. Zanatta, and S. Zeppenfeld (2023). Atmospheric and surface processes, and feedback mechanisms determining Arctic amplification: A review of first results and prospects of the (AC)3 project. *Bulletin of the American Meteorological Society*, 104(1): pp. E208–E242. doi:10.1175/BAMS-D-21-0218.1.

Wentz, F. J. and T. Meissner (2000). Algorithm theoretical basis document: AMSR ocean algorithm, version 2. Technical report, Remote Sensing Systems, Santa Rosa, CA.

Wever, N., L. Rossmann, N. Maaß, K. C. Leonard, L. Kaleschke, M. Nicolaus, and M. Lehning (2019). Version 1 of a sea ice module for the physics based, detailed, multi-layer SNOWPACK model. preprint, Cryosphere. doi:10.5194/gmd-2019-97.

Wiesmann, A. and C. Mätzler (1999). Microwave Emission Model of Layered Snowpacks. *Remote Sensing of Environment*, 70(3): pp. 307–316. doi:10.1016/S0034-4257(99)00046-2.

Wilheit, T., W. Nordberg, J. Blinn, W. Campbell, and A. Edgerton (1971). Aircraft measurements of microwave emission from Arctic sea ice. *Remote Sensing of Environment*, 2: pp. 129–139. doi:10.1016/0034-4257(71)90087-3.

Wivell, K., S. Fox, M. Sandells, C. Harlow, R. Essery, and N. Rutter (2023). Evaluating Snow Microwave Radiative Transfer (SMRT) model emissivities with 89 to 243 GHz observations of Arctic tundra snow. *The Cryosphere*, 17(10): pp. 4325–4341. doi:10.5194/tc-17-4325-2023.

Woods, C. and R. Caballero (2016). The role of moist intrusions in winter Arctic warming and sea ice decline. *J. Clim.*, 29(12): pp. 4473–4485. doi:10.1175/JCLI-D-15-0773.1.

Woods, C., R. Caballero, and G. Svensson (2013). Large-scale circulation associated with moisture intrusions into the Arctic during winter. *Geophys. Res. Lett.*, 40: pp. 4717–4721. doi:10.1002/grl.50912.

Ye, Y., G. Heygster, and M. Shokr (2016a). Improving multiyear ice concentration estimates with reanalysis air temperatures. *IEEE Transactions on Geoscience and Remote Sensing*, 54(5): pp. 2602–2614. doi:10.1109/TGRS.2015.2503884.

Ye, Y., M. Shokr, G. Heygster, and G. Spreen (2016b). Improving multiyear sea ice concentration estimates with sea ice drift. *Remote Sensing*, 8(5): p. 397. doi:10.3390/rs8050397.

Zhang, D. (2023). MWR Retrievals (MWRRET1LILJCLOU). Atmospheric Radiation Measurement (ARM) user facility. doi:10.5439/1027369. [Dataset].

Zhang, P., G. Chen, M. Ting, L. Ruby Leung, B. Guan, and L. Li (2023). More frequent atmospheric rivers slow the seasonal recovery of Arctic sea ice. *Nature Climate Change*, pp. 1–8. doi:10.1038/s41558-023-01599-3.

Zhou, L., L. Tsang, V. Jandhyala, Q. Li, and C. H. Chan (2004). Emissivity simulations in passive microwave remote sensing with 3-D numerical solutions of Maxwell equations. *IEEE Transactions on Geoscience and Remote Sensing*, 42(8): pp. 1739–1748. doi:10.1109/TGRS.2004.830639.

Acknowledgments

Being a PhD candidate was an overall splendid time despite a pandemic and the numerous drawbacks one encounters when doing research. I can hugely attribute the good times to the outstanding supervision, the wonderful working environment and the exceptional support from my friends and family. So I would like to use the last pages of my (already long) thesis to say thank you. I am very grateful to my supervisor Dr. Gunnar Spreen, and to Dr. Christian Melsheimer and Dr. Marcus Huntemann for the countless discussions, suggestions and encouragements throughout the entire thesis process. While the discussions sometimes left us "still confused but on a higher level" they were always shaped by appreciation. Writing my first study about sea ice together with Dr. Philip Rostosky was a great experience and even though it took long Philip always stayed positive. I very much appreciate everyone in the working group *Remote Sensing of Polar Regions*, especially my fellow doctoral candidates, Linda, Hannah and Alex. Their constructive feedback, ideas, and attentive ears helped immensely. I am grateful to Julia who has made moving to Bremen and starting at the IUP a lot easier and to my former colleague Valentin who introduced me to Bremen in a lock-down.

I would like to thank Prof. Dr. Susanne Crewell for being the second examiner of this thesis and for her support within $(AC)^3$. I would like to express my appreciation to the whole $(AC)^3$ consortium, especially to the IRTG coordinators and the early career researchers, for their mentoring and support, including the organization of conferences, workshops and the winter school in Finland; and of course for the marvelous opportunity for me to continue doing what I have come to enjoy so much and to further pursue my research in the third phase of $(AC)^3$ as a postdoc.

Joining the ATWAICE expedition was a fantastic chance: I want to thank the crew and scientists (on board and those who helped enabling it beforehand, in particular the WALSEMA team) for these research and learning opportunities, especially Andreas and Hannah (Hannah also happened to be the best bunkmate on Polarstern that I could have wished for).

My thanks to my thesis committee, namely Dr. Kerstin Ebell, Dr. Marcus Huntemann, Dr. Christian Melsheimer, Dr. Raul Scarlat, and Dr. Gunnar Spreen who provided excellent guidance throughout every year of my dissertation. I very much appreciate the

contribution of my co-authors to the manuscripts on which Chapter 3.3, Chapter 4 and parts of Chapter 5 are based on.Thank you to Christian, Fredde, Hannah, Jonas, Julia, Karl, Leon, Linda, Malte, Marcus, Moritz and Valentin for proofreading parts of this thesis; and to Svenja, thank you for our peer-mentoring. I am also grateful for the people who encouraged me along my scientific journey before joining the IUP, in particular Prof. Dr. Carsten Timm.

The importance of my friends and family cannot be highlighted enough. Thank you, Fredde, for your constant support, for climbing real mountains and mountains of challenges with me, I can always rely on you. To my friends: you supported me throughout the last years and beyond, and without you, this work would not have been possible! Thank you to old and new friends, especially all the wonderful women in my life who empower and inspire me, including Hilke, Luzie, Paula, Julia, Lena and Co. To my brother Leon, and my parents: thank you, for everything, for your love and unconditional support. We have faced hard times but we kept a sense of humor!